MICROCOPY RESOLUTION TEST CHART

NATIONAL BUREAU OF STANDARDS-1963-A

AD-A134 230

AN INVESTIGATION OF AIRFOIL DYNAMIC STALL WITH LARGE AMPLITUDE MOTIONS

FINAL REPORT

DTIC
ELECTE
NOV 1 1983

A
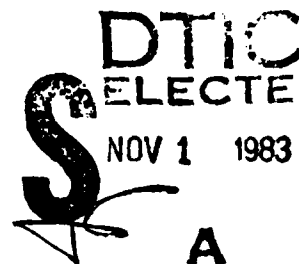
CAPTAIN MICHAEL S. FRANCIS
CAPTAIN JOHN E. KEESEE
MAJOR JOHN P. RETELLE, JR.

PROJECT 2307-F1-36

DTIC FILE COPY

AIR FORCE SYSTEMS COMMAND
UNITED STATES AIR FORCE

83 10 31 030

This document was prepared by the Mechanics Division, Directorate of Aerospace-Mechanics, Frank J. Seiler Research Laboratory, United States Air Force Academy, Colorado Springs, CO. The research was conducted under Project Work Unit Number 2307-F1-36, Major John P. Retelle, Jr. was the Project Scientist in charge of the work.

When U.S. Government drawings, specifications or other data are used for any purpose other than a definitely related government procurement operation, the government thereby incurs no responsibility nor any obligation whatsoever, and the fact that the government may have formulated, furnished, or in any way supplied the said drawings, specifications or other data is not to be regarded by implication or otherwise, as in any manner licensing the holder or any other person or corporation or conveying any rights or permission to manufacture, use or sell any patented invention that may in any way be related thereto.

Inquiries concerning the technical content of this document should be addressed to the Frank J. Seiler Research Laboratory (AFSC), FJSRL/NH, USAF Academy, Colorado Springs, CO 80840. Phone AC 303 472-3122.

This report has been reviewed by the Commander and is releasable to the National Technical Information Service (NTIS). At NTIS it will be available to the general public, including foreign nations.

This technical report has been reviewed and is approved for publication.

HENRY C. HELIN, 2DLT, USAF
Task Manager

ALBERT J. ALEXANDER, Major, USAF
D'rector, Aero-Mech Sciences

THEODORE T. SAITO, Lt Col, USAF
Commander

Copies of this report should not be returned unless return is required by security considerations, contractual obligations, or notice on a specific document.

Printed in the United States of America. Qualified requestors may obtain additional copies from the Defense Technical Information Center. All others should apply to: National Technical Information Service
                                    6285 Port Royal Road
                                    Springfield, Virginia 22161

REPORT DOCUMENTATION PAGE

1a. REPORT SECURITY CLASSIFICATION	1b. RESTRICTIVE MARKINGS
UNCLASSIFIED	

2a. SECURITY CLASSIFICATION AUTHORITY	3. DISTRIBUTION/AVAILABILITY OF REPORT
	Approved for public release; distribution unlimited
2b. DECLASSIFICATION/DOWNGRADING SCHEDULE	

4. PERFORMING ORGANIZATION REPORT NUMBER(S)	5. MONITORING ORGANIZATION REPORT NUMBER(S)
FJSRL-TR-83-0010	

6a. NAME OF PERFORMING ORGANIZATION	6b. OFFICE SYMBOL (If applicable)	7a. NAME OF MONITORING ORGANIZATION
Frank J. Seiler Research Lab	NHM	

6c. ADDRESS (City, State and ZIP Code)	7b. ADDRESS (City, State and ZIP Code)
USAF Academy Colorado Springs, Colorado 80840	

8a. NAME OF FUNDING/SPONSORING ORGANIZATION	8b. OFFICE SYMBOL (If applicable)	9. PROCUREMENT INSTRUMENT IDENTIFICATION NUMBER

8c. ADDRESS (City, State and ZIP Code)	10. SOURCE OF FUNDING NOS.			
	PROGRAM ELEMENT NO.	PROJECT NO.	TASK NO.	WORK UNIT NO.
11. TITLE (Include Security Classification) An Investigation of Airfoil Dynamic Stall With Large Amplitude Motions (U)	61102F		2307-F1	36

12. PERSONAL AUTHOR(S) Francis, Michael S., Captain, AFOSR/NA
Keesee, John E., Captain, BMO/SYMS   Retelle, John R., Jr., Major, HRL/MNRTE

13a. TYPE OF REPORT	13b. TIME COVERED	14. DATE OF REPORT (Yr., Mo., Day)	15. PAGE COUNT
Final	FROM Jun 76 TO Jun 83	1983 October	159

16. SUPPLEMENTARY NOTATION

17. COSATI CODES			18. SUBJECT TERMS (Continue on reverse if necessary and identify by block number)
FIELD	GROUP	SUB. GR.	Fluid Mechanics, Airfoil Aerodynamics, Unsteady Flow, Separated Flow, Dynamic Stall, Vortices, Separation Vortex
0101	2004	0102	

19. ABSTRACT (Continue on reverse if necessary and identify by block number)

The results of an experimental investigation of airfoil dynamic stall involving large amplitude pitching motions are described. The discussion is focused on constant pitch rate motion histories. Measurements of unsteady surface pressure distributions for both NACA 0012 and NACA 64-A012(13) profiles have been employed to infer the onset and evolution of an energetic leading edge separation vortex over a wide range of flow and motion conditions. These data have also been integrated to provide estimates of the time histories of the lift, pressure drag and moment coefficients. The effectiveness of the various motions for achieving lift enhancement has been determined through the introduction of a dimensionless impulse parameter which accounts for both the magnitude and duration of the additional lift increment during the post-stall period.

20. DISTRIBUTION/AVAILABILITY OF ABSTRACT	21. ABSTRACT SECURITY CLASSIFICATION
UNCLASSIFIED/UNLIMITED ☒ SAME AS RPT. ☒ DTIC USERS ☐	UNCLASSIFIED

22a. NAME OF RESPONSIBLE INDIVIDUAL	22b. TELEPHONE NUMBER (Include Area Code)	22c. OFFICE SYMBOL
MICHAEL S. FRANCIS, Captain, USAF	(202) 767-4935	AFOSR/NA

DD FORM 1473, 83 APR   EDITION OF 1 JAN 73 IS OBSOLETE.

AN INVESTIGATION OF AIRFOIL DYNAMIC

STALL WITH LARGE AMPLITUDE MOTIONS

-by-

Captain Michael S. Francis*
Captain John E. Keesee**
Major John P. Retelle, Jr.+

Frank J. Seiler Research Laboratory
USAF Academy, Colorado

* current address – AFOSR/NA, Bolling AFB, DC
** current address – BMO/SYMS, Norton AFB, California
\+ current address – HRL/MNRTE, Williams AFB, Arizona

TABLE OF CONTENTS

ii

LIST OF FIGURES

ABSTRACT

The results of an experimental investigation of airfoil dynamic stall involving large amplitude pitching motions are described. The discussion is focused on constant pitch rate motion histories. Measurements of unsteady surface pressure distributions for both NACA 0012 and NACA 64_1A012(13) profiles have been employed to infer the onset and evolution of an energetic leading edge separation vortex over a wide range of flow and motion conditions. These data have also been integrated to provide estimates of the time histories of the lift, pressure drag and moment coefficients. The effectiveness of the various motions for achieving lift enhancement has been determined through the introduction of a dimensionless impulse parameter which accounts for both the magnitude and duration of the additional lift increment during the post-stall period.

I. INTRODUCTION

The problem of airfoil dynamic stall has been researched extensively
since it became a prominant topic during the late 1960's. Most studies
of this interesting aerodynamic phenomenon have been motivated by the
desire to understand the source and behavior of torsional helicopter
blade oscillations and their effect on high speed rotor performance. As
a consequence, most of the available results have been generated for a
range of conditions and lifting configurations which attempt to emulate
the rotor flight environment.[1-9]

The present investigation is concerned with the evolution of the
dynamic stall flowfield from a more fundamental perspective and with a
decidedly different motivation. Specifically, it is focused on several
aspects of the process including unsteady vortex lift generation with an
orientation toward potential productive applications.

The essential features of the dynamic stall flowfield created by
harmonic airfoil oscillations in an otherwise steady and uniform free-
stream have been described by McCroskey and his coworkers.[1-3] The
behavior of the flow for what has been termed the "deep stall" case is
of special significance here. For large amplitude oscillations in pitch,
the flow near the airfoil surface is observed to remain "attached" during
the airfoil upstroke to a point well beyond the static stall incidence
angle. This delay in incipient separation is followed by the formation
of an energetic vortex structure near the airfoil leading edge which
grows with time and convects downstream as the airfoil motion proceeds.
A steep suction peak in the instantaneous pressure distribution on the
upper surface is observed to remain coincident with the location of the

vortex. The resulting high lift transient and subsequent severe nose down pitching moment (sometimes referred to as "moment stall") are now familiar to many aerodynamists.

Several, more general observations can be distilled from an examination of these results. The first of these is that this class of flow behavior must be viewed and treated as a "process;" that is, these unsteady flows are comprised of a sequential time history of events whose characteristics, at any instant, are the result of a complex interaction between the external flow environment, the past flow history and the continuously changing, time dependent boundary conditions. More profoundly, these results suggest that the term "flow separation" be redefined to accommodate the notion of flowfield reorganization, if only on a transient basis, which is apparent in many of these unsteady flow problems. In this context, the term separation is not meant to infer a spatially local event,[10] but rather to describe the global flow behavior associated with a particular configuration and its time history of motion.[1,11]

In this light, the unsteady separation process associated with dynamic airfoil excursions might be viewed as a possible vehicle for extracting freestream kinetic energy for the purpose of enhanced aerodynamic lift generation. Of course, this process must result in an increase in the overall airfoil drag coefficient, but there may be applications where this concomitent high lift, high drag phenomenon could be productively exploited, e.g., for flight vehicle maneuver enhancement.

Special emphasis is placed on the role of the dynamic separation vortex in the unsteady lift generation process. In this regard, it is of interest to consider those conditions which might result in increased energization of the vortex and the separate, but related, problem of

optimizing the entrapment time of the vortex structure near the airfoil surface. The concept of employing an externally "trapped" vortex for enhanced lift is not original here,[12] but the idea of generating and controlling the characteristics of an unsteady separation vortex for this purpose is unique. (This idea is also being explored independently by Chow and his coworkers.[13]) The problem can be viewed as one of optimizing the time dependent boundary conditions to maximize the lift augmentation.

As a first step, experiments have been devised to provide new insight into the influence of the motion time history on the dynamic stall flow-field and resultant airfoil loading. This report describes and discusses the results of a preliminary investigation which focuses on anharmonic unsteady airfoil motions with large amplitude variations. Instantaneous pressure measurements have been obtained over upper and lower airfoil surfaces and used in the reconstruction of phase-averaged pressure distributions. These, in turn, have been integrated spatially to estimate force and pitching moment time histories. All measured time-dependent variables have been correlated with the appropriate airfoil motion history.

The study was restricted to conventional (i.e., rigid shape) airfoil geometries due to limitations in available experimental capabilities. In principal, however, it could have been extended to include the effects of arbitrary, time dependent airfoil shapes. The concept of employing a "flexible" lifting surface in combination with equivalent rigid body motions to optimize unsteady separation effects is an intriguing one.

Although acknowledged to have a potentially profound effect on the dynamic stall process, the "motion time history" is one of the least understood contributors to the overall flow development.[7,8] Several

prior studies have been performed in an attempt to assess the signifi-
cance of this facet of behavior. Besides pure pitching motion, unsteady
free stream (or, surge) oscillations have been investigated for fixed
airfoil incidence conditions.[14,15] Limited studies of combined pitching
and surging oscillations have also been conducted.[16,17] Plunging airfoil
motion has received recent attention.[18] Despite these efforts, a unified
and physically consistent picture of the effects of motion time history
has yet to emerge. This is due, in part, to the extremely large range
of parametric variables which must be considered to adequately characterize
these effects.

Some progress has been made for the case of pure pitching oscilla-
tions about a point interior to the airfoil. Early experiments involving
anharmonic pitch motions revealed the importance of pitch rate $(\dot{\alpha})$ as a
dominant variable. This was suggested by Kramer[19] as early as 1932 and
confirmed in relatively recent measurements by Ham and Garelick[6] and
Kawashima, et al.[20]

The present experimental investigation was designed to complement
prior studies by extending the range of conditions of known important
parameters (such as pitch rate) and examining the effects of motion
variables and combinations of variables which have not yet been adequately
studied. A unique model oscillation system described in the next section
provided a capability to study motion in two degrees of freedom simul-
taneously - one in rotation (pitch), and one in translation (either
surging or plunging motion). To date, experiments have been performed
to examine:

(a) constant pitch rate motion $(\dot{\alpha} = constant)$

(b) constant pitch rate motion followed by sudden reversal in
pitch direction

(c)   constant pitch acceleration ($\ddot{\alpha}$ = constant)

(d)   harmonic pitch oscillations with variable termination angle

(e)   combined constant pitch rate and constant axial acceleration

(f)   combined constant pitch rate and constant axial deceleration, and

(g)   combined constant pitch rate and constant axial translation rate (impulsive surge).

Because of the large parameter space, the amount of data involved in assessing even this limited class of motions over a reasonable range is quite extensive. This report is therefore confined to a discussion of the measurements of constant pitch rate only. Because of the importance of this variable in establishing the character of the dynamic stall flowfield, a disproportionately large number of measurements were obtained for this condition [cases (a) and (b)]. The effects of other airfoil motion combinations will be discussed in a later report.

The parametric effects described in this report include the influence of nondimensional pitch rate (described through the variable, $k \equiv \dot{\alpha}c/2U_{\infty}$), and the pitch amplitude, α_{max}. The pitch rate range was varied over nearly three orders of magnitude ($0.001 < k < 0.2$). All motion was initiated at an initial airfoil incidence angle of zero degrees. The amplitude variation extended to extremely high incidence angles ($\alpha_{max} \cong 60°$) well in excess of values employed in any known prior studies.

The influence of airfoil shape was also investigated to the extent that two different airfoil models were employed in the study. A 6-inch chord (c = 15.24 cm) NACA 0012 airfoil model was used in an initial test sequence and later complemented by an 8-inch chord (c = 20.32 cm) NACA

64_1A012(13) airfoil model. The use of these two different shapes provided a limited measure of the influence of airfoil leading edge radius (as suggested by McCroskey[2]) as well as the effect of different static airfoil pressure gradients, if any, for the case of large amplitude motions.

II. DESCRIPTION OF THE EXPERIMENT

II.1 MODEL OSCILLATOR SYSTEM

An investigation of the effect of arbitrary motions on the dynamic
stall process is highly dependent on the development of a suitable model
oscillation mechanism capable of offering a wide range of motion alterna-
tives. To that end an apparatus capable of providing simultaneous motions
of an airfoil or wing model in both pitch and translation was designed
and fabricated. In combination with the measurement techniques described
below, the concept affords a high degree of cycle-to-cycle repeatability
and a potential to generate any of a virtually infinite variety of simul-
taneous complex motions in both rotation and translation. The system
was specifically designed and constructed to interface with the U.S. Air
Force Academy's 2 foot (61 cm) x 3 foot (91 cm) subsonic wind tunnel -
the facility in which these studies were conducted. A detailed descrip-
tion of this flow facility and its characteristics are provided in
reference 21.

The model oscillation system is functionally composed of four elements:
(1) the mechanical assembly or "motion transfer apparatus," (2) dual
hybrid servo drive units, (3) microcomputer control system, and (4) the
model and model interface collar. These elements are depicted schemati-
cally in Figure II-1. The function and operation of each of these elements
will be described briefly. For a more complete discussion of the oscilla-
tion system and its characteristics, the reader is referred to reference
22.

II.1.1 Motion Transfer Apparatus

The motion transfer apparatus is a mechanical assembly consisting of various drive train components mounted on an aluminum frame which transfers mechanical energy from the drive motors to the wind tunnel model. During operation, the unit is located outside of and below the wind tunnel test section so that only the model protrudes into the air stream. A perspective view of the complete apparatus is provided in Figure II-2, as viewed from the downstream quarter.

The drive system is configured in a dual yoke arrangement which provides uncoupled motions in rotation (pitching motion, in this case) and a single degree of translation. The pitch drive assembly, including the pitch motor, is "piggy-backed" on the translational drive unit.

Pitch motion is generated through the pitch yoke subassembly depicted in a top view in Figure II-3. The mechanical transfer function which relates the instantaneous model pitch angle (α) to the motor shaft displacement angle (θ_1) can be written:

$$\alpha - \alpha_o = \frac{r_2}{r_1} (1 - \cos \theta_1) \tag{1}$$

where

r_1 = spur gear pitch radius,

and

r_2 = fly wheel attachment radius.

The maximum pitch angle which could be attained is observed to be a function of the flywheel and gear radii, namely,

$$\alpha_{max} = \alpha_o + 2 \frac{r_2}{r_1} \tag{2}$$

The entire pitch oscillation mechanism, including model and drive motor, is mounted directly to the translational drive yoke assembly. This unit is shown in Figure II-4 (top view), which also depicts the relative location of the pitch oscillator components. The mechanical operation of the translational drive train is functionally similar to that of the pitch assembly. However, it was not employed in the pitch-only experiments described in this report, and will not be further discussed. Precision, linear, servo-mount potentiometers interfaced with the mechanical drive assemblies serve as reference position trans-ducers. Their outputs provide model angle and position measurements with less than 0.05% offset error for unidirectional motions.

II.1.2 Hybrid Servo Drive Units

The selection of a suitable drive concept to power the two oscillator stages was severely impacted by two demanding performance requirements, namely, (1) maximization of system dynamic response, and (2) the selectable variation of the time histories of the motion parameters, $\alpha(t)$ and $x(t)$. The first of these is readily attainable through the application of closed loop control techniques. The latter requirement, it was believed, could best be satisfied through the use of real time computer control. Ultimately, both requirements were met by employing both of these ideas and utilizing a device known as a "servo-translator."

The operation of the resultant servo system utilizes both velocity and position feedback to achieve effective control. Such a mechanism is shown schematically in Figure II-5. The input voltage to the servo controller is a "velocity command" which is instantaneously and continu-ously compared to the velocity feedback signal provided from a tachometer

attached to the drive motor. The difference, the velocity-error voltage, is greatly amplified by a preamplifier and applied to a power amplifier to command motor current. The current generates torque which, in turn, alters the motor speed to reduce the velocity error voltage. Thus, the servo controller is always trying to reduce the velocity error to zero.

A separate position feedback loop controls position in the same manner that the servo controller controls speed. A position command generated by an external source is compared with a position feedback signal provided by a linear feedback transducer sensitive to position.

Closed-loop position control is provided by an input stage device termed an Absolute Digital Translator Subtractor (ADTS)[*] which accepts command information in the form of serial data pulses. Pulse information is compared with the feedback signal from a non-pulse counting type of transducer (termed a resolver) to close the loop. This design increases noise immunity since the requirement for encoders or other pulse-counting feedback circuits is eliminated. Errors due to "accumulation" associated with these techiques are also eliminated.

The resultant operating system is controlled in real time by the incoming command pulse train. Each pulse received will cause the motor to move one increment in the selected direction, and the rate at which the pulses are received determines the instantaneous motor speed. The resolution (magnitude of an angular increment) is regulated in the design of the ADTS stage in the servo translator. Input pulses can be generated through a number of techniques including the output of a digital computer.

---

[*]Patent applied for, Control Systems Research Corporation

II.1.3 Microcomputer Control System

The choice of a suitable motion control computer was dictated primarily by the nature of the pulse train which must be produced as an input for the servo translator. To generate the dual pulse trains required for simultaneous operation of the drive systems, a Digital Equipment Corporation PDP 11/03 microcomputer was chosen for dedicated motion control. The unit was configured with 32 k-words random access memory (RAM) which provided operating system overhead and program support.

Control of the two motor drive systems was implemented through a single digital output port using select pins for the various pulse and voltage level command functions. Pulses were generated by momentary "toggling" of the voltage at the appropriate output voltage register pin from the low to high state. Timing of the pulses for each control channel was accomplished in software by indexing a "pointer" through a binary array. In this process, each bit is examined as the pointer reaches it, resulting in a toggle command to the appropriate output port if a "1" is detected. Bits set to "0" are ignored. Succeeding bits from the two arrays which determine pitch and translational motion are examined alternately. The pointer indexing rate is regulated by the internal computer instruction clock, and, in this manner, a pulse train having a prescribed time history can be generated programmatically. Resulting motion is then a single cycle pattern which can be repeated as many times as required by relocating the pointer to the top of the arrays and restarting the sequencing program.

II.2 AIRFOIL MODELS AND MODEL INTERFACE

Two airfoil shapes were employed in the present studies. Initially, a model having a NACA 0012 cross-section was fabricated with rectangular planform dimensions of 14 inch span (35.6 cm) and 6 inch chord (15.2 cm). The model was constructed from three solid aluminum pieces and excavated to provide interior mounting locations for nineteen (19) miniature piezo-resistive pressure transducers. A side view of the airfoil showing the pressure measurement locations is provided in Figure II-6.

The small physical size of the model precluded flush-mounted transducers and necessitated a compromise installation method. Short pieces of flexible vinyl tubing were used to interconnect the transducer heads to short brass tubes which extended to small holes in the model's upper and lower surfaces. Although this configuration resulted in a somewhat reduced frequency response, the upper rolloff limit of each measurement channel was maintained at an acceptable level ($f_{max} \geq 1$ kHz).

To examine the influence of airfoil shape on deep dynamic stall behavior, a NACA 64_1A012(13) profile was also selected for use in subsequent experiments. This profile possesses a somewhat smaller leading edge radius than the NACA 0012. McCroskey, et al[2] have suggested this as a potentially important parameter which can influence the evolution of the dynamic stall flowfield. In addition, this airfoil possesses a longer favorable pressure gradient region over the forward portion of the surface characteristic of modern aircraft wing sections. For example, the F-15 aircraft employs the 12% thickness-to-chord ratio version of this airfoil shape in the wing root region.

Construction of the second airfoil was similar to that of the original except for the physical size - 14 inch span (35.6 cm) with an 8 inch chord (20.3 cm). The slightly larger chord of the second model was chosen to increase the effective spatial resolution and improve the ease of transducer installation. It was designed to accommodate 20 internally mounted pressure transducers as shown in Figure II-7.

Note that neither model was constructed to fully span the wind tunnel test section. Limits on the practical spanwise length were imposed by inertial considerations which influence realizable model accelerations during unsteady motions. To approximate true airfoil characteristics and maximize flow two-dimensionality, plexiglass endplates were constructed for both models. These nearly rectangular, spanwise adjustable pieces were configured to project at least 0.20 chord lengths upstream and downstream of the leading and trailing edges, respectively. They also extended approximately one-half of a chordlength in the cross-stream direction from the upper and lower airfoil surfaces. When positioned for the tests described in subsequent sections, they were placed equidistant from the pressure tap centerline to give an effective geometric aspect ratio of 1.3 for both airfoil models. Care was exercised to place the lower endplate (nearest the wind tunnel floor) out of the test section wall boundary layer.

Both models were designed to accommodate an interface collar which could be coupled directly to the pitch drive assembly. The pitch drive spur gear mentioned in Section II.1 is permanently attached to the hollow model support shaft which is, in turn, fastened to the lower portion of the aluminum mainframe by two alignment bearings. The model is coupled to the shaft through a 'tang' which protrudes from the base of the model.

The tang was fabricated to be inserted into the upper opening of the support shaft and held in place with recessed set screws. The tang posesses an oblong cross-section and is hollow to accommodate transducer wires passing from the model's interior to outside electronic signal conditioning instrumentation. A sketch of the model mount arrangement is provided in Figure II-8.

Due to model size and shape limitations, the pitch rotation points of the two airfoils are slightly different. The NACA 0012 model rotates about the 31.7 per cent chord point while the NACA $64_1A012(13)$ model rotates at the 37.5 per cent chord location. Previous studies have indicated that the location of the pitching axis has little effect on the peak loading value but can influence the angle at which stall actually occurs.[6] Comparisons, in this case, should be made with caution.

II.3 PRESSURE MEASUREMENT SYSTEM

Unsteady pressures were measured by miniature, dynamic piezo-resistive transducers possessing a high frequency response. For the current experiments, Endevco Model 8507-2 transducers specified over nearly a 100 kHz bandwidth and nominally yielding 120 mv/psi sensitivity at 10 volts excitation were employed. The specified sensitivity of these transducers to acceleration is minimal at 0.0005 psi/g, maximum. The devices are also temperature compensated to provide minimal drift from this sensitive parameter during operational use. The short piece of flexible tubing connecting each transducer with the appropriate surface measurement port reduced the overall upper frequency response limit to levels no lower than 1 kHz in the worst case.

To provide a stable reference for the unsteady flow experiments, the "reference" side of each of the transducers was connected to atmospheric pressure in the room exterior to the wind tunnel. This arrangement was judged preferable to alternative schemes using in-tunnel reference sources which might otherwise introduce errors due to unsteady phase lag variations. Steady flow total and static pressures in the test section were measured using Statham Model PM5TC transducer units. An interconnection diagram of the pressure measurement system is provided in Figure II-9. Using this system, the transducer outputs sampled were

$$\Delta p_{1_1} = P_1 - P_{room} = K_1 e_{o_1} \tag{3}$$

$$\Delta p_2 = P_{s_o} - P_{room} = K_1 E_1 \tag{4}$$

and

$$\Delta p_3 = P_{t_o} - P_{s_o} = \frac{1}{2} \rho U_{\infty_o}^2 = K_2 E_2 \tag{5}$$

The unsteady pressure coefficients were computed using the following relationship:

$$C_{p_1} = \frac{\Delta p_{1_1} - \Delta p_2}{\Delta p_3} = \frac{P_1 - P_{s_o}}{\frac{1}{2} \rho U_{\infty_o}^2} \tag{6}$$

where the "o" subscript denotes reference steady flow conditions.

Each of the dynamic pressure transducers was excited by a separate, regulator-isolated, DC power supply at 10 volts. A transducer bridge balance circuit provided coarse and fine adjustments of the desired reference level of the individual output voltages. The low-level output signals were directed to preamplifier units located at the extremities of the transducer lead wires to minimize noise interference effects.

The preamplified signals were then channelled to Dynamics Model 7521B variable gain amplifier units to optimize the signal level to a value compatible with the data acquisition system. A complete schematic of the electronic signal conditioning system is provided in Figure II-10.

II.4 DATA ACQUISITION SYSTEM

Although the microcomputer control system described earlier was adequate to achieve motion control, its limited memory and lack of storage peripherals severely restricted its use in program development. Therefore, a larger minicomputer (DEC Model PDP 11/45) was employed for overall experimental control and data acquisition. The central processor was configured with 128k words of memory (16 bits per word) and 20 mega-words of disk storage capacity. [Of this capacity, a maximum of 32k-words of memory were available to a single user under the RSX 11-M operating system.] Additional mass storage was accessible through a network link (DECNET) to other PDP 11 computing systems, as well as a magnetic tape drive and other peripherals.

This system was equipped with a laboratory peripheral system (DEC Model LPS-11) having a 32 analog channel input capacity, as well as three 16-bit digital input-output ports. The LPS-11 module was equipped with a high-speed real time clock, multiple Schmitt triggers, relays and other hardware interface subsystems designed for use in laboratory applications.

A capability was developed to interface the larger machine with the smaller one for transfering task images using a "down-line load" technique. The simple network allowed for program development and editing in the larger minicomputer system. A more complete discussion of the elements of motion control can be found in reference 22.

II.5 MEASUREMENT PROCEDURES

Unsteady pressure measurements during actual model tests were preceded by an involved calibration and alignment sequence designed to minimize sources of potential measurement error. This procedure began with the careful adjustment and alignment of all mechanical components to minimize friction and wear and to maximize cycle-to-cycle repeatability of the model motion waveform. Several reference variables including the initial angle of attack, reference steady freestream velocity and other reference pressures required in the experiment were initialized and measured prior to each test sequence. The maximum incidence angle was also independently verified. Immediately prior to the "flow on" condition, adjustments of the zero set point (reference condition) for each of the dynamic transducers were accomplished. These reference values were rechecked immediately after concluding the test to determine the output drift of all data channels. A variation of less than 1% of the maximum measured level for any channel was required to validate the data.

During the experiments, the typical response amplitudes of the dynamic pressure transducers reached a small fraction of their rated value ($\pm$ 2 psid) rendering the manufacturer's calibration constants suspect. As a result, individual "system" calibrations were conducted for each of these units on a regular basis to minimize calibration errors as well as to identify defective instrumentation which may have been damaged during prior experiments. With one exception (failure of transducer #19 - lower surface, near trailing edge - in the NACA 0012 airfoil during an early test series), no calibration drift variations greater than 3% were detected during the experiments.

In addition to the involved pressure and velocity measurement calibrations, extreme care was also exercised in the assessment of model motion parameters. Motion repeatability was assessed both prior to and following each of the tests. In all cases where appropriate care in alignment had been exercised, motion variations were not discernable on an oscillograph trace (less than 0.5% variation between the initial and final curves.)

The actual acquisition of data involved repetitive sampling of each of the pressure channels over 25 cycles to obtain an ensemble average before proceeding to the next adjacent transducer. This process was repeated around the airfoil until all transducers had provided the requisite output. The model motion time history was also stored as part of the data file.

II.6 DATA REDUCTION AND ANALYSIS

Data were analyzed using several programs developed for the PDP 11/45 data acquisition system. Ensemble-averaged, unsteady pressure time histories for each transducer were stored as elements of a file representing a given, unique test condition. These results were subsequently converted to time-frozen, pressure distributions representative of fixed temporal phase points during the motion cycle.

The integration of the surface pressure data was accomplished with an algorithm based on the trapezoidal rule and appropriate coordinate transformations to convert normal and chord forces to lift and drag forces. This process incorporated local values of the model surface slope, as well as the instantaneous chord line orientation to determine the appropriate transformation angles. The integration of these lift

coefficient data to calculate the lift-impulse function (see Section V) was also accomplished using similar numerical procedures.

No attempt was made to apply wind tunnel corrections to any of the unsteady pressure data. The original choice of relatively small airfoil models was prompted by the desire to minimize errors due to wall effects.

II.7 SOURCES OF EXPERIMENTAL ERROR

The influence of the wind tunnel wall proximity on the measurements is undoubtedly a factor of concern for any assessment of dynamic forces, especially when the motion amplitudes are large as in the present case. Tunnel blockage, lift effect and other conventional steady flow corrections are expected to be augmented by unsteady counterparts whose magnitudes are unknown and largely unpredictable given the current state of unsteady flow measurement technology. Correction factors would be expected to be functions of time (or motion phase angle).

The periodic (albeit, anharmonic) character of these motions introduces another possible source of "contamination," namely, the influence of flow phenomena which are either multiples or subharmonics of the oscillation period. Related acoustic effects which might affect the behavior of dynamic Lagrangian vortices could conceivably introduce sizeable errors. It is believed that these error sources were minimized by verifying that the convective tunnel time constant was sufficiently large compared to the period of model motion and also insuring that it was not an integral multiple of that value. No perceptible acoustic interference was detected during the conduct of any of the measurements. It is believed that the very energetic character of the separation vortices will overwhelm any weak excitation provided by experimentally related acoustic field effects

at least during the important, high lift portions of the cycle although
this assertion is speculative.

The selection of the record size necessary for an accurate representa-
tion of the phase-locked average flow behavior was another issue of
concern. A related issue was the accompanying cycle deviation from this
average. A previous investigation[4] has suggested that a 50 record
ensemble is suitable in tests of this type. Due to the need to minimize
electronic drift and given the lengthy measurement times anticipated
(several hours), it was decided to compromise at a total of 25 records
for each transducer to calculate the phase averaged pressures. The
choice of this value was the result of a series of preliminary tests
under several model oscillation conditions which examined 1, 5, 10, 20,
25, 50 and 100 record averages. Although the 25 record average is a
compromise, worst case errors resulting from this limitation were esti-
mated not to exceed 10% even under turbulent flow conditions.

A final factor which bears on the validity and extendability of
these results is that of the Reynolds number regime in which the experi-
ments were conducted. Chord Reynolds numbers in the range of the present
measurements and associated boundary layer development are known to lie
within what is considered the "transitional" regime for typical steady
flow conditions. However, it is believed that the violent large amplitude
motions employed in the deep dynamic stall experiments described here
will readily dominate local shear layer instabilities immediately prior
to stall and afterward when energetic separation vortices are present.
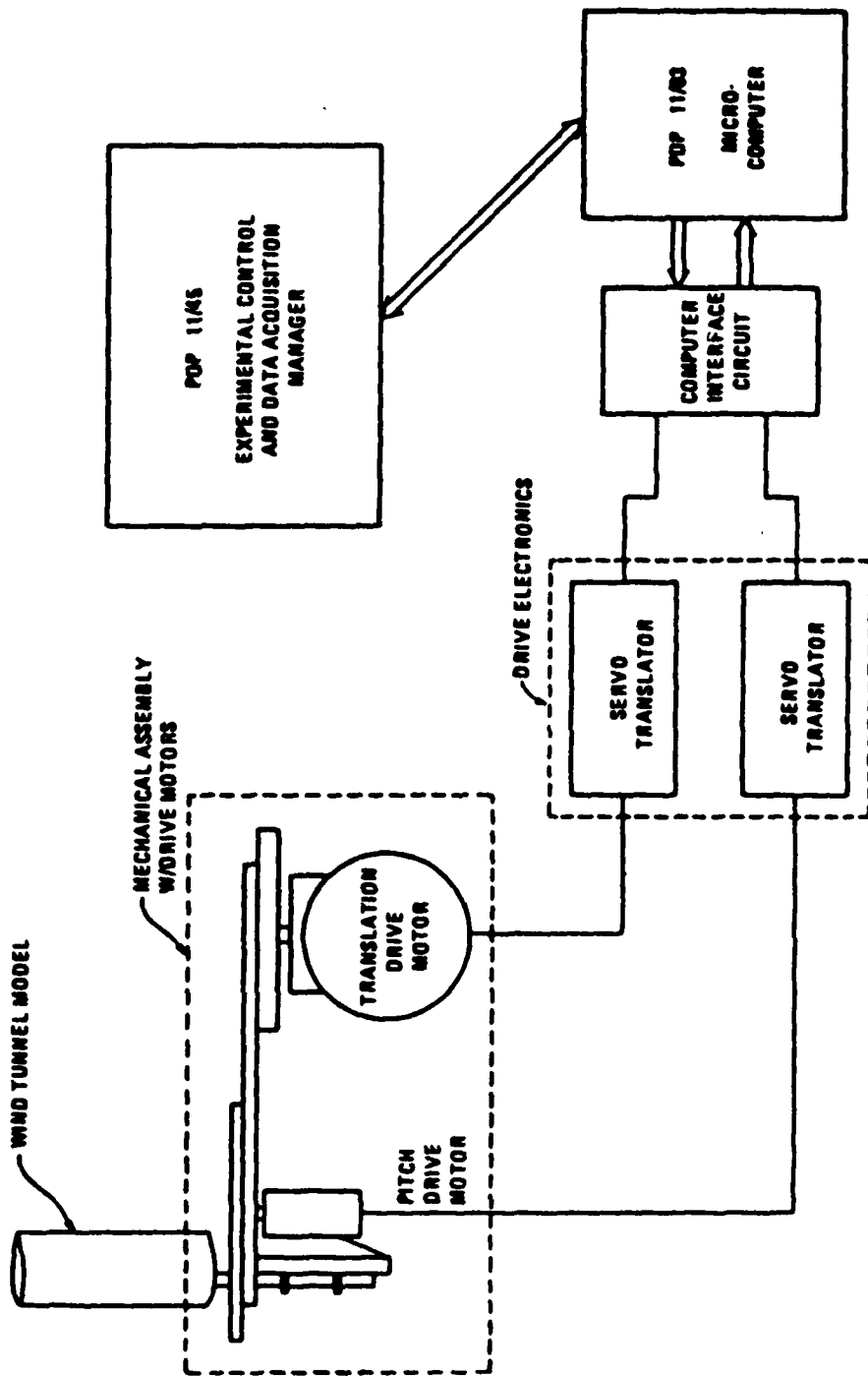
FIGURE II-1
TWO-DEGREE-OF-FREEDOM APPARATUS, FUNCTIONAL SCHEMATIC
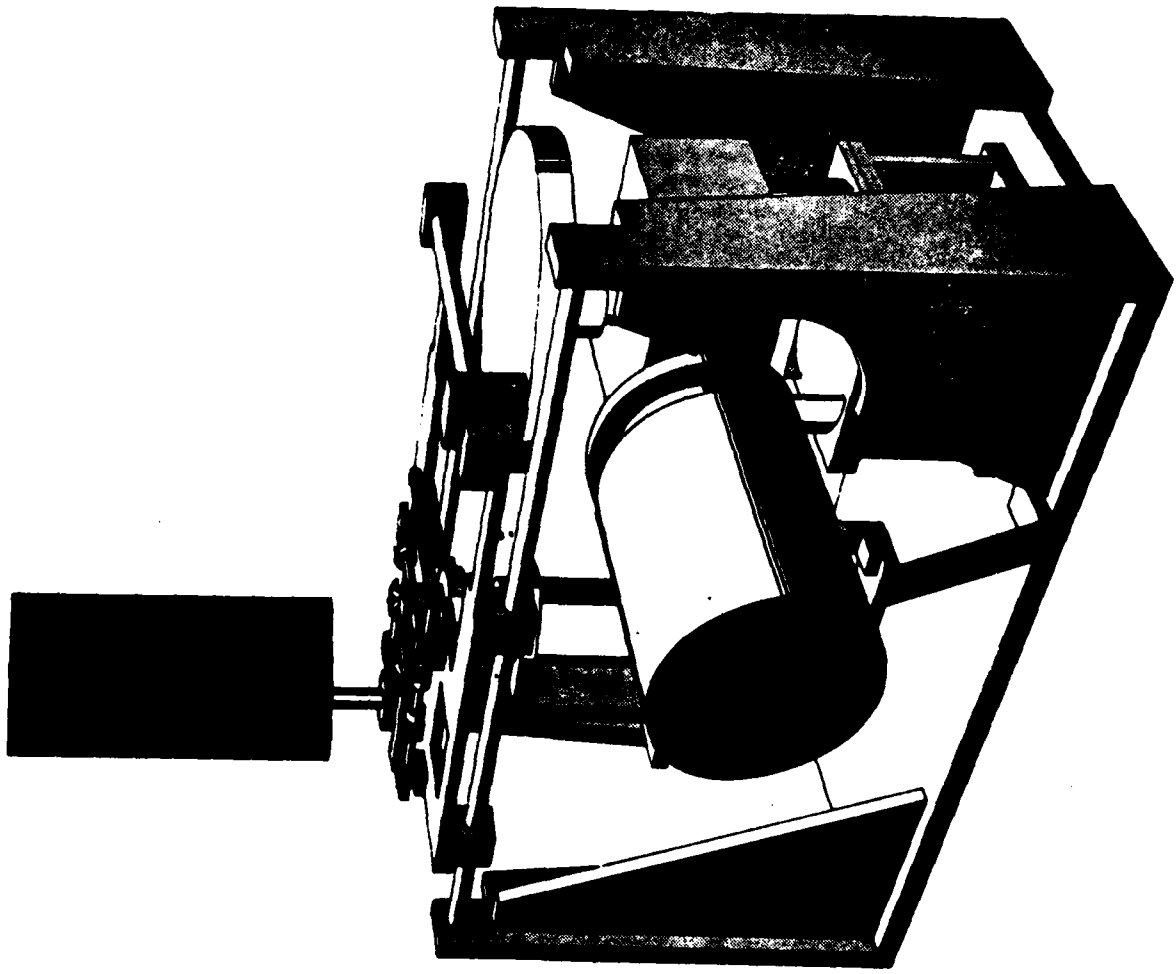
FIGURE II -2
MECHANICAL OSCILLATION ASSEMBLY
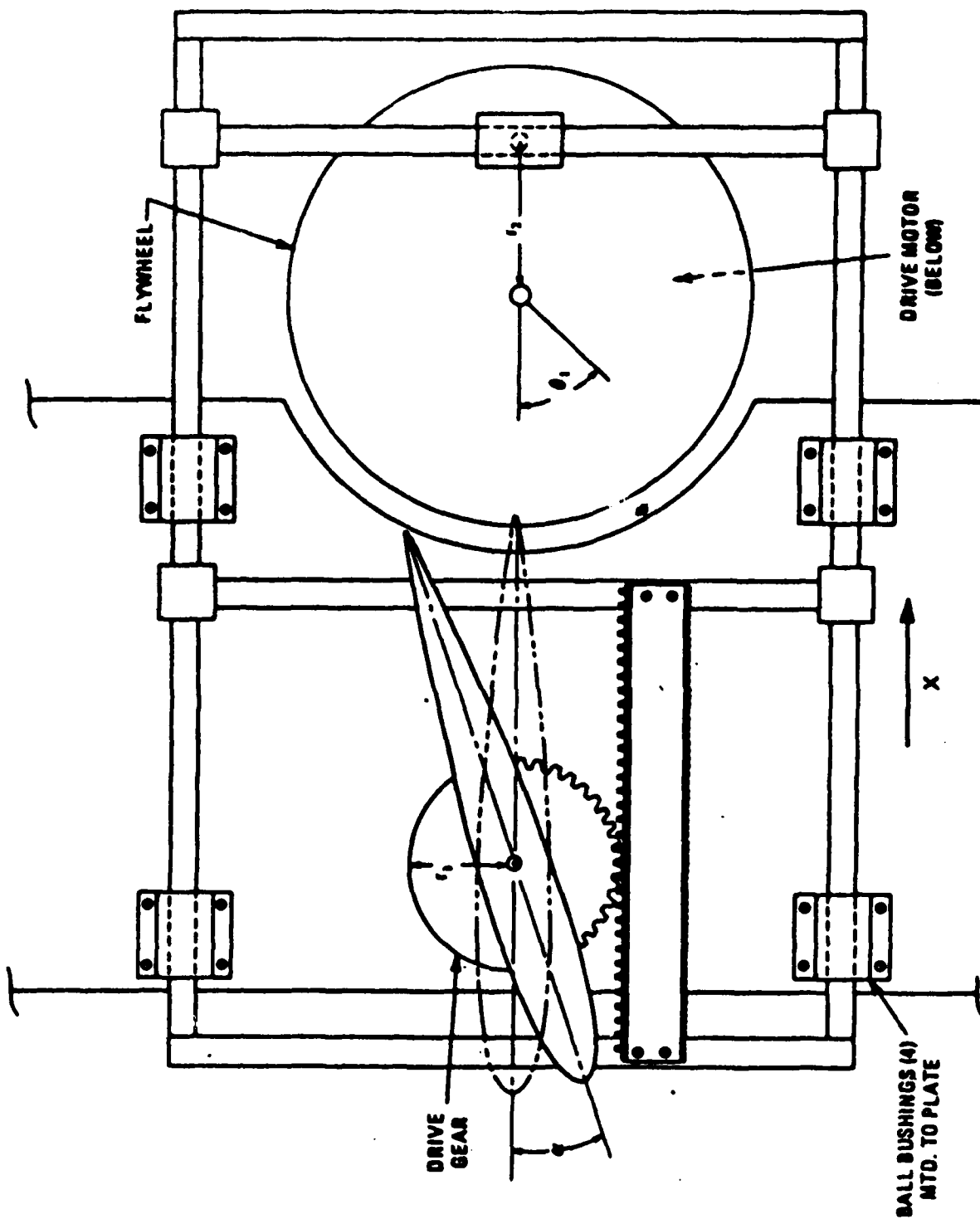
FIGURE II-3
PITCH YOKE SUB-ASSEMBLY

TRANSLATION MOTOR

PITCH MOTOR (BELOW)

TRANSLATION

PITCH YOKE SUB-ASSEMBLY

AIRFOIL

FREE STREAM
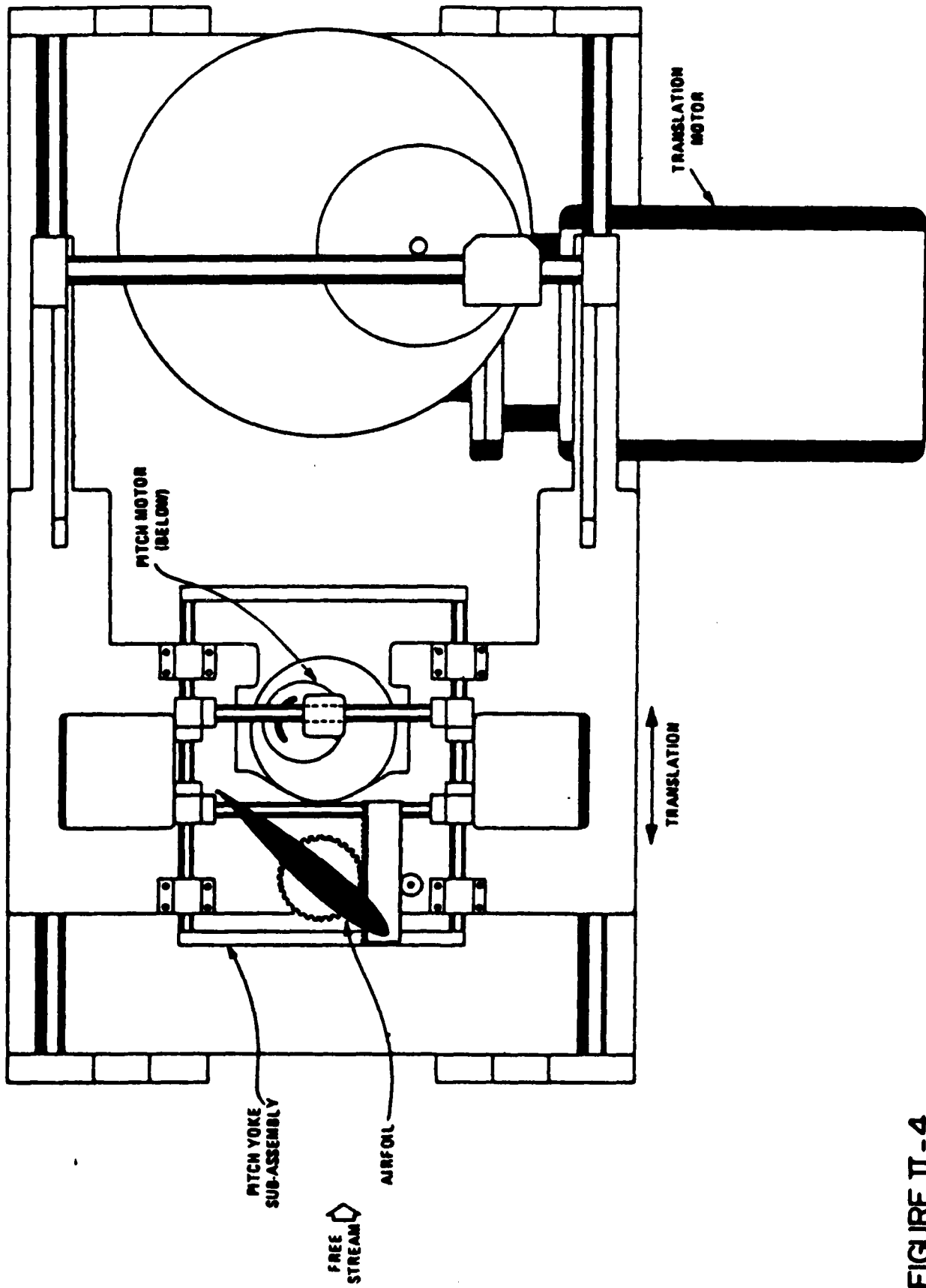
FIGURE II-4
TRANSLATION ASSEMBLY
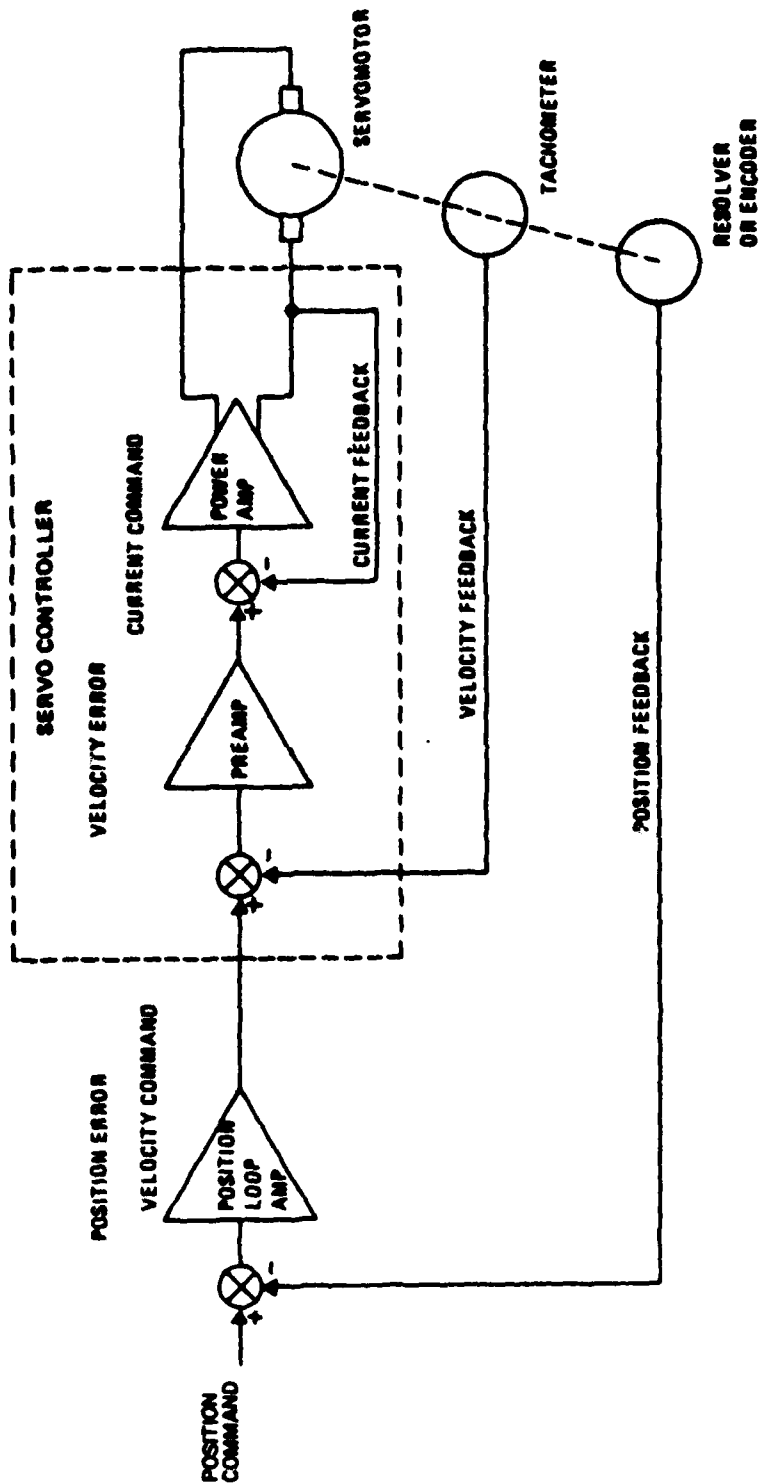
FIGURE II-5
SERVO DRIVE ELECTRONICS-SCHEMATIC
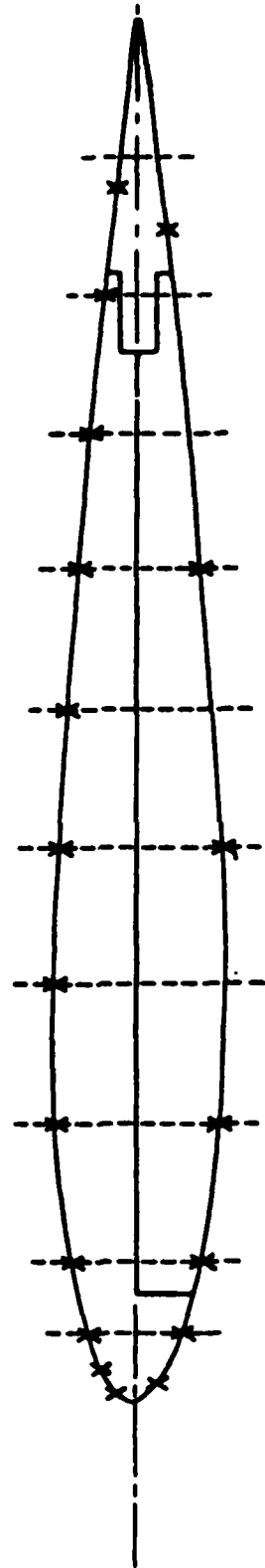
X = PRESSURE TRANSDUCER OPENING

FIGURE II-6
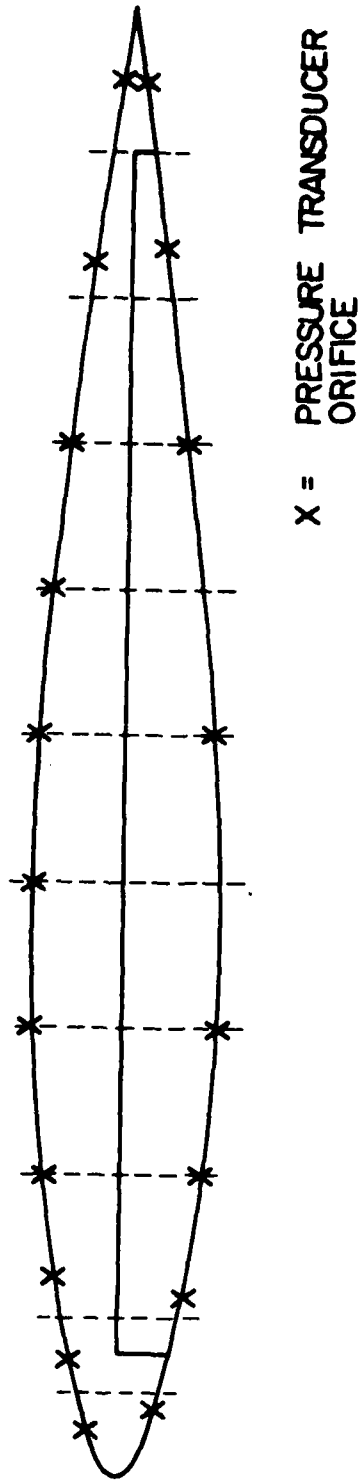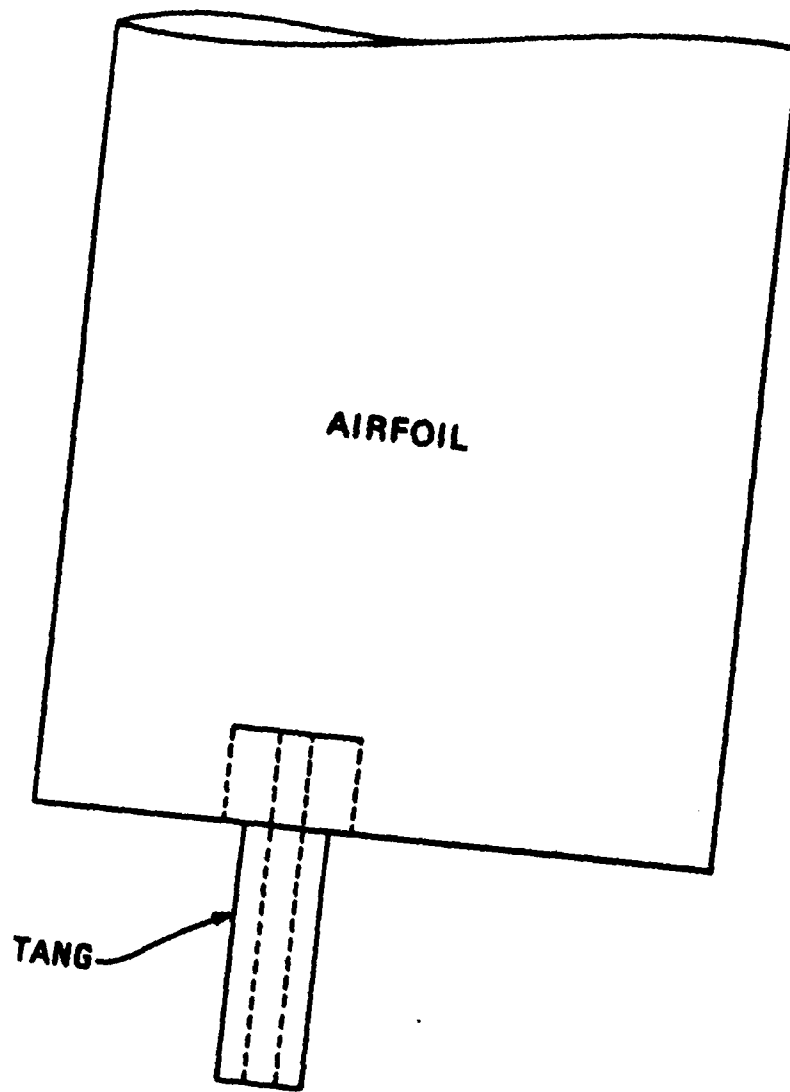NACA 0012 AIRFOIL MODEL CROSS SECTION WITH PRESSURE MEASUREMENT LOCATIONS

X = PRESSURE TRANSDUCER
ORIFICE

FIGURE II-7
NACA 64₁A012 (I3) AIR FOIL MODEL - CROSS-SECTION WITH PRESSURE MEASUREMENT LOCATIONS.

AIRFOIL

TANG

Side View

Bottom View

FIGURE II -8
MODEL MOUNTING DETAIL

PITOT-STATIC SYSTEM
(REFERENCE VELOCITY)

P_r

P_s

3

2

Statham PM5TC (2)

Endevco
8507-2 (20)

P_i

Reference
Pressure (P_r)
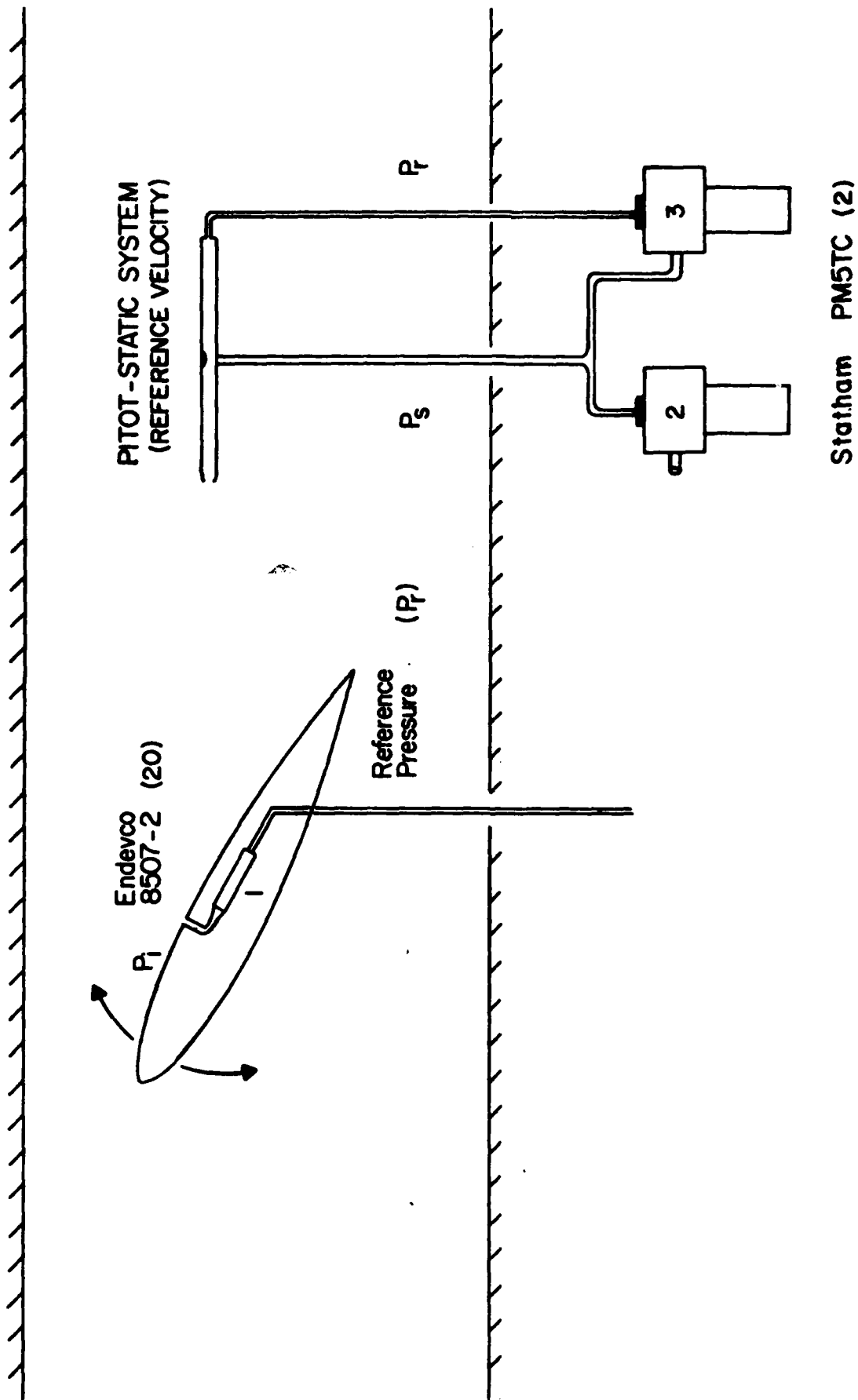
FIGURE II-9,
PRESURE MEASUREMENT SYSTEM- INTERCONNECTION DIAGRAM
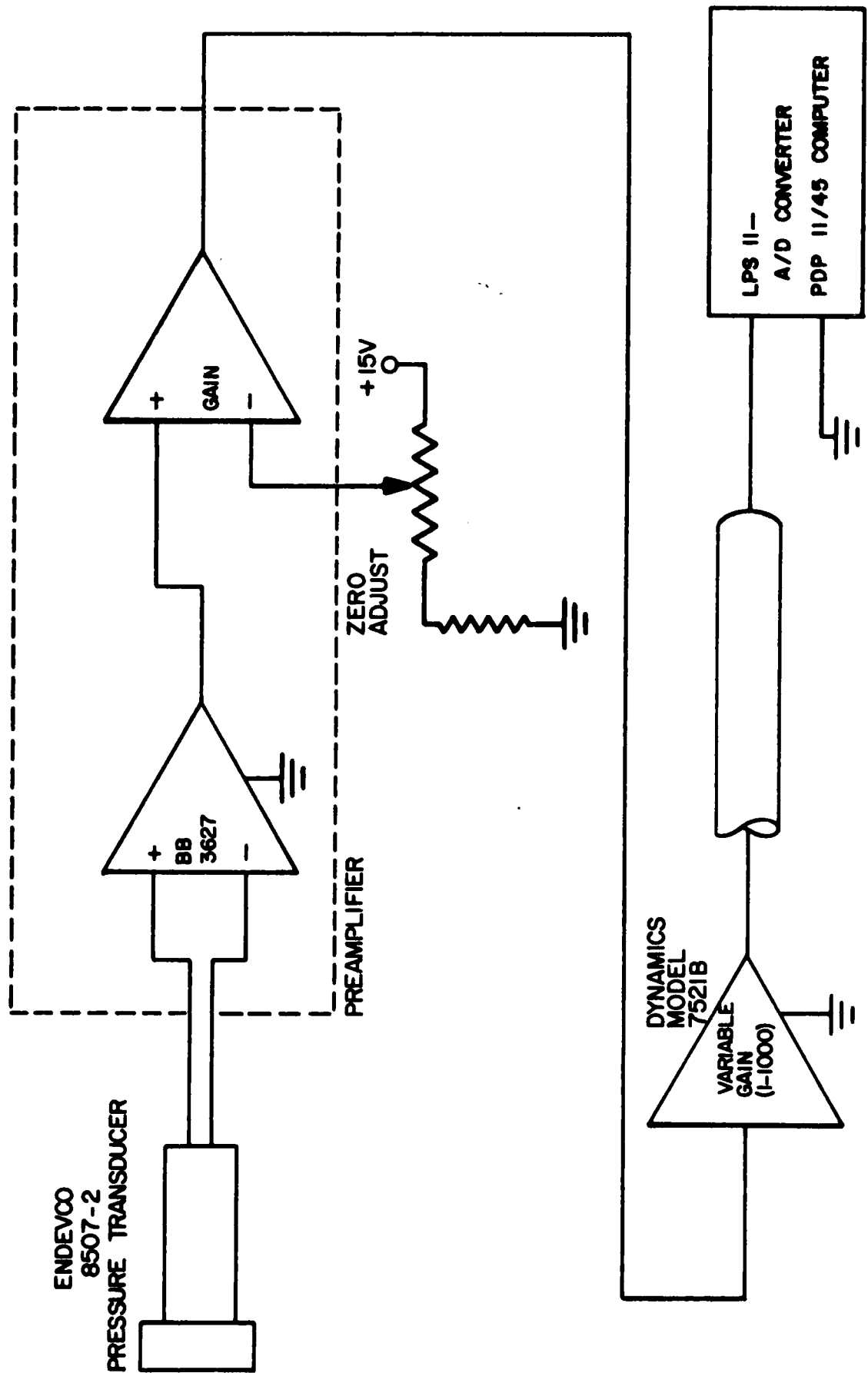
FIGURE II-10
PRESSURE MEASUREMENT SYSTEM-ELECTRONIC SIGNAL CONDITIONING CIRCUITRY

III. AIRFOIL PRESSURE DISTRIBUTIONS

Dynamic pressure measurements have been obtained for both airfoil models over a wide parametric range of model motion and reference flow conditions. Displayed in the form of instantaneous distributions over the airfoil surface, these data are useful not only for quantifying airfoil performance as a function of time, but also assist in the detection of anamolous flow behavior characteristic of dynamic stall phenomena. Phase locked, ensemble-averaged values of the pressure coefficient are presented as functions of the chordwise position coordinate in the displays discussed below.

III.1 REFERENCE CONDITIONS - STEADY FLOW

Before conducting surface pressure measurements in the unsteady flow environment, data were obtained for both airfoils at prescribed, fixed incidence angles under steady freestream conditions. Some of these results are displayed in Figures III-1 and III-2 for representative freestream conditions and for several values of the incidence angle. These data were obtained to further confirm the accuracy and test the stability of the dynamic pressure transducer measurement system and to serve as a reference data source for comparison with unsteady flow results.

In these figures and in other computer-generated graphics displayed in this report, experimental data points are not explicitly identified but have been connected with straight line segments in the graphics software program. Actual data points can be found by observing those locations where the interconnecting straight line segments abruptly change slope or, alternatively, noting the airfoil pressure measurement

locations. Also note that the polarity of the ordinate is reversed between each of the two figures. All remaining pressure distributions discussed in this report are displayed with positive pressure increasing upward on the page (in the sense of Figure III-2).

Although results for only a single freestream velocity are depicted for each airfoil, data over a range of freestream speeds were observed to exhibit identical trends with changing incidence angle. These distributions were found to be remarkably insensitive to the chord Reynolds number over the range examined, except for results obtained near the static stall angle.

The large rearward extent of the adverse pressure gradient on the upper airfoil surface at moderate to high incidence angles is not unexpected for the classes of airfoils employed. The presence of a separation "bubble" over the first quarter chord is also anticipated at higher incidence angles. The region of favorable pressure gradient on the upper (suction) surface is more extensive for the 64-series airfoil at lower angles of attack.

Results of the NACA 0012 measurements of Figure III-1 have been compared with Navier-Stokes computations by Hegna[23], who obtained numerical results for identical reference flow conditions. Good qualitative and quantitative agreement was achieved with a slight discrepancy in the trend of the distributions toward the airfoil trailing edge. The overall magnitude of disagreement has been approximated to be within the range of 5 to 8 per cent for all cases where a comparison is available.

Integral results associated with these distributions are discussed in Section IV.

III.2 UNSTEADY TEST CONDITIONS

A complete matrix of unsteady test conditions employed in this series of experiments is provided for both airfoils in Tables III-1 and III-2 in the Appendix. The model motion parameters listed are based on measured performance as determined from data from pitch and translation position transducers. The test matrix was designed to maximize the range of the test parameters which could be varied in assessing airfoil performance throughout the separation regime. Although there is some overlap in the motion range for the two airfoils (nearly identical test conditions), there are also a significant number of cases for which no comparison is available.

A graphical depiction of various motion waveform shapes is presented in Figure III-3 to assist in the interpretation of reference data provided in the Tables. The use of anharmonic motions greatly facilitated the attainment of large amplitudes at comparatively high instantaneous pitch rates, a major objective of this investigation. Although a wide variety of motion histories have been examined, this report addresses only those cases involving pure pitching motions at constant rate, i.e., $\dot{\alpha}$ = constant. The remaining motions, including combined two-degree-of-freedom experiments, will be addressed in a subsequent technical report.

Large amplitude, constant rate, pitching motions such as those characterized by case A in Figure III-3 were the subject of study for several reasons. These motions are capable of providing a direct correlation between what is believed to be the most significant motion variable, pitch rate ($\dot{\alpha}$), and leading edge separation behavior. Unlike the many previous dynamic stall studies involving harmonic pitch oscillations, the development of the leading edge vortex is not 'forced' by a decrease

in airfoil pitch rate ($\dot{\alpha} \to 0$) near a relatively low maximum incidence angle. The stall process develops as the motion continues unaltered well beyond the onset of separation. The occurrence of leading edge separation and stall vortex development prior to reaching the maximum incidence then represents a unique physical situation of special interest to this investigation.

In contrast, the idea of "trapping" a separation vortex to achieve some measure of lift enhancement requires that the airfoil "respond" to the vortex after it has formed. For this purpose, it was thought that the sudden discontinuation of the nose up pitching motion at some optimum intermediate angle might delay the passage of the vortex in the blockage region behind the high incidence configuration.

The pursuit of lift enhancement under post-stall conditions was also the motivation for studying motions such as those shown in case B (constant rate pitch motion to maximum incidence angle followed by an abrupt decrease in incidence). In this case, the sudden reduction in pitch angle was accomplished to strengthen (or energize) the shed stall vortex by increasing the local shear stress near the airfoil leading edge.

In all cases, the cycle duration was prolonged to allow for a relaxation of induced unsteady effects following the completion of motion. For example, subsequent to a constant pitch rate motion (type A), the airfoil was kept in the maximum incidence position until static stall conditions were achieved. This constraint insured that cycle-to-cycle coupling effects induced by neighboring vortex interactions were eliminated.

To insure a complete relaxation to steady flow, stall conditions during each cycle of motion, the delay time for airfoil position reset; that is, the time between the initiation of motion and the reset command was calculated from the following relationship:

$$t_d \geq \frac{\alpha_{max}}{\dot{\alpha}} + \frac{3c}{U_\infty} \tag{7}$$

A range of pitch rates over nearly three orders of magnitude was employed to study constant rate motion for the NACA 0012 airfoil. Maximum incidence angles ranging from nearly 20 degrees to over 60 degrees were considered. The low end of the rate and amplitude ranges extended from conditions studied by previous dynamic stall investigators to an opposite extreme in which incidence angles well in excess of the induced separation orientation could be achieved for even the highest pitch rates generated. A generally higher range of pitch rates was employed for the NACA 64_1A012(13) airfoil experiments.

III.3 SHAPE OF THE DISTRIBUTIONS

Despite the variations of motion type and the range of motion parameters employed in the experiments, many of the qualitative features associated with the shapes of the surface pressure distributions as they evolve in time are similar over the entire measurement range. To examine this behavior, consider the typical historical record depicted in Figure III-4. This example illustrates a case where the apparent separation angle is exceeded by the maximum amplitude of model motion. At values less than the static stall angle (a), the shape of the pressure distribution is similar to that expected for steady conditions except for an apparent time lag in the pressure coefficient magnitudes. As the inci-

dence angle increases to and beyond the static stall value, an "attached flow" distribution persists with suction pressure magnitudes in excess of equivalent steady flow values.

As the incidence angle continues to increase (b), the suction peak is observed to "break away" from the leading edge region on the airfoil upper surface and move downstream along the surface. This behavior is highly suggestive of the dynamic stall vortex observed in previous airfoil experiments since the evolution of the distribution is identical and in the same relative range of incidence angles for comparable pitch rates. The increased amplitude of the suction peak also suggests that the "vortex" is energized as the incidence angle continues to increase over a range determined by the model rotation rate ($\dot{\alpha}$).

At incidence angles well in excess of the static stall value (c), the pressure peak begins to decrease in magnitude and broaden over the surface as it continues to move rearward. A possible interpretation of this behavior is that the dynamic stall vortex begins to lose energy as it continues to translate into the blocked "wake region" created by the large pitch angle of the airfoil. As this rotating fluid loses energy, the vortex structure becomes more diffuse as it ultimately evolves into a separated free shear layer emanating from the airfoil leading edge.

As the motion continues further (or, in some high rate cases, after the motion is halted), the flow field relaxes to a state which is essentially that of a bluff body wake (d). The pressure distributions over the upper and lower surfaces flatten considerably and attain levels of nearly plus/minus unity, respectively.

Experimental results confirm that the extent of these behavioral trends is a strong function of the model motion parameters, especially

the pitch rate and the pitch amplitude. Increased pitch rate tends to delay the onset of leading edge unsteady separation and, in general, extend the apparent attached flow behavior to higher incidence angles. As suggested earlier, the maximum incidence angle can have a major impact on the shape of the distributions especially if it does not exceed the value at which the separation would otherwise occur. These amplitude effects are addressed more completely in sections IV and V.

Representative distributions for both airfoils are displayed in Figures III-5 through III-10. These data facilitate a comparison of separated flow performance for both airfoils at three comparable levels of reduced pitch rate. In all cases, the angle for which unsteady separation occurs is well exceeded by the amplitude of motion, α_{max}, of approximately 60 degrees. The shapes of the distributions for both airfoil models are found to exhibit the same general qualitative features. However, the suction peak associated with the NACA 64-series airfoil was observed to be steeper and more pronounced at high pitch rates and was also observed to "detach" from the leading edge at high incidence angles. The shape of the NACA 0012 distribution did not exhibit the same accentuated behavior under similar conditions.

Additional similarities in the pressure time histories become apparent through an examination of the amplitude of the minimum pressure coefficient associated with the suction peak as it evolves with increasing incidence angle. These results are displayed in Figures III-11 through III-13. Although some differences in amplitude levels are apparent, the results are observed to be in good agreement when compared to the variation in dimensionless pitch rate.
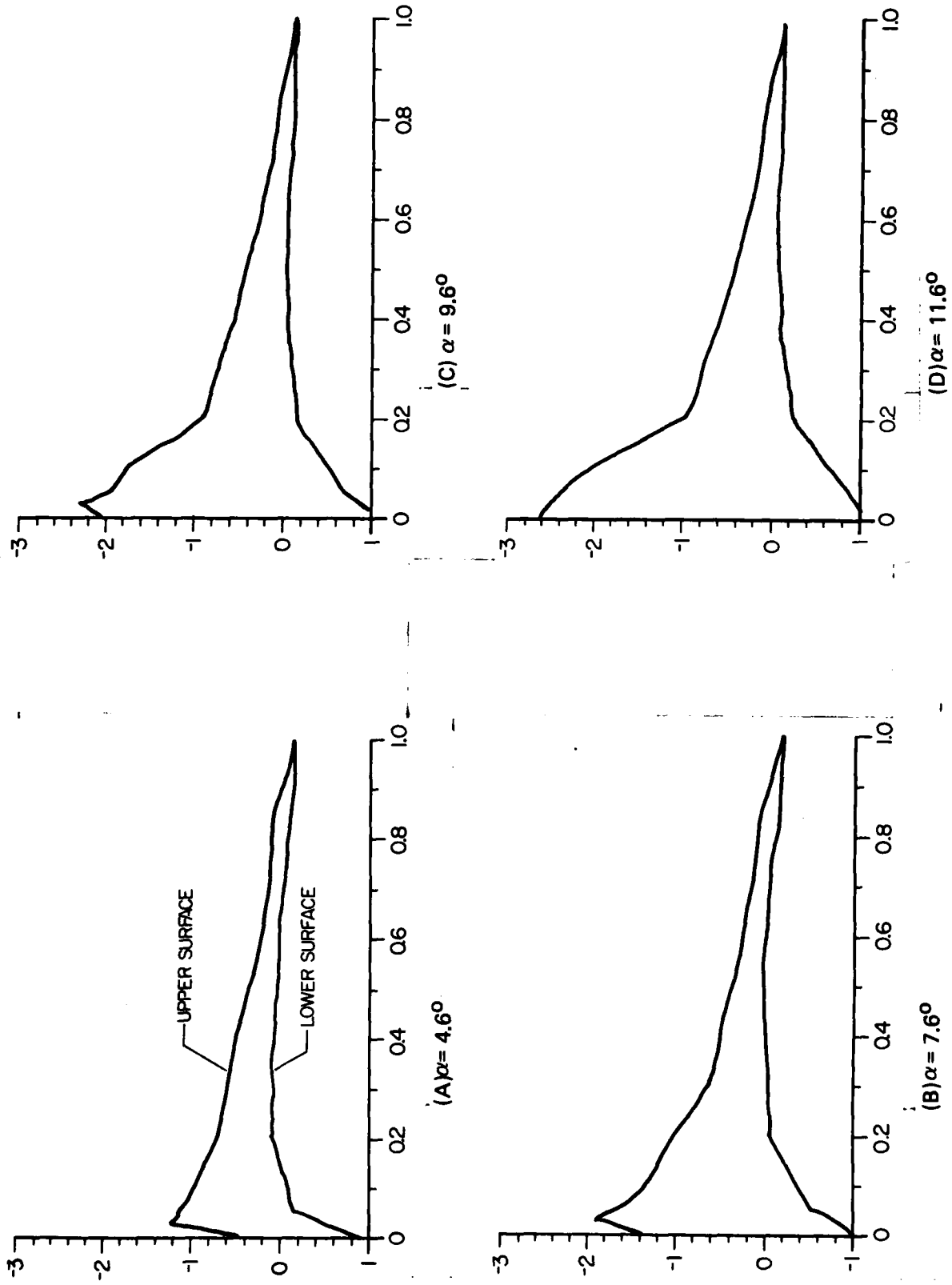
FIGURE III-1

STEADY FLOW PRESSURE DISTRIBUTIONS, NACA 0012
REYNOLDS NUMBER - 170,000, U_∞ = 71.8 FT/SEC.
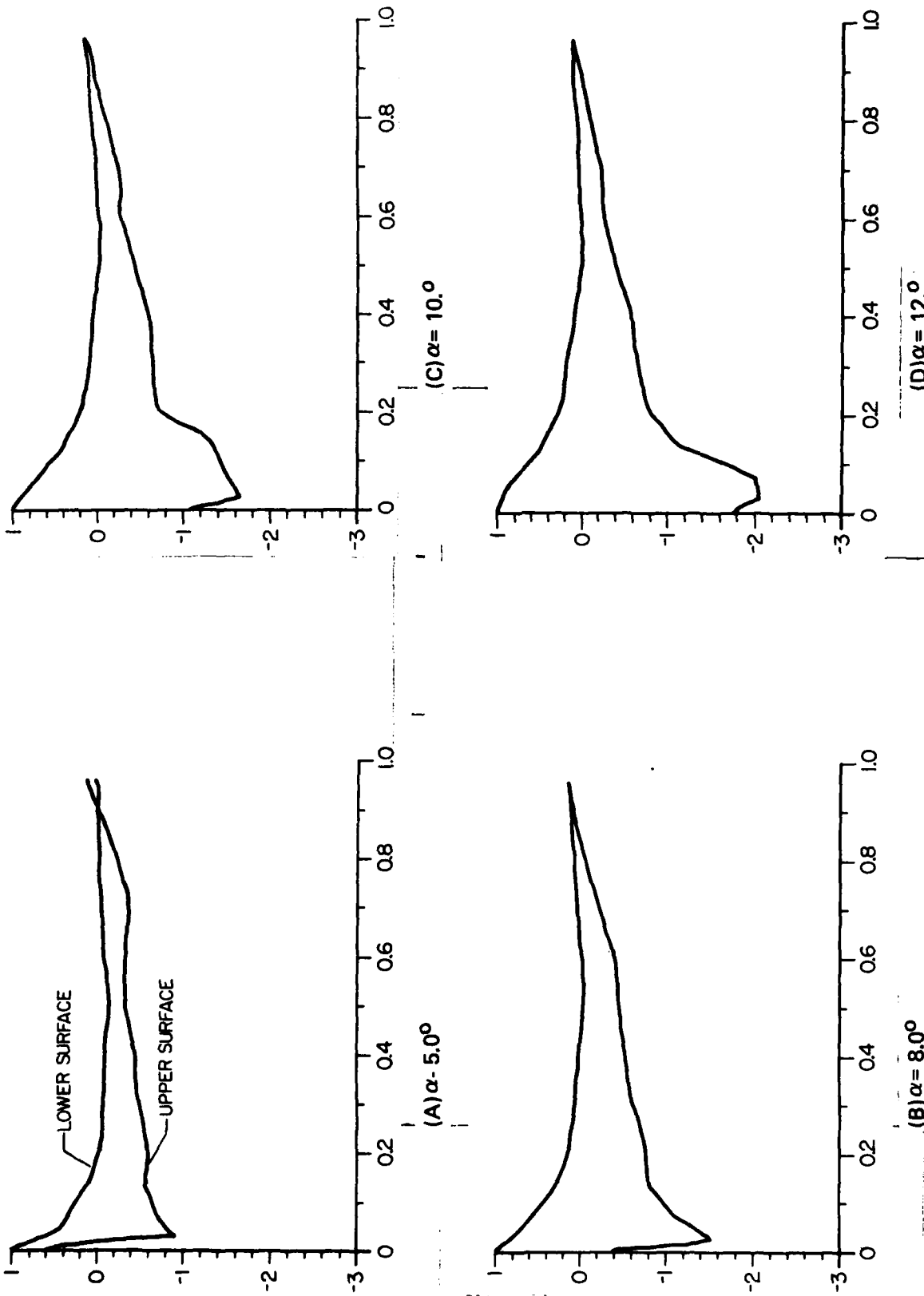
FIGURE III-2

STEADY FLOW PRESSURE DISTRIBUTIONS, NACA $64_1A012(13)$
REYNOLDS NUMBER - 102,000, U_∞ = 31.5 Ft./SEC.
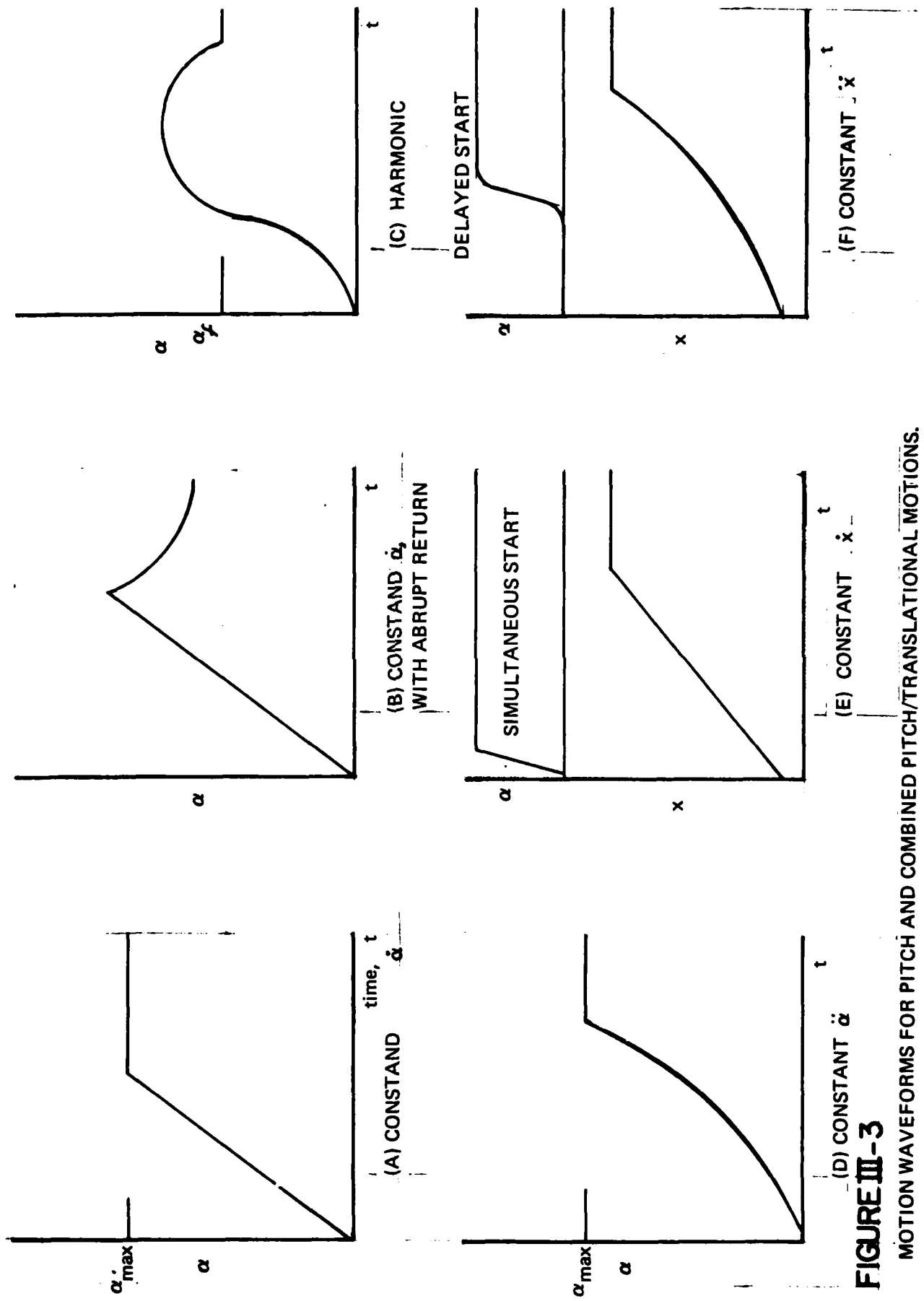
FIGURE III-3

MOTION WAVEFORMS FOR PITCH AND COMBINED PITCH/TRANSLATIONAL MOTIONS.
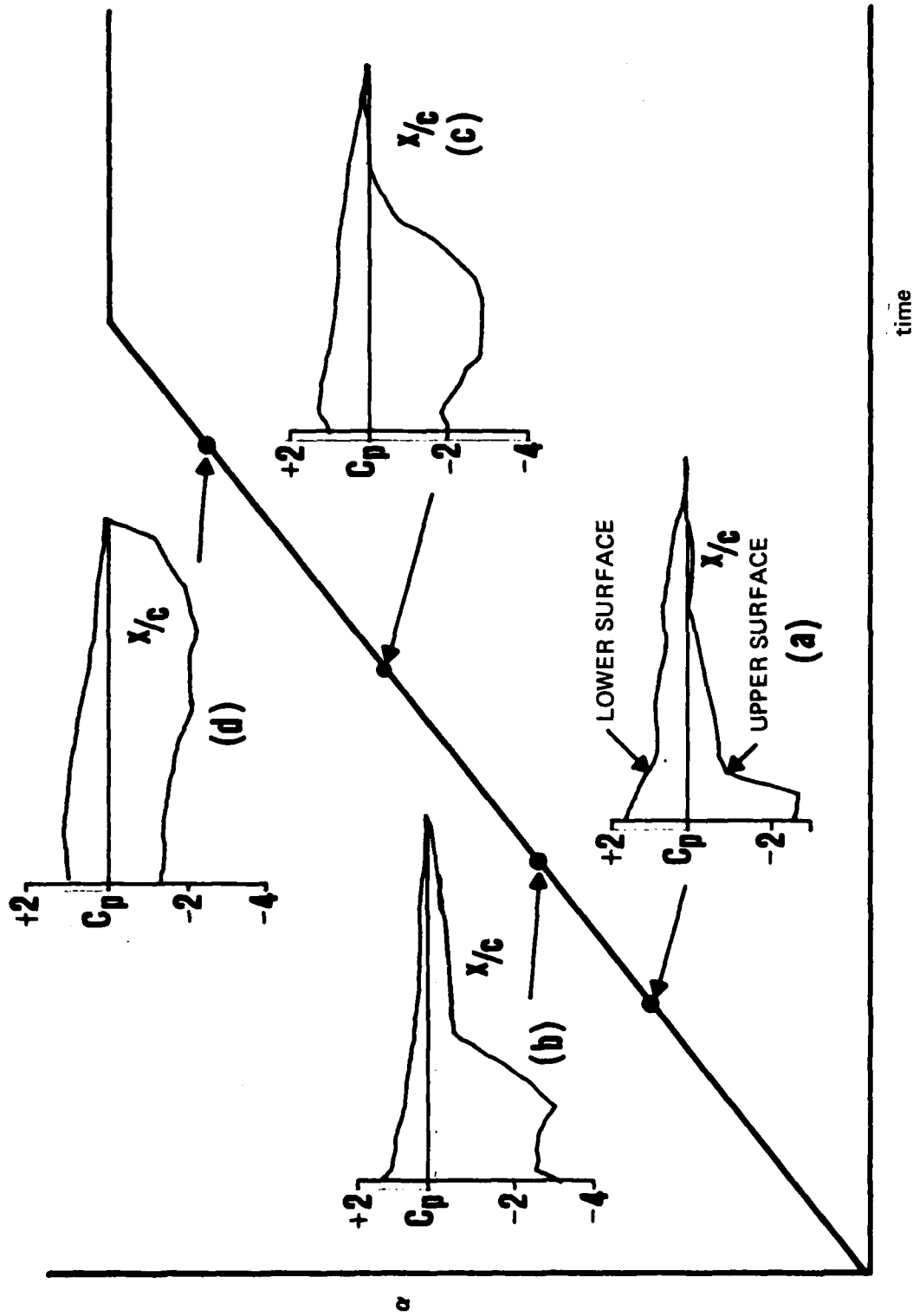
FIGURE III-4 TYPICAL CORRELATION BETWEEN PRESSURE DISTRIBUTIONS AND PITCH MOTION TIME HISTORY.
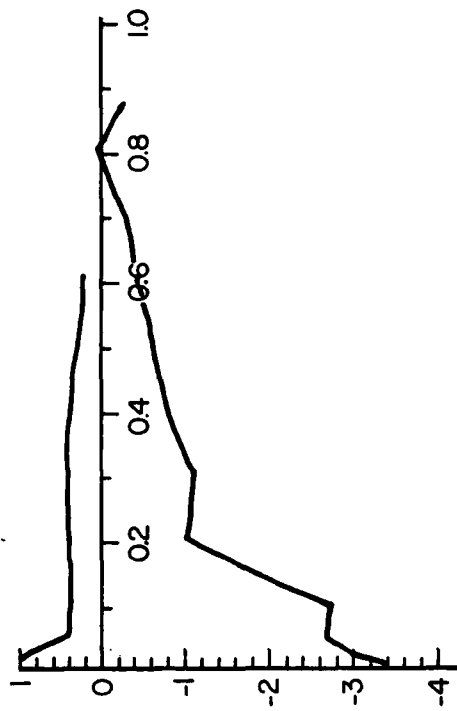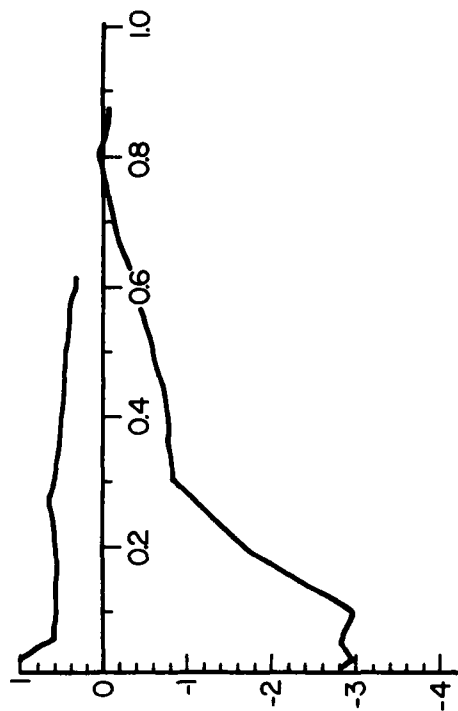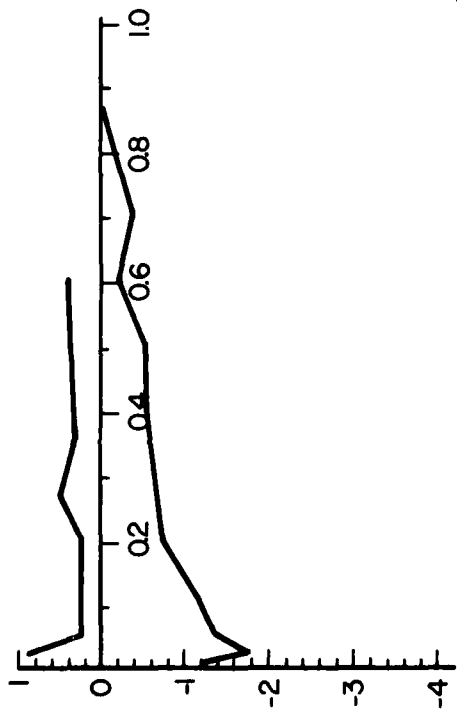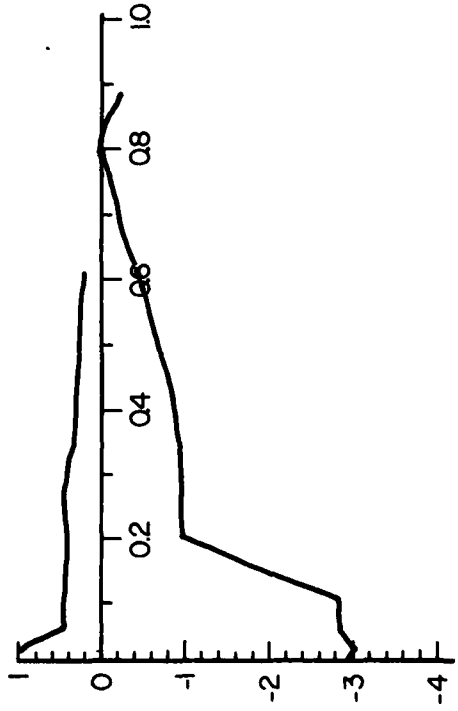
FIGURE III-5

UNSTEADY PRESSURE DISTRIBUTIONS, NACA 0012, $k = 0.047, \alpha_{max} = 60^{o}$, $U_{\infty} = 33.1$ fps

(A) 8.6^{o}

(B) 15.8^{o}

(C) 17.2^{o}

(D) 18.6^{o}
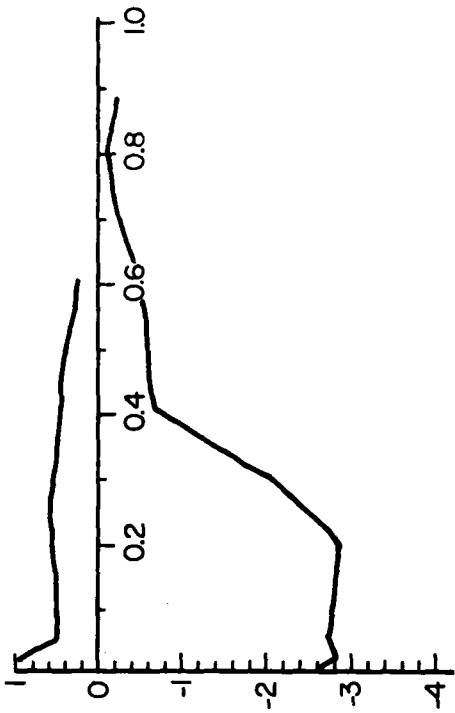
(E) 19.8°

(F) 21.1°
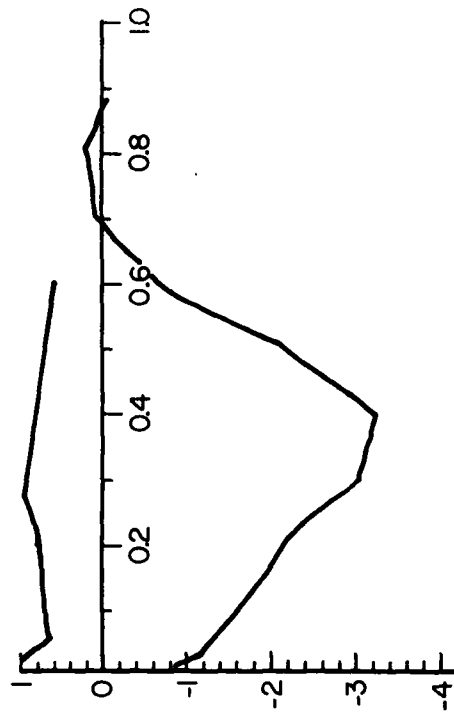
(G) 22.9°

(H) 28.7°
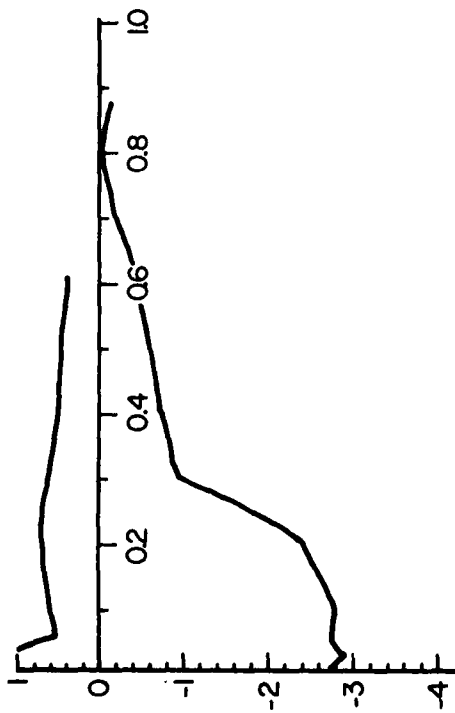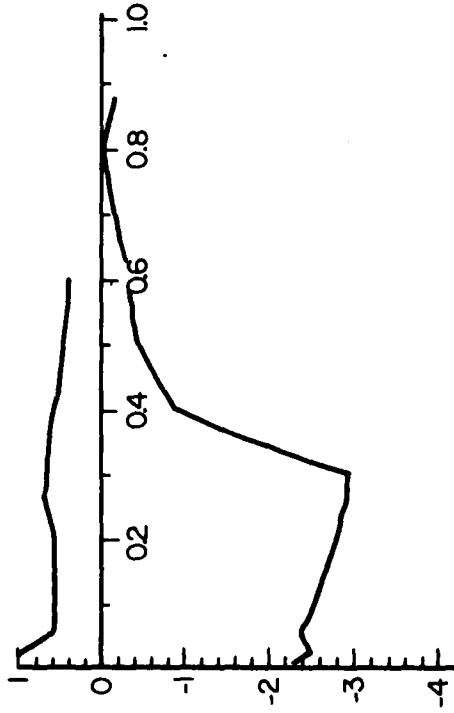
FIGURE III-5
CONTINUED

(I) 36.8°

(J) 43.3°
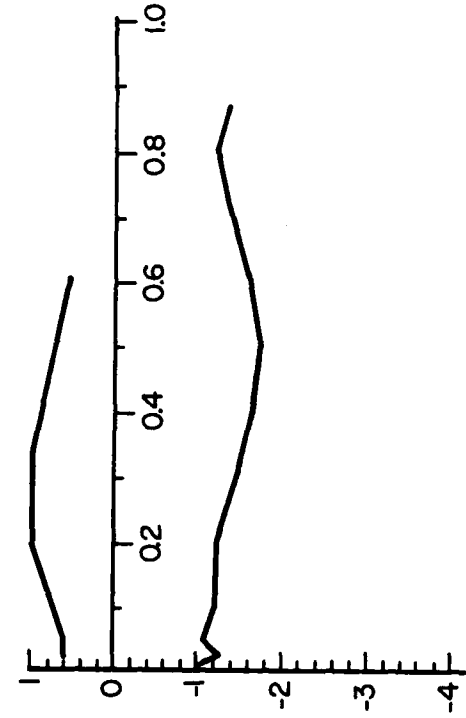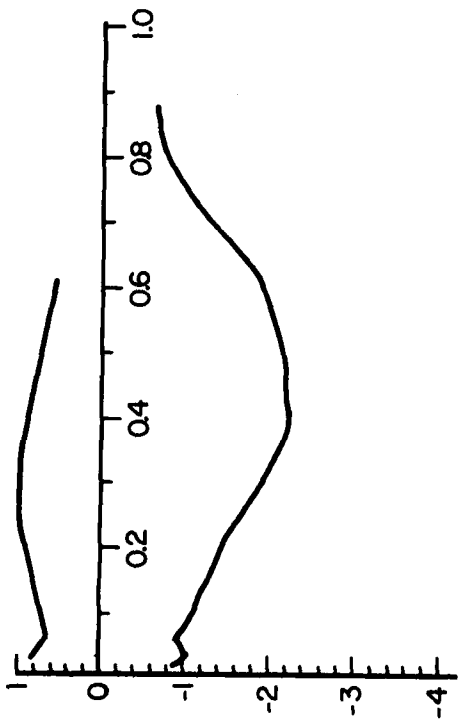
FIGURE III-5
CONTINUED
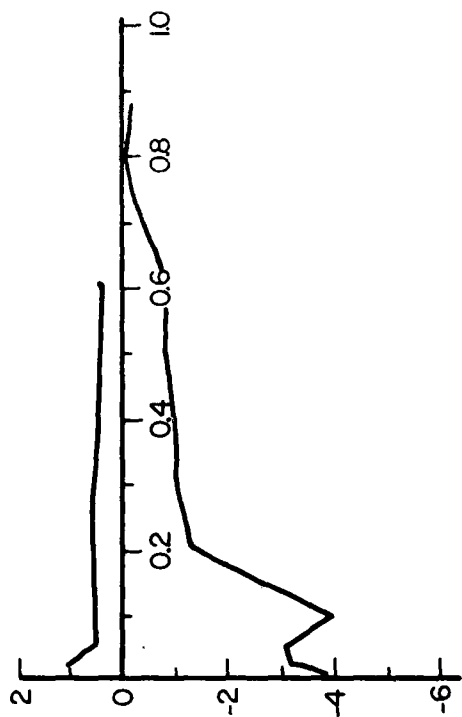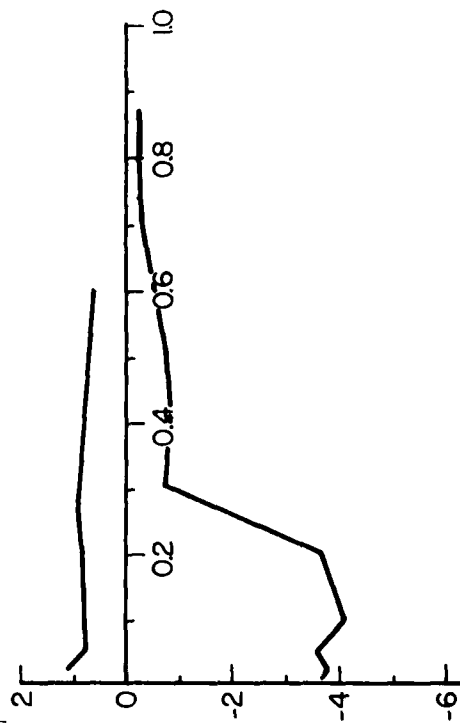
(A) 15.5°   (B) 17.2°
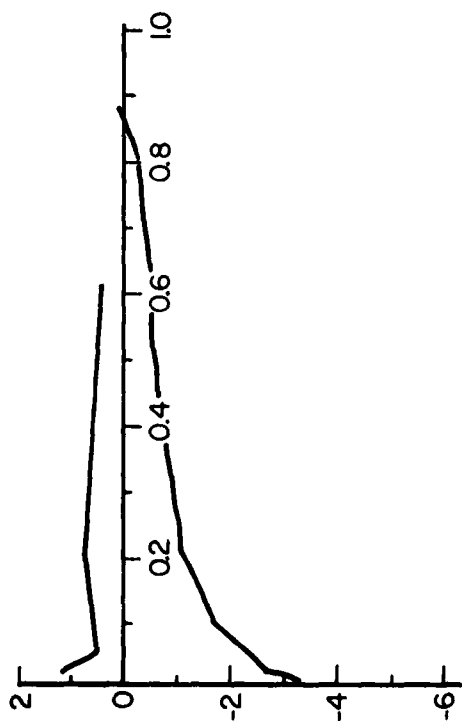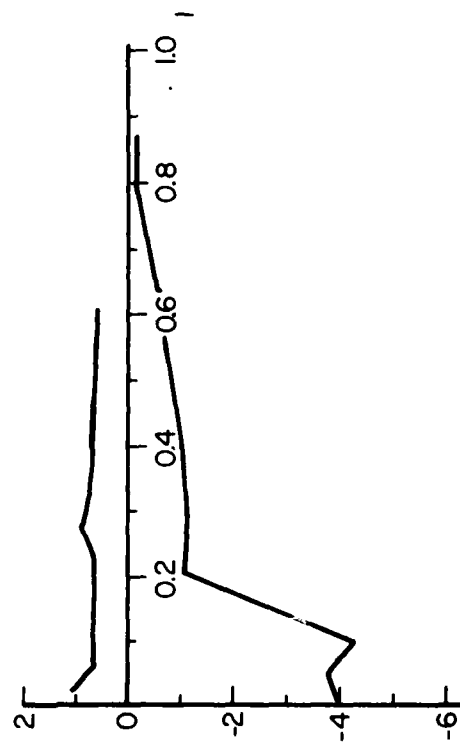
(C) 21.5°   (D) 24.4°

FIGURE III-6 — UNSTEADY PRESSURE DISTRIBUTIONS, NACA 0012, $k = .089$, $\alpha_{max} = 56°$, $U_\infty = 33.1$ fps.

FIGURE III-6
CONTINUED

(I) 39.8°

(J) 46.2°

(K) 51.9°

(L) 55.9°
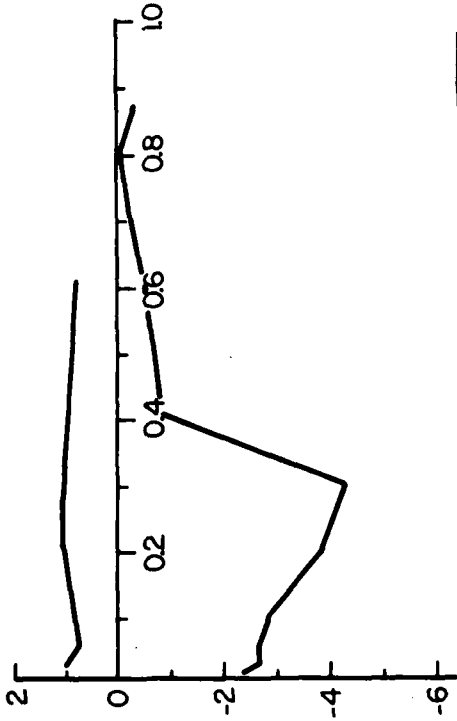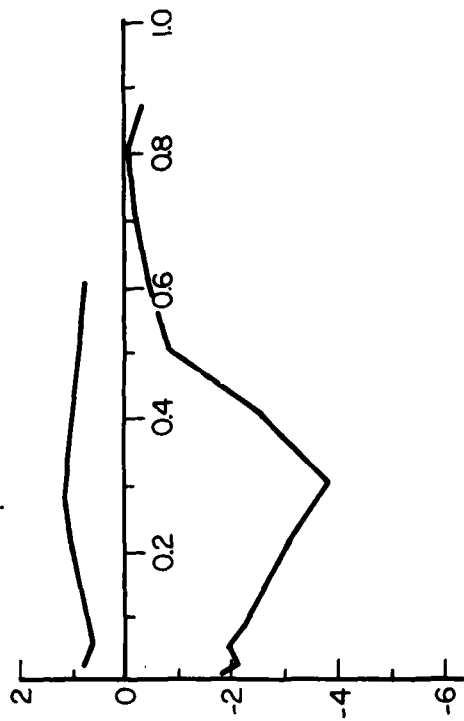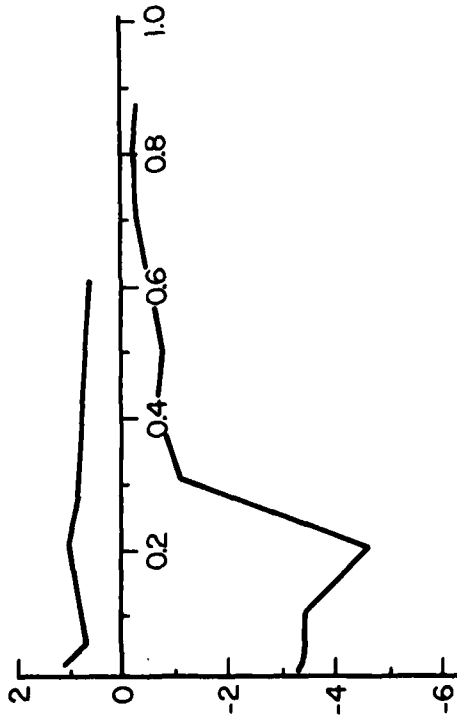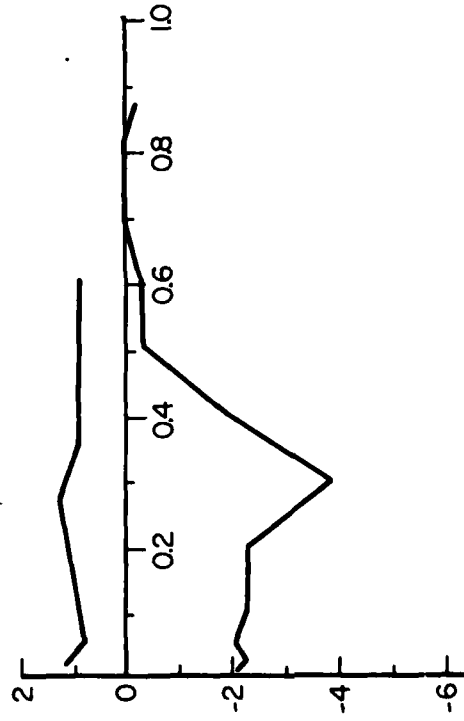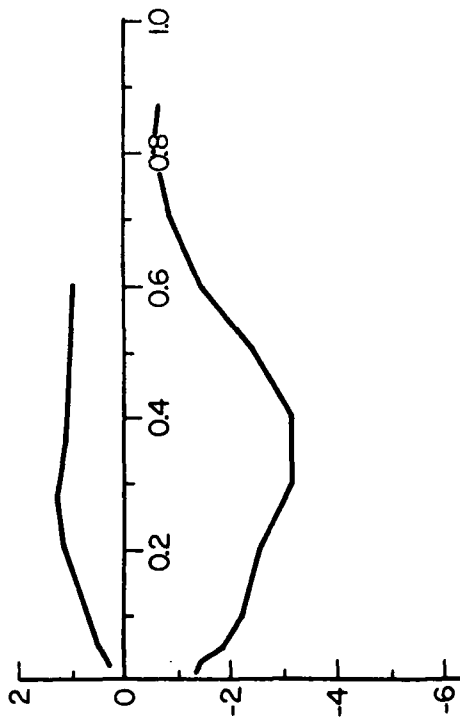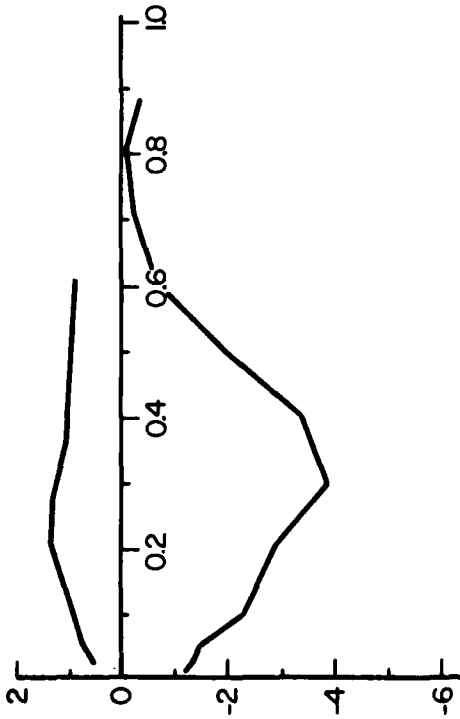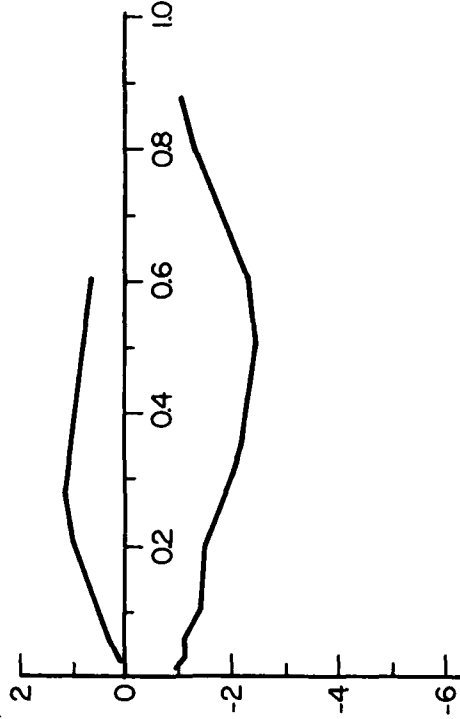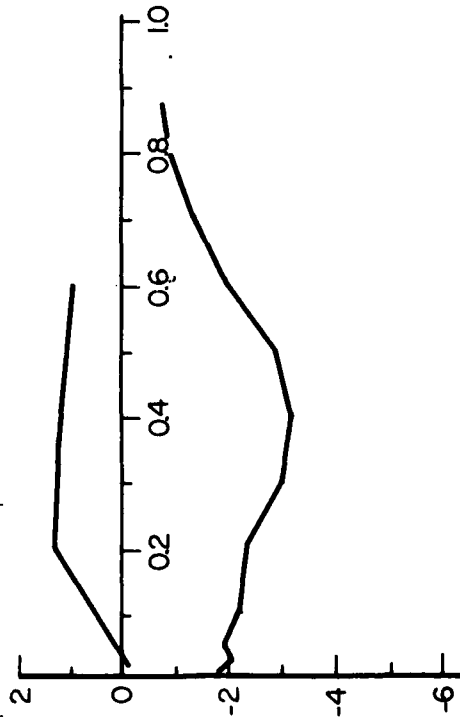
FIGURE III-6
CONTINUED
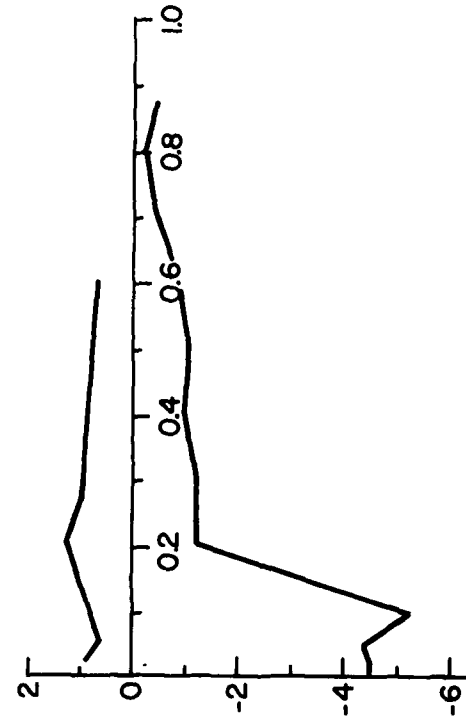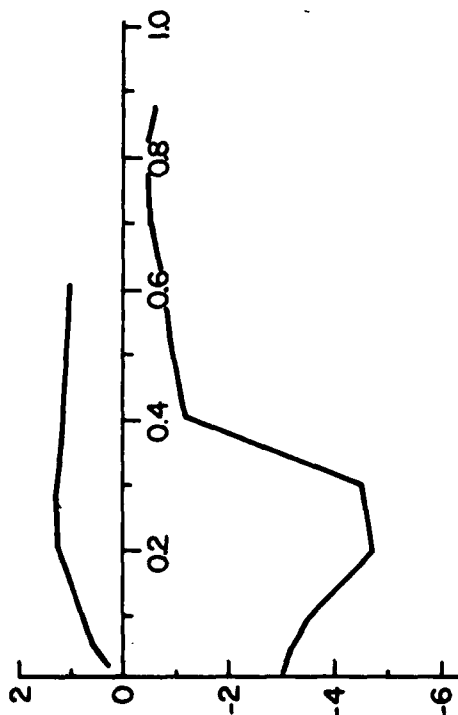
(A) 20.0°
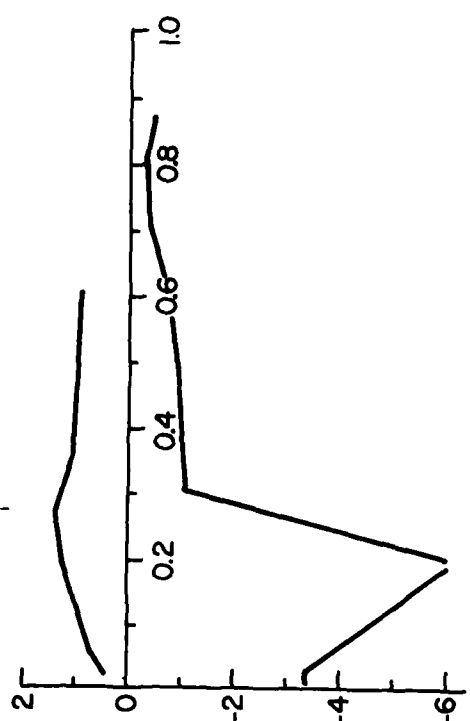
(B) 24.1°
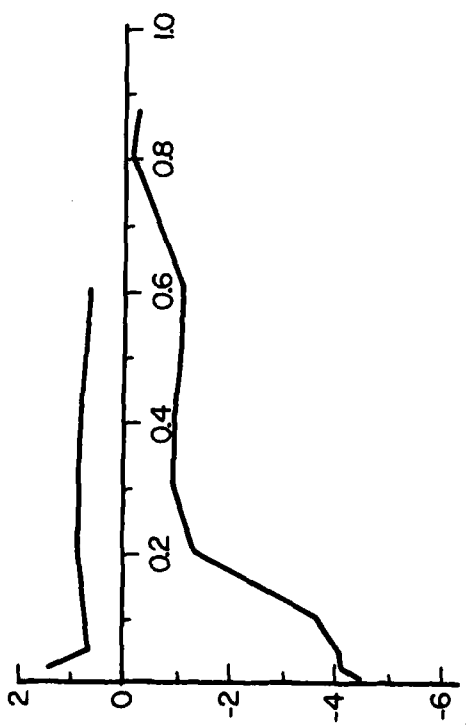
(C) 27.5°
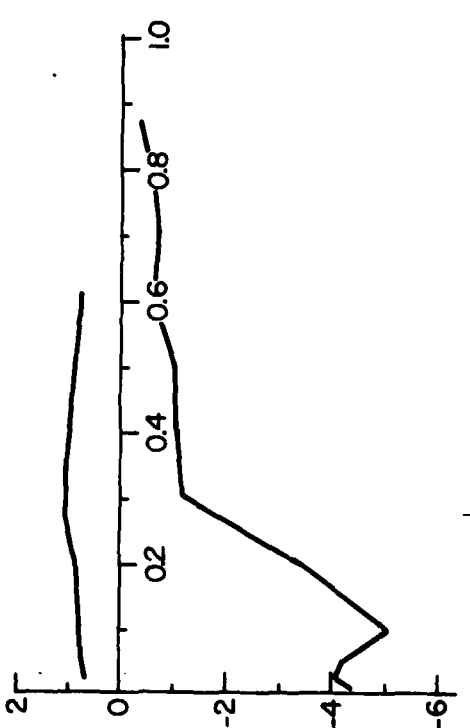
(D) 30.9°

FIGURE III-7.
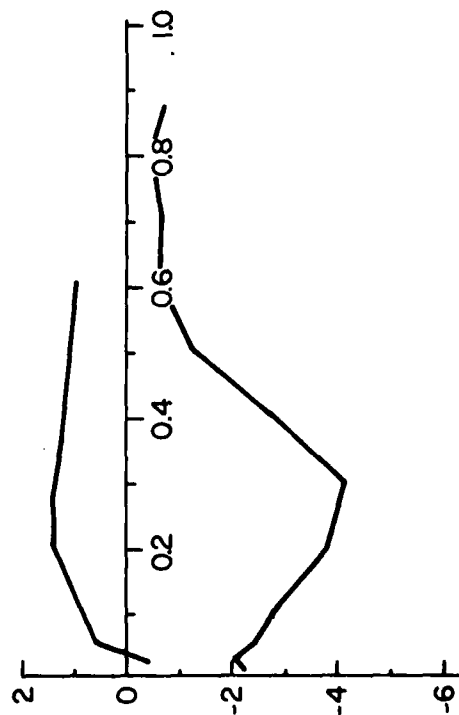UNSTEADY PRESSURE DISTRIBUTIONS, NACA 0012 $k = 0.130$, $\alpha_{max} = 55°$, $U_\infty = 33.9$ fps.
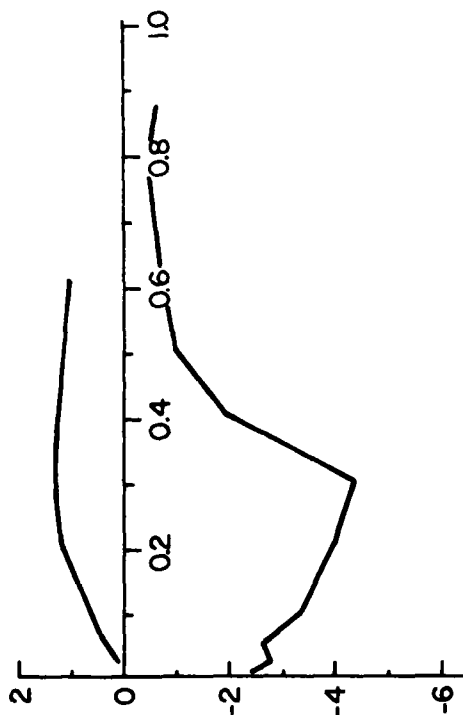
FIGURE III-7
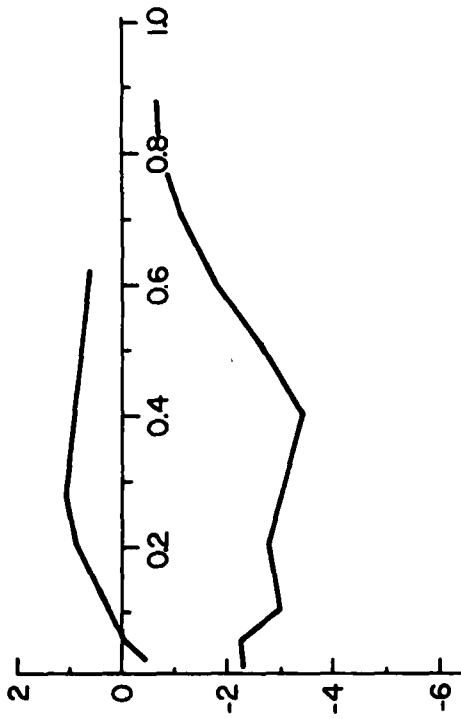CONTINUED
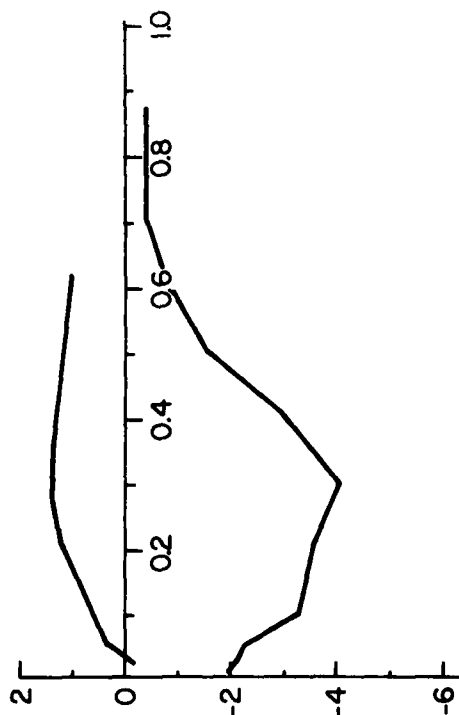
(I) 52.7°

(J) 53.6°

(K) 54.4°

(L) 55.3°
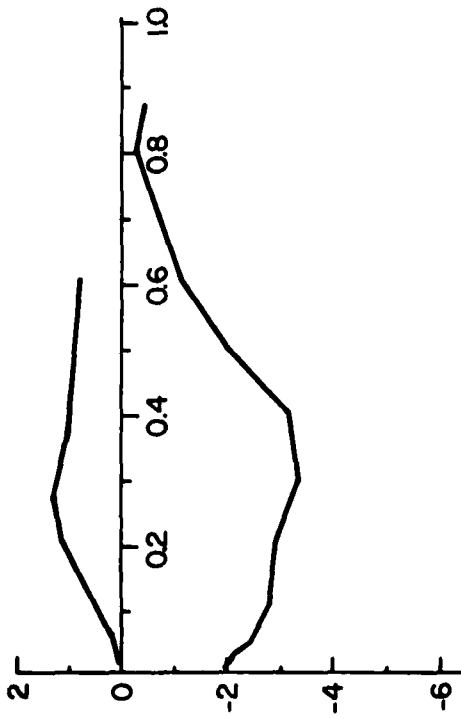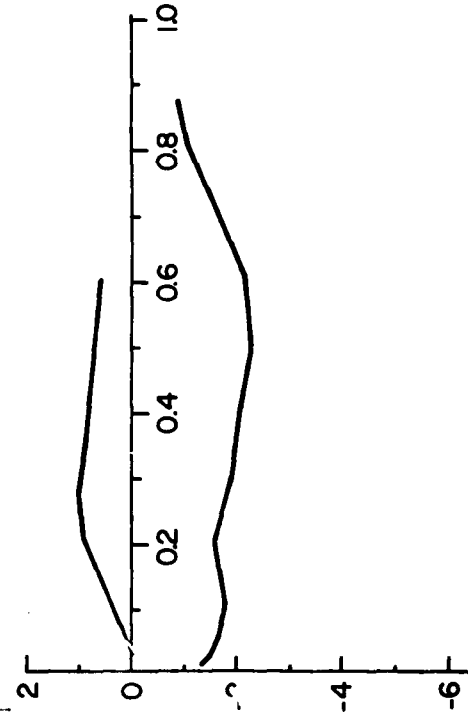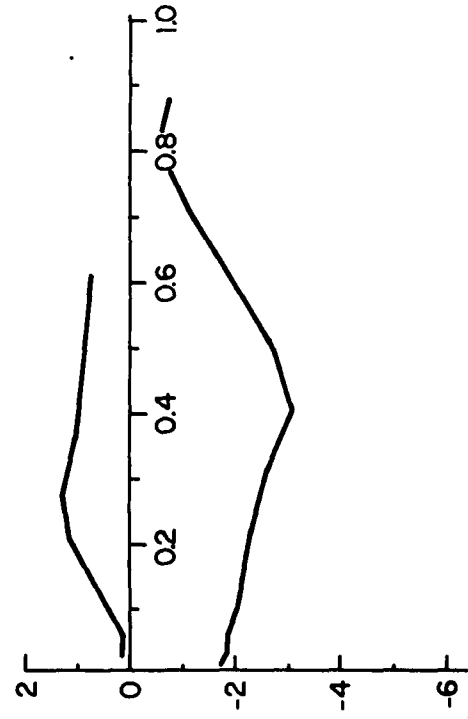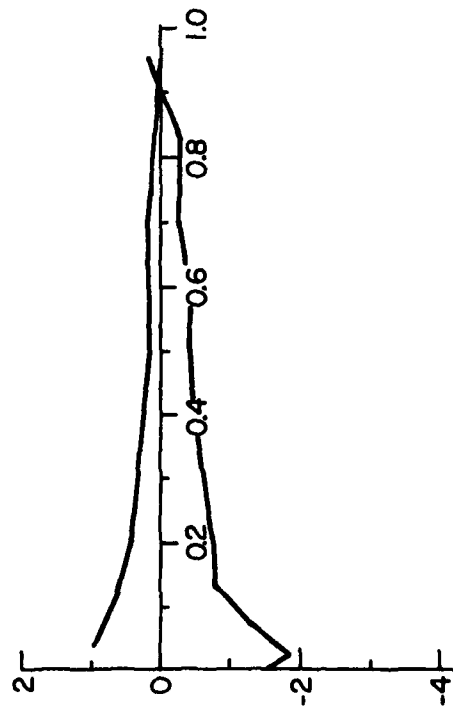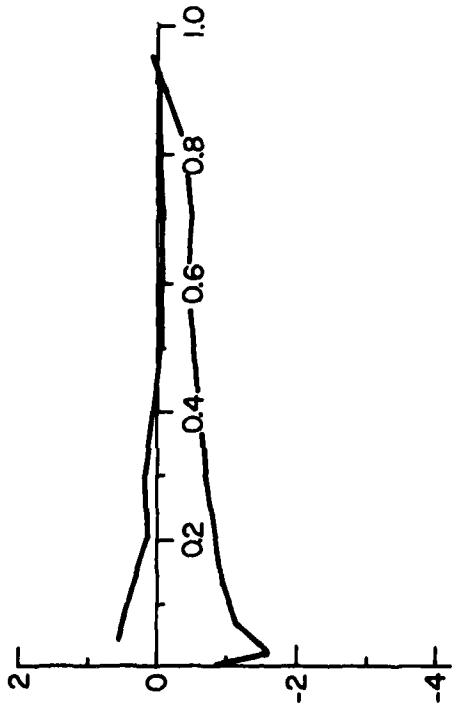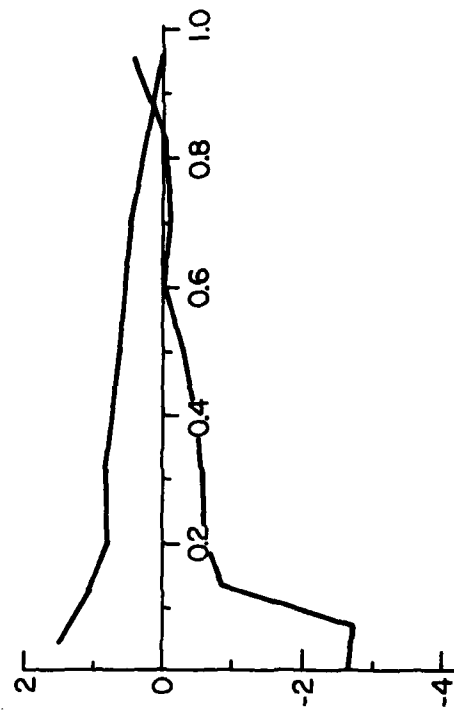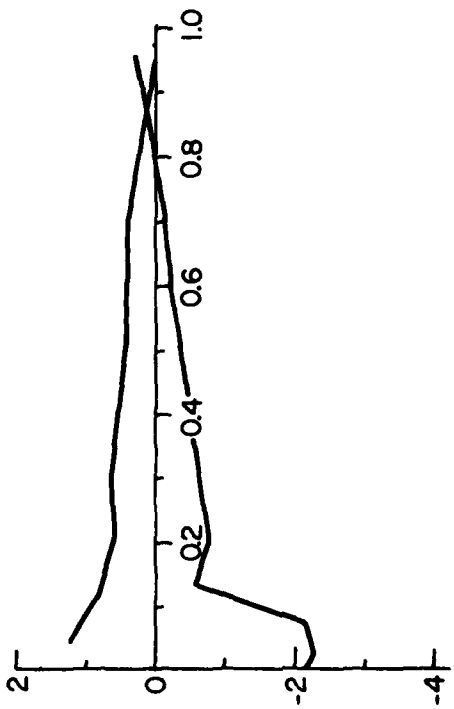
FIGURE III-7
CONTINUED

FIGURE III-8

UNSTEADY PRESSURE DISTRIBUTIONS, NACA 64,A012(13) $k = 0.045$, $\alpha_{max} = 58^o$, $U_\infty = 32.1$ fps.

(A) 8.9°

(B) 11.2°

(C) 12.9°

(D) 15.1°

(E) 18.3°

(F) 20.6°

(G) 23.0°

(H) 25.6°
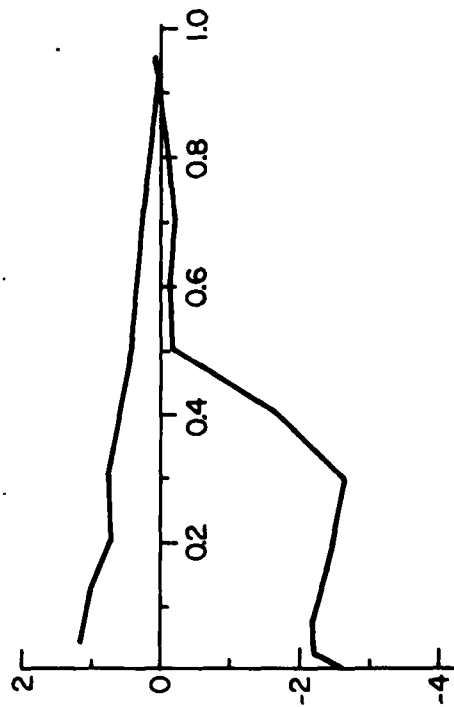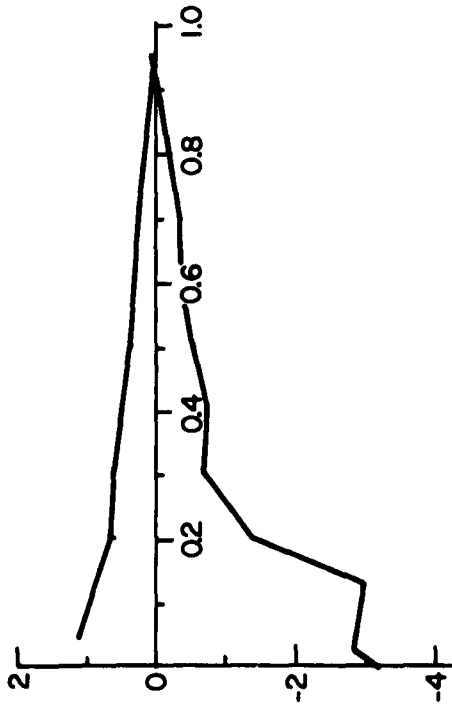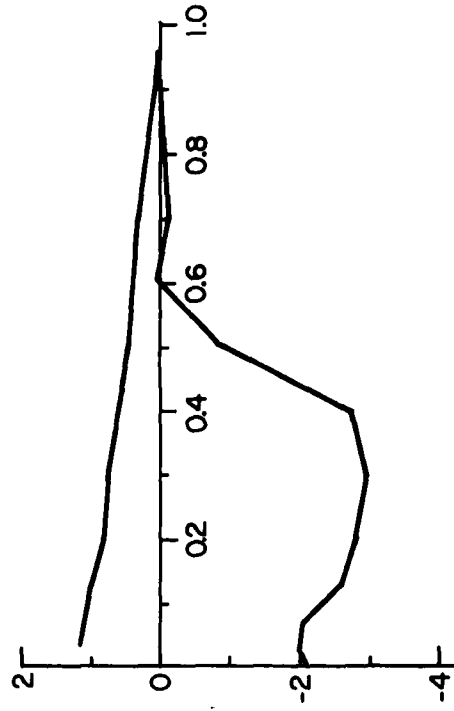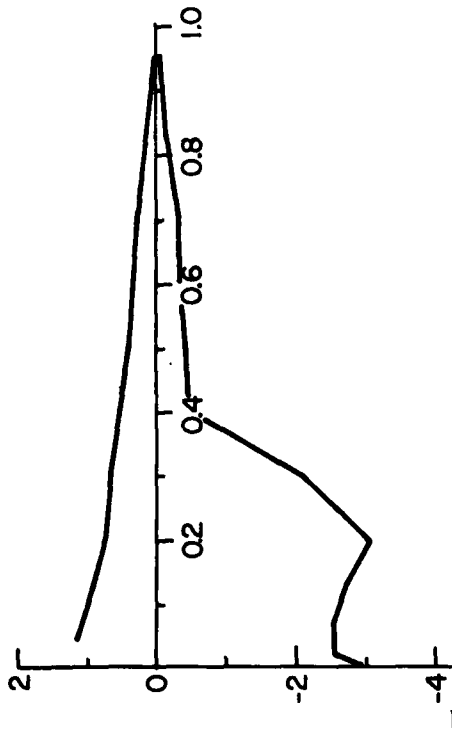
FIGURE III-8
CONTINUED
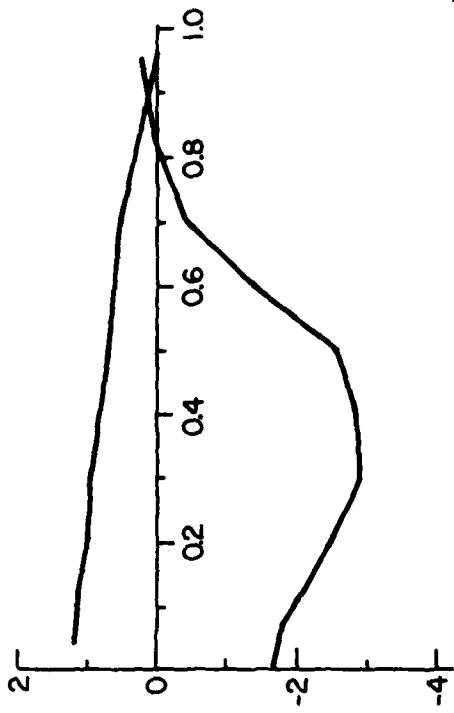
(I) 27.6°
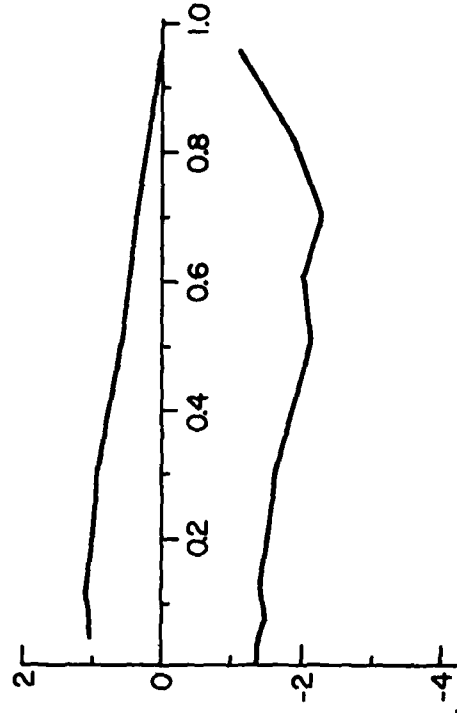
(J) 30.7°
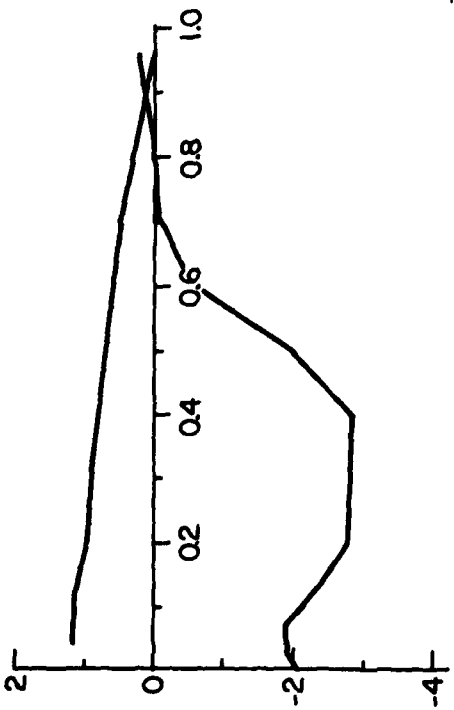
(K) 35.0°
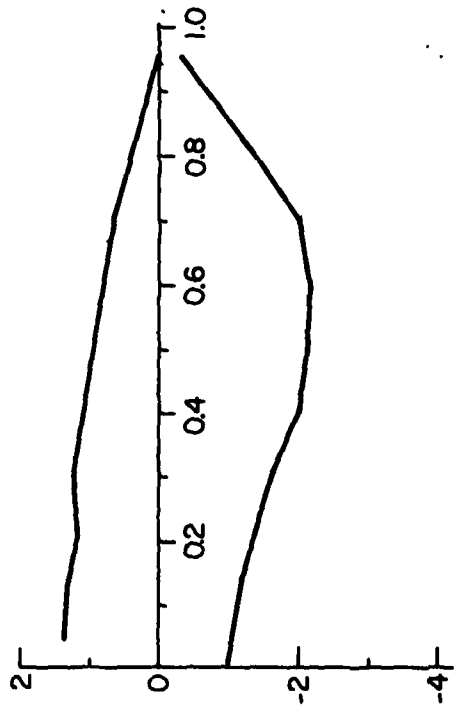
(L) 37.2°

FIGURE III-8

CONTINUED
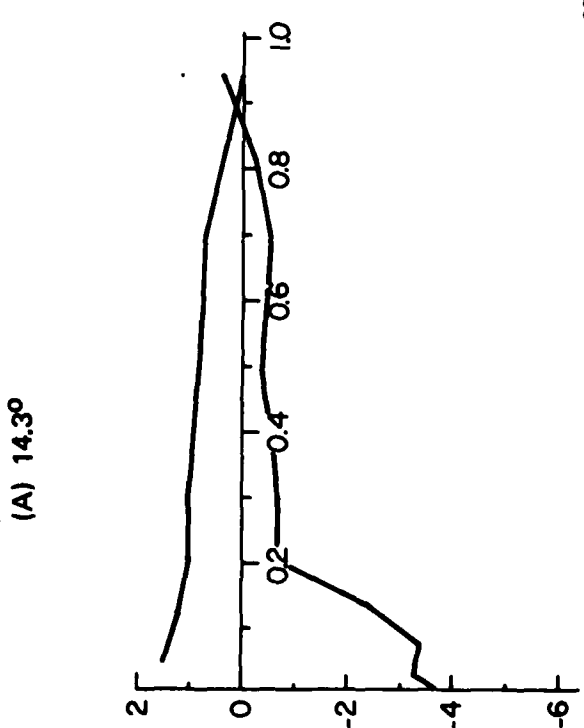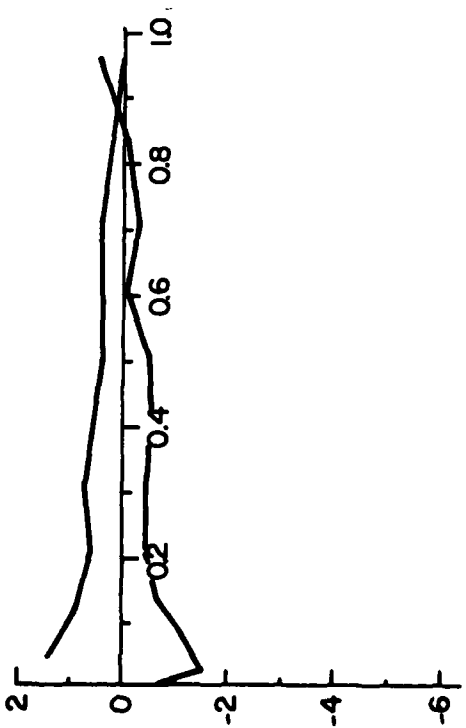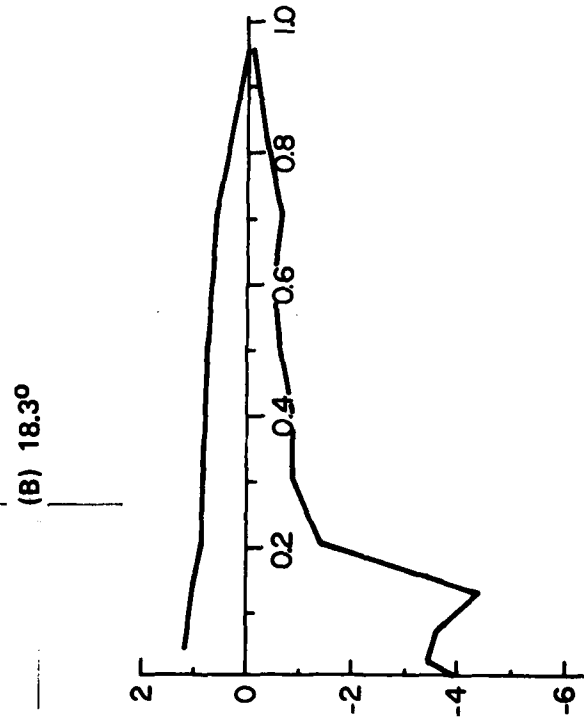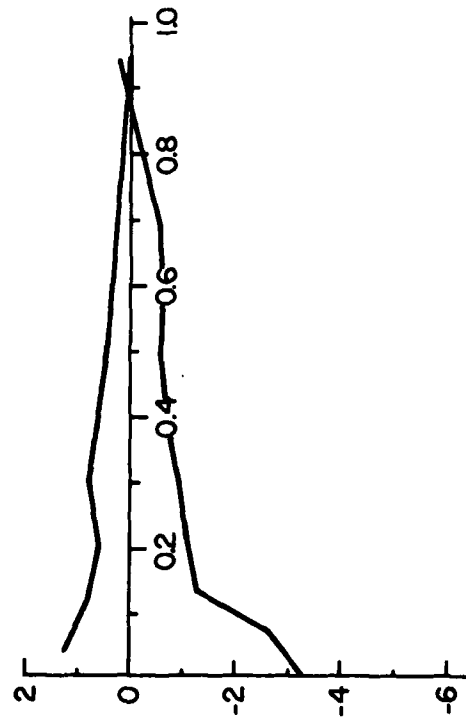
FIGURE III-9 — UNSTEADY PRESSURE DISTRIBUTIONS, NACA 64,A012(13) $k = 0.094, \alpha_{max} = 59^o$, $U_\infty = 32.1$ fps.

(A) 14.3°

(B) 18.3°

(C) 22.9°

(D) 25.2°
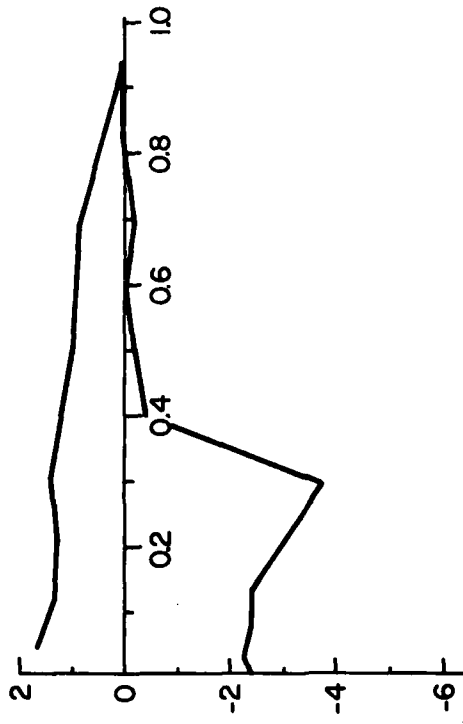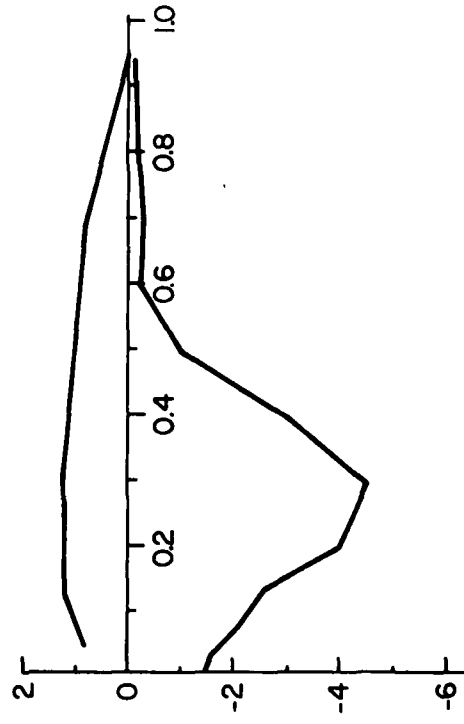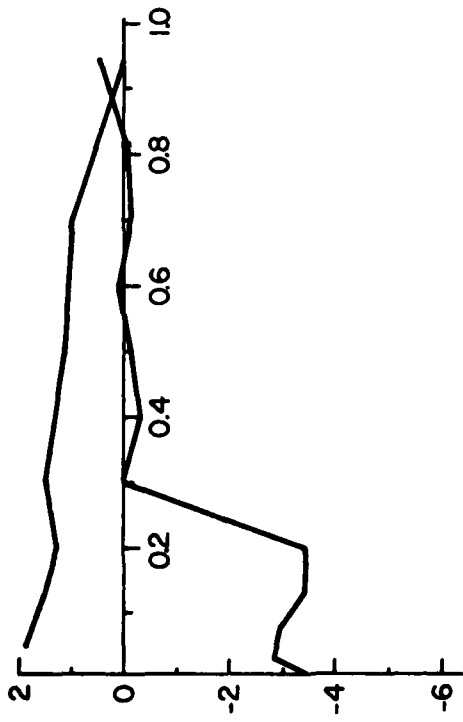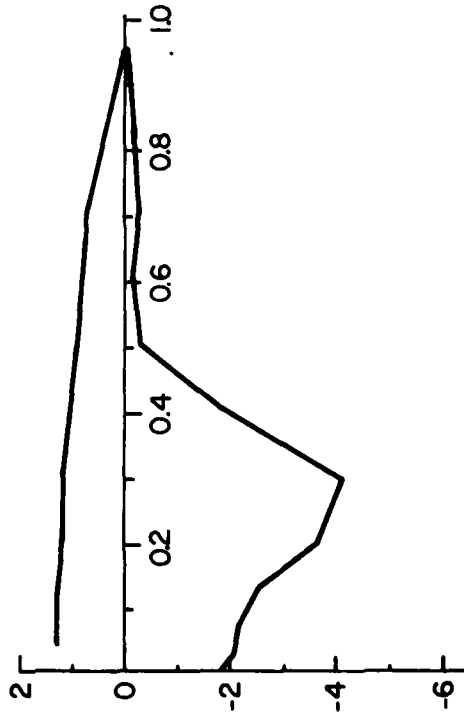
FIGURE III-9
CONTINUED
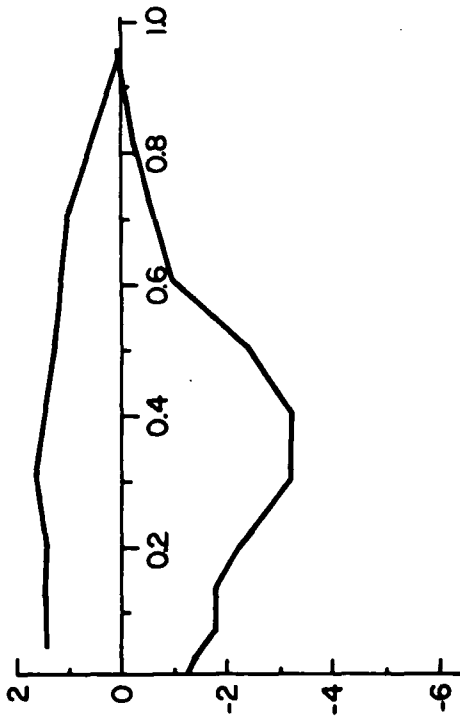
(I) 49.6°
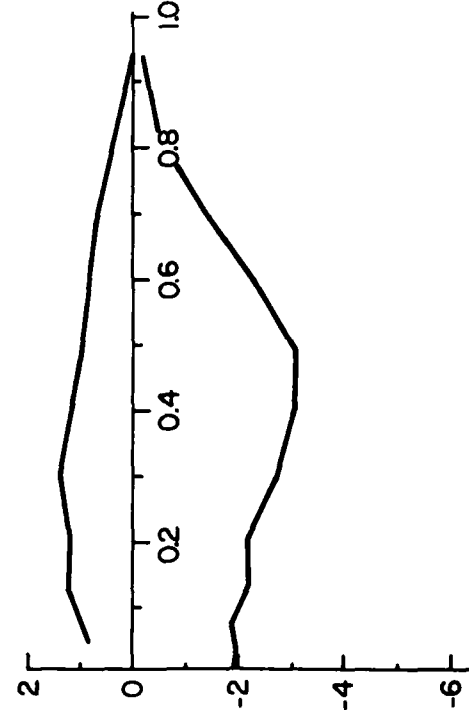
(J) 53.3°
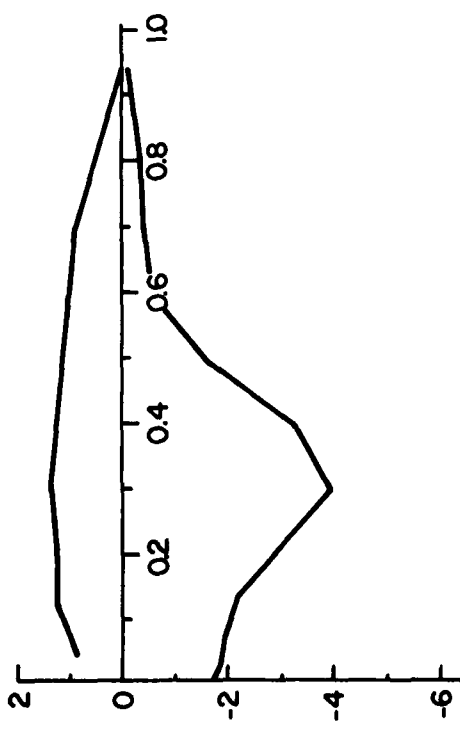
(K) 55.6°
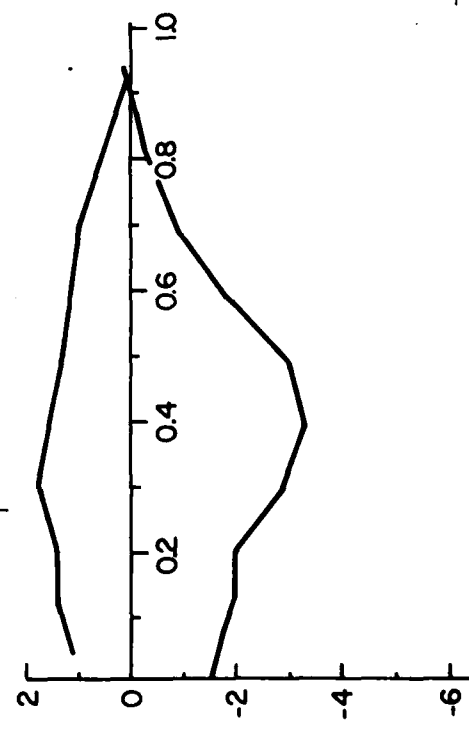
(L) 58.4°

FIGURE III-9
CONTINUED
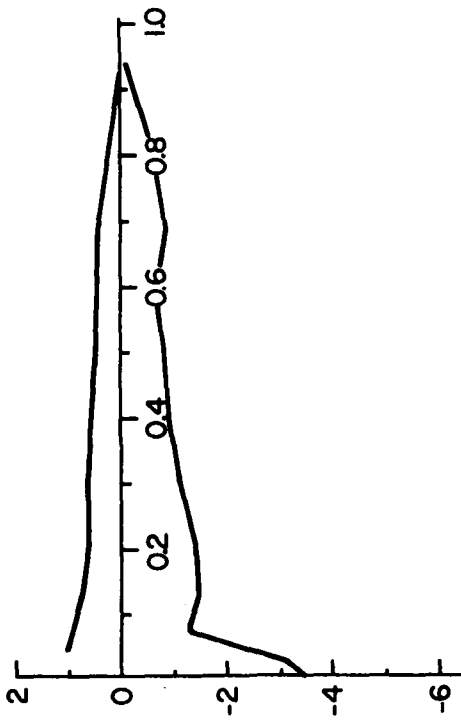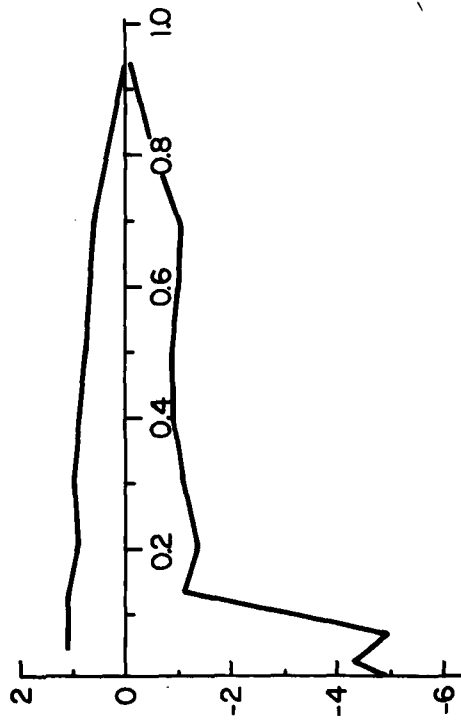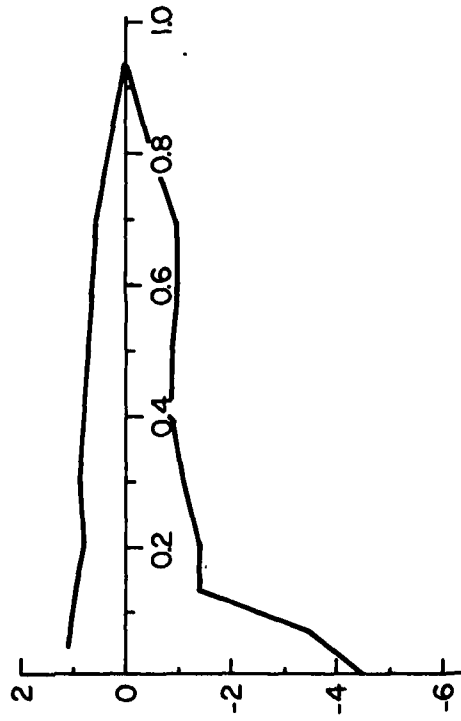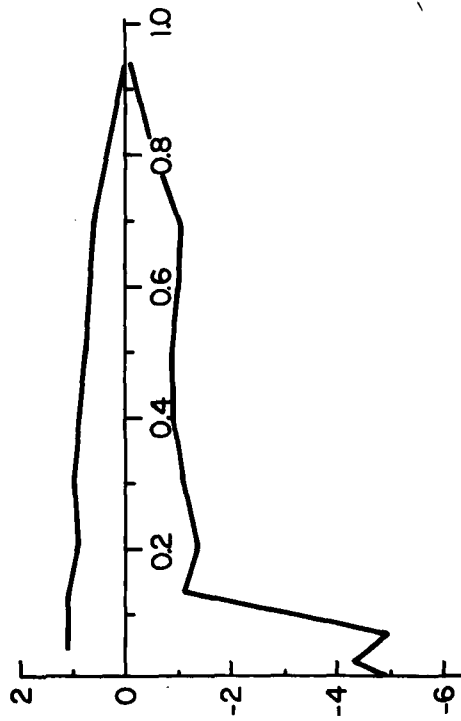
FIGURE III-10

UNSTEADY PRESSURE DISTRIBUTIONS, NACA 64,A012(13) $k = 0.136$, $\alpha_{max} = 59^o$, $U_\infty = 32.5$ fps.
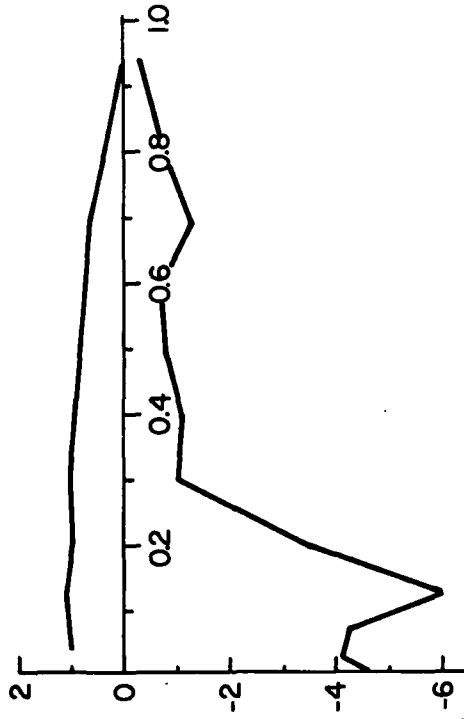
(E) 25.8°

(F) 29.2°
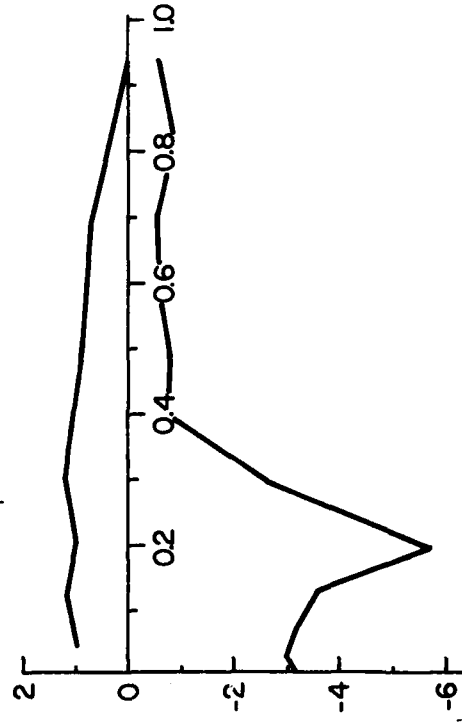
(G) 32.7°

(H) 35.8°
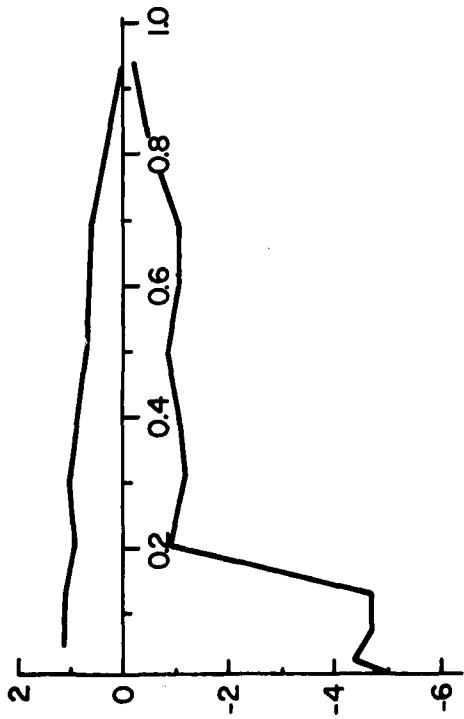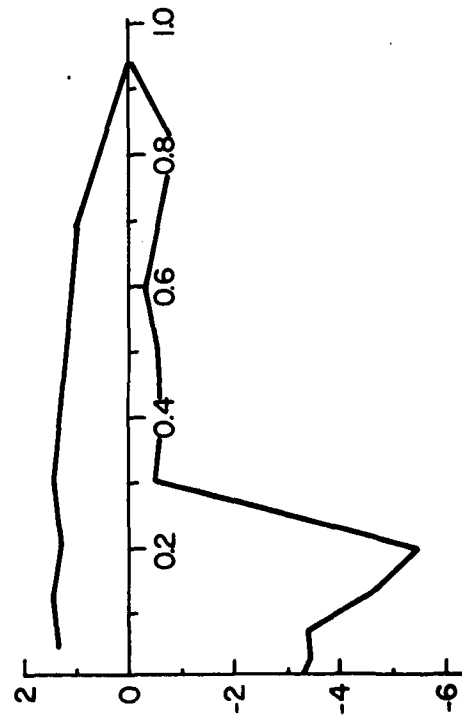
FIGURE III-IO
CONTINUED
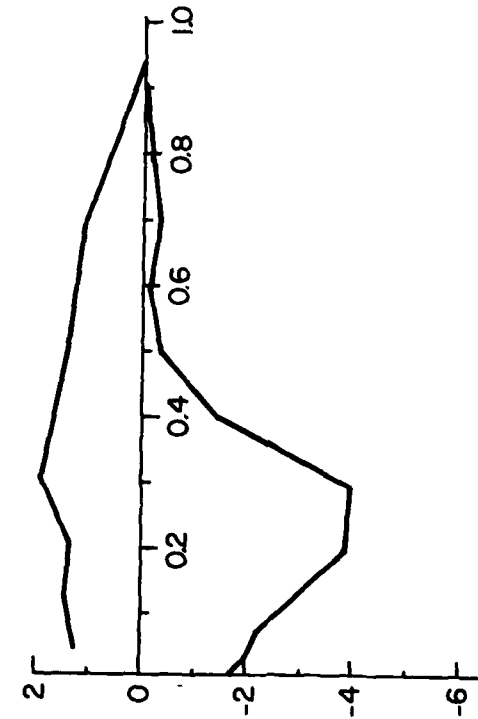
(I) 38.7°
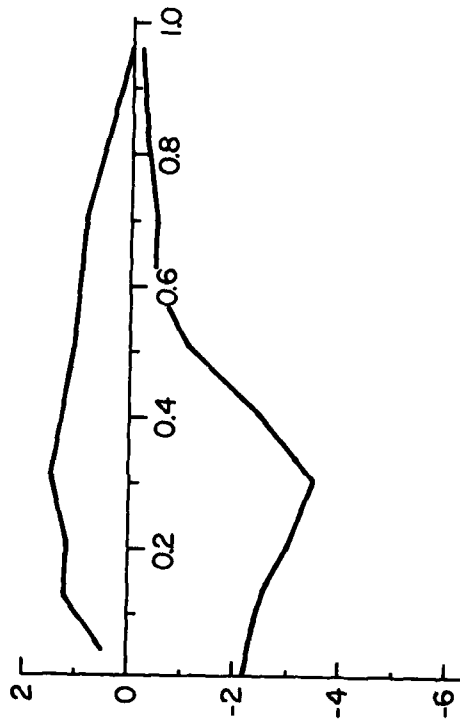
(J) 45.8°
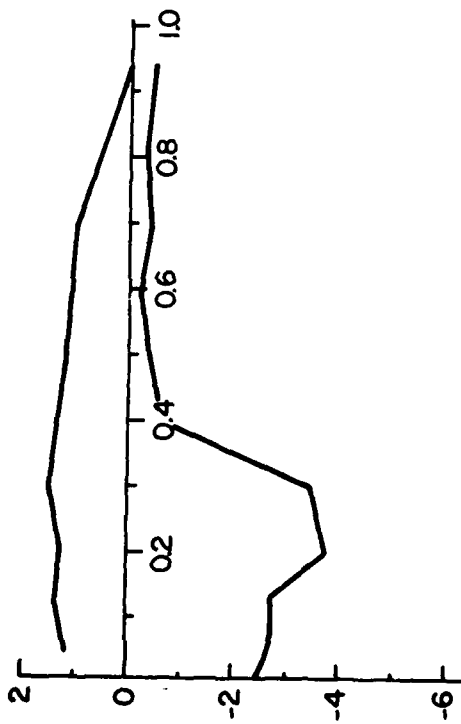
(K) 52.7°
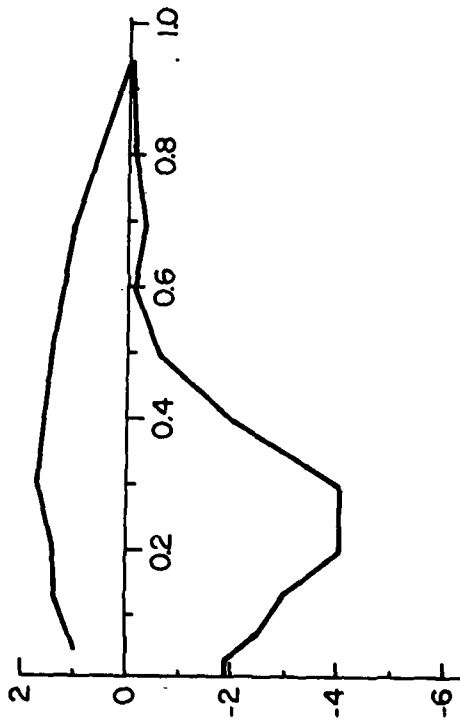
(L) 57.9°

FIGURE III-10
CONTINUED
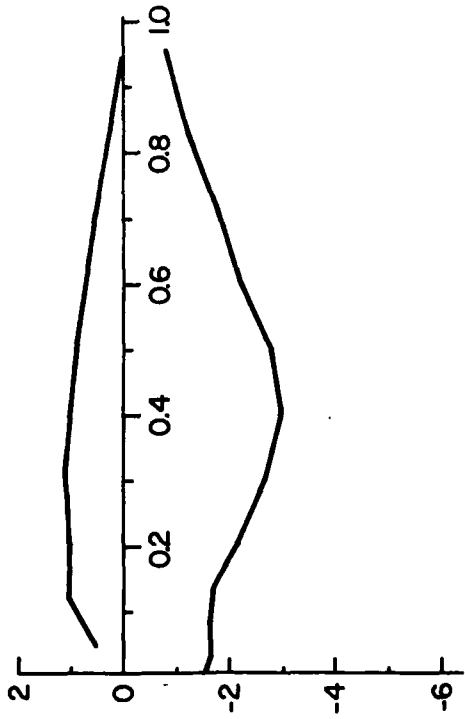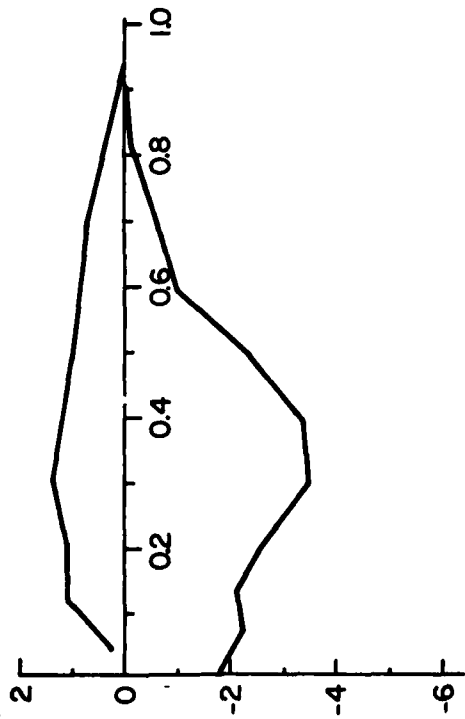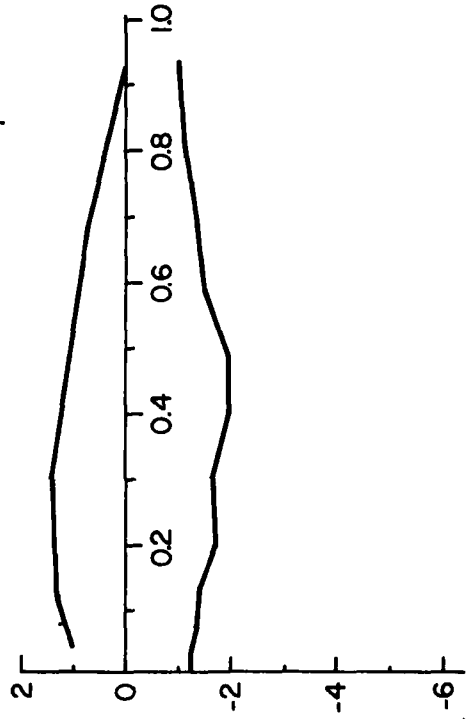
FIGURE III-10
CONTINUED

O – NACA 0012, k = .047, TEST 10
Δ – NACA 64,A012(13), k = .045, TEST 31
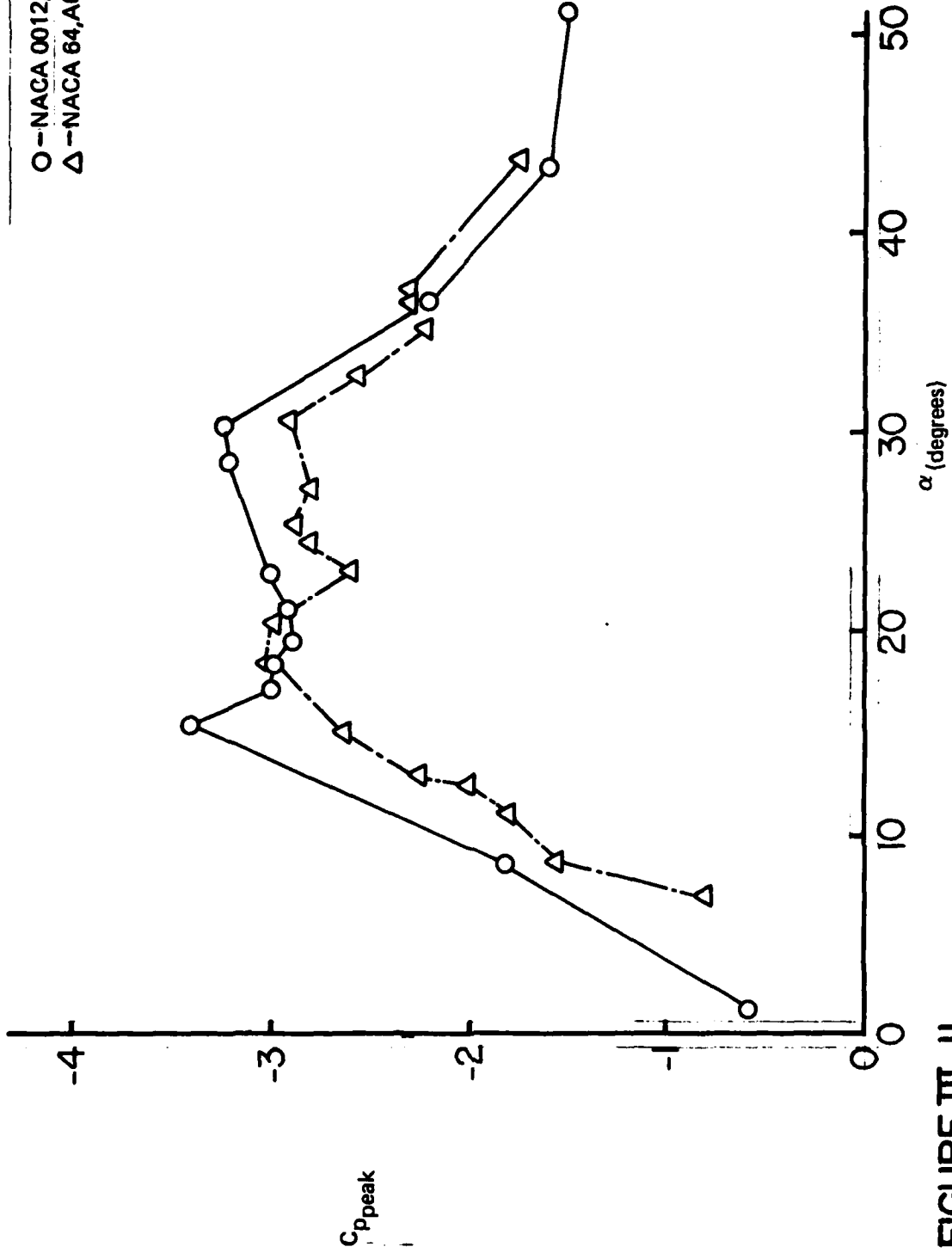
FIGURE III-11

MOVEMENT OF PRESSURE PEAK (MINIMUM) WITH INCIDENCE ANGLE,
AIRFOIL COMPARISON.
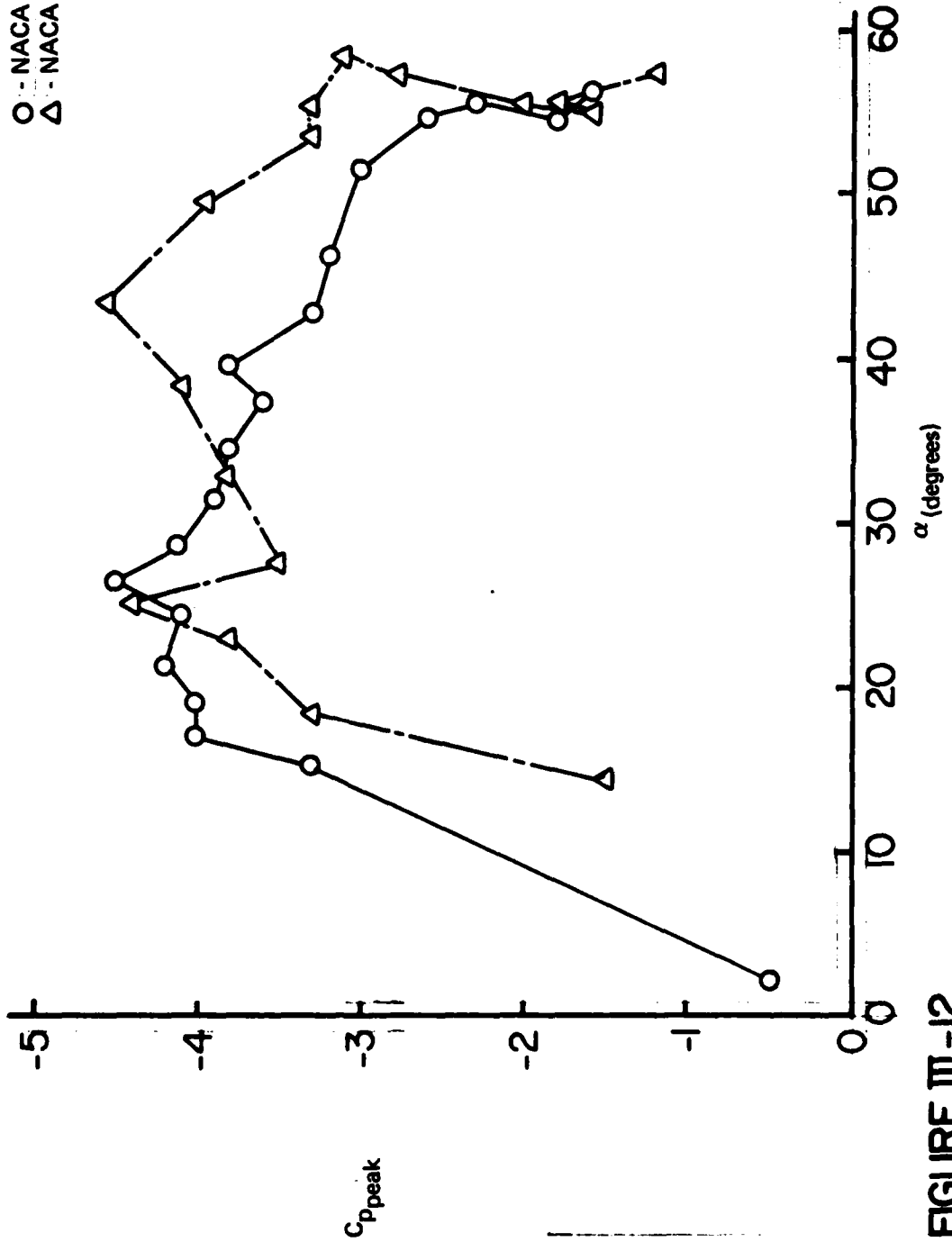
FIGURE III-12

MOVEMENT OF PRESSURE PEAK (MINIMUM) WITH INCIDENCE ANGLE, AIRFOIL COMPARISON.
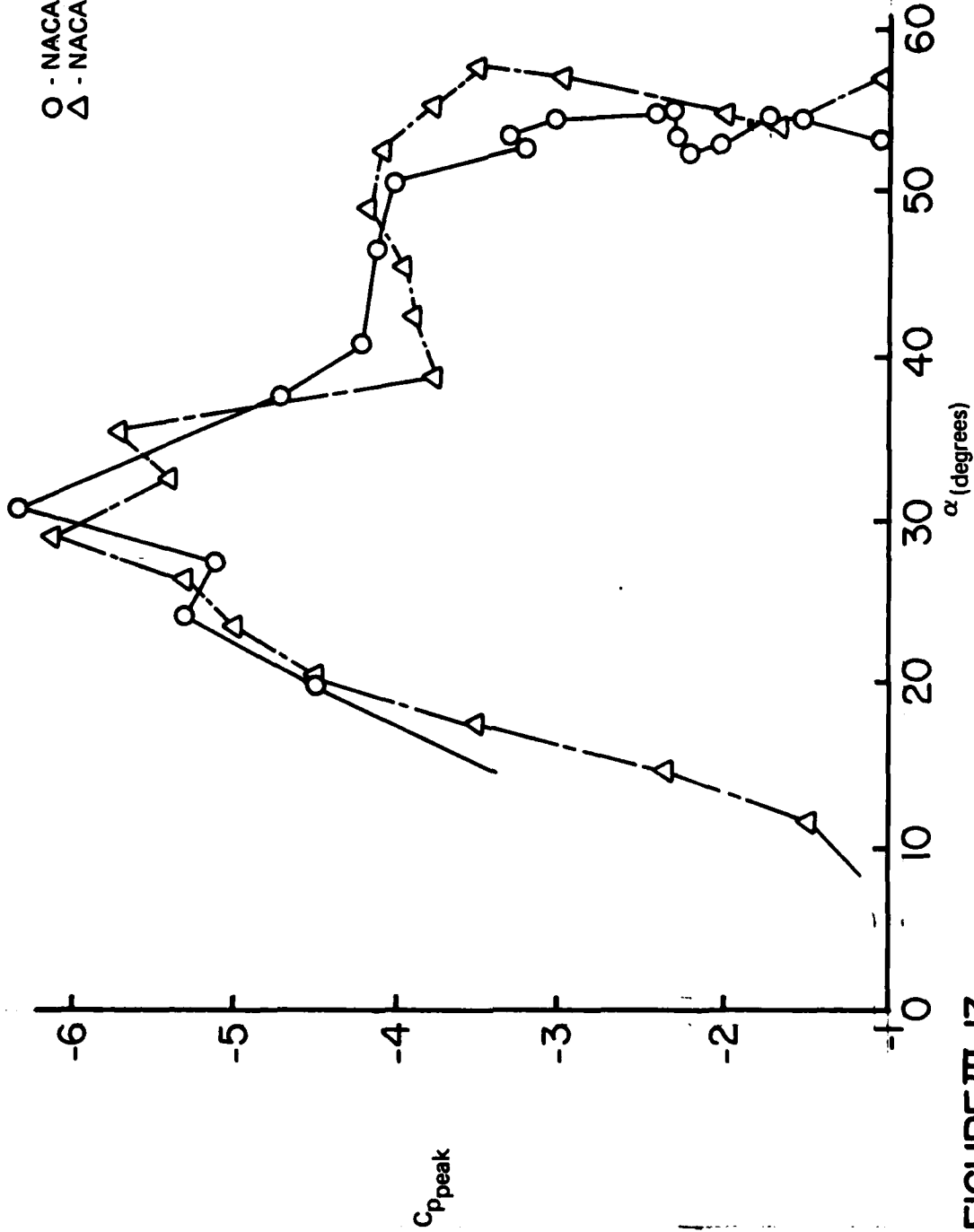
FIGURE III-13

MOVEMENT OF PRESSURE PEAK (MINIMUM) WITH INCIDENCE ANGLE, AIRFOIL COMPARISON.

IV.   INTEGRAL MEASUREMENT RESULTS

The pressure distributions described in the preceding section have
been integrated to provide load and moment time histories for each of
the test cases examined. As indicated in Section II, numerical integra-
tion programs provided values of airfoil normal force coefficient (C_n),
lift coefficient (C_l), moment coefficient about the quarter chord (C_m),
and pressure drag coefficient (C_d) as functions of time and, implicitly,
incidence angle. Available computer graphics capabilities provided
cross plc ` of these variables, with time and incidence angle as potential
parameters.

Graphs of lift coefficient versus incidence angle for steady free-
stream and static model conditions are displayed for both airfoils in
Figures IV-1 and IV-2. Maximum values of the static lift coefficient
are also shown. NACA 0012 data are plotted with results of a Navier-
Stokes computation[23] and are observed to be in good agreement. The low
value of the initial lift curve slope as well as the nonlinear behavior
at higher incidence angles are believed to be attributable to the test
Reynolds number range. Note, however, that the variation in lift
characteristics over the range of Reynolds numbers studied here (factor
of 2) is small compared to the departure from ideal airfoil behavior.

Unsteady lift, moment, and drag data for both airfoils are displayed
in Figures IV-3 through IV-12 for several sets of reference conditions.
These data sets were selected to afford a basis for comparing performance
of the two airfoils at nearly identical pitch rates and amplitudes.
Note that the lift coefficient is displayed instead of the more tradi-
tional normal force coefficient, since the primary objective of this

report is an assessment of aerodynamic lifting performance. Normal and chord force coefficients have been converted to lift and drag coefficients through a cartesian coordinate transformation which accounts for the instantaneous airfoil orientation.

Lift stall characteristics are observed to be comparable for the two airfoils at low and moderate pitch rates (k = 0.045 and 0.09, respectively) with large amplitude displacements. However, the NACA 0012 airfoil is observed to provide a slightly less severe moment stall (large nose down moment) in this range. When the maximum amplitude of motion is less than or comparable to the incidence angle at which unsteady leading edge separation would otherwise occur (Figures IV-9 through IV-12), the moment stall associated with both airfoils is observed to be comparable and severe at the maximum incidence angle. An abrupt decrease in moment coefficient is also evident in the plot of C_m with time. The overall shape of the lift curves is similar for the two airfoils under any comparable set of flow and motion conditions.

The pressure drag force is also important in assessing overall airfoil performance. Drag coefficients of relatively large magnitude are observed in conjunction with dynamic stall; a fact which is physically consistent with a notion that energetic unsteady separation results in a tightly wound vortex-like structure during the initial stages of the process. If the airfoil were performing in a free flight environment, its large increasing drag force would result in an axial deceleration in the freestream direction. Alternatively, it can be hypothesized that the transient lift associated with the dynamic stall vortex is provided through an extraction of freestream kinetic energy due to the airfoil motion. The mechanics of this process may be more fully understood

by considering airfoil pitching motions which are coupled to time
dependent behavior of the freestream. A discussion of some preliminary
results which address this issue will be the subject of a later report.

The shape of the drag coefficient curves are similar for the two
airfoils with one notable exception. Initially, the drag increases less
rapidly for the NACA $64_1A012(13)$ airfoil as the incidence angle rises.
However, this is followed by a rapid increase in the drag coefficient to
the maximum value. The rate of drag increase of the NACA 0012 is more
uniform over the range of angles of attack.

The occurrence of separation and stall prior to reaching the maximum
incidence of motion is again evident from the time history data shown in
Figure IV-13. These results suggest that the unsteady separation "vortex"
is shed at some lower angle which coincides with the formation and progres-
sion of the pressure suction peak. Force-time curves of this type are
useful in assessing overall airfoil performance as discussed in the next
chapter.

An interesting feature apparent in the lift coefficient versus time
curves is that of a "notch"-like indentation which is noticeably larger
than the more random smaller amplitude fluctuations. The notch is
depicted schematically in Figure IV-14. It occurs as a depression in
the lift coefficient between two local maxima and may well be caused by
the appearance of a secondary vortex structure or possibly other vortex
behavior which must be documented through flowfield measurements. Using
the notation illustrated in Figure IV-14, the notch location (time
difference between its occurrence and that of the maximum lift) is
plotted as a function of dimensionless frequency in Figure IV-15. Notch
location is observed to be only a weak function of frequency but is

different for the two airfoils. For cases of high maximum incidence
(α_{max} = 60 degrees) and low pitch rate, the notch is observed to occur
in advance of the time that the airfoil reaches its maximum lift coeffi-
cient. With increasing pitch rate, the notch is observed to appear
later in the cycle and eventually will occur subsequent to the maximum
lift point. This result is especially apparent for the case of the NACA
64_1A012(13) airfoil. The rate of shift in notch location for the two
airfoils is roughly comparable for high levels of maximum incidence in
the region of overlap. The notch phenomenon was also observed for cases
of lower maximum incidence angle (α_{max} = 35-40 degrees). However, in
those cases, it was always observed to occur after the attainment of
maximum lift. The repeatability of this behavior and persistence of the
notch-like depression suggests that the responsible viscous-inviscid
interaction occurs regularly on airfoils undergoing deep dynamic stall.
This behavior is recommended as the subject of future study.
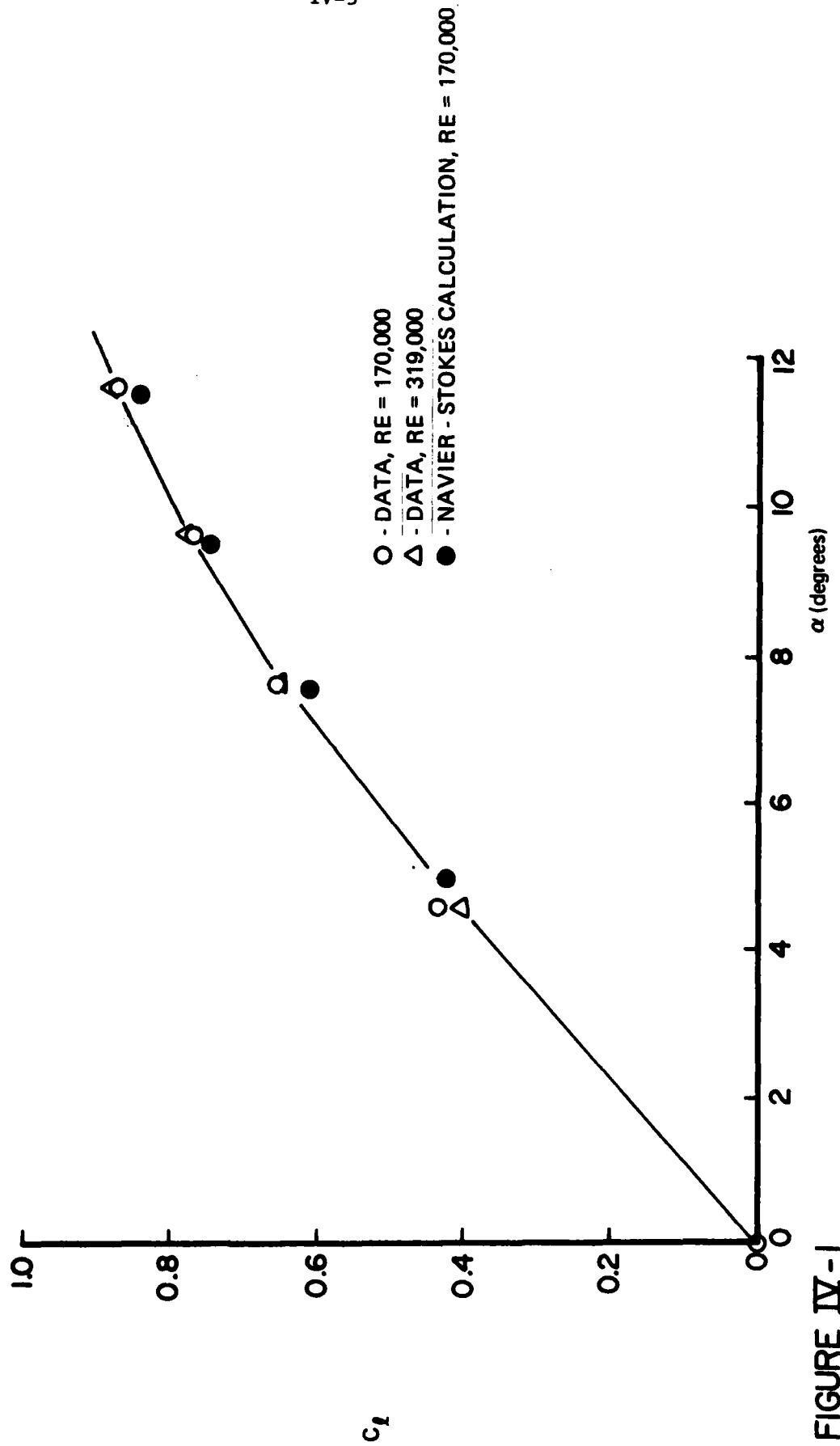
FIGURE IV-1

STEADY FLOW LIFT COEFFICIENTS, NACA 0012 AIRFOIL

O - DATA, RE = 170,000
△ - DATA, RE = 319,000
● - NAVIER - STOKES CALCULATION, RE = 170,000
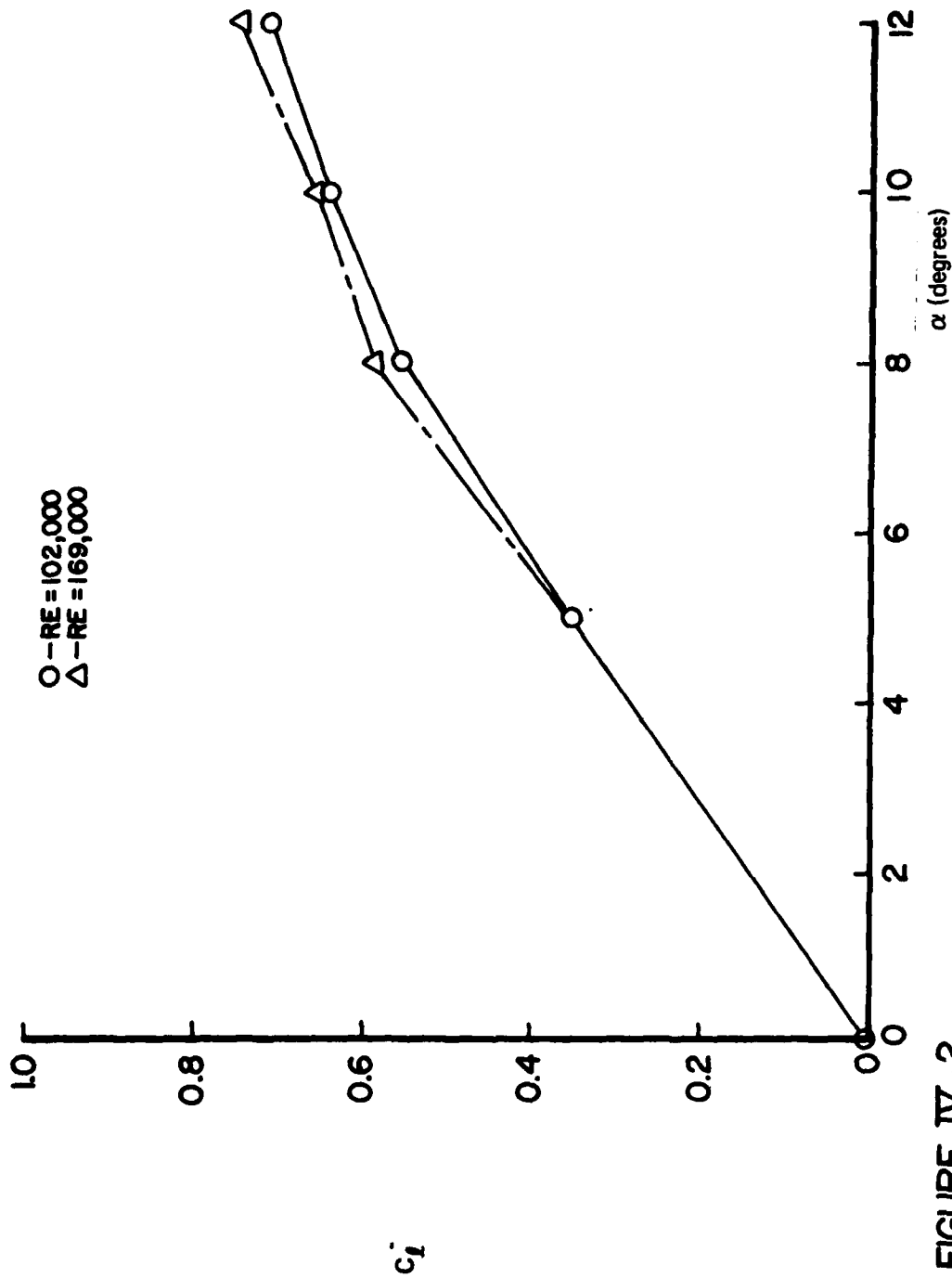
FIGURE IV-2
STEADY FLOW LIFT COEFFICIENTS, NACA 0012 AIRFOIL
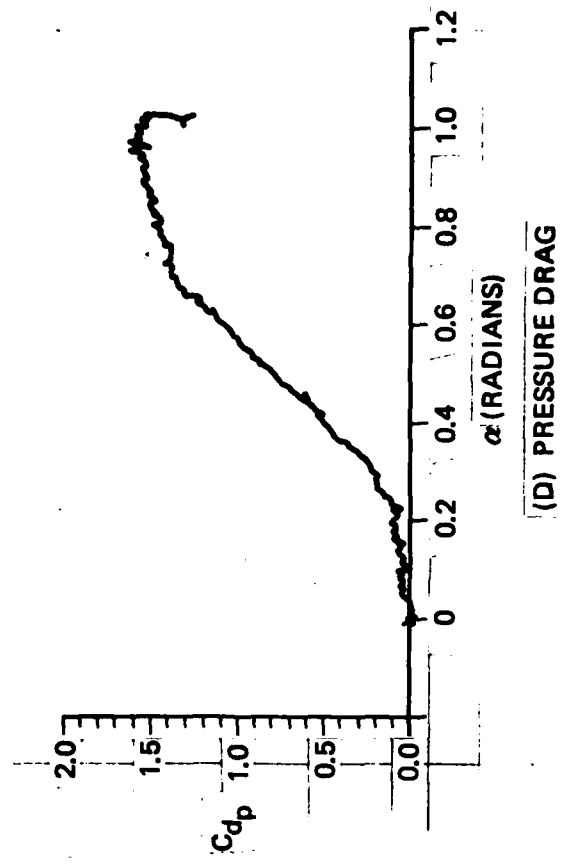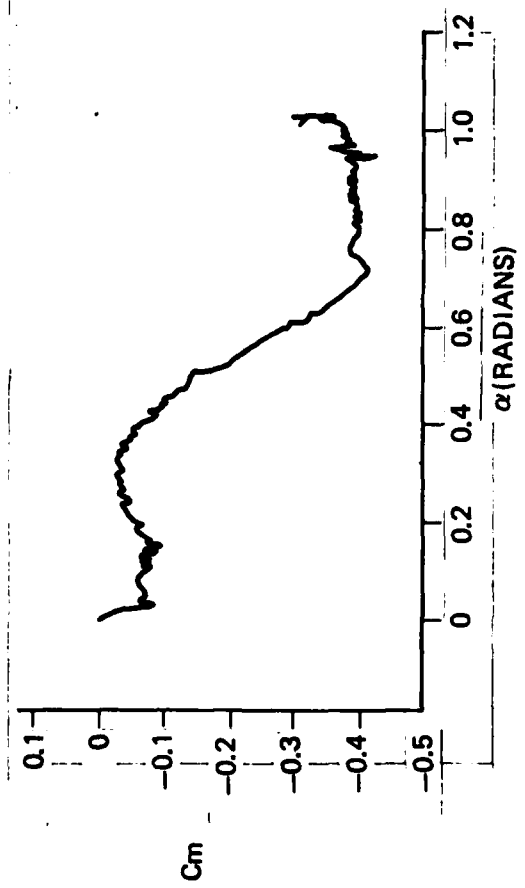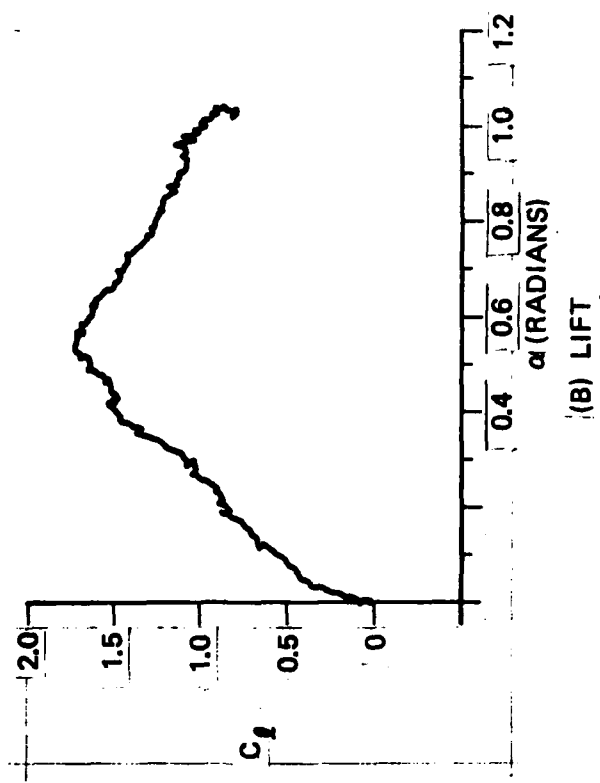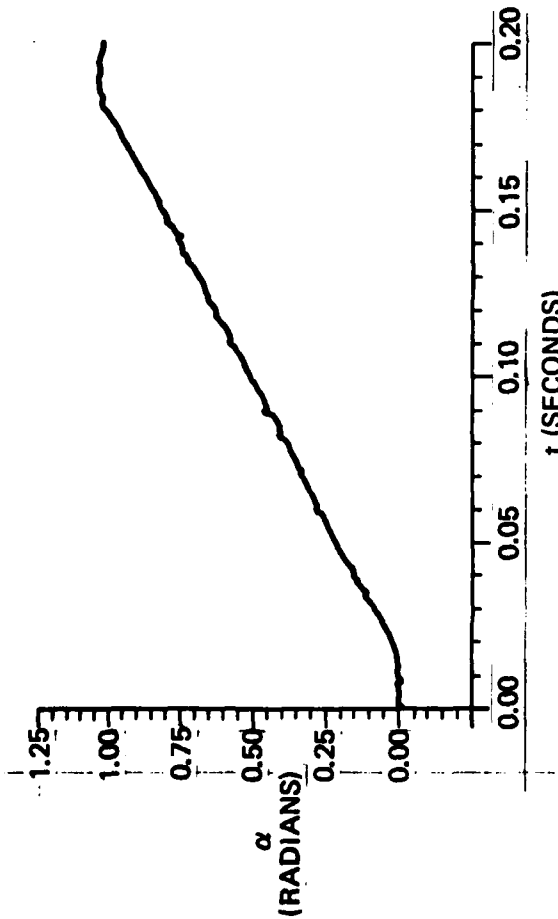
FIGURE IV-3

FORCE AND MOMENT CHARACTERISTICS, NACA 0012, $k = 0.047, \alpha_{max} = 60^{\circ}, U_{\infty} = 33.1$ fps.
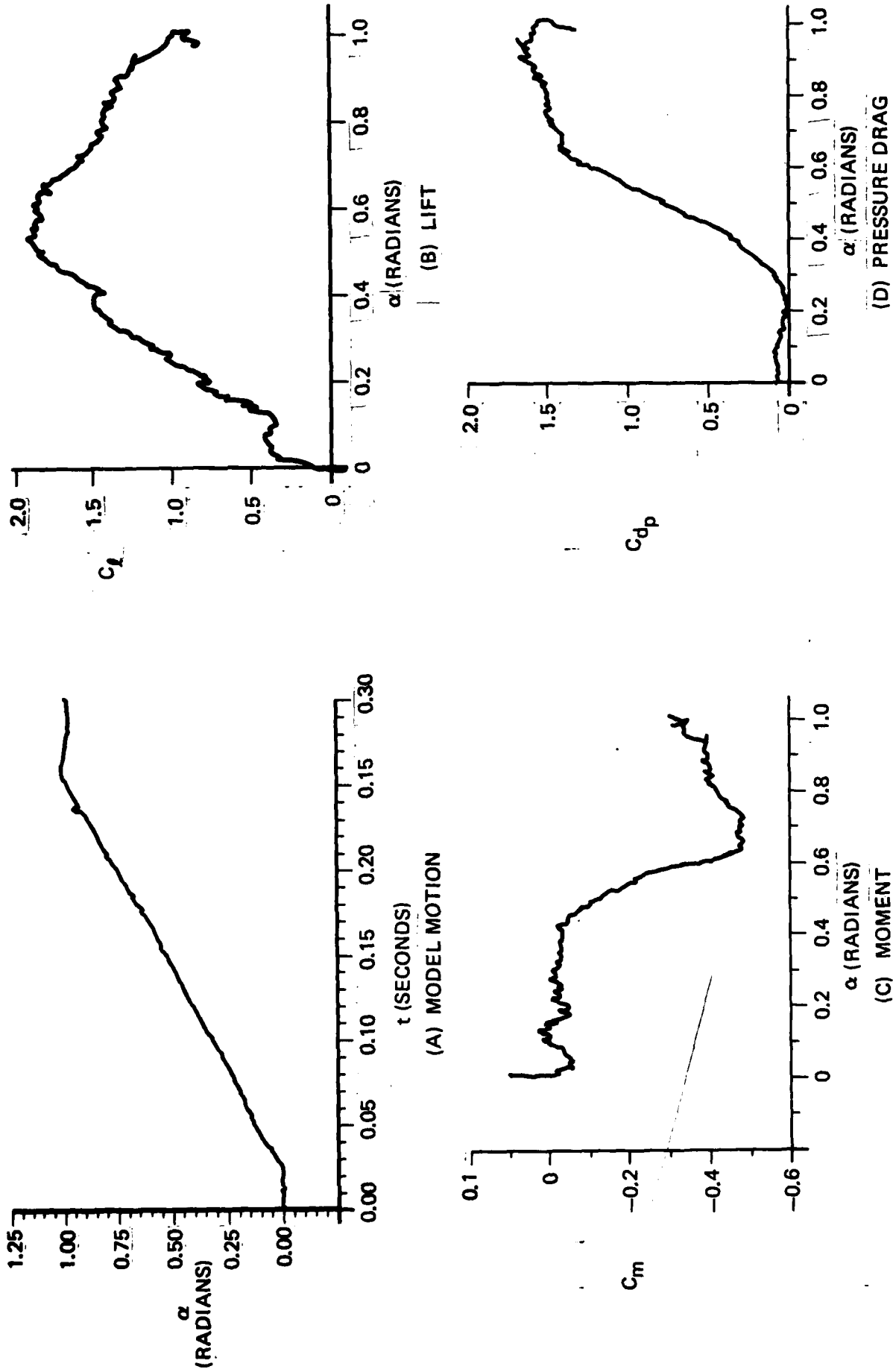
FIGURE IV-4

FORCE AND MOMENT CHARACTERISTICS, NACA 64,A012(13) , $k = 0.045, \alpha_{max} = 58^o$, $U_\infty = 32.1$ fps.
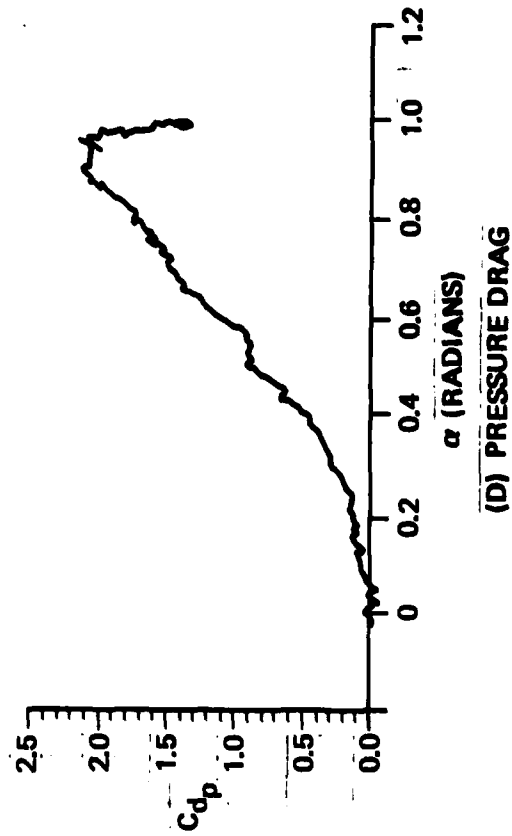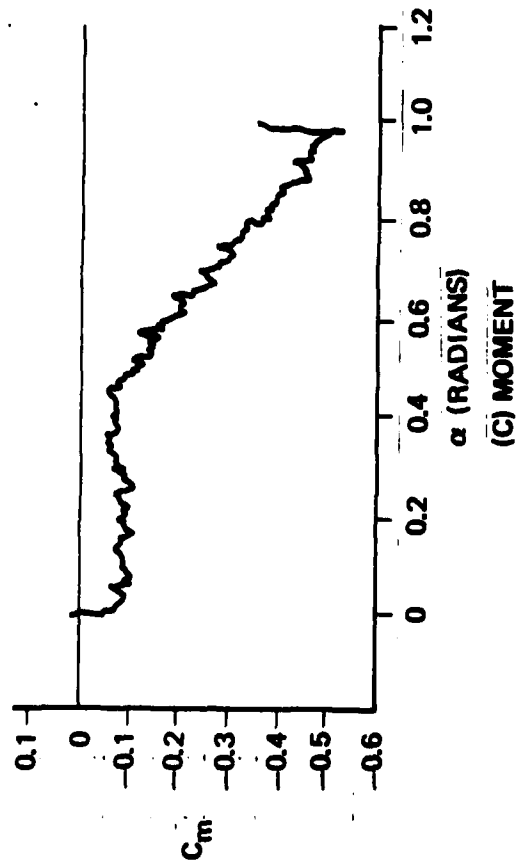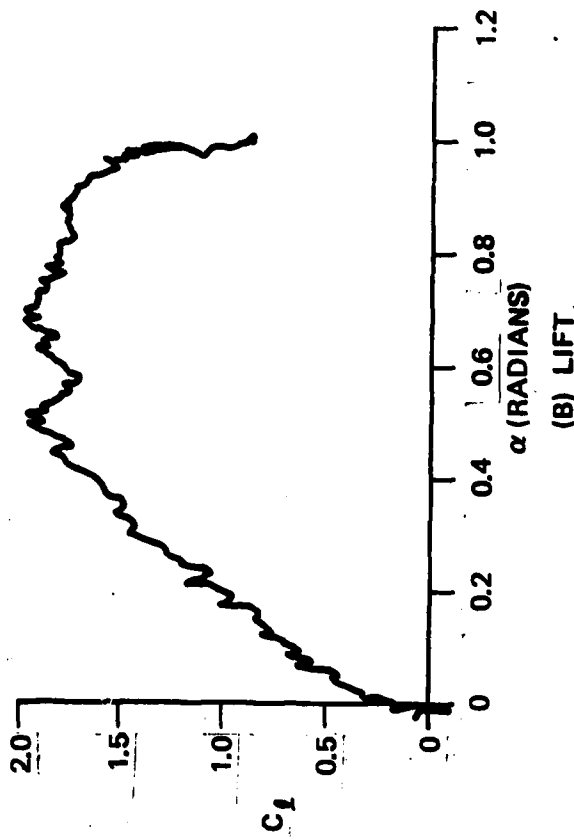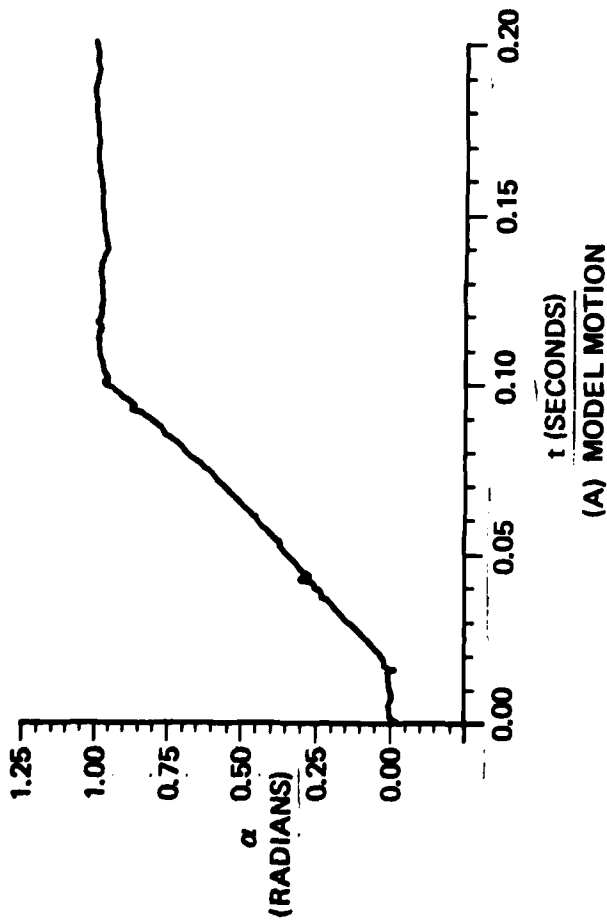
FIGURE IV-5
FORCE AND MOMENT CHARACTERISTICS, NACA 0012, k = 0.089, α_{max} = 56°, U_∞ = 33.1 fps.
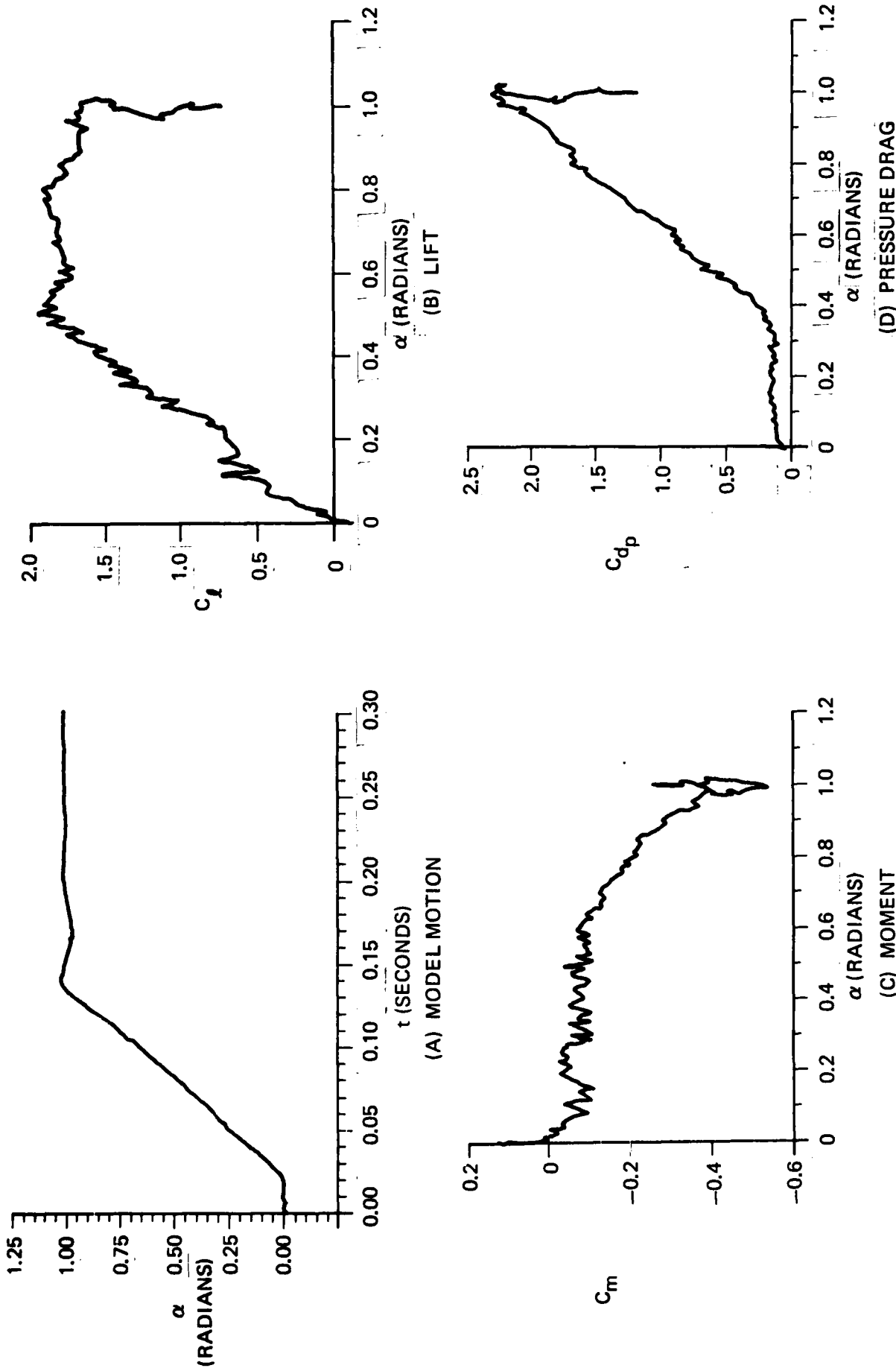
FIGURE IV-6

FORCE AND MOMENT CHARACTERISTICS, NACA 64,A012(13) , $k = 0.094, \alpha_{max} = 59^0$, $U_\infty = 32.1$ fps.
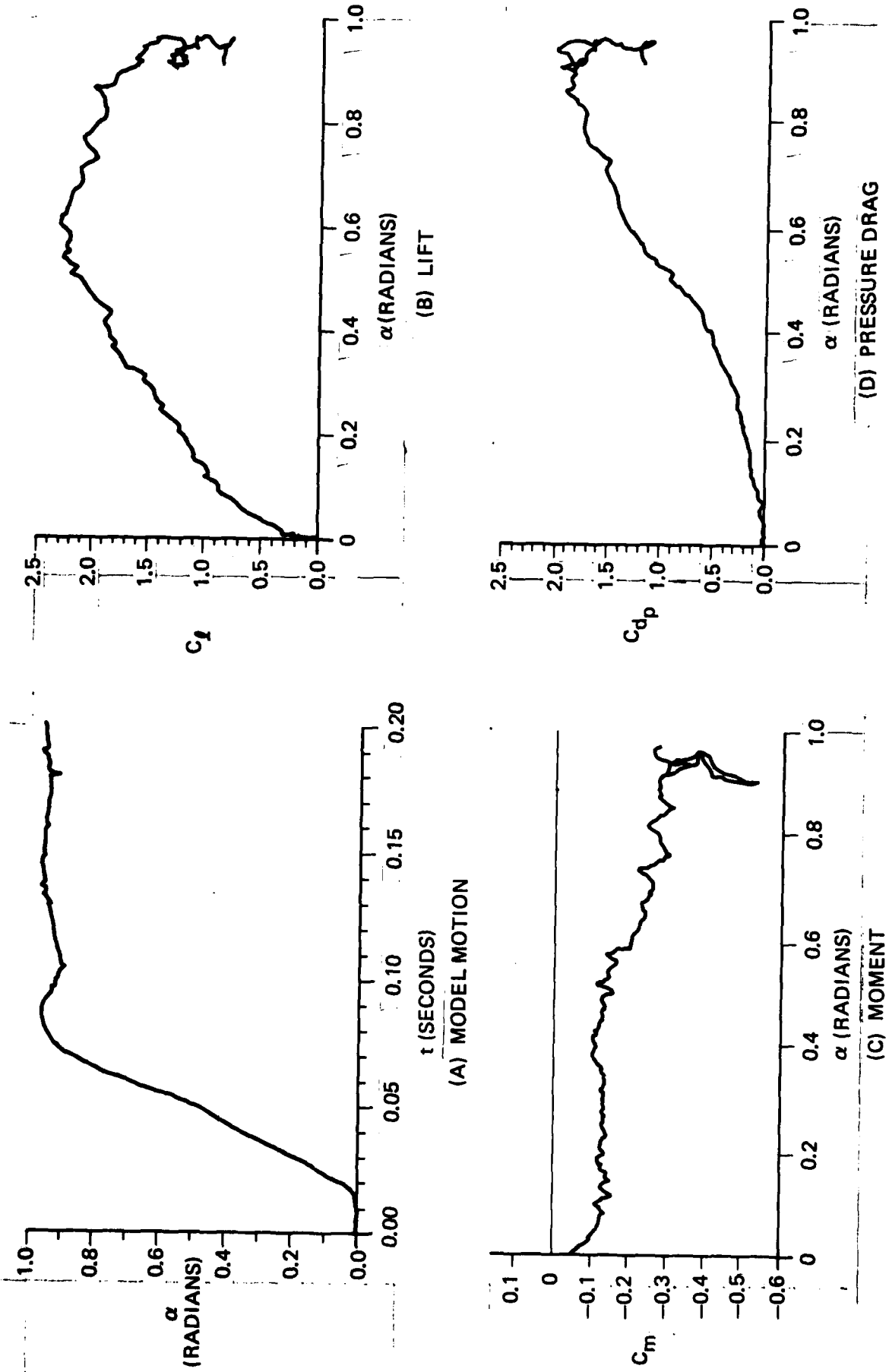
FIGURE IV-7

FORCE AND MOMENT CHARACTERISTICS, NACA 0012 , $k = 0.130, \alpha_{max} = 55^{o}$, $U_{\infty} = 33.9$ fps.
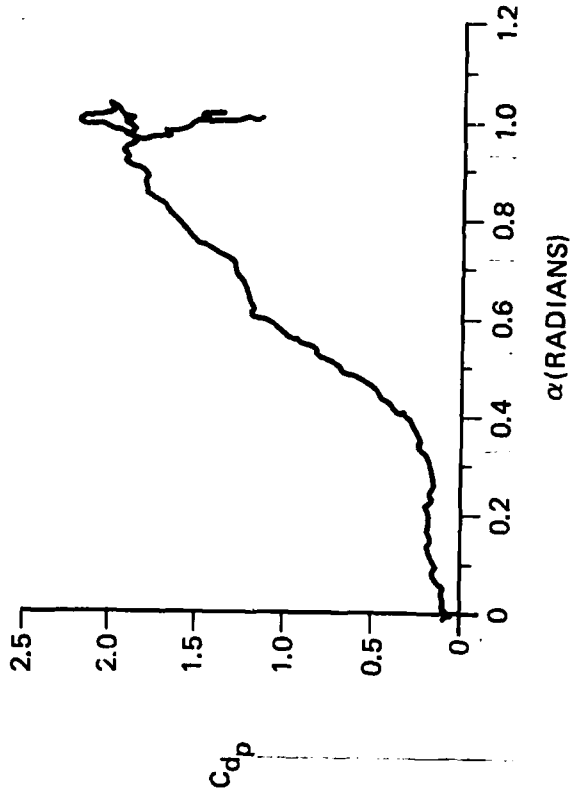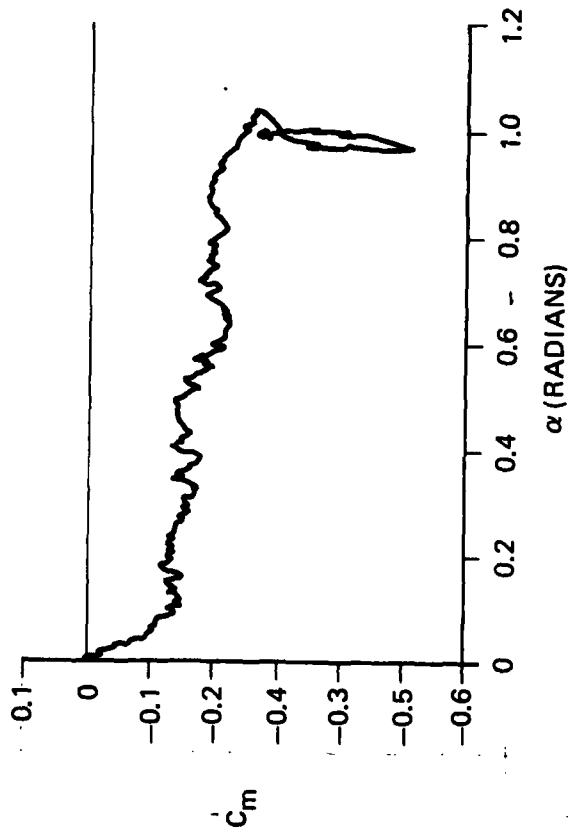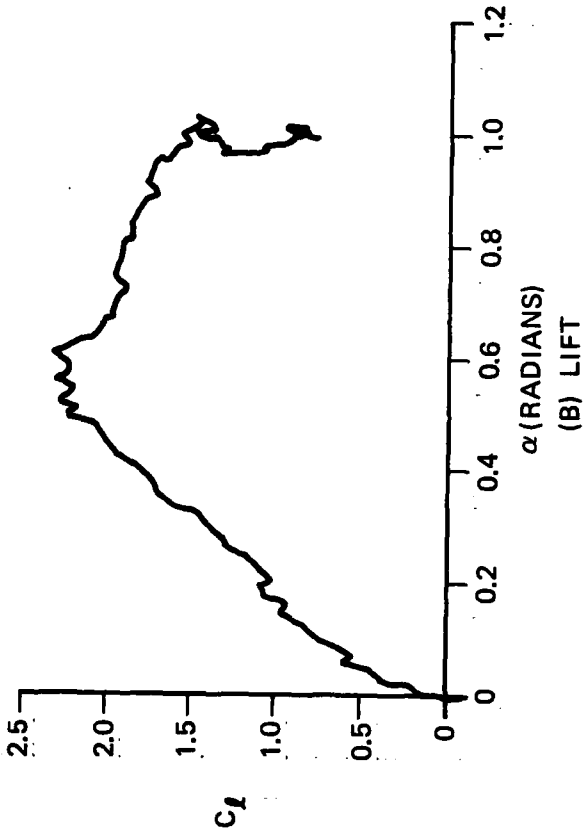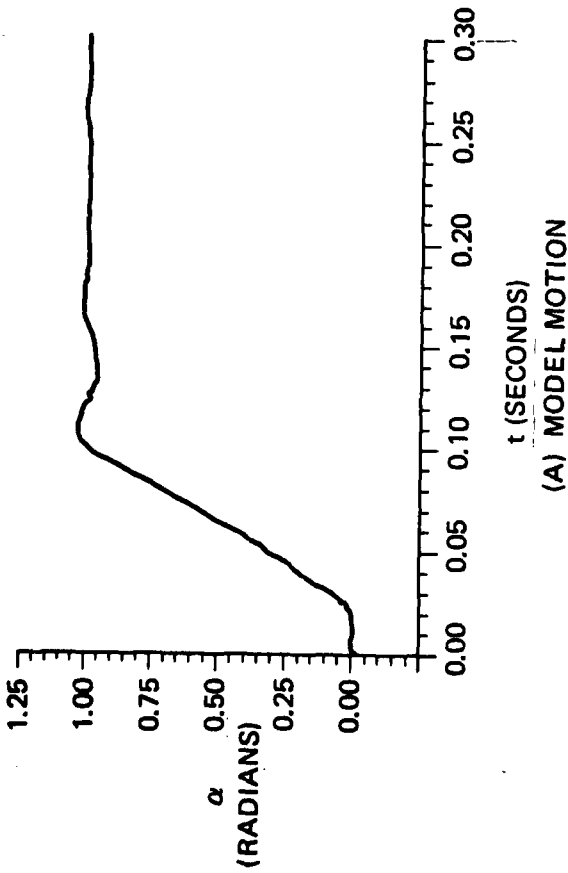
FIGURE IV-8

FORCE AND MOMENT CHARACTERISTICS, NACA 64_1 A012(13), $k = 0.136, \alpha_{max} = 59°$, $U_\infty = 32.5$ fps.

(A) MODEL MOTION

(B) LIFT

(C) MOMENT

(D) PRESSURE DRAG
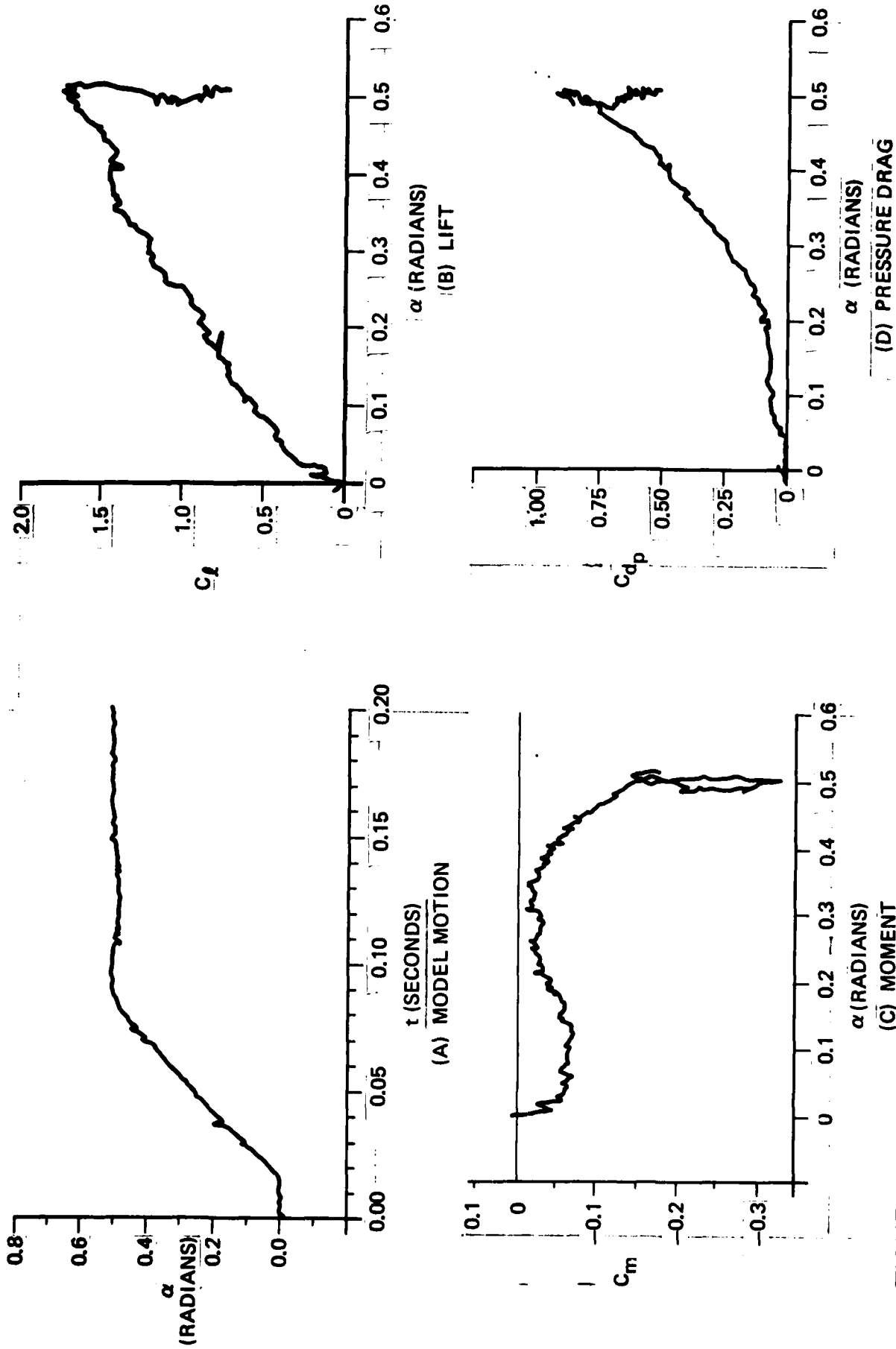
FIGURE IV-9

FORCE AND MOMENT CHARACTERISTICS, NACA 0012, $k = 0.045$, $\alpha_{max} = 30°$, $U_\infty = 41.7$ fps.

(A) MODEL MOTION

(B) LIFT

(C) MOMENT

(D) PRESSURE DRAG
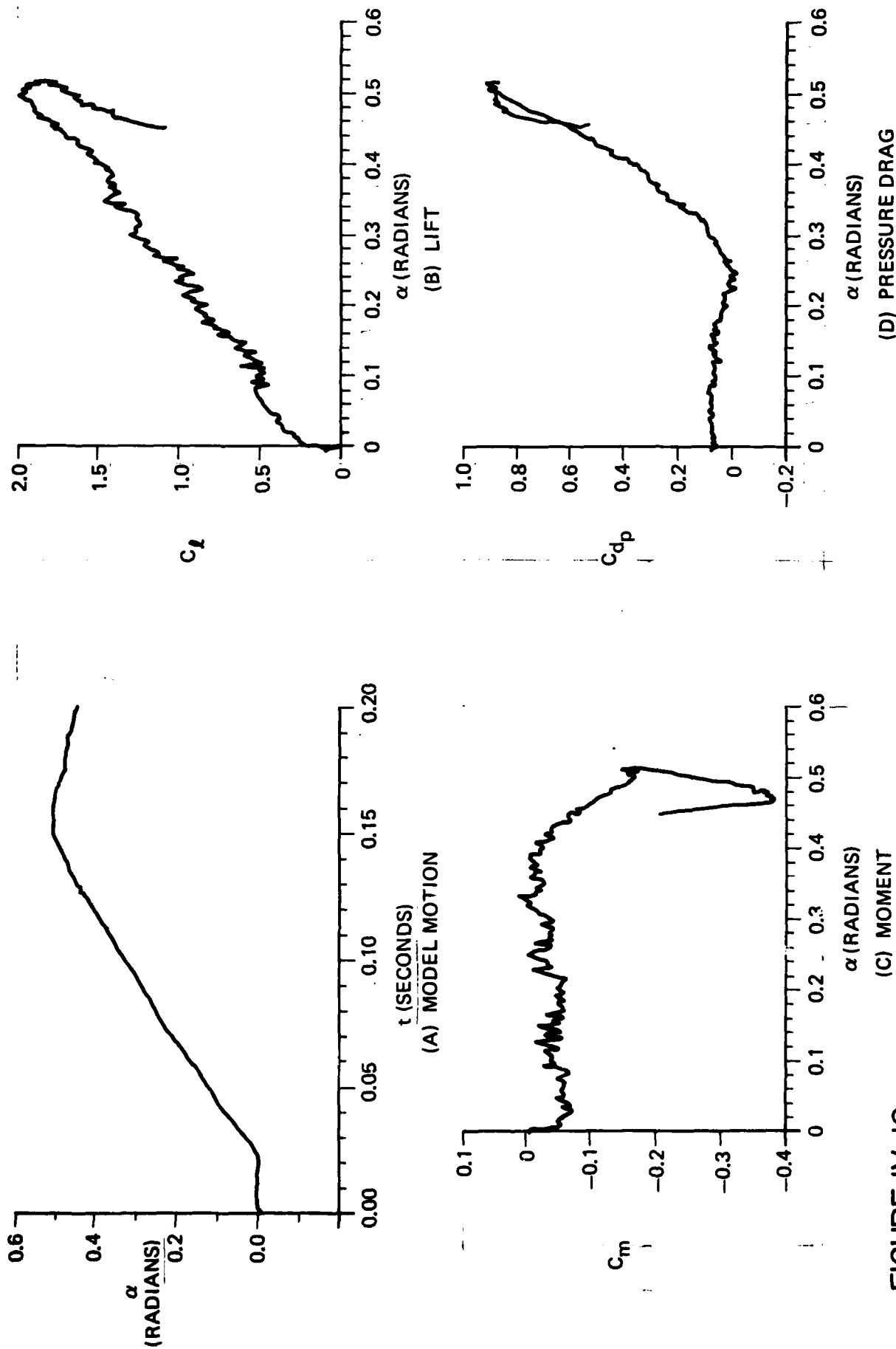
FIGURE IV-10

FORCE AND MOMENT CHARACTERISTICS, NACA 64,A012(13)., k = 0.043, α_{max} = 29°, U_∞ = 32.1 fps.
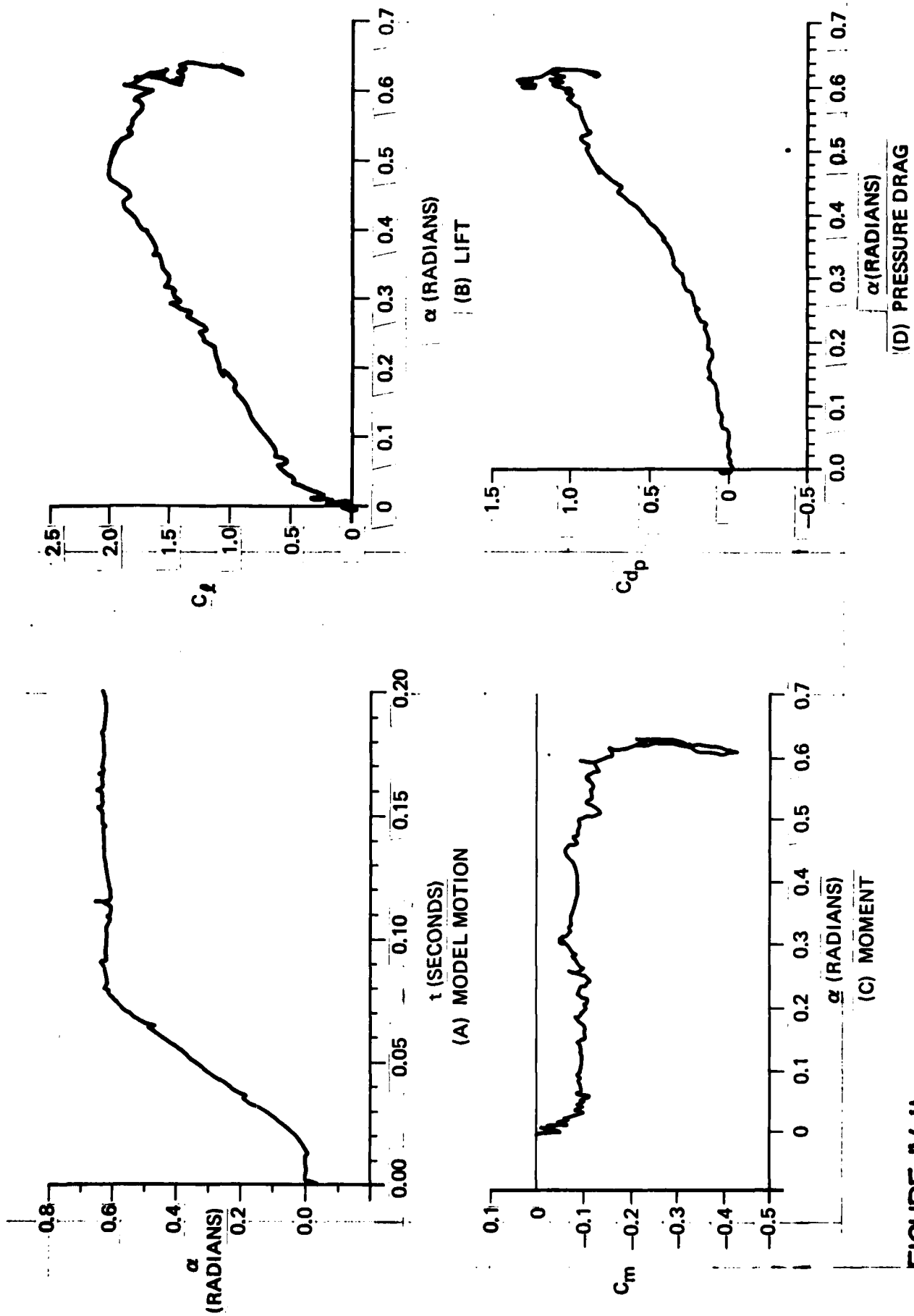
FIGURE IV-II

FORCE AND MOMENT CHARACTERISTICS, NACA 0012, $k = 0.079$, $\alpha_{max} = 34°$, $U_\infty = 33.2$ fps.
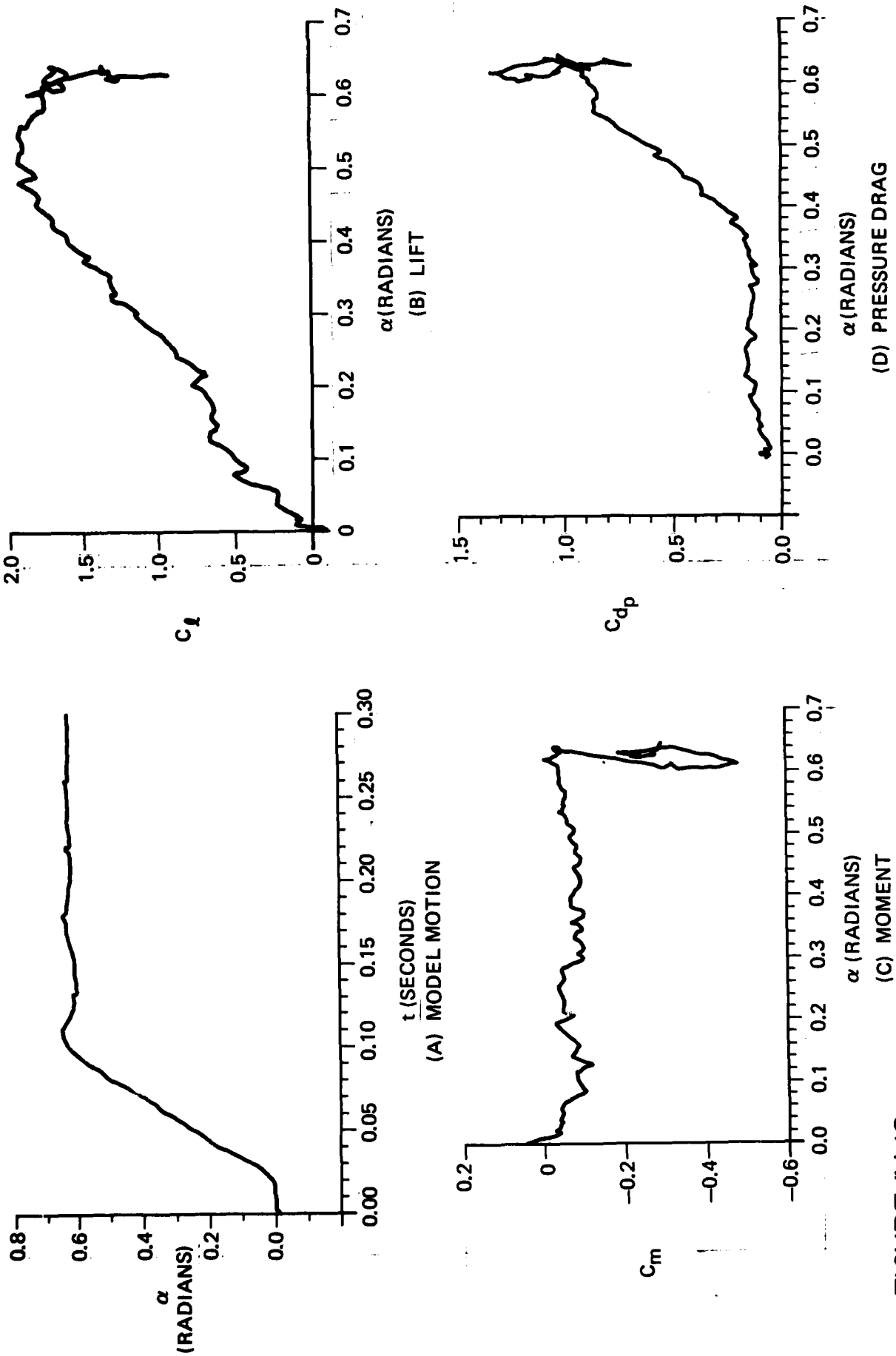
FIGURE IV-12

— FORCE AND MOMENT CHARACTERISTICS, NACA 64,A012(13), k = 0.084, α_{max} = 37°, U_∞ = 32.1 fps.

(A) MODEL MOTION

(B) LIFT

(C) MOMENT

(D) PRESSURE DRAG
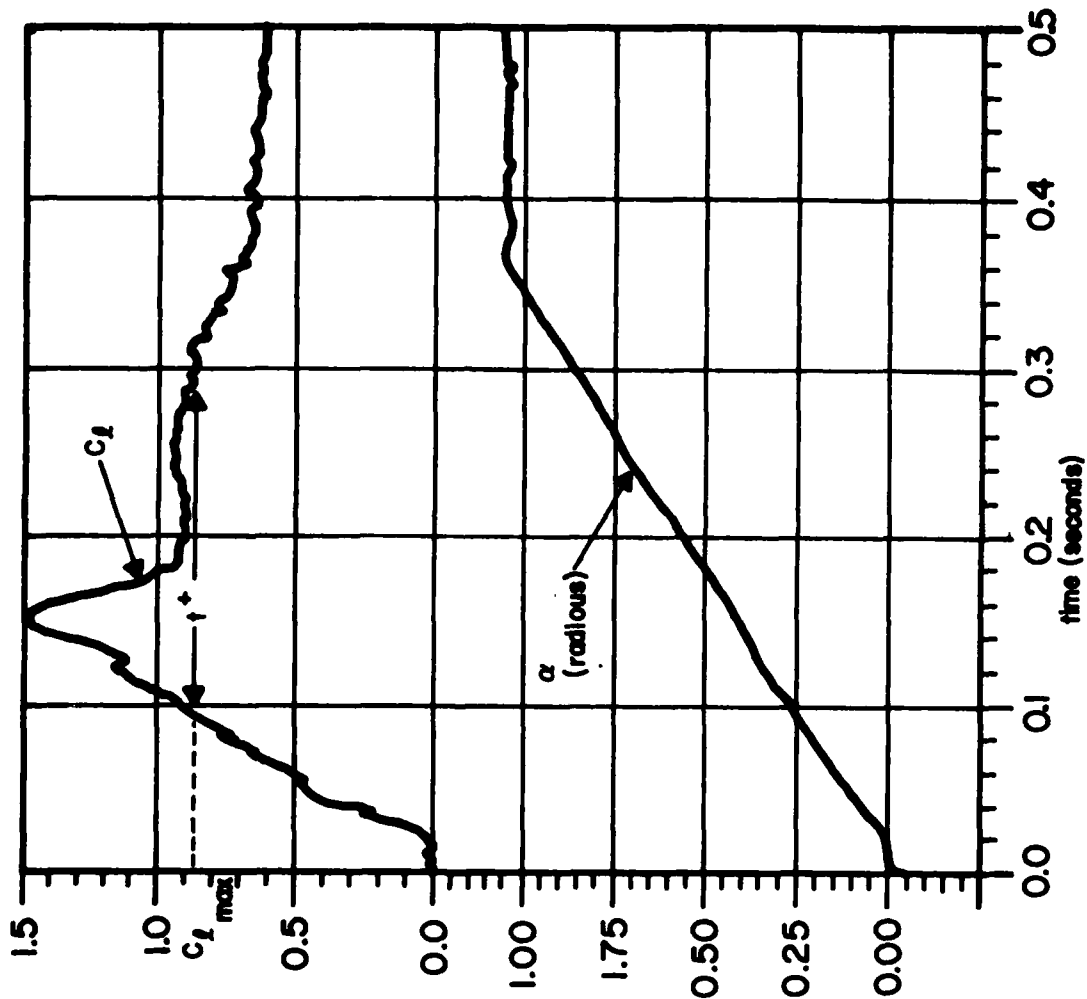
FIGURE Ⅳ-13
COMPARISON OF LIFT AND MODEL MOTION TIME HISTORY - EXAMPLE

'NOTCH' DEPRESSION
IN LIFT CURVE

$t_{max} \cdot C_\ell$

t_n

time

C_ℓ
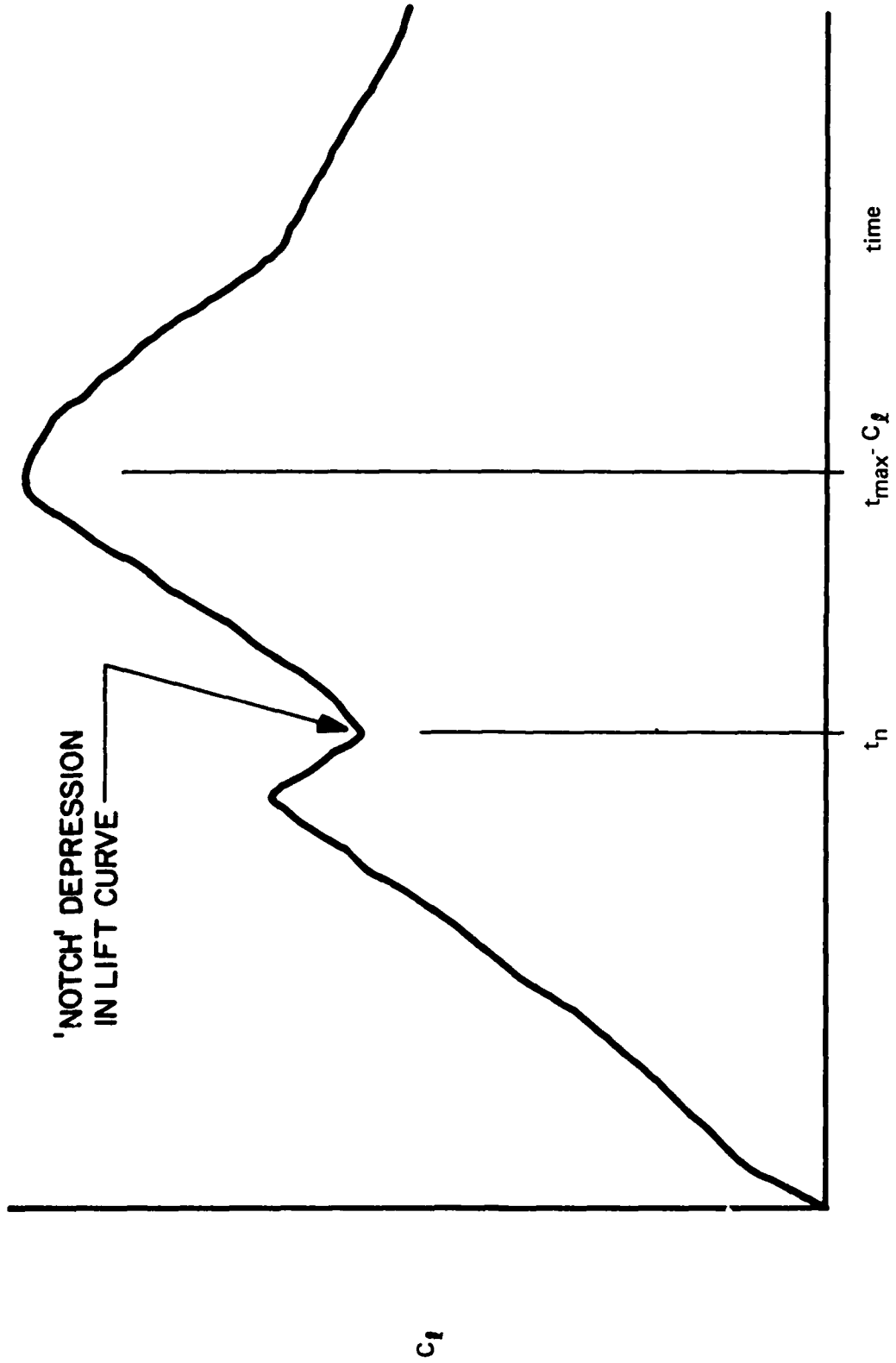
FIGURE IV-14

DESCRIPTION OF "NOTCH" DEPRESSION IN TIME EVOLUTION OF LIFT COEFFICIENT

IV-19

○ - NACA 0012, $_{max} = 60^O$
● - NACA 64, A012(13), $_{max} = 60^O$
△ - NACA 0012, $_{max} = 35^O$
▲ - NACA 64, A012(13), $_{max} = 35^O$

$$\frac{t_n}{t_{Cl_{max}}}$$
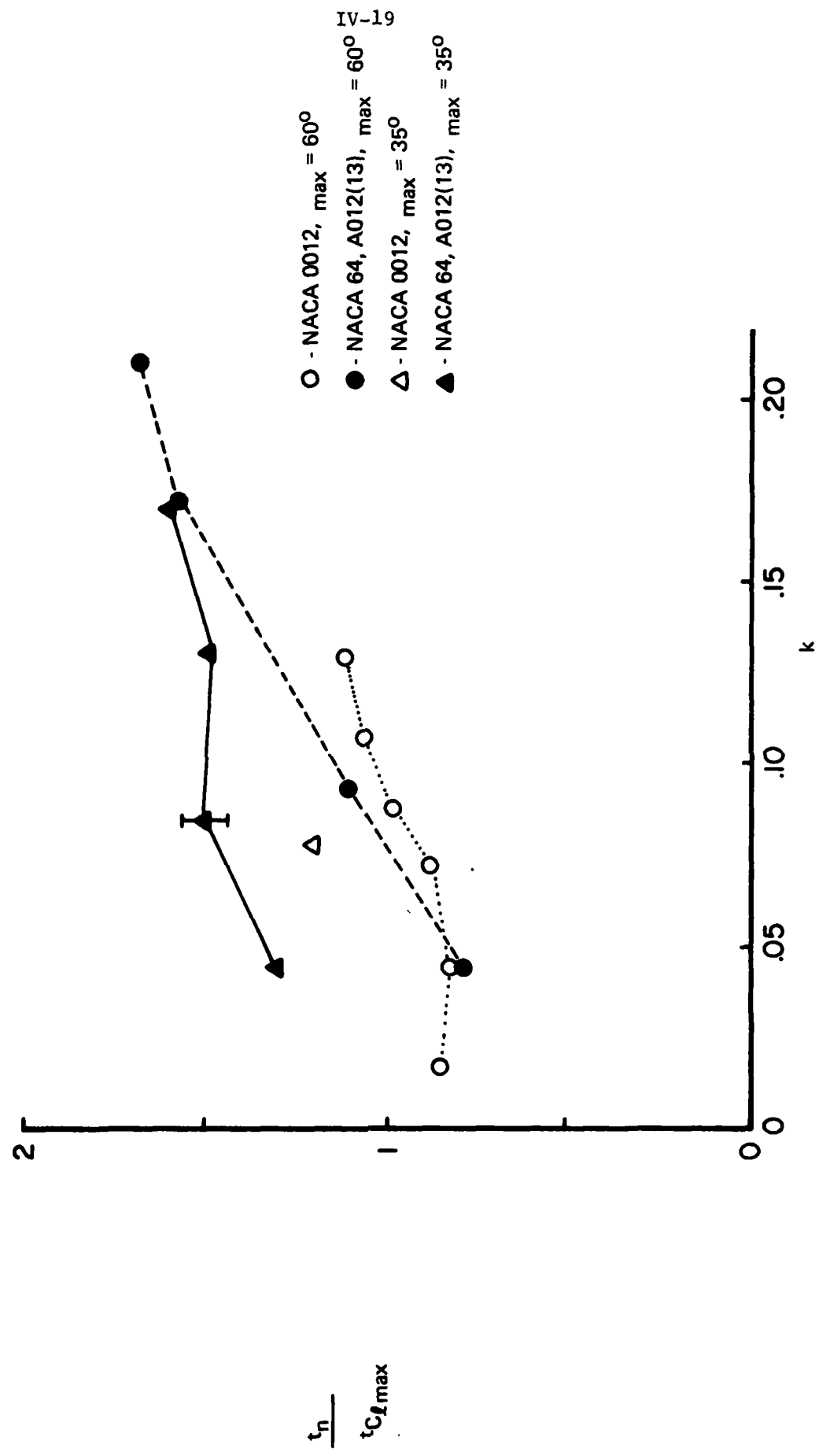
FIGURE IV-15

VARIATION OF "NOTCH" BEHAVIOR WITH DIMENSIONLESS FREQUENCY

V. PARAMETRIC COMPARISONS

To compare airfoil performance over the broad range of flow and motion conditions examined in this preliminary study, it is useful to exploit the common parameters which appear in the test matrix. This section of the report will focus on several key performance "indicators" and explore their variation with motion amplitude, dimensionless pitch rate, and Reynolds number.

V.1 BEHAVIOR OF THE SUCTION PEAK

The influence and behavior of the suspected dynamic stall vortex can be inferred by examining the evolution of the airfoil upper surface suction peak. One description of this behavior is provided by charting the trajectory of this minimum pressure location as a function of the instantaneous angle of attack. These results are shown in Figures V-1 through V-3 for three different values of the dimensionless frequency for which a comparison between airfoils was possible.

The lowest rate case displayed, k = 0.045, is also the minimum in the test matrix for which a characteristic vortex-induced behavior was observed. Although unsteady effects (including time lags in the distributions) were observed at much lower values of $\dot{\alpha}$, an identifiable suction peak which "detached" from the leading edge location was not observed under these conditions. As Figure V-1 shows, the suction peak location varies linearly with the incidence angle and, therefore, time, over a portion of the curve and appears to be independent of airfoil type in this region. For the specific cases described, maximum lift coefficients were observed to occur in the 23-28 degree incidence range which approximately coincides with the onset of nonuniformities in the suction peak

trajectories in the three curves. In both NACA 0012 tests displayed
(different Reynolds numbers), the streamwise rate of passage of the
suction peak is observed to decrease as the maximum lift point is reached.
In contrast, the NACA $64_1A012(13)$ airfoil exhibited a rather unusual
behavior characterized by an initial decrease in suction peak longitudinal
velocity followed by a rapid increase as the incidence angle continued
to increase.

At a higher dimensionless pitch rate (k = 0.09), Figure V-2 reveals
that the initial onset of suction peak motion occurs at a higher incidence
angle when compared to the previous results. The residence of the suction
peak near the airfoil leading edge is reminiscent of steady flow behavior
at unstalled incidence angles. Once suction peak movement in the down-
stream direction begins, it proceeds at an almost constant rate. At
this point, a major departure from the behavior observed in the lower
rate case occurs. Over a range of angles, the location of the suction
peak is observed to remain nearly stationary as the incidence angle
continues to increase. This result, suggestive of a "trapped" vortex
condition, is observed for both airfoils, although the conditions for
which it occurs are somewhat different. As the incidence angle increases
further, the suction peaks once again begin to traverse in the downstream
direction at a nearly constant rate until the maximum amplitude of motion
is reached. It is useful to note that for both of these experiments,
the maximum lift coefficient occurred within the band of stationary
suction peak behavior.

At the highest pitch rate shown (Figure V-3), another variation in
behavior is observed. The initial departure of the suction peak from
the leading edge region occurs at yet higher incidence angles and in a

more nonlinear trajectory than for the lower rate cases. In both examples shown here, the suction peak traversal speed decreases with increasing incidence angle and, therefore, time. Once again, a stationary suction peak is found but at different chordwise locations for the two airfoils. This location is near the 30 per cent chord point for the NACA 0012 airfoil and occurs between 40 and 50 degrees in angle of attack. For the NACA $64_1A012(13)$ airfoil model, the suction peak remains nearly stationary at or near the 20 per cent chord point between 32 and 44 degrees angle of attack at a comparable dimensionless rate of motion. This result is not unexpected given the predicted influence of the pitching axis on angle at which stall occurs.[6] Subsequent motion of the peak downstream is observed to be rapid for both airfoils up to the maximum incidence angle. Comparisons in this range should be made cautiously, however, since high deceleration rates were experienced near the maximum amplitude condition.

At this point, it is important to realize that observed trends and behavioral variations such as those described above are somewhat affected by the spatial resolution of the measurements. This situation is a direct result of the limited number of transducers and distribution of pressure measurement locations. For example, what may appear as an absolutely stationary phenomenon (as suggested by the curves in the preceding figure) is probably dynamic but not readily resolved due to the local transducer spacing in the region of interest. However, the "relative" stationarity of these results compared to other portions of the cycle is discernable. The use of the term "stationary" in ensuing paragraphs is employed in this relative sense recognizing the constraints imposed by the limited spatial resolution of the measurements.

The effects of maximum motion amplitude (incidence angle) on the suction peak evolution at fixed dimensionless pitch rates are displayed in Figures V-4 and V-5. In Figure V-4, this variation for a maximum incidence angle of 34 degrees is compared with the very large amplitude case described previously. A mid-range value of the dimensionless pitch rate is considered here. The close agreement between the two curves at low values of incidence angle is testimony to the repeatability of motion and accuracy of the measurements in these experiments. Departures between the two trajectories begin to occur when the maximum angle of incidence is reached in the lower amplitude case. However, it cannot be inferred that vortex entrapment does not occur in this case, because the abscissa, α, does not continue to vary linearly in time once the maximum amplitude of motion is reached. Similar behavior is documented for the NACA $64_1A012(13)$ airfoil at a comparable dimensionless pitch rate as shown in Figure V-5.

In addition to examining the trajectories of the suction peaks, it would be useful to quantify the effectiveness of the separation vortex using the magnitude of the suction peak as it traverses the surface. These results are displayed in Figures V-6 through V-14. In these diagrams, the minimum pressure coefficient is plotted against the instantaneous suction peak location. Figure V-6 illustrates this variation for the NACA 0012 airfoil at high incidence parameterized by different values of the dimensionless pitch rate. Note that while the magnitude of the suction peak increases substantially with increased pitch rate, its subsequent decay rate is also commensurately greater. By the time the suction peak has reached the 40 per cent chord location, the pressure coefficient has increased to an almost constant value of -3.0. Subsequent
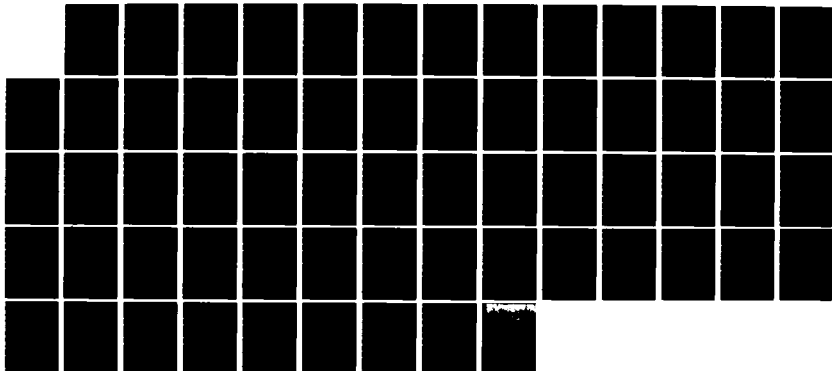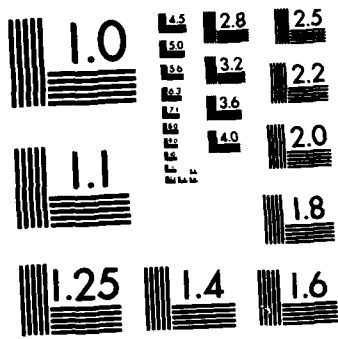
MICROCOPY RESOLUTION TEST CHART

NATIONAL BUREAU OF STANDARDS-1963-A

variations of this parameter as the pressure peak traverses downstream follow a similar trend for all three cases.

The insensitivity of the separation flowfield to airfoil type is perhaps best illustrated in Figures V-7 through V-9 in which a comparison of the two models is provided for three different dimensionless pitch rates. All three cases involve motion to very large incidence angles ($\alpha \doteq 60$ degrees). While some differences are obvious between the two airfoils at a given pitch rate, these differences are small compared to the variations that occur as a function of pitch rate.

One observation apparent from Figure V-7 is that the suction peak retains its "identity" further downstream on the NACA 64 series airfoil than on the NACA 0012 airfoil.

Figure V-8 displays comparable results for a higher value of reduced frequency again showing similar trends between the two airfoils. A noticeable difference from the lower rate case occurs for both airfoils near the 30 per cent chord point. Coincident with the stationary vortex behavior described earlier, the suction peak amplitude of the NACA 64_1A012(13) airfoil is observed to increase by nearly 20 per cent. This suggests a strengthening of the separation vortex during that period when it remains nearly stationary. The NACA 0012 airfoil also exhibits an unusual behavior at this point which is apparent in the pressure coefficient amplitude time history. Specifically, an initial decrease in peak amplitude is followed by a small increase which is, in turn, followed by another decrease as the suction peak continues to traverse downstream.

In Figure V-9, even higher pressure coefficient magnitudes are observed, but the increase in suction peak amplitude at the stationary

vortex location is not evident. It is apparent from these figures and those described above that the dynamical behavior of the separated flow region changes markedly as the pitch rate is varied. It further suggests that the concept of identifying the local surface suction peak with a single, colocated dynamic stall vortex is probably an oversimplified model of the actual physical situation.

Figures V-10 through V-12 provide more detailed results on the evolution of suction peak magnitudes with location for the NACA $64_1A012(13)$ airfoil model. In these cases, the effects of maximum incidence angle on flowfield evolution are addressed. For the lowest rate case ($k = 0.045$) shown in Figure V-10, the three sets of results appear very similar. This suggests that natural separation occurs at a value of lower than the minimum value of α_{max} for which data were obtained. The suction peak is observed to reach its maximum intensity at a chordwise location close to the leading edge in all three cases.

A similar result is found for a somewhat higher pitch rate as shown in Figure V-11. Of interest here is the fact that the reintensification of the suction peak occurs at the same chordwise location and is of approximately the same relative magnitude independent of the maximum incidence angle. Even after the peak is reached, the variation in the suction peak amplitude between the two curves is not significant.

An even stronger similarity in behavior is apparent in Figure V-12 which shows the same result for the highest pitch rate case. Again, the three sets of results seem to point at the dimensionless pitch rate as being a singularly important parameter which dominates the physical development of these flows.

V.2 LIFT AND MOMENT PEAKS

An assessment of unsteady airfoil performance characteristics is difficult given the number and range of influential performance parameters and the additional complication of arbitrary airfoil motion time history. In this section, several possible measures of lift enhancement related to separation vortex entrapment are proposed and described. Resulting parametric comparisons using these variables are discussed in detail. Because of the significance of moment stall effects, similar results for peak negative moment coefficient will also be discussed.

The simplest measures of airfoil performance evident from force and moment time histories are a class of variables which can be termed "peak parameters" since they refer to the maximum and/or minimum conditions which occur during the motion cycle. These include but are not limited to the angle of attack for which the lift coefficient is a maximum, $\alpha_{C_{l_{max}}}$, the maximum lift coefficient, $C_{l_{max}}$, and comparable measures of the minimum in the moment coefficient, namely $\alpha_{C_{m_{min}}}$ and $C_{m_{min}}$. The maximum lift coefficient is used as a measure of the severity of the dynamic stall and the influence of the separation vortex on airfoil lift. The angle of attack at which the lift coefficient achieves its maximum is hypothesized to be associated with a well-developed separation vortex, although the absence of detailed flow field data precludes a complete verification of this assumption. Similarly, the angle $\alpha_{C_{m_{min}}}$ is considered representative of a separation process which has matured, since the dynamic stall model associates this event with the passage of the stall vortex over the trailing edge region of the airfoil. The minimum moment coefficient, $C_{m_{min}}$, can be viewed as a measure of vortex organization during the latter stages of the separation process.

The variation of $\alpha_{C_{1_{max}}}$ as a function of dimensionless pitch rate for the two airfoils is depicted in Figure V-13. The differences in the test ranges of the two models are readily apparent. Results have been provided for several values of the maximum amplitude of motion, α_{max}. Figure V-13a illustrates that, at lower pitch rates, $\alpha_{C_{1_{max}}}$ increases in linear fashion virtually independent of the maximum incidence involved in the airfoil incidence time history. At higher pitch rates and for lower values of α_{max}, the angle for maximum lift coefficient and the maximum amplitude of motion are nearly coincident. Even for extremely large amplitude motions, the value of $\alpha_{C_{1_{max}}}$ appears to level off at approximately 30 degrees for the NACA 0012 airfoil.

A comparable plot for the NACA $64_1A012(13)$ airfoil indicates a similar trend near a value of $k = 0.1$, as shown in Figure V-13b. Proceeding to higher pitch rates, however, revealed a resumption in the increase of the maximum lift angle with pitch rate. This behavior is somewhat anomolous but is not believed to be uniquely related to wind tunnel characteristics or other test environment idiosyncracies. This behavior is recommended as a subject of future investigation. A comparison of both airfoils in the region of measurement overlap shows good agreement between the two sets of results.

The above results indirectly suggest that the onset of unsteady vortex generation might be affected more significantly at low values of the dimensionless pitch rate than at high values. That is, a point of diminishing returns is soon reached for lift enhancement as one proceeds to higher values of pitch rate.

The maximum lift coefficient, $C_{1_{max}}$, plotted as a function of the dimensionless pitch rate is depicted for the two airfoils in Figure

V-14. The overall shape of the curves is remarkably similar to that found for a corresponding incidence angle variation. The maximum lift coefficient increases rapidly and monotonically at low pitch rates with a decrease in the rate of rise as a value of $k = 0.1$ is approached. The magnitude of the maximum lift coefficient is observed to be dependent on the maximum incidence angle of airfoil motion. This result also suggests that the rate parameter is not the only variable which can influence airfoil lift performance.

The results depicted for the NACA $64_1A012(13)$ airfoil in Figure V-14b confirm that the growth of $C_{l_{max}}$ with increased pitch rate is not as large at high values of k as it is for lower values. Finally, it is instructive to compare results for both airfoils. Despite the small range of overlap, striking similarities in gross airfoil performance as measured by the maximum lift coefficient are apparent.

As indicated earlier, the strength of the unsteady separation vortex near the end of the useful cycle can perhaps best be characterized by the magnitude of the minimum pressure peak, $C_{m_{min}}$. The variation in this parameter as a function of the dimensionless pitch rate for both airfoils is depicted in Figure V-15. From the results of Figure V-15a, there appears to be a significant relationship between the severity of the moment stall and the maximum amplitude of motion, α_{max} for the NACA 0012 airfoil. At higher pitch rates, more severe moment stall appears to occur at yet higher values of incidence angle. In cases of low maximum incidence angle, those for which separation would otherwise occur at values higher than the actual maximum incidence of motion, the minimum peak pressure coefficient is actually observed to increase (magnitude of minimum pressure spike decreases) with increasing pitch rate.

A comparable result for the NACA $64_1A012(13)$ airfoil shown in Figure V-15b appears anomolous, especially for the largest incidence angle depicted. However, the trend to higher suction peaks with increasing motion amplitude is again evident except for the very highest pitch rates measured. A comparison of the two airfoils in the overlap region again shows good agreement.

The anomolous behavior in minimum pressure coefficient at the highest reduced frequencies has not been adequately explained by any companion measurements, and remains a topic for future investigation. However, an interesting observation can be made by comparing the variation of maximum lift coefficient with that of the minimum moment coefficient. While both parameters initially increase with pitch rate (or frequency), the maximum lift coefficient appears to reach a plateau at a lower value of the dimensionless pitch rate than the corresponding minimum moment coefficient. The lack of correlation of these results is also recommended as a subject of further study.

V.3 AIRFOIL PERFORMANCE COMPARISONS – COMPLETE MOTION CYCLE

Although the peak values of the variables described in the preceding section provide a gross comparison between the various test cases, they do not fully account for the effects of the model motion time history on overall airfoil performance. It is useful, therefore, to devise other parameters which can more completely characterize the integral performance effects over the motion cycle. It would also be useful to devise a parametric scheme which would allow for comparison of airfoil performance between cases where the motion time history is fundamentally different.

In examining the various force and moment coefficient time histories, the most obvious parameter to be included in any such characterization

is the time itself. In addition, the time associated with any given

event can be nondimensionalized by a characteristic time which can either

be associated with the model performance or one related to the reference

flow conditions. If a nondimensionalization independent of the model

motion time history is desired, a reference time scale based on external

flow conditions must be employed. In this case, $\tau = c/U_{\infty}$, is selected,

where τ is the time it takes for a freestream fluid element to travel a

distance equal to the length of the airfoil chord.

Another important question is concerned with the definition of an

appropriate time measurement which characterizes the effectiveness of a

given motion cycle. There appears to be no single best answer to this

question since the resulting measurement depends to some degree on the

element of performance to be assessed. Since this report deals primarily

with the optimization of airfoil lift characteristics, the time that

defines the persistence of lift coefficient above the static stall value,

t^+ (as shown in Figure IV-13), will be employed here. Referenced to the

freestream variable, τ, this temporal parameter is hereafter referred to

as the duration coefficient, C_t, where

$$C_t \equiv \frac{t^+}{\tau}$$

The variation of this parameter with the dimensionless pitch rate

for the two airfoils is shown in Figure V-16. In part (a) of this figure,

results for the NACA 0012 airfoil model are depicted for several different

pitch amplitudes. The symbols are used to characterize results which

are within $\pm$ 3 degrees of a nominal value. These results can then facili-

tate a comparison of the two airfoils under comparable conditions. The

increase in duration coefficient occurs rapidly and monotonically for

low values of the dimensionless pitch rate (k < 0.015). A single anomolous

data point occurred at a k-value of 0.0182 where C_t was measured to be 17.2. The potential error in this measurement is estimated to be high due to the shallow negative slope of the C_l - time history curve near the static stall point. The remaining data indicate that, in the mid-range region, the rate of increase slows until a nearly constant value is achieved over the highest set of pitch-rates examined. The effect of maximum pitch amplitude on this characteristic cannot be determined with any degree of accuracy due to the sparcity of available data. However, the evidence suggests that the maximum value of the incidence angle for constant rate and hold motion does play a role in the determination of this coefficient.

Results for the NACA $64_1A012(13)$ airfoil are shown in Figure V-16b. Although these data cover a wider range of reduced pitch rates, insufficient results are available at the lowest values to assess trends in that region. However, the curve representing the highest amplitude motion ($\alpha_{max} \cong 60^o$) does provide yet another interesting insight. In contrast with previous trends, the duration coefficient is observed to decrease with continued increases in the pitch rate. This is not the case at the lower value of the maximum incidence angle plotted in the figure. More significantly, measured values of the duration coefficient for the 40 degree case are higher than their counterparts for the higher maximum incidence angle at comparable values of the reduced pitch rate. The single data point plotted for the lowest rate suggests that a decrease of an additional 10 degrees in the value of α_{max} results in a much decreased value of the duration coefficient. These combined results suggest that airfoil performance improvements do not necessarily correlate directly with increases in the pitch amplitude of motion, but that an optimum

value of α_{max} exists and probably depends on the pitch rate and other flow conditions. This inference will be examined more completely later in this report.

While the duration coefficient provides a useful relative measure of performance comparison, it is susceptible to large inherent errors due to the lack of repeatability of deterministic flow processes (stall vortex coherence) near the end of the motion cycle. Under some conditions, the statistical scatter in the measurement of t^+ can be unacceptably high. Moreover, the duration coefficient does not account for the magnitude of lift overshoot or its variation in time. A more comprehensive indicator must, therefore, incorporate these effects in some integral fashion. An obvious candidate that satisfies these criteria and which is also independent of the type of motion is the area under the force-time curve which denotes an effective additional impulse, I_L. Since lift optimization is a principal objective of this investigation, the parameter is here defined for values of lift greater than the maximum steady flow value. In dimensional form,

$$I_L \equiv \int_0^T \Delta L \cdot dt$$

for all

$$\Delta L \equiv L - L_{max_s} \geq 0$$

A non-dimensional version of this relationship yielding a lift impulse coefficient can be written, in general, as

$$I_{C_1} = \int_0^T \Delta C_1 \cdot \frac{dt}{t_n} \qquad (8)$$

for all

$$\Delta C_1 \equiv C_1 - C_{1_{max_s}} \geq 0$$

where t_n is an appropriate reference time scale.

Two non-dimensionalization schemes (reference time scales) are physically significant. If t_n is taken as the total time for which the lift exceeds the maximum steady flow value, then,

$$t_n = t^+$$

The impulse relation then becomes

$$\overline{\Delta C_1} = \int_0^1 \Delta C_1 \cdot d(\frac{t}{t^+}) \tag{9}$$

for all

$$\Delta C_1 \equiv C_1 - C_{1_{max_s}} \geq 0$$

In this case, the result is equal to the average value of the excess lift increment.

The behavior of this average excess lift parameter for the NACA 0012 airfoil is documented in Figure V-17. The upper (a) portion in this figure illustrates the variation with dimensionless pitch rate for the highest motion amplitudes examined ($\alpha_{max} \cong 60^o$). The effect of motion amplitude is documented separately in Figure V-17(b).

The average excess lift coefficient is observed to vary with pitch rate in a manner not unlike that documented for the section pressure peak described earlier. A rapid increase with pitch rate at low values of that parameter are followed by a gradual flattening of the curve until a nearly constant level is achieved at the highest levels. A least squares curve is fitted through the available data. Reynolds number independence over the range of study is evident by the similarity in results achieved at a all of $k = 0.045$.

The variation of maximum incidence angle with the average incremental lift coefficient (Figure V-17b) shows that, at least for higher rates of motion, the optimum incidence angle lies above the static stall value, but not at the highest angles examined. It appears that optimum lift performance might be achieved when the maximum incidence angle of the motion is comparable to the expected separation angle associated with the pitch rate employed.

A similar result for the NACA $64_1A012(13)$ airfoil is provided in Figure V-18. Both pitch rate and maximum amplitude effects have been condensed to a single set of curves in this case. Several overlap points from the NACA 0012 data have been plotted to compare the two airfoils. The insensitivity of airfoil type under these motion extremes is again evident. Note that the excess lift is nearly constant with a slight downward trend over this range of high pitch rates. In addition, it is very apparent that the lower value of α_{max} results in consistently higher performance in these instances. It is also evident that a larger number of test cases is desirable if the excess lift is to be maximized.

Recalling the non-dimensional impulse relation, eqn. (8), it is useful to consider a different reference time scale based on the free-stream flow conditions, i.e.,

$$t_n = \frac{c}{U_\infty} = \tau$$

Then, we can write

$$I_c = \int_o^{T^*} \Delta C_l \cdot d(\frac{t}{\tau}) \qquad (10)$$

where

$$\Delta C_l \equiv C_l - C_{l_{max_s}} \geq 0$$

and
$$T^* \equiv \frac{TU_\infty}{c}$$

The variable, I_c, will be referred to as the "dimensionless impulse."
This parameter is a versatile measure of performance since it incorporates
both lift magnitude and duration. In addition, it is capable of providing
equitable comparisons of highly dissimilar motion time histories since
the freestream time scale is accounted for implicitely.

The variation of I_c with dimensionless pitch rate for the NACA 0012
model is shown in Figure V-19a. Results are depicted for several common
and approximately equal ($\pm$ 3°) values of the maximum pitch incidence
angle. The characteristic shape of the maximum incidence ($\alpha_{max} \cong 60^\circ$)
characteristic is familiar by now. A rapid increase in the impulse
parameter at low pitch rates is followed by a more gradual increase at
the higher rates of motion. The tendency of the curve to "flatten" and
achieve a local maximum is not apparent in the behavior of this parameter.

The limited results available for other values of maximum pitch
amplitude preclude a detailed discussion of their behavior in the context
of this figure. However, a limited comparison of motion amplitude can
be effected through the crossplots provided in Figure V-19b. From these
curves, one observes that the incidence angle selected for maximum perfor-
mance is very much dependent on the pitch rate employed.

A comparable set of results for the NACA 64$_1$A012(13) airfoil is
provided in Figure V-20. For this wider range of reduced pitch rates,
several contradictory trends are observed. Tests at high incidence
angle ($\alpha_{max} \cong 60^\circ$) resulted in a reduction in the dimensionless impulse
with increased values of the reduced pitch rate (on the average) as
shown in Figure V-20a. A nearly opposite trend is observed when the

maximum incidence of motion approximates the angle at which leading edge

separation would otherwise occur had the motion continued without inter-

ruption.

The significance of maximum incidence amplitude is even more apparent

in Figure V-20b. For all pitch rates plotted, the optimum airfoil perfor-

mance occurred at an incidence angle of approximately 40 degrees. This

coincides with values close to the observed angle for leading edge separa-

tion (i.e., suction peak detachment) in this pitch rate range.

A comparison of the results in the region of measurement overlap

shows reasonable agreement at a reduced pitch rate near k = 0.10. How-

ever, there is a substantial disagreement in the results at lower pitch

rates (k = 0.05). The source of this disagreement warrants further

investigation.

V.4 CORRELATION OF SUCTION PEAK BEHAVIOR WITH AIRFOIL PERFORMANCE

The influence of the motion and magnitude of the suction peak (and,

therefore, of the unsteady vortex) on airfoil lift performance can be

assessed through several parametric cross comparisons. One useful measure

is provided by relating the suction peak trajectory to corresponding

values of instantaneous lift coefficient. These results are provided

for large amplitude motion cases in Figures V-21 through V-24.

The effect of dimensionless pitch rate on performance of the NACA

0012 airfoil is evident in the plots of Figure V-21. For the lowest

value of k, the maximum lift coefficient is observed to occur when the

suction peak resides at a chordwise location of approximately 40 per

cent. For the intermediate pitch rate case, the location of the suction

peak for maximum lift appears to move forward to nearly the 30 per cent

chord point. The unusual reenergization behavior discussed previously is also apparent in this middle curve. Its appearance in this figure confirms that the increase in suction peak intensity during the stationary period coincides with a net increase in airfoil lift. The net increase in lift during this static phase is nearly 12 per cent in the present case.

A comparison of the two airfoils is provided in Figures V-22 through V-24. The lowest pitch rate case of Figure V-22 illustrates comparable behavior until the suction peak reaches the 30 per cent chord location. At this point, the lift of the NACA 64_1A012(13) is observed to increase substantially as the suction peak remains near stationary.

Figure V-23 describes the situation for a higher reduced pitch rate and one in which a stationary suction peak was observed for both airfoils. The increase in peak suction coincides with an increase in the lift coefficient. However, the percentage change in the lift force is some- what smaller than the net change in the local suction peak amplitude.

A similar comparison provided in Figure V-24 for the highest pitch rate case indicates that, although the shapes of the two curves are similar, the characteristic trajectory is slightly shifted between the two airfoils. The maximum lift occurs earlier in the evolution of the suction peak (separation vortex) for the 64-series airfoil than for the NACA 0012. These discrepancies may be attributable to the difference in pivot (rotation) location between the two airfoils and not necessarily to the variations in airfoil shape.

The influence of pitch rate on the suction peak location for which the lift is maximum is most easily observed in a consolidated version of the previous figures which is provided in Figure V-25. It is apparent

that the primary effect of increasing the pitch rate for any given set

of flow conditions is to cause the location of the separation vortex for

maximum lift to move nearer to the leading edge.

Finally, one can examine the variation in lift coefficient with the

magnitude of the suction peak as it evolves along the surface. Curves

illustrating this behavior for the same cases described in the preceding

paragraphs are provided in Figures V-26 through V-30.

These results for the NACA 0012 airfoil are overlaid for a range of

reduced pitch rates in Figure V-26. The correspondence between increasing

lift coefficient and increasing amplitude of the suction peak is evident.

The hysteresis behavior in these time histories is also apparent. Figure

V-27 shows a comparison between the NACA 0012 airfoil and the NACA

$64_1A012(13)$ airfoil at nearly identical pitch rates and very high values

of the maximum incidence. As has been the case in most cases discussed

previously, the behavioral differences between the two airfoils are

small compared to those related to the dimensionless pitch rate variation.

This is equally apparent in Figures V-28 and V-29. A comparison of

these high amplitude motion cases reveals that increases in the pitch

rate result in correlatable increases in both the suction peak magnitude

and the overall lift coefficient. That is, the lifting capability of

the airfoil under these large amplitude excursions is inextricably linked

to the strength of the developing unsteady separation vortex manifested

through the magnitude of the suction peak.

The influence of maximum incidence angle at nearly comparable values

of the reduced pitch rate (a 12 per cent variation, in this case) is

displayed in Figure V-30 for the NACA 0012 airfoil. While minor discrep-

ancies appear to occur following the onset of separation, the evolutionary

behavior of the two curves is very similar when compared to similar curves for different values of k.

An additional correlation of these results is possible from the condensed format provided in Figure V-31. The nearly linear increase with pitch rate confirms the relationship between suction peak and lift coefficient and reinforces the notion that separation vortex strength plays an important role in determining airfoil performance characteristics after separation occurs.
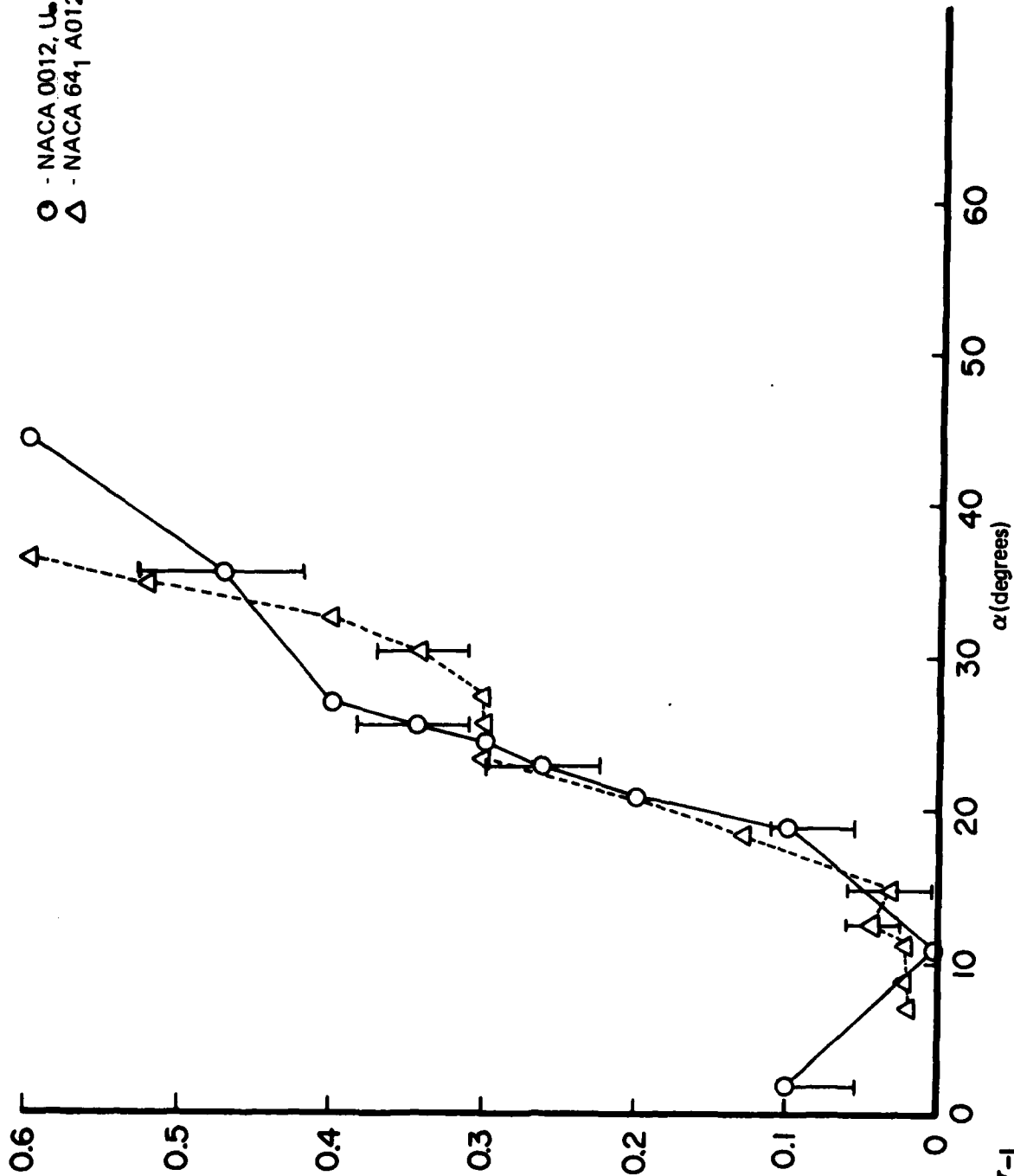
FIGURE $\underline{\text{V}}$-1

VARIATION OF MINIMUM PRESSURE LOCATION WITH ANGLE-OF-ATTACK, k = 0.045, $\alpha \simeq 60°$
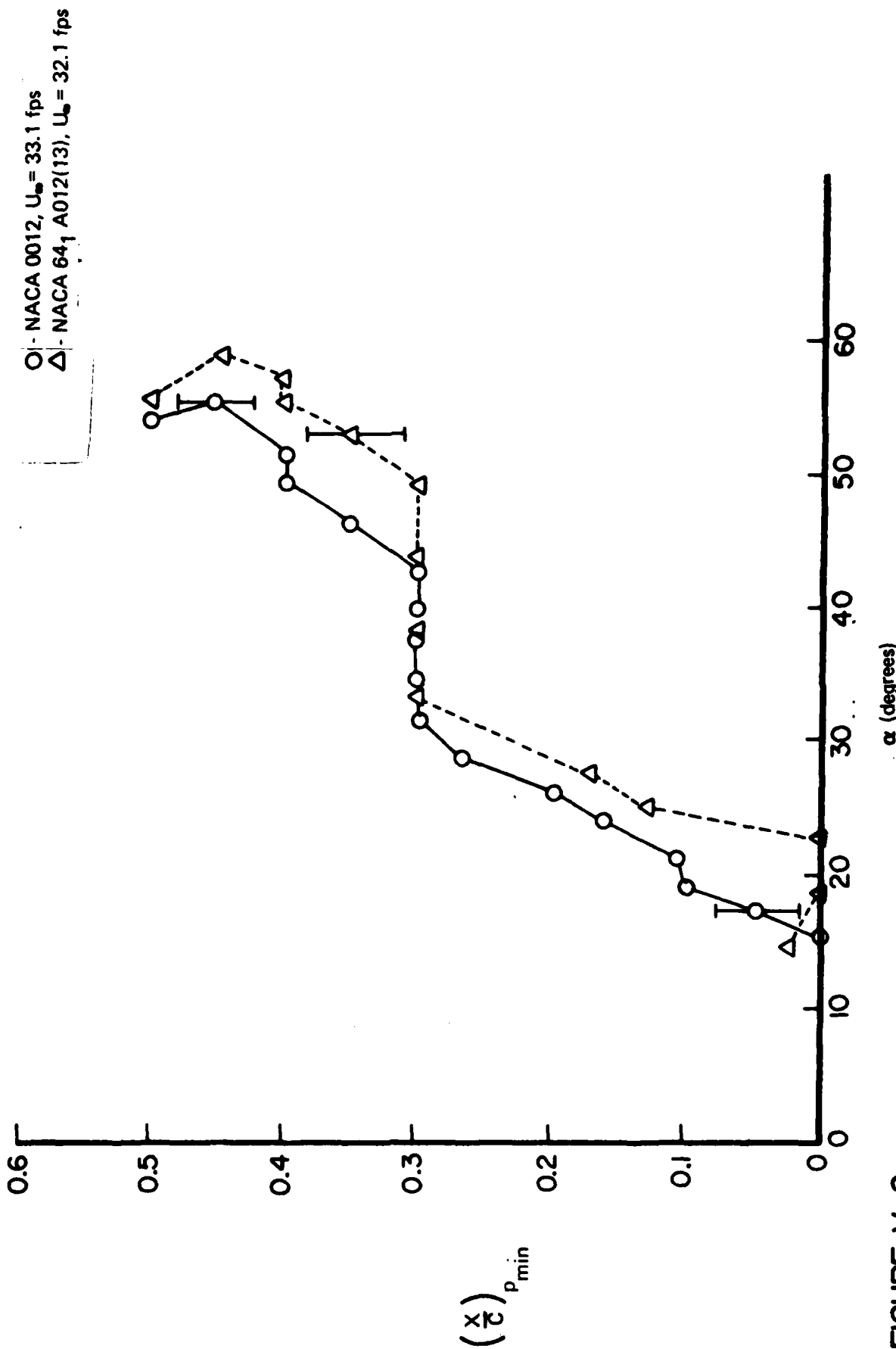
FIGURE V-2

VARIATION OF MINIMUM PRESSURE LOCATION WITH ANGLE-OF-ATTACK, $k = 0.09, \alpha_{max} = 60^\circ$

O— NACA 0012, U_∞ = 33.9 fps
△— NACA 64_1 A012(13) U_∞ = 32.5 fps

$\left(\dfrac{x}{c}\right)_{p_{min}}$

α (degrees)
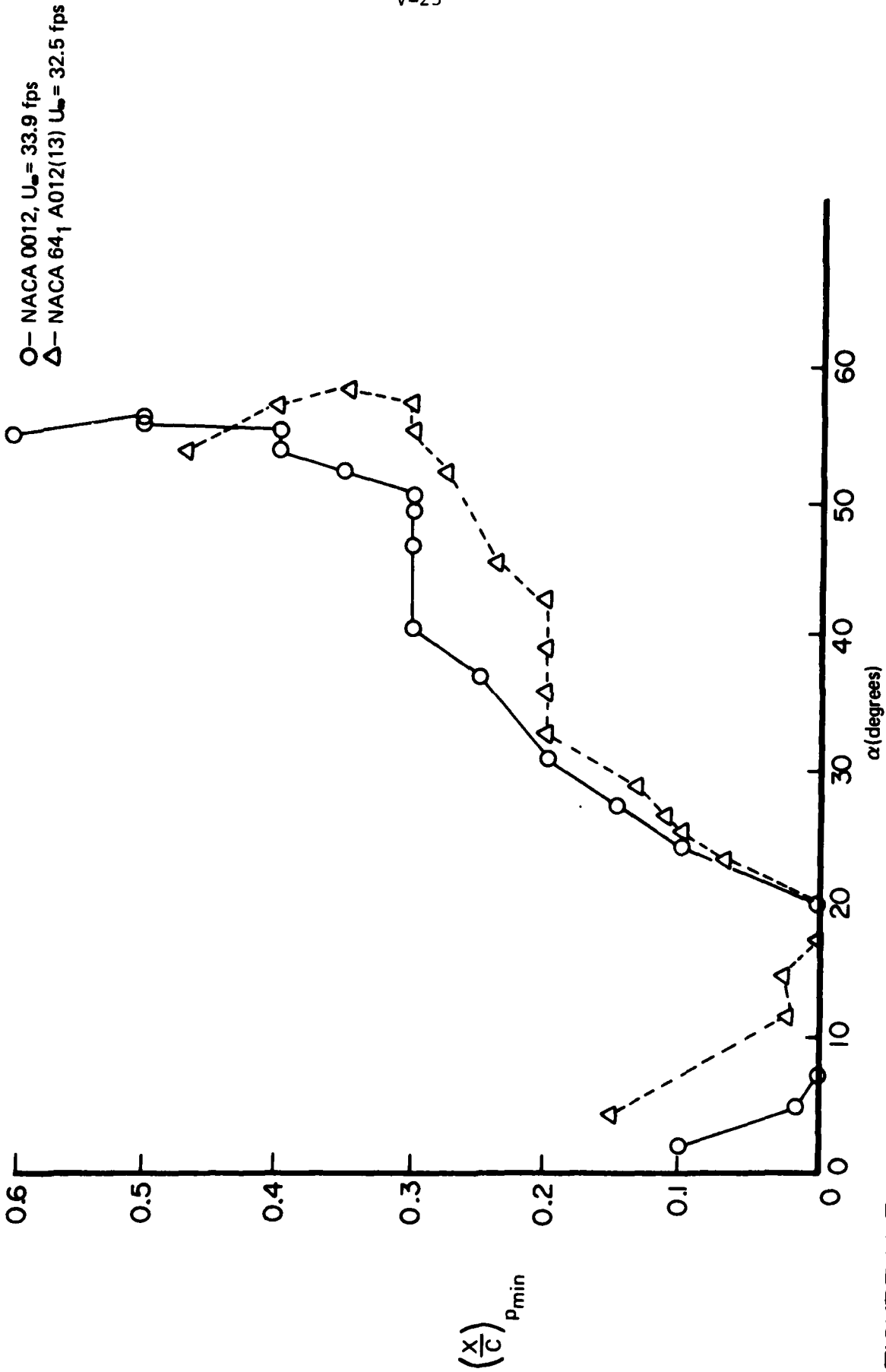
FIGURE V-3

VARIATION OF MINIMUM PRESSURE LOCATION WITH ANGLE-OF-ATTACK, k = 0.133, $\alpha_{max} \cong 60^\circ$
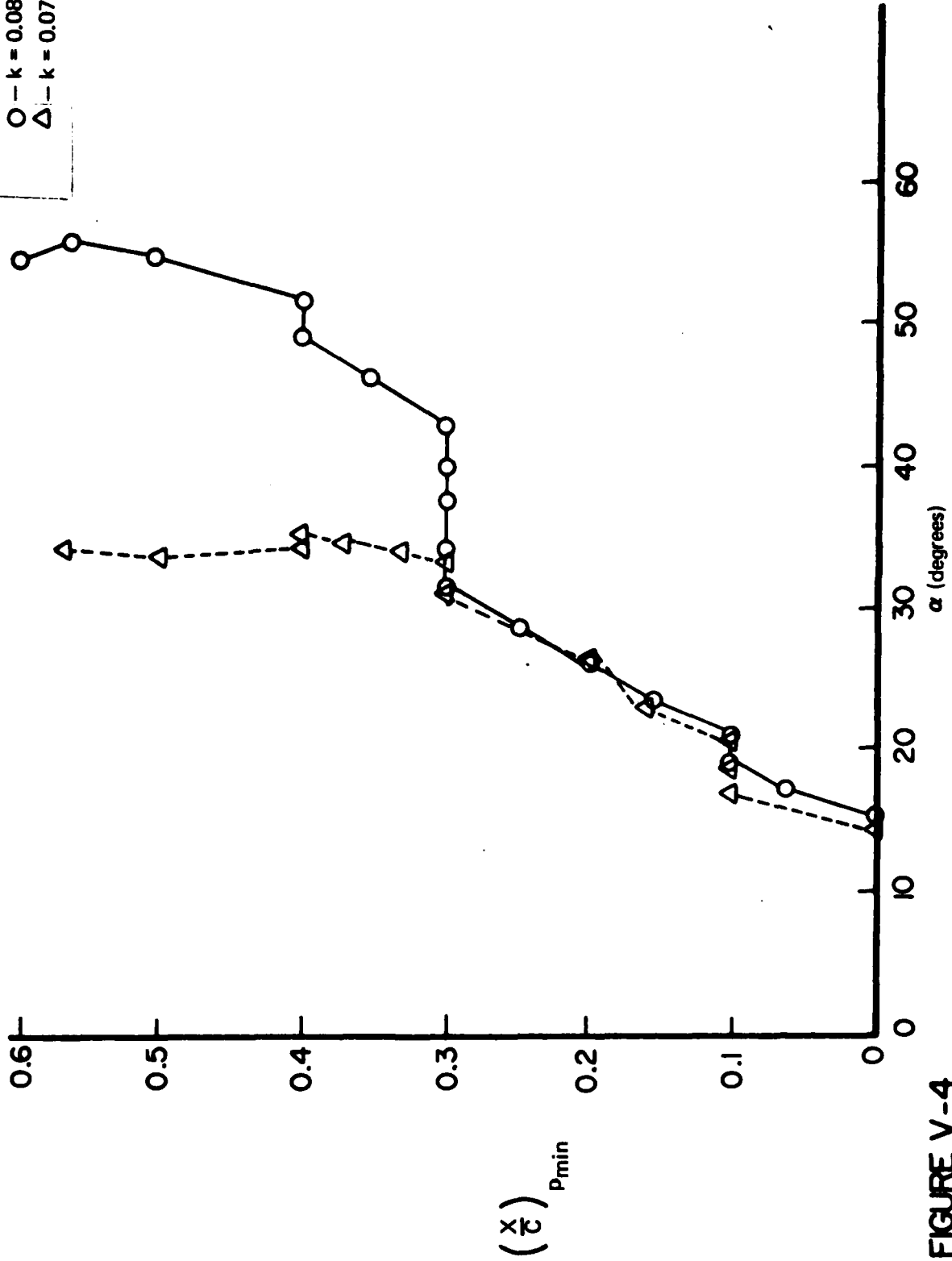
FIGURE V-4

VARIATION OF MINIMUM PRESSURE LOCATION WITH ANGLE-OF-ATTACK, NACA 0012, $U_\infty = 33.2$ fps
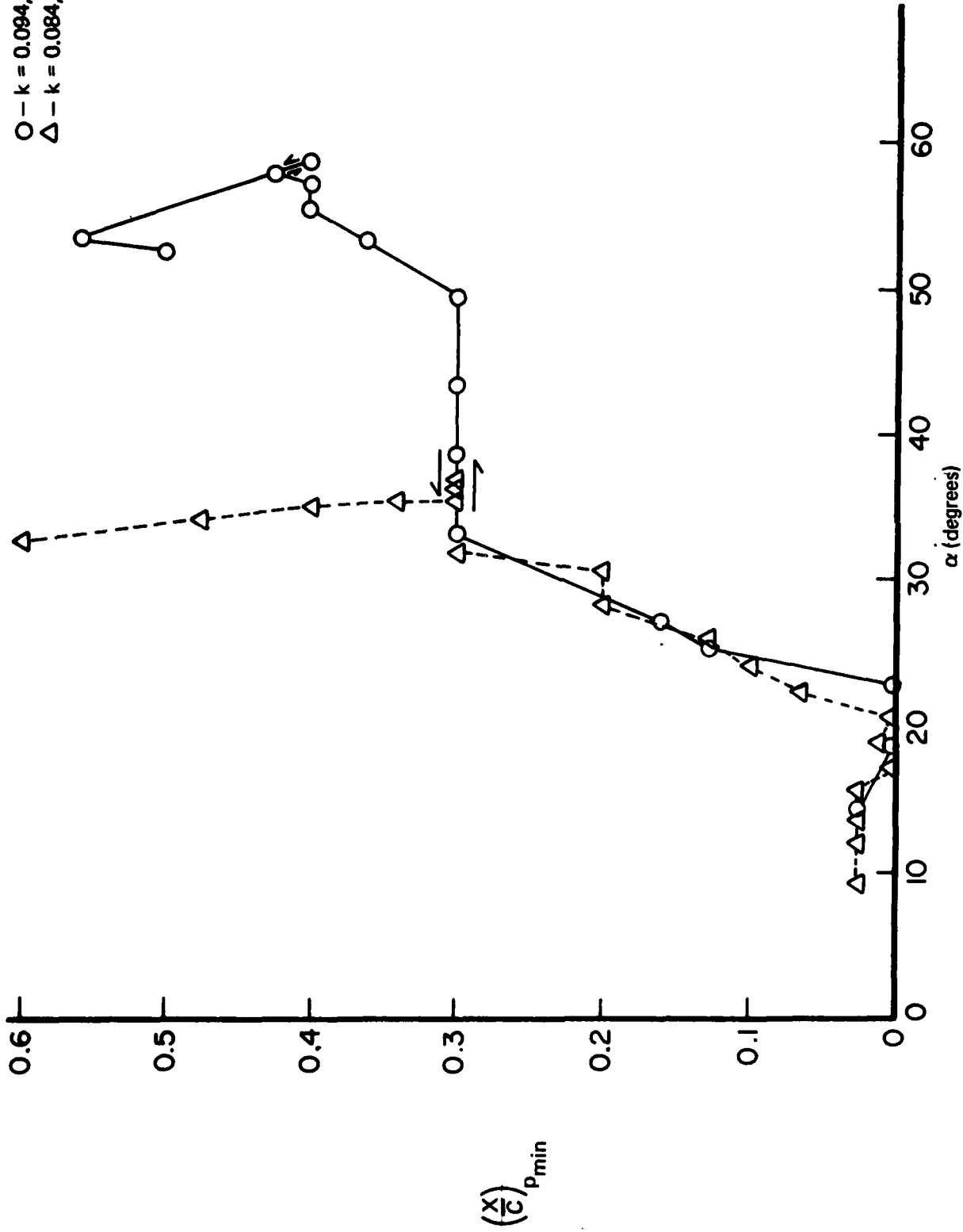
FIGURE V-5

VARIATION OF MINIMUM PRESSURE LOCATION WITH ANGLE-OF-ATTACK, NACA 64_1 A012(13), U_∞ = 32.1 fps
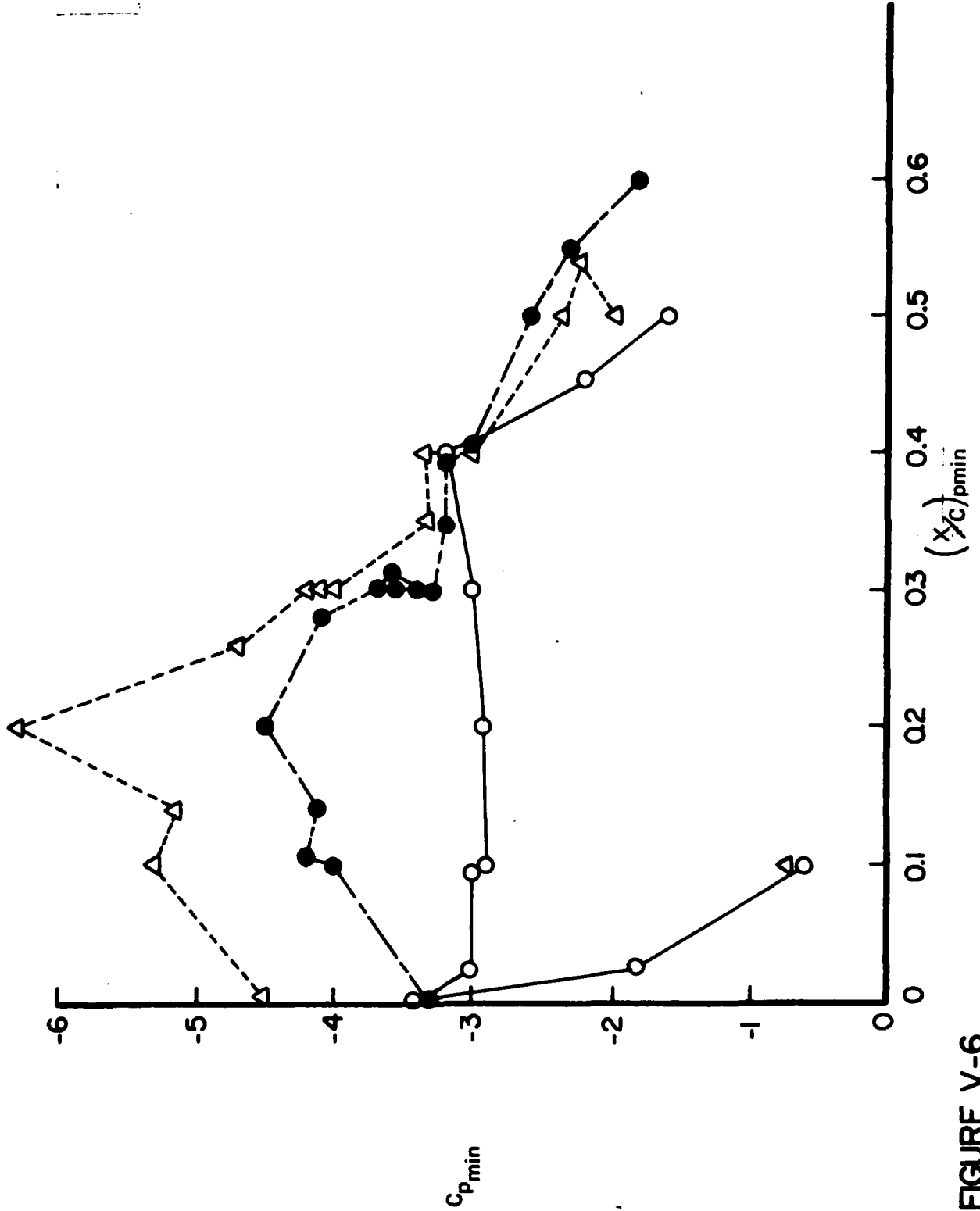
FIGURE V-6

VARIATION OF MINIMUM PRESSURE COEFFICIENT WITH SUCTION PEAK LOCATION, NACA 0012,
$U_\infty = 33 - 34$ fps, $\alpha_{max} = 60^0$
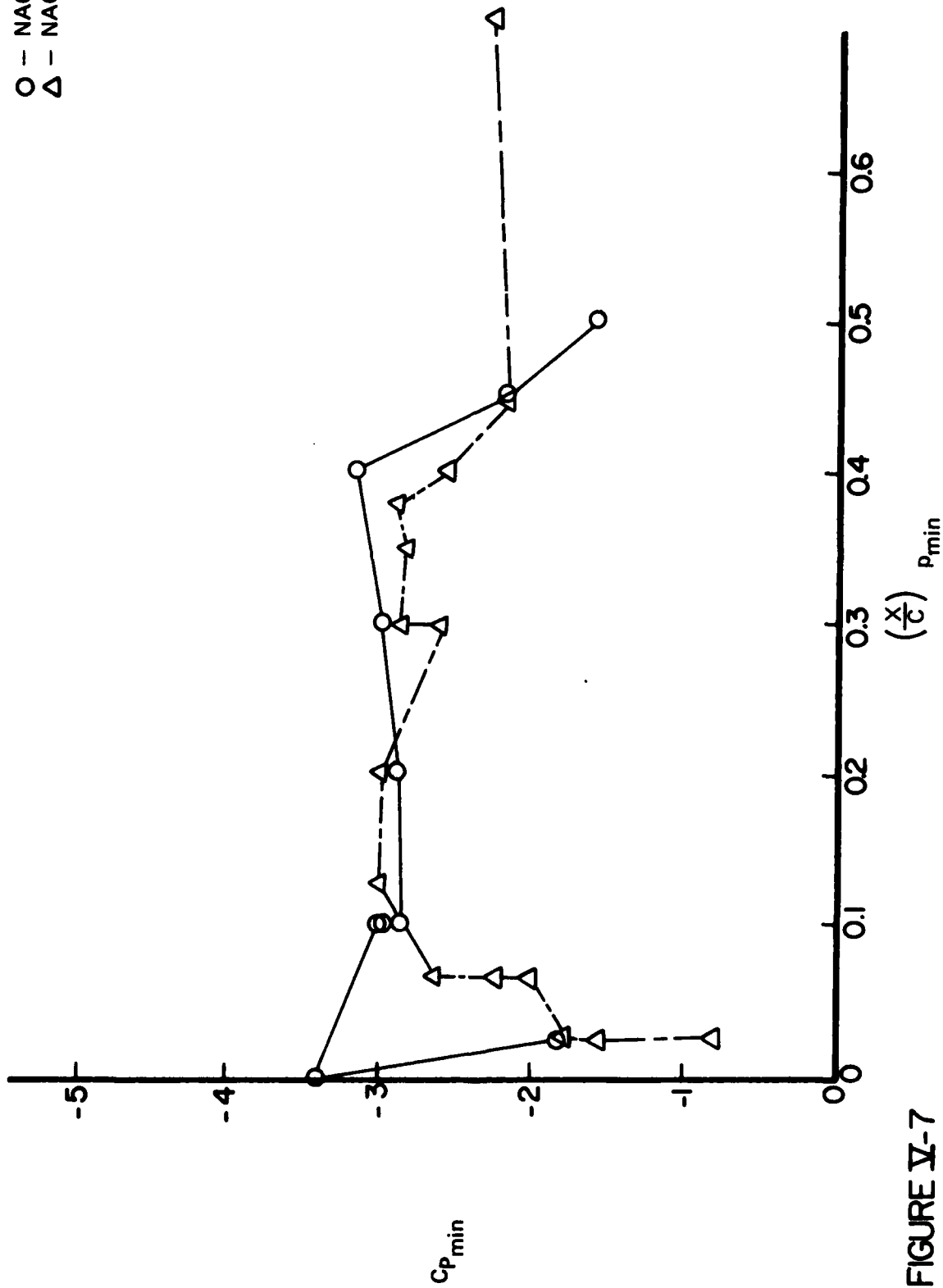
FIGURE V-7

VARIATION OF MINIMUM PRESSURE COEFFICIENT WITH SUCTION PEAK LOCATION,
$k \cong 0.046$, $U_\infty = 33.1$ fps, $\alpha_{max} = 60°$
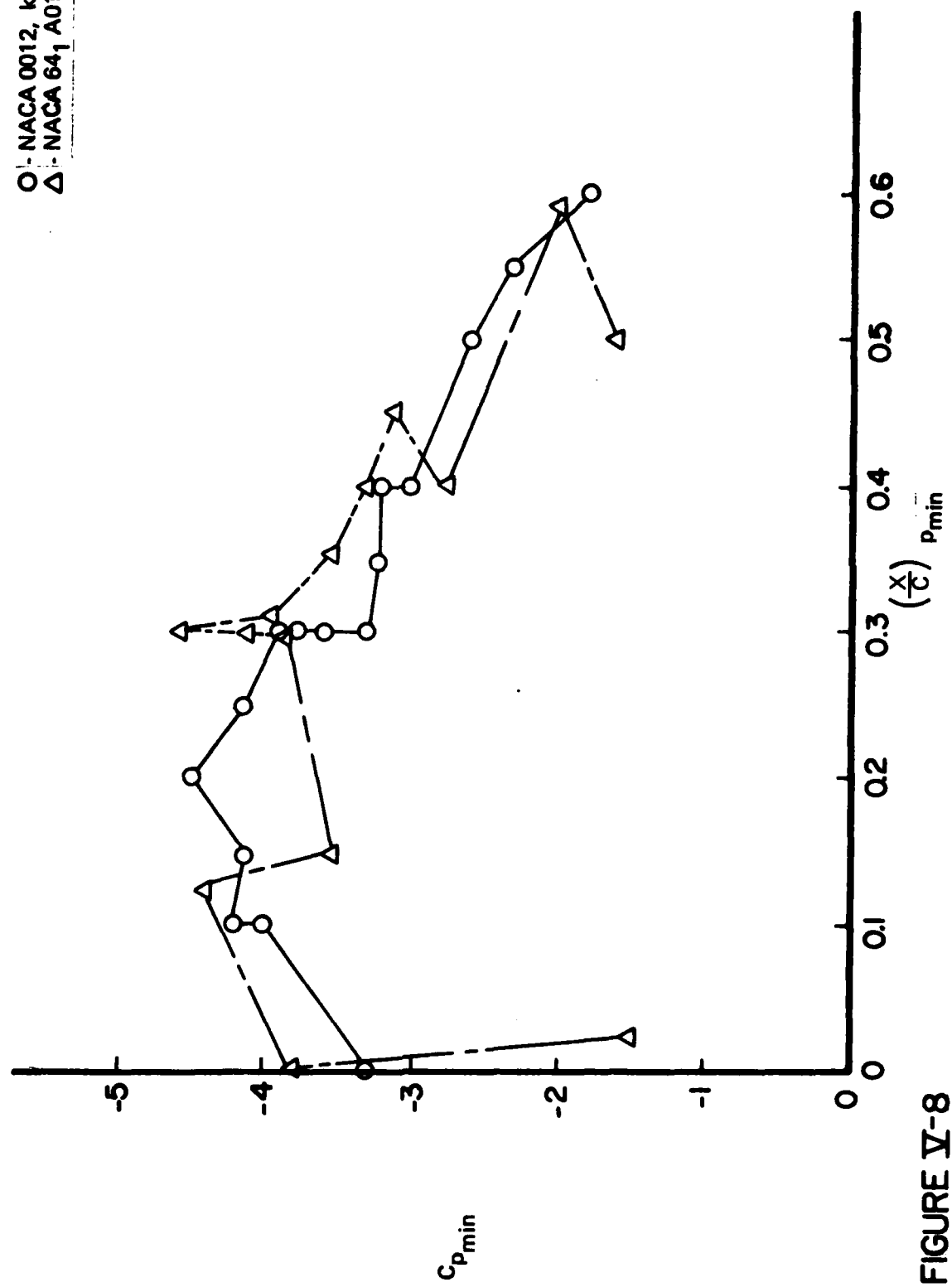
FIGURE V-8

VARIATION OF MINIMUM COEFFICIENT WITH SUCTION PEAK LOCATION, $\overline{U}_\infty = 32 - 33$ fps, $\overline{\alpha}_{max} \cong 60^\circ$

O - NACA 0012, k = 0.089
△ - NACA 64_1 A012 (13), k = 0.094

O – NACA 0012, U_∞ = 33.9 fps
Δ – NACA 64_1 A012(13), U_∞ = 32.5 fps

$C_{p_{min}}$

$\left(\dfrac{x}{c}\right)_{p_{min}}$

FIGURE V-9

VARIATION OF MINIMUM PRESSURE COEFFICIENT WITH SUCTION PEAK LOCATION, k = 0.133, $\alpha_{max} \cong 60°$
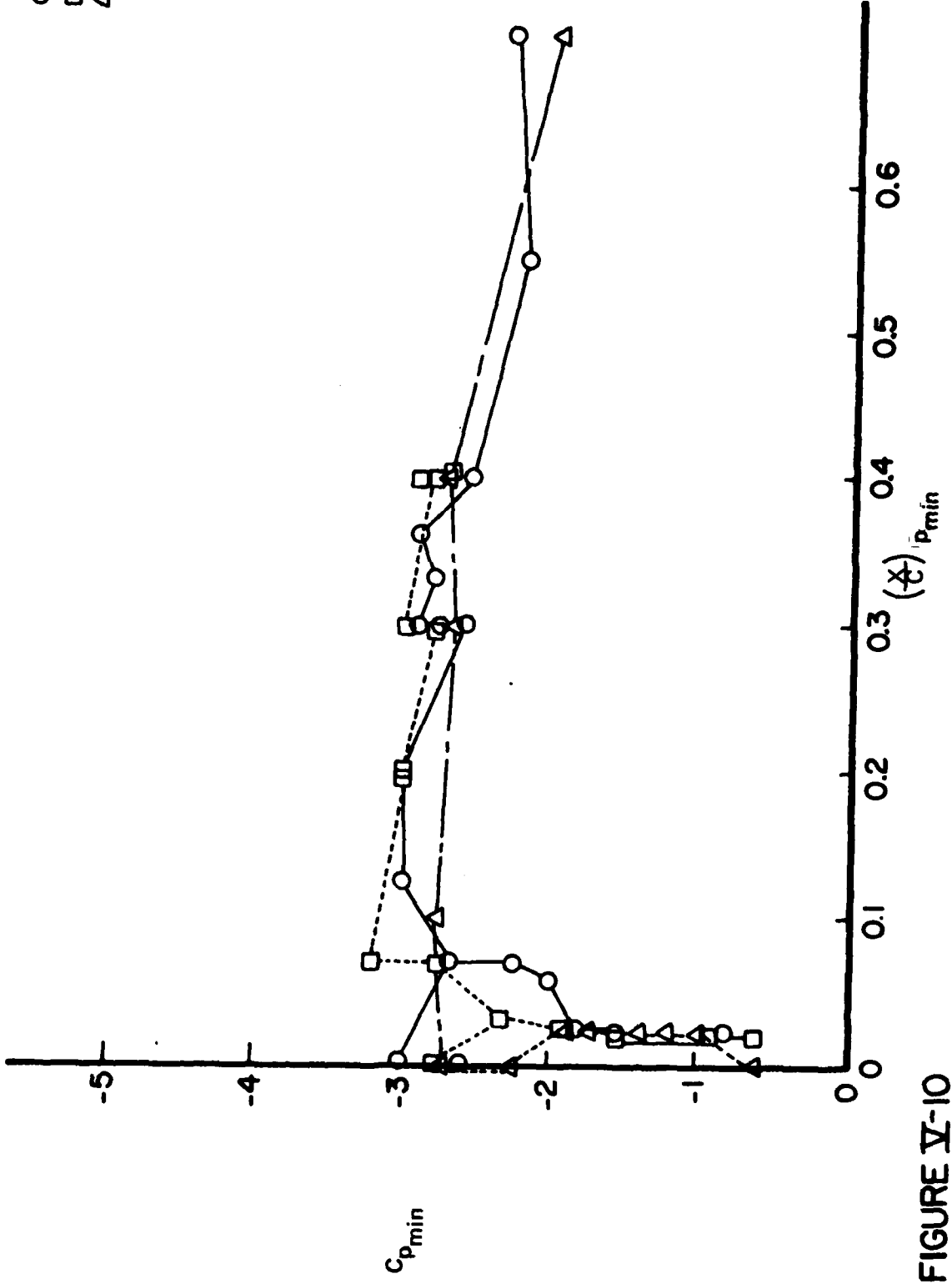
FIGURE V-10

VARIATION OF MINIMUM PRESSURE COEFFICENT WITH SUCTION PEAK LOCATION, NACA 84₁ A012 (13),
$k \cong 0.045$, $U_\infty = 32.1$ fps
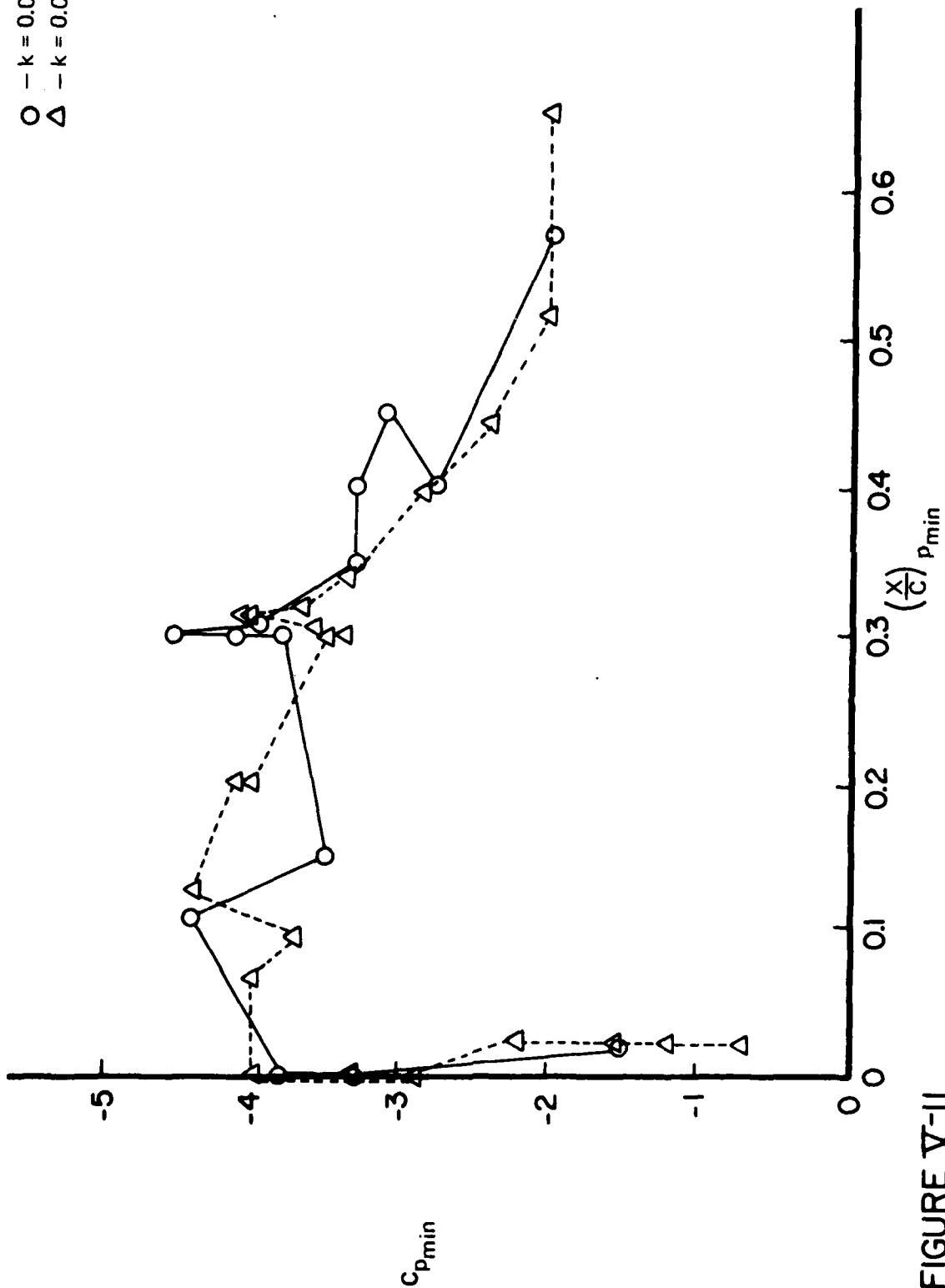
FIGURE V-II

VARIATION OF MINIMUM COEFFICIENT WITH SUCTION PEAK LOCATION, NACA 64, A012(13)
$U_\infty = 32.1$ fps

O — $k = 0.094, \alpha_{max} = 58.7^o$
$\triangle$ — $k = 0.084, \alpha_{max} = 37.0^o$
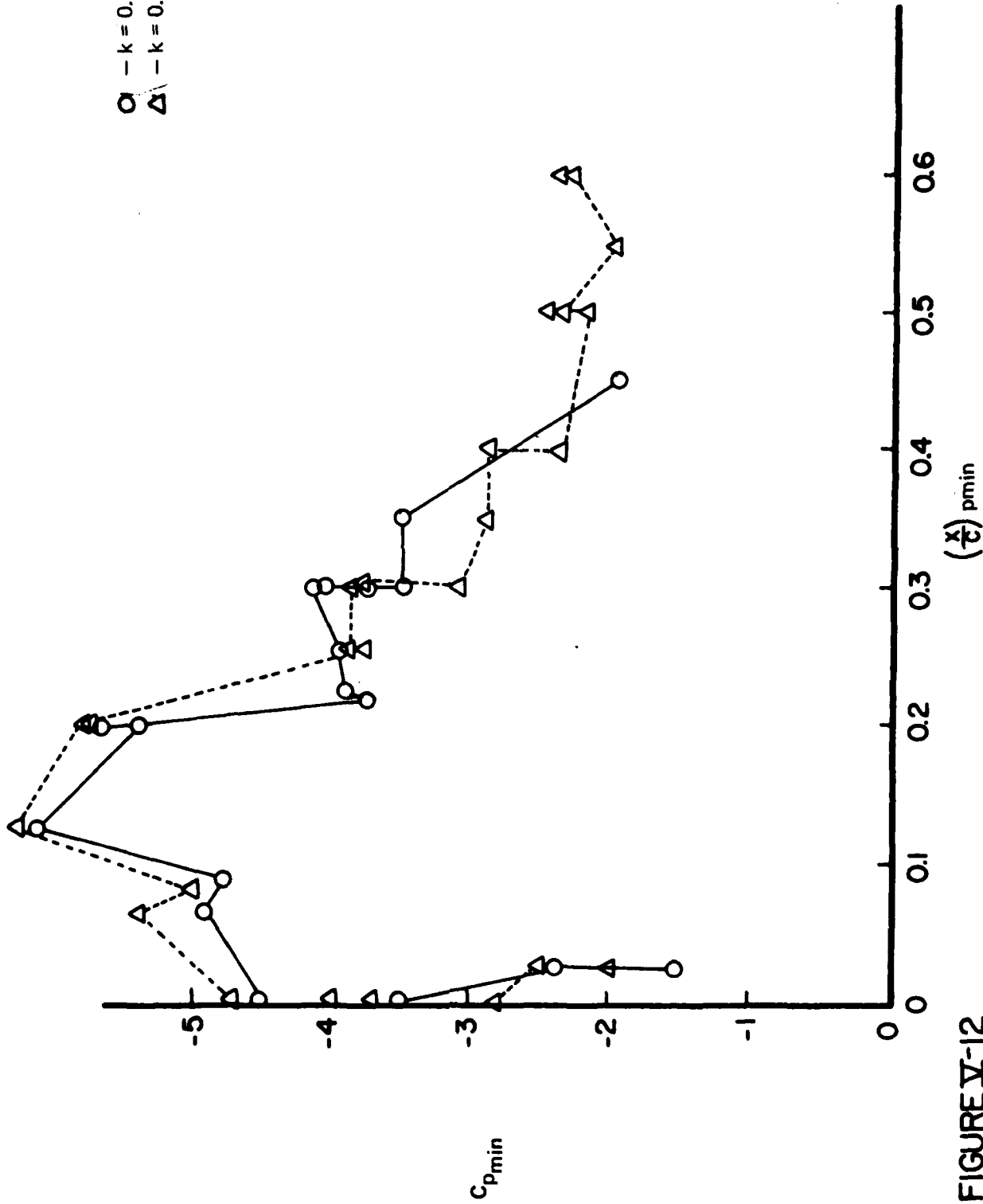
FIGURE V-12

VARIATION OF MINIMUM PRESSURE COEFFICIENT WITH SUCTION PEAK LOCATION, NACA 64$_1$ A012(13), U_∞ = 32 fps
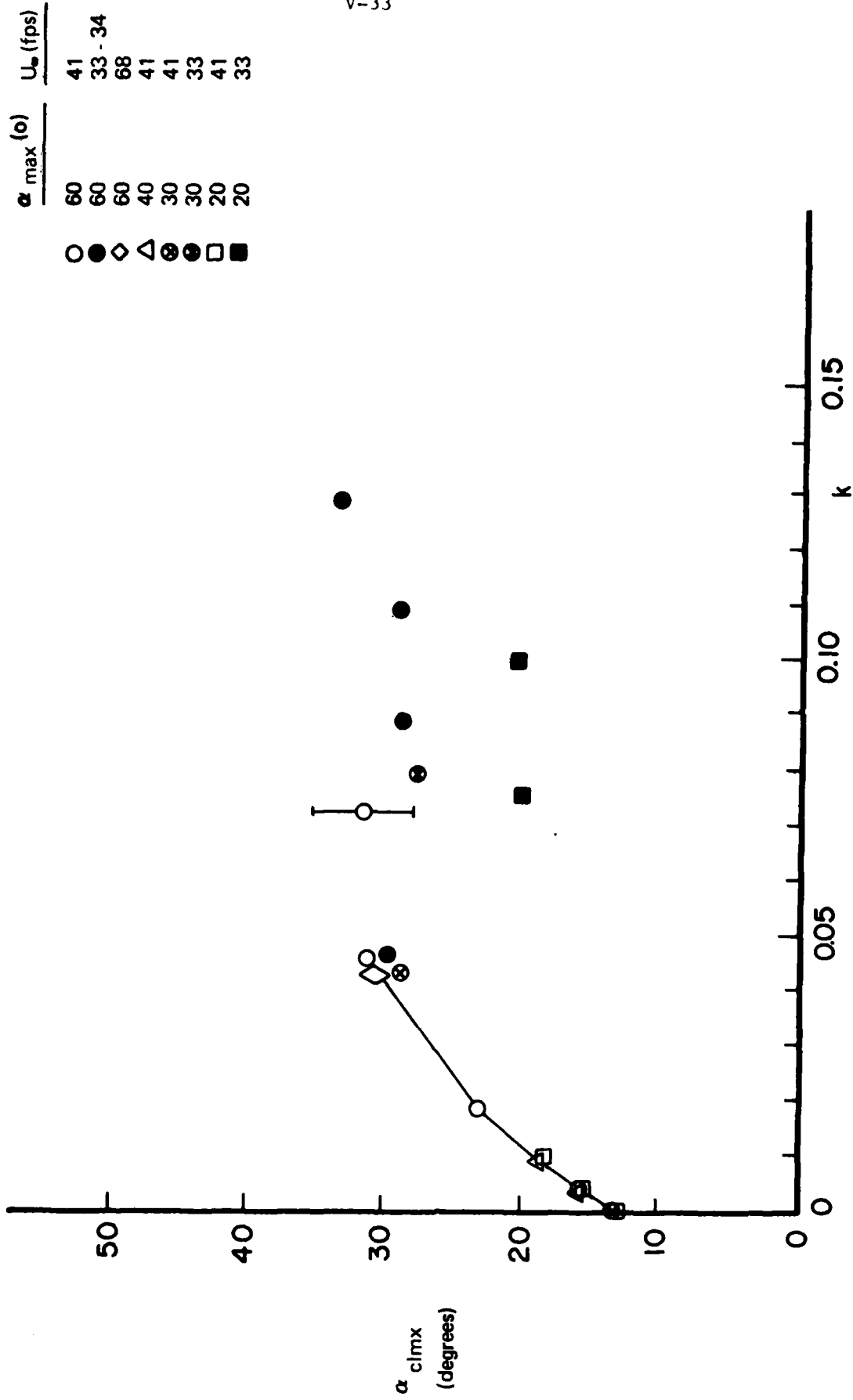
O — k = 0.136, α_{max} = 58.7°
Δ — k = 0.131, α_{max} = 38.1°

$\left(\dfrac{x}{c}\right)_{pmin}$

$c_{p_{min}}$

FIGURE $\underline{V}$-13 (A) NACA 0012
ANGLE-OF-ATTACK FOR MAXIMUM LIFT COEFFICIENT-VARIATION WITH PITCH RATE.
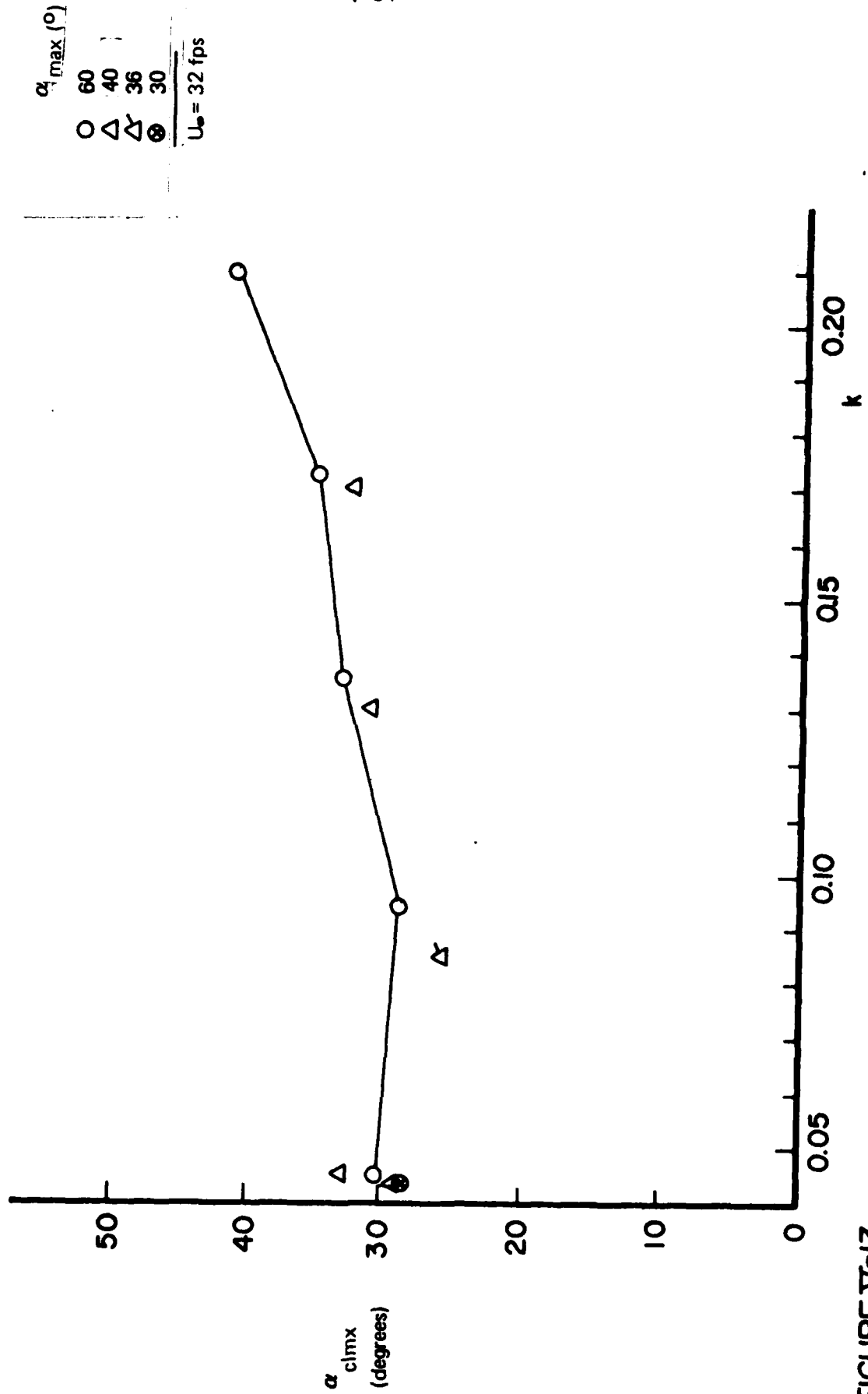
FIGURE V-13 (b) NACA 64_1 A012 (13)
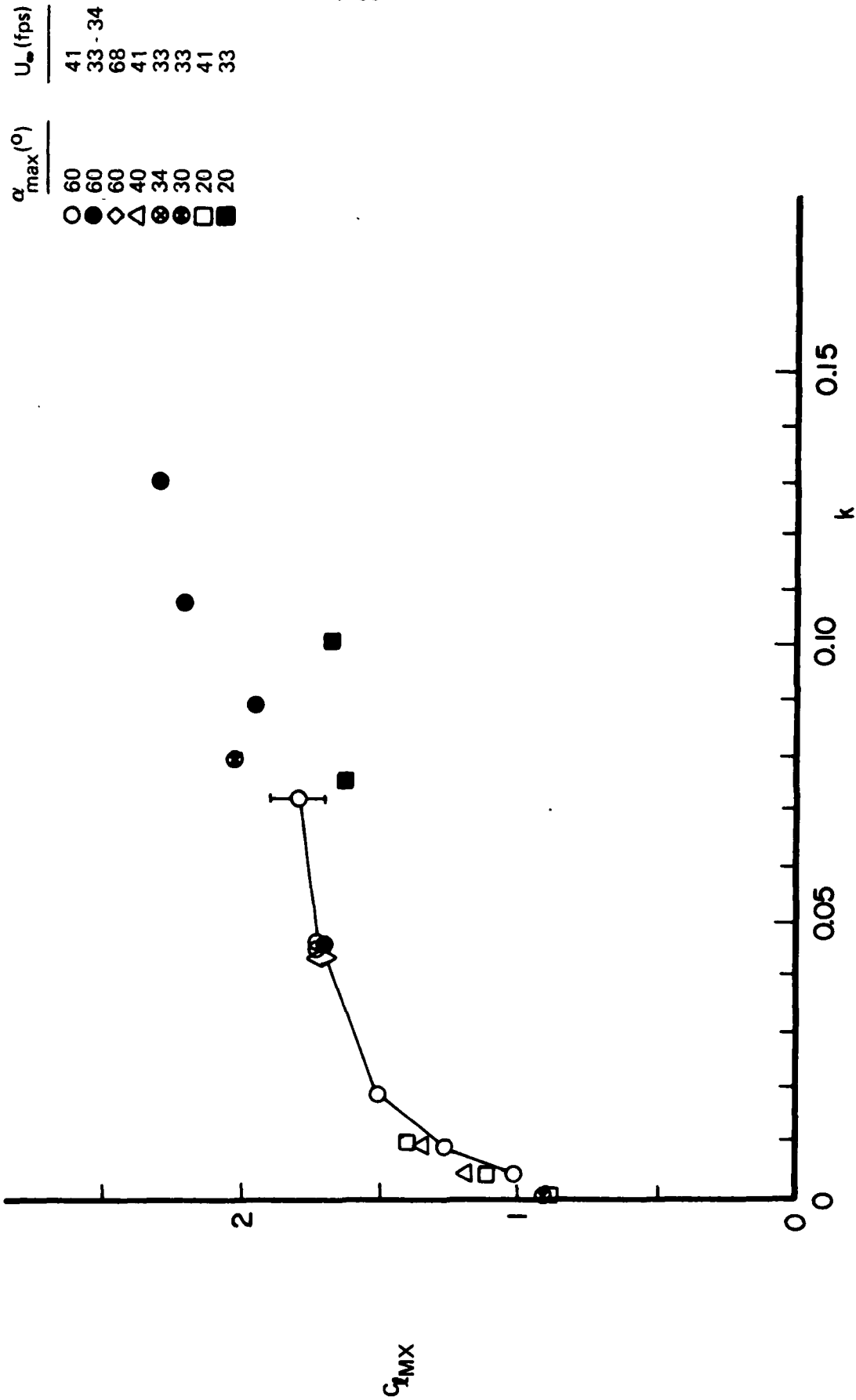ANGLE-OF-ATTACK FOR MAXIMUM LIFT COEFFICIENT-VARIATION WITH PITCH RATE

FIGURE V-14 (a) NACA 0012

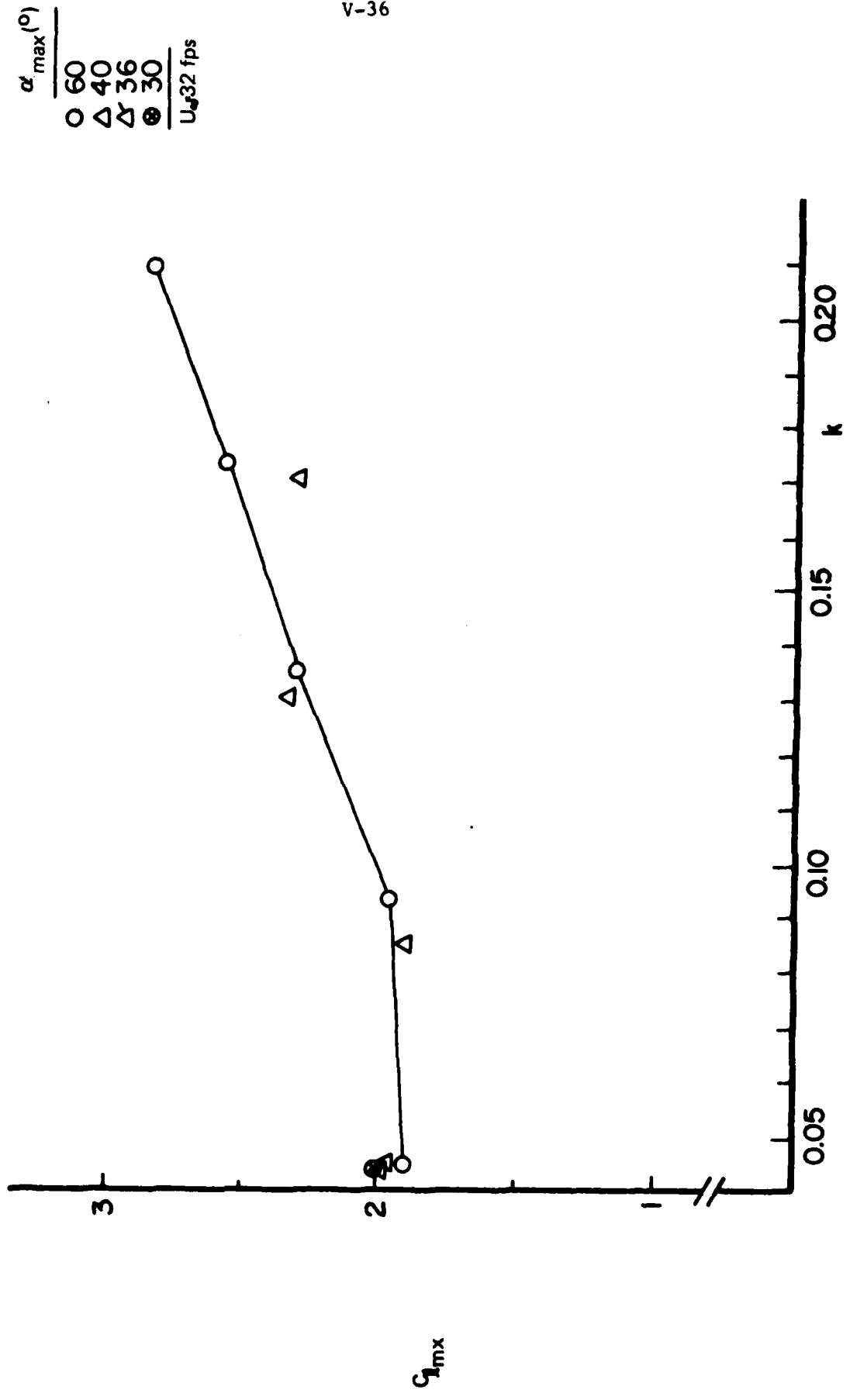MAXIMUM LIFT COEFFICIENT VARIATION WITH PITCH RATE

FIGURE V-14 (b) NACA 64_1A012 (13)
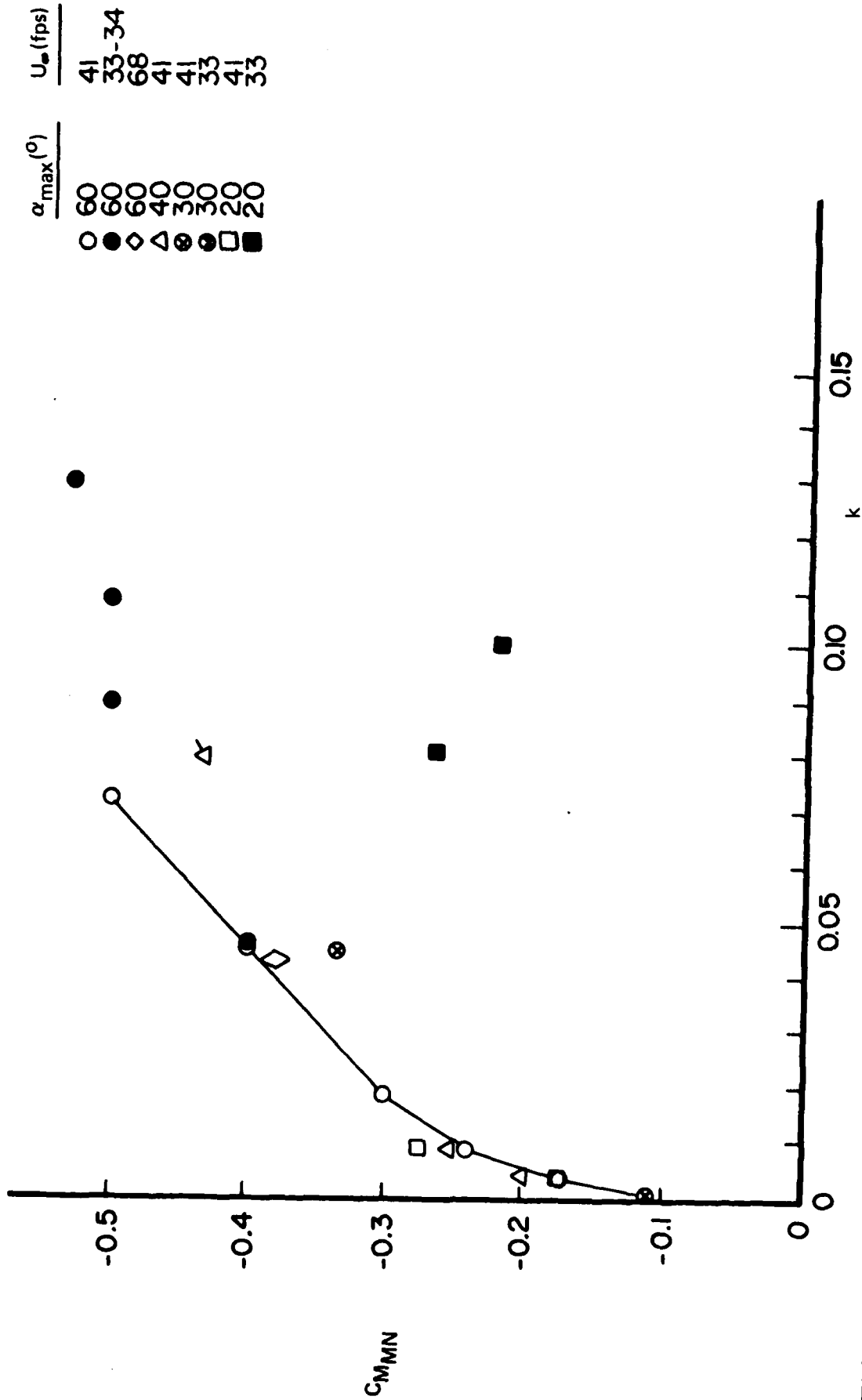MAXIMUM LIFT COEFFICIENT VARIATION WITH PITCH RATE

FIGURE $\overline{V}$-15 (a) NACA 0012

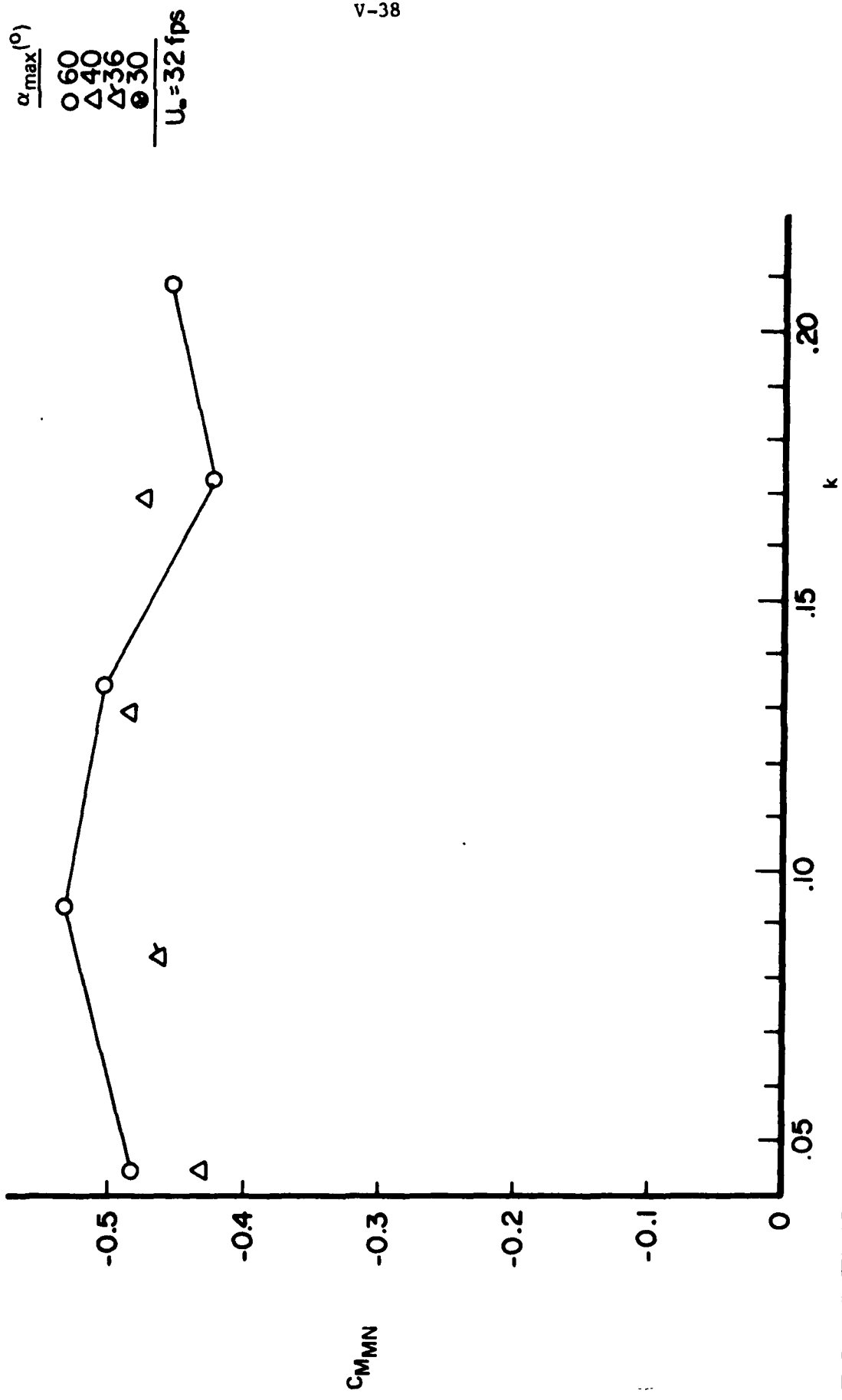MINIMUM PRESSURE COEFFICENT VARIATION WITH PITCH RATE

FIGURE V-15 (b) NACA 64₁ A012 (13)

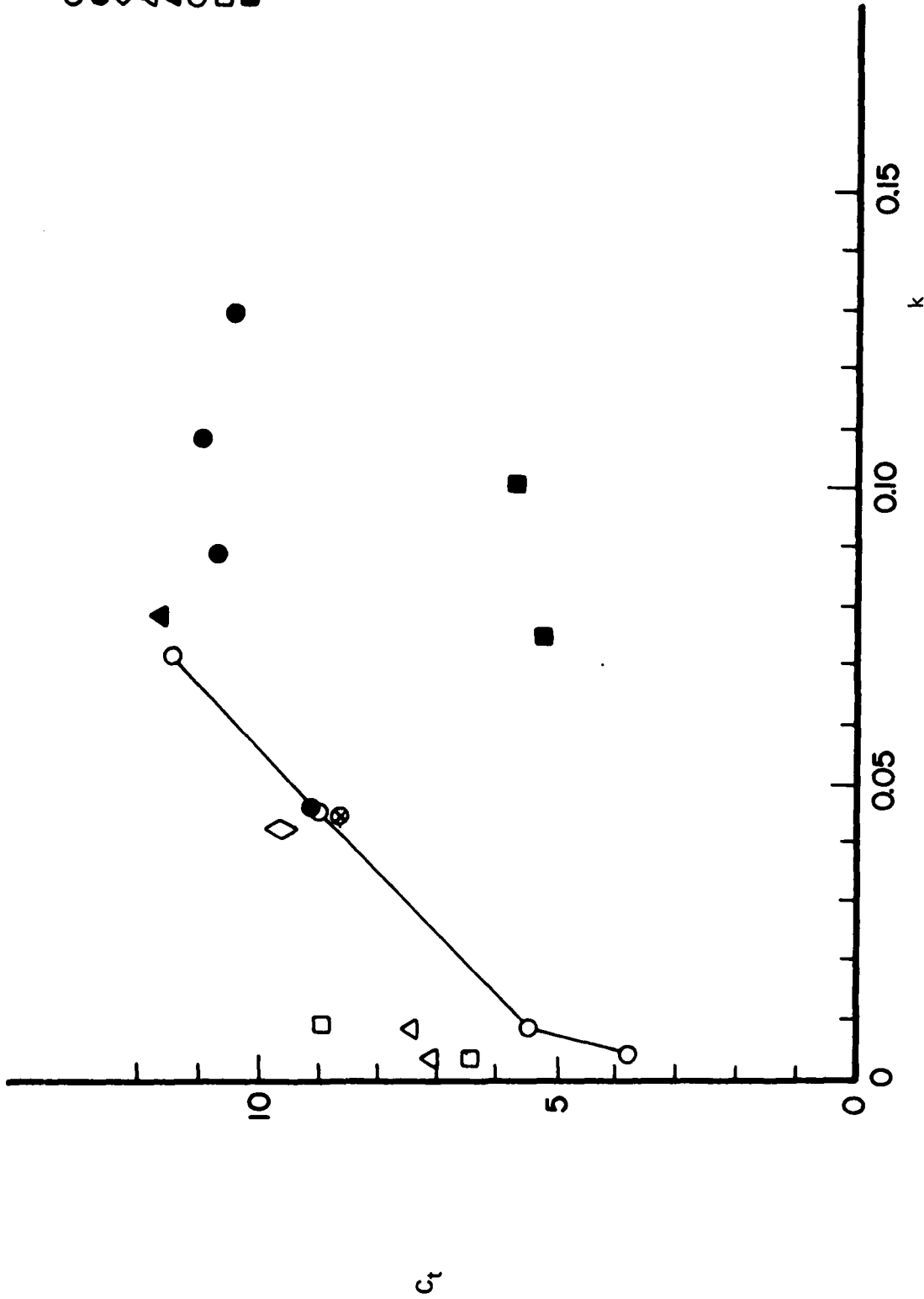MINIMUM PRESSURE COEFFICIENT VARIATION WITH PITCH RATE

FIGURE V-16 (a) NACA 0012
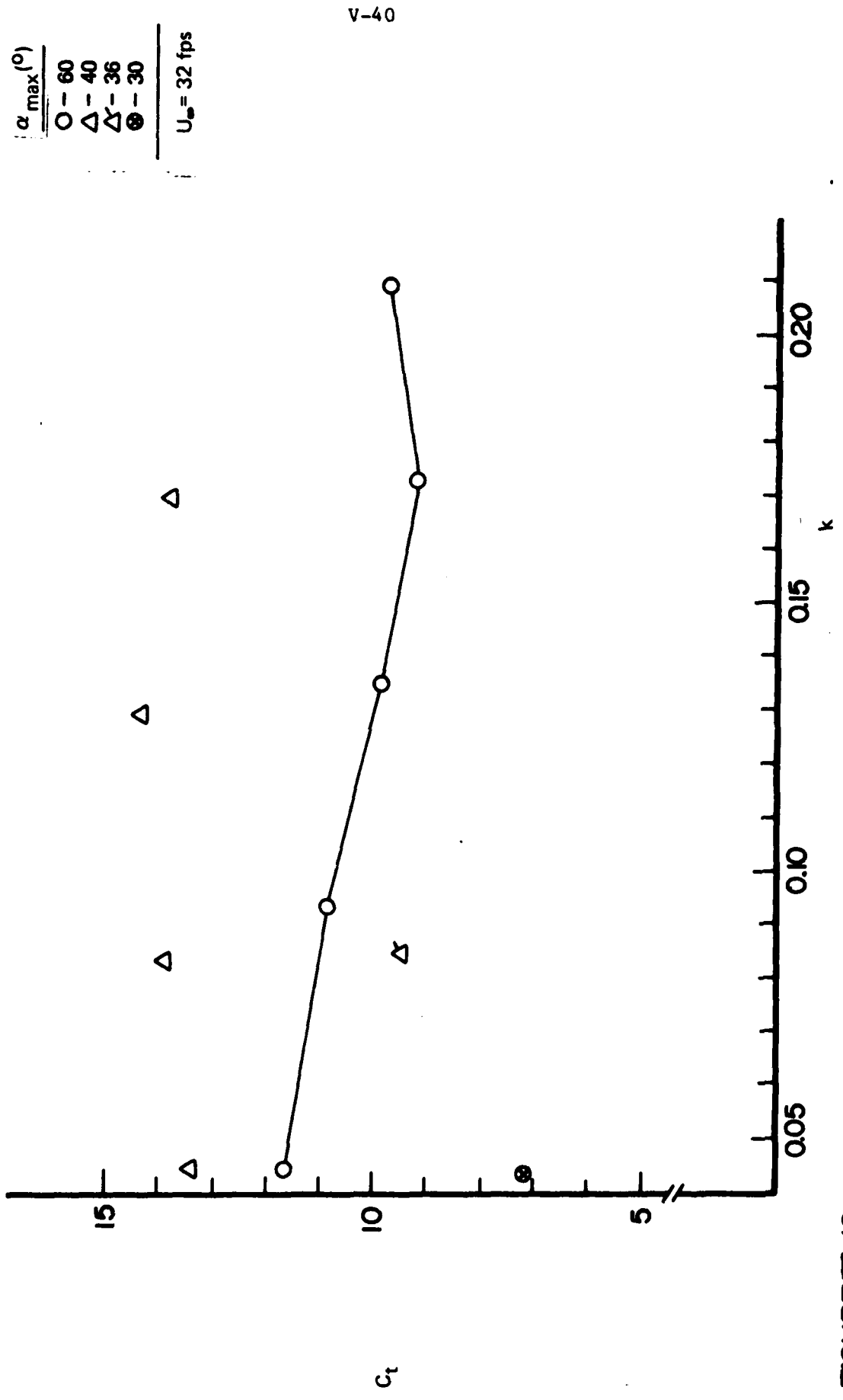DURATION COEFFICIENT VARIATION WITH PITCH RATE

FIGURE V-16 (b) NACA 64$_1$ A012 (13)
DURATION COEFFICIENT VARIATION WITH PITCH RATE
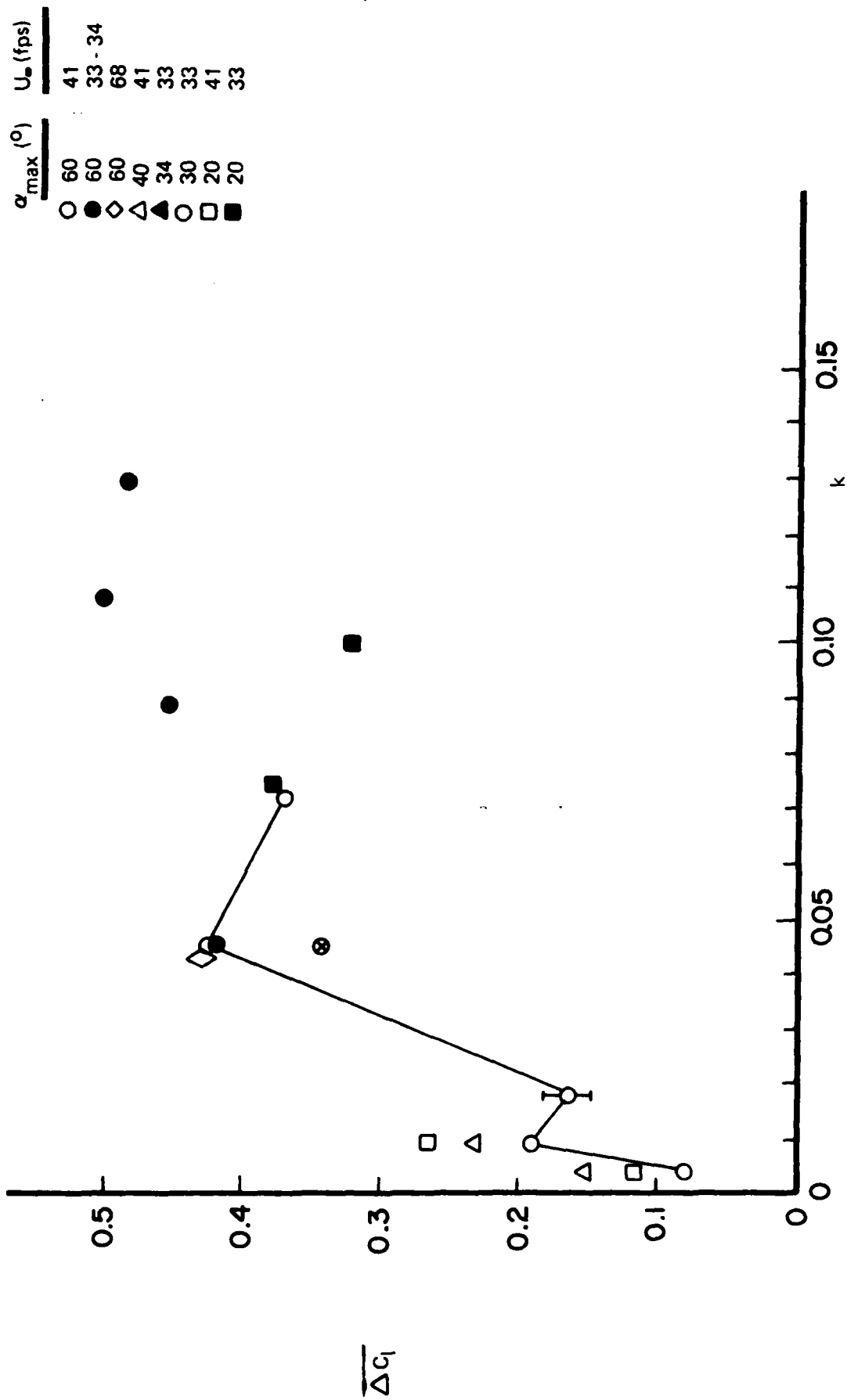
FIGURE V-17 (a)   AVERAGE EXCESS LIFT INCREMENT – NACA 0012   VARIATION WITH PITCH RATE
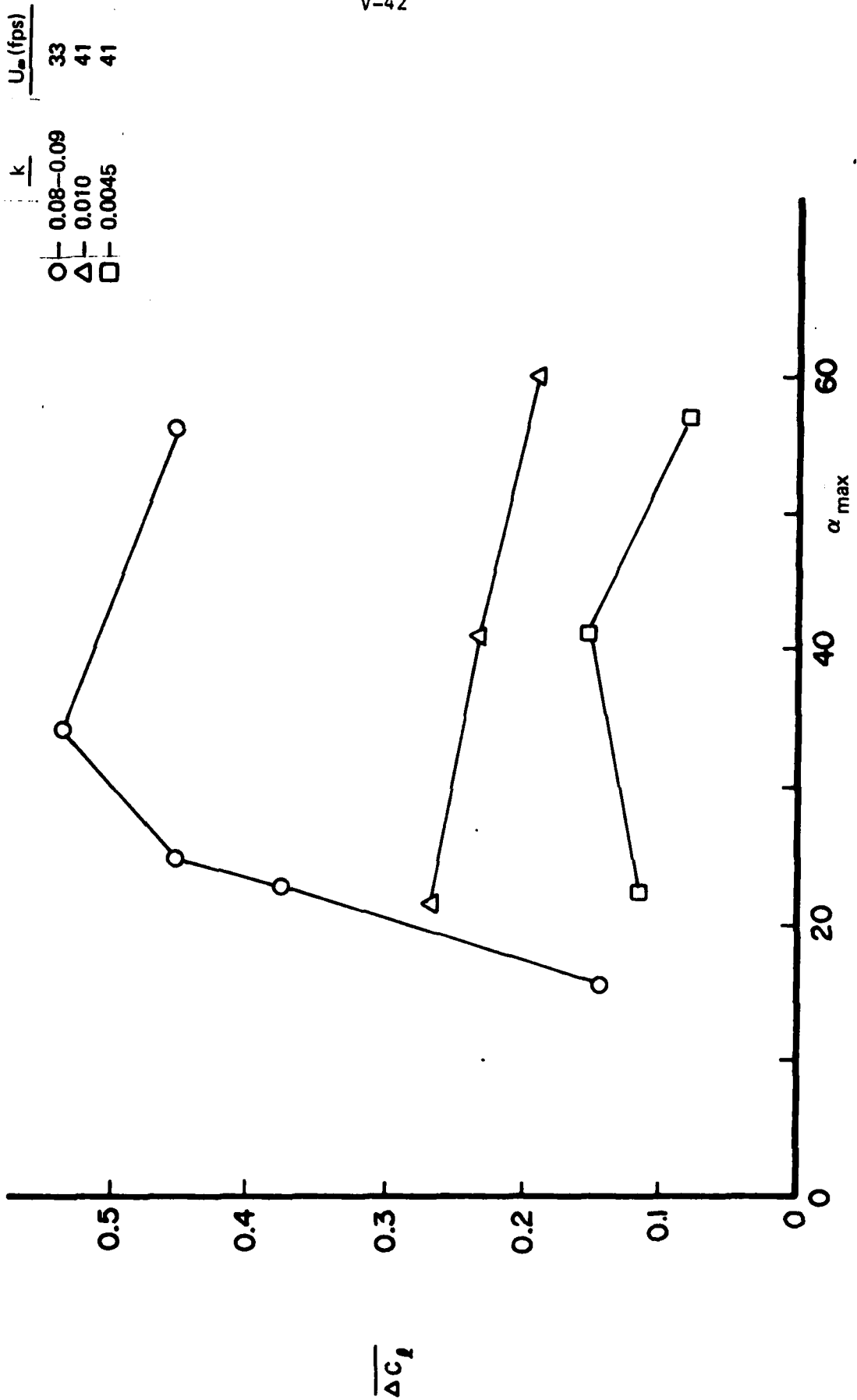
FIGURE $\underline{\text{V}}$-17 (b)

AVERAGE EXCESS LIFT INCREMENT – NACA 0012   VARIATION WITH α_{max}
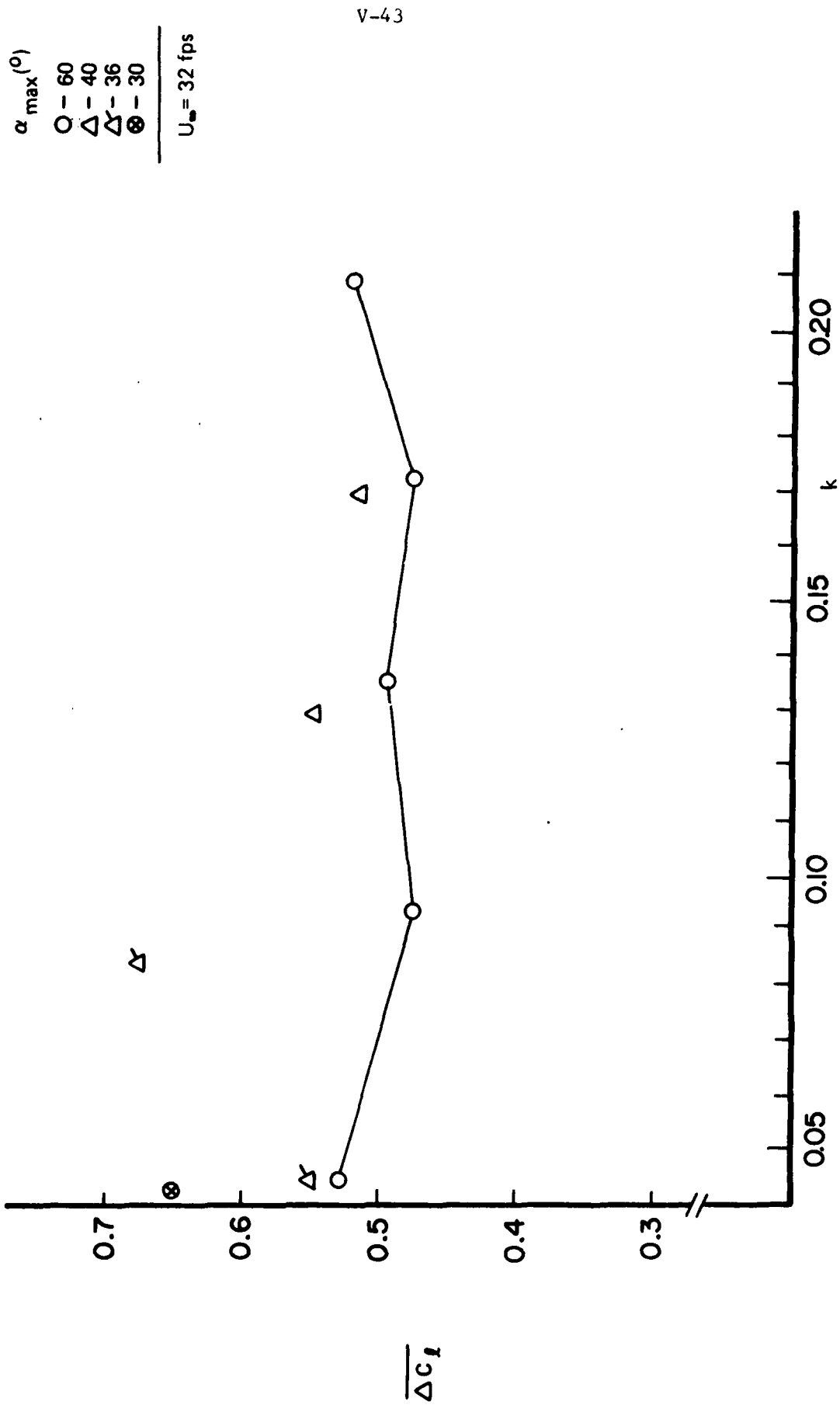
FIGURE V-18

AVERAGE EXCESS LIFT INCREMENT — VARIATION WITH PITCH RATE, NACA 64_1 A012 (13)
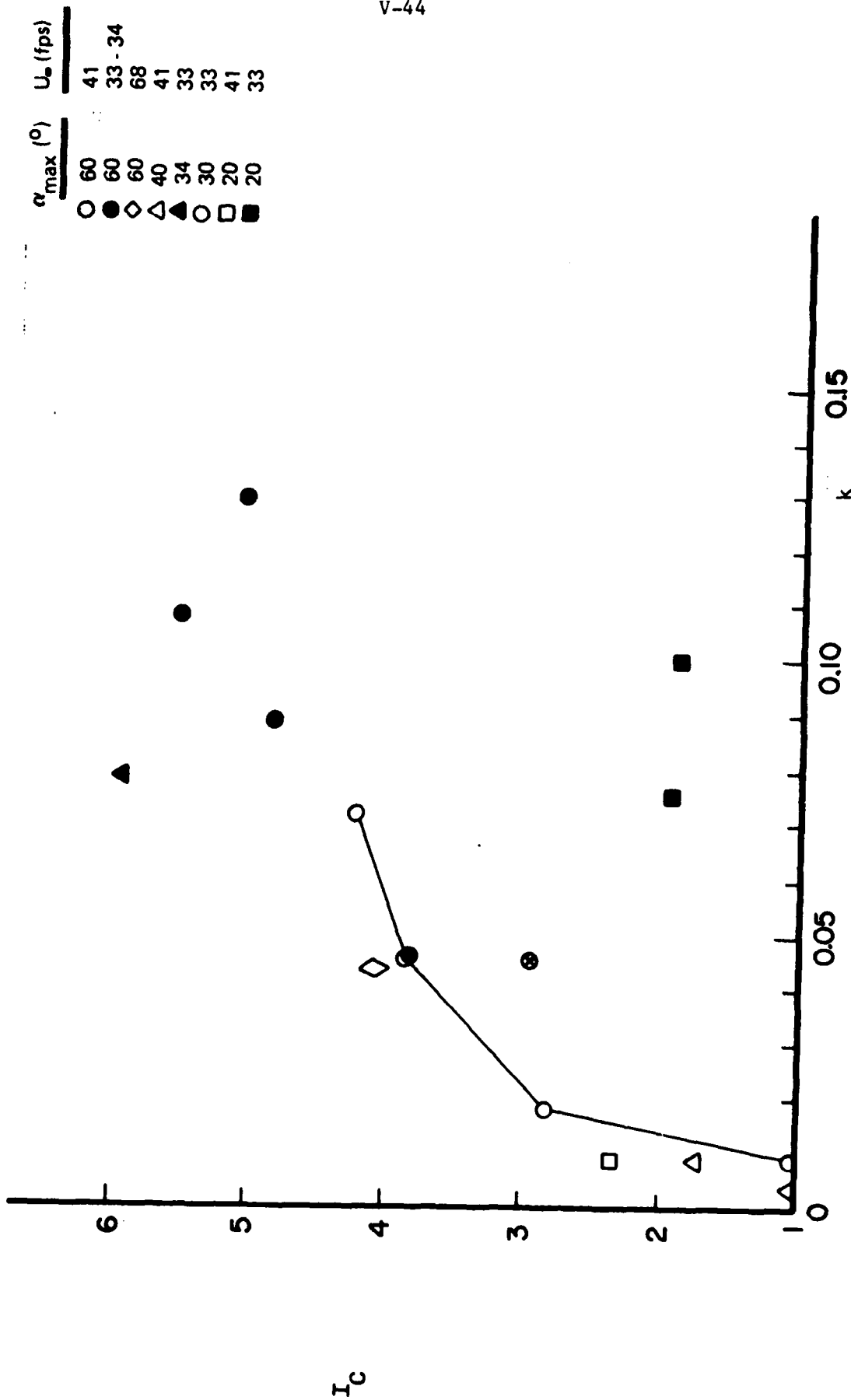
FIGURE V-19 (a)   DIMENSIONLESS IMPULSE, NACA 0012   VARIATION WITH PITCH RATE

O — k = 0.08 – 0.09, U_∞ = 33.2 fps
△ — k = 0.01, U_∞ = 41.f fps
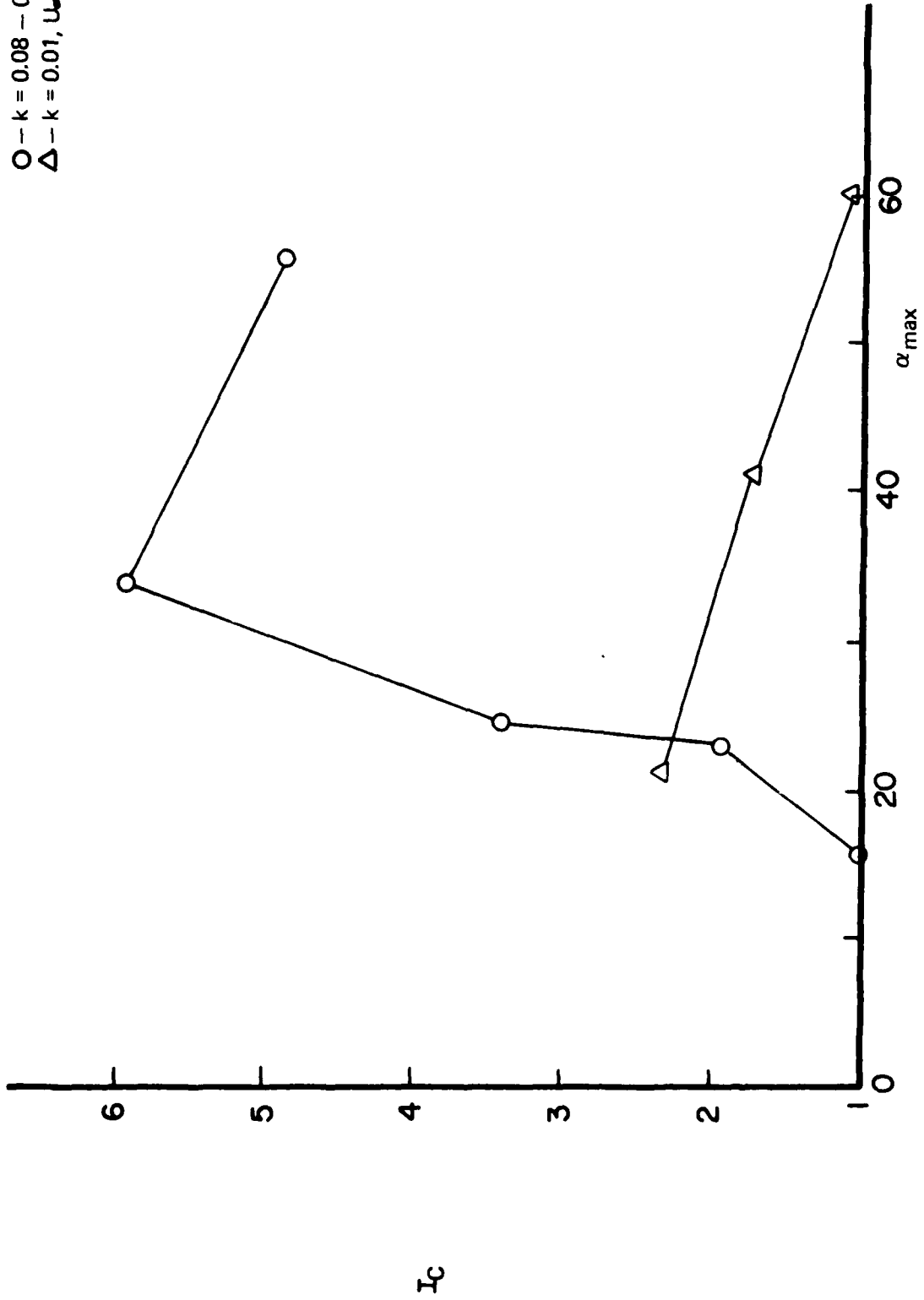
FIGURE V-19 (b)

DIMENSIONLESS IMPULSE, NACA 0012, VARIATION WITH α_{max}
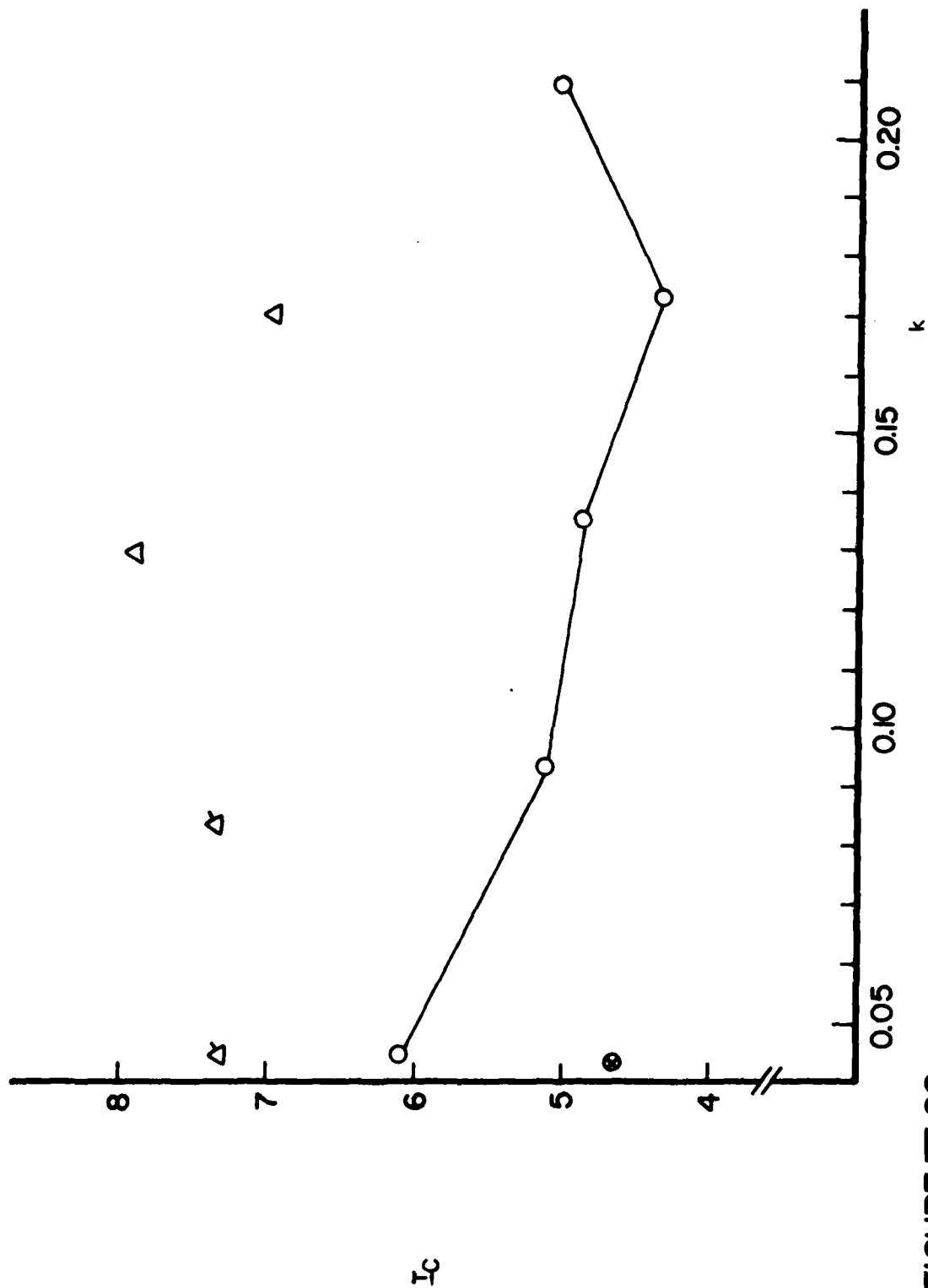
FIGURE V-20 (a)
DIMENSIONLESS IMPULSE, NACA $64_{,1}A012(13)$, VARIATION WITH PITCH RATE
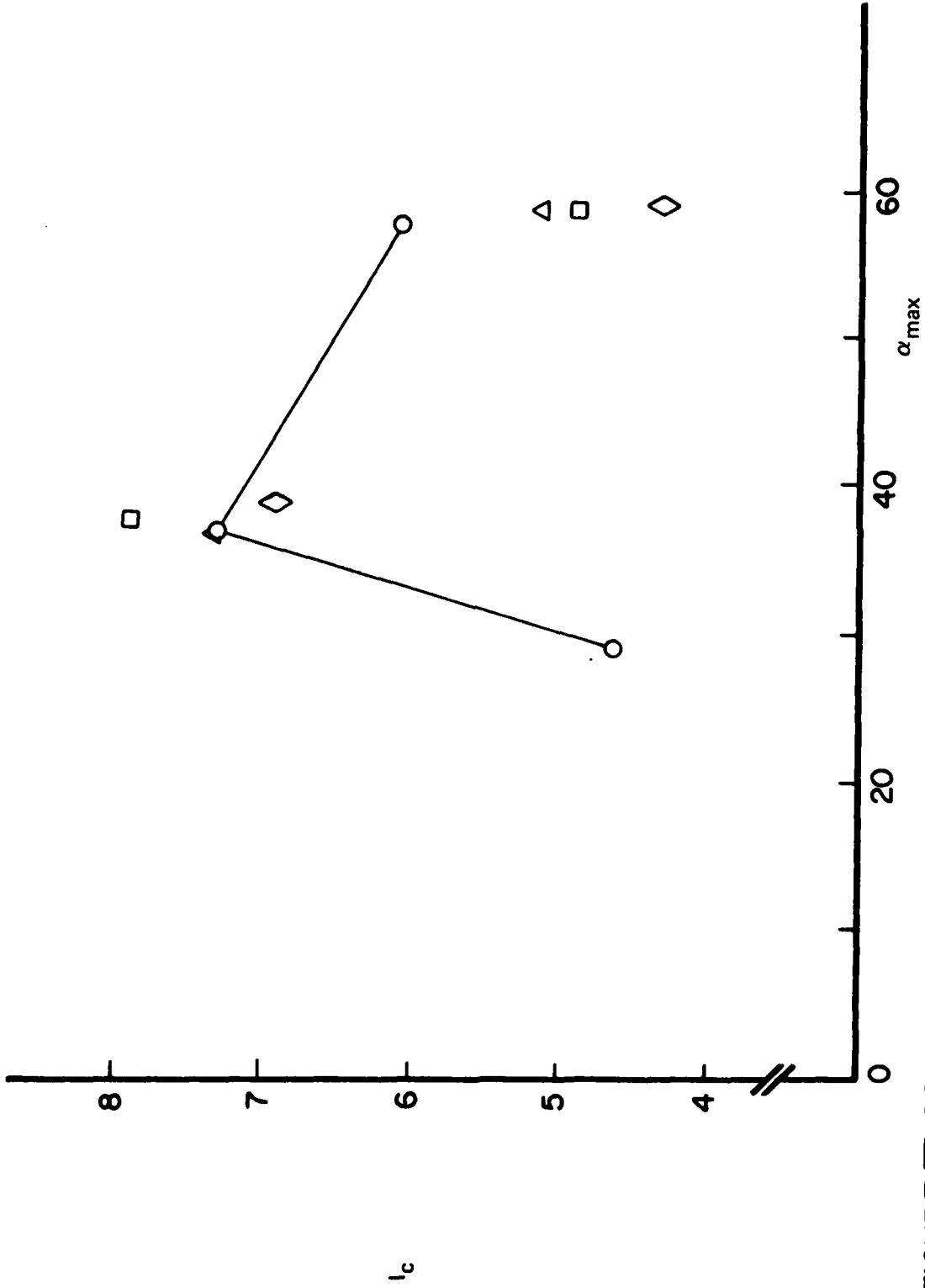
FIGURE V-20 (b)
DIMENSIONLESS IMPULSE, NACA $64_1A012(13)$, VARIATION WITH α_{max}
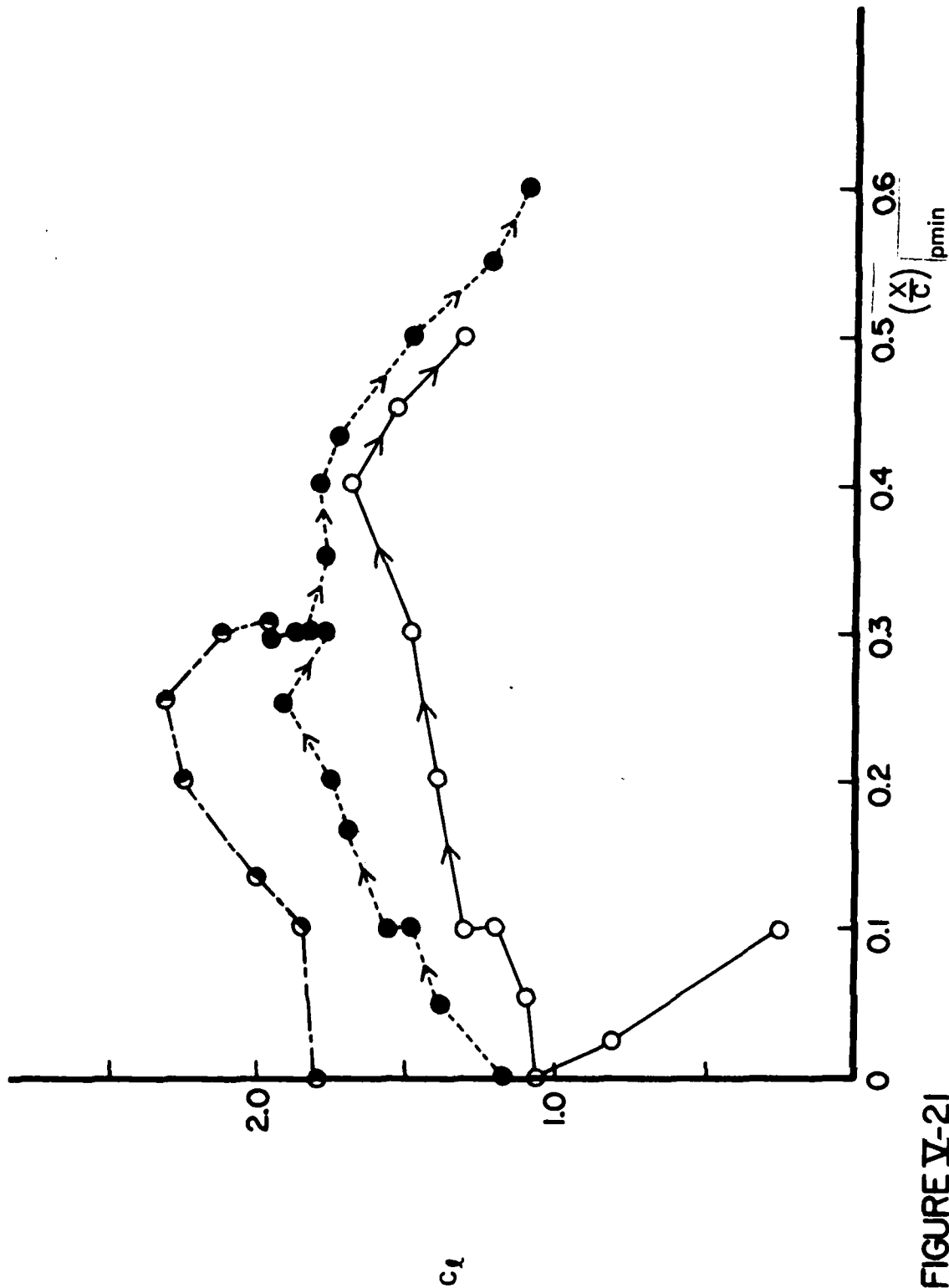
FIGURE V-21

VARIATION OF LIFT COEFFICIENT WITH SUCTION PEAK LOCATION (UPPER SURFACE), NACA 0012, $U_\infty = 33$ fps, $\alpha_{max} = 60°$
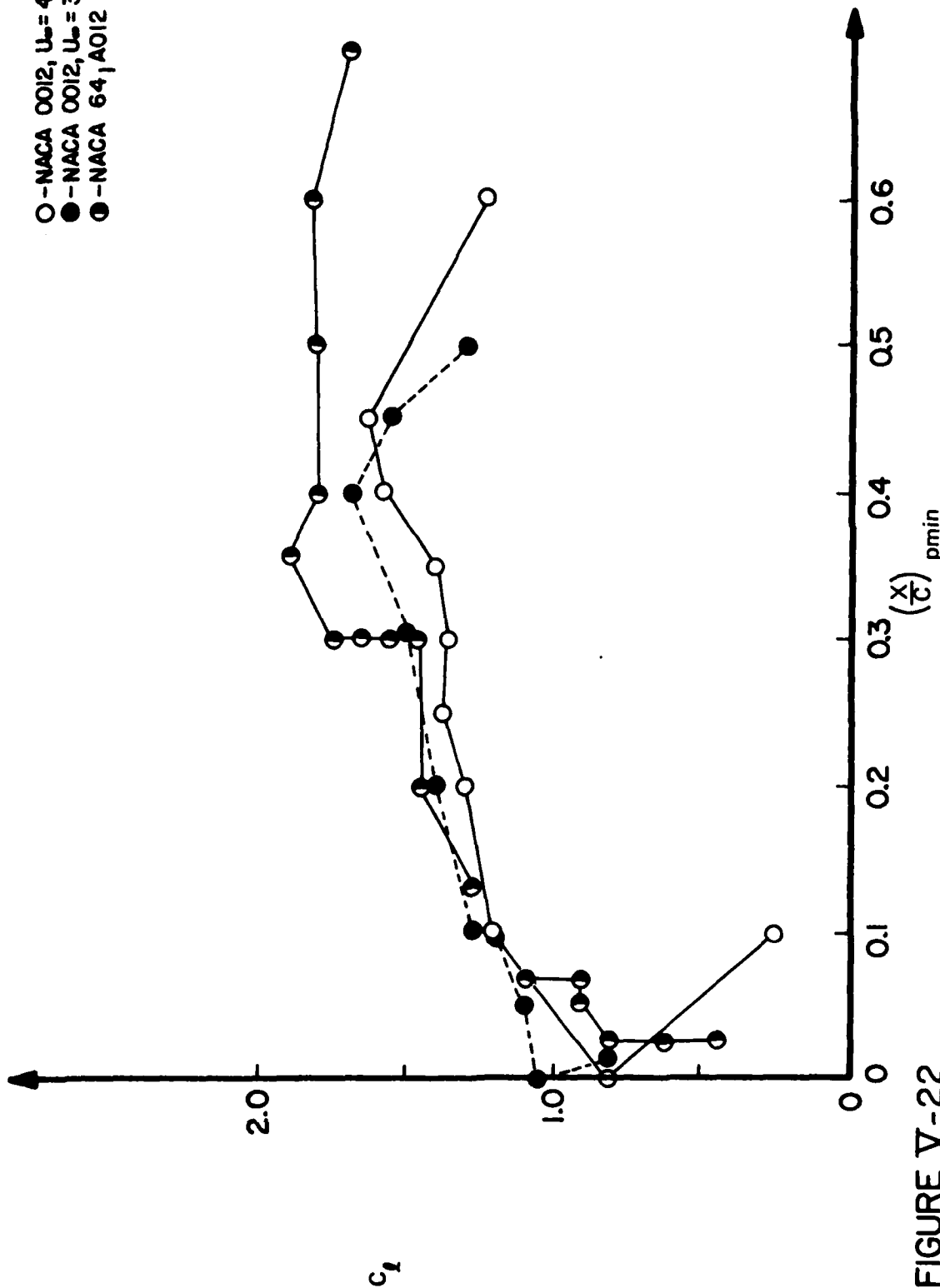
FIGURE V-22

VARIATION OF LIFT COEFFICIENT WITH SUCTION PEAK LOCATION (UPPER SURFACE), $k = 0.045, \alpha_{max} = 60^0 q$
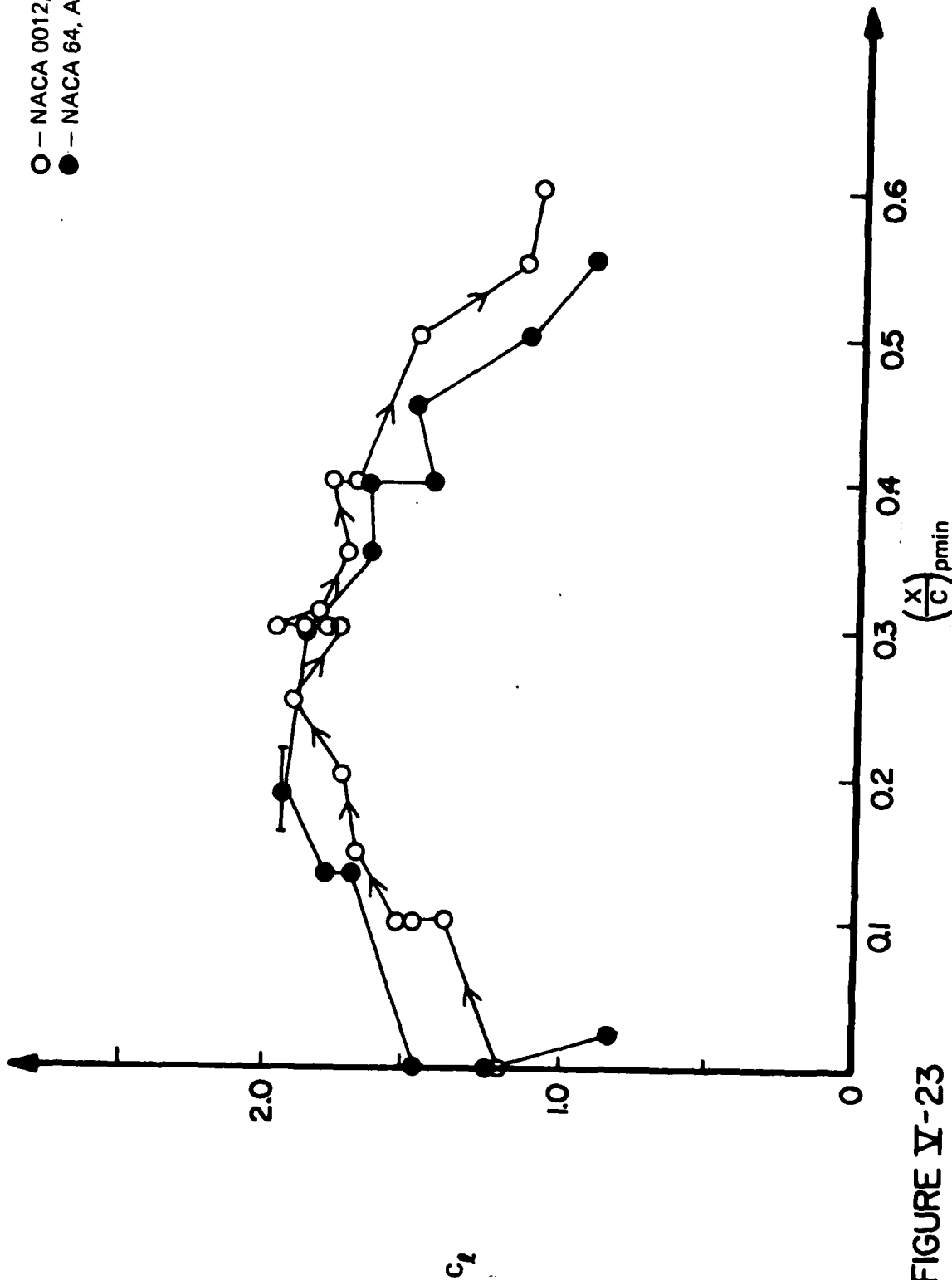
FIGURE $\mathbb{V}$-23

VARIATION OF LIFT COEFFICIENT WITH SUCTION PEAK LOCATION (UPPER SURFACE), $k \cong 0.09, \alpha_{max} = 60^0$

O – NACA 0012, k = 0.130

● –NACA 64, A012(13), k = 0.138

$\left(\dfrac{X}{C}\right)_{pmin}$

C_{ℓ}
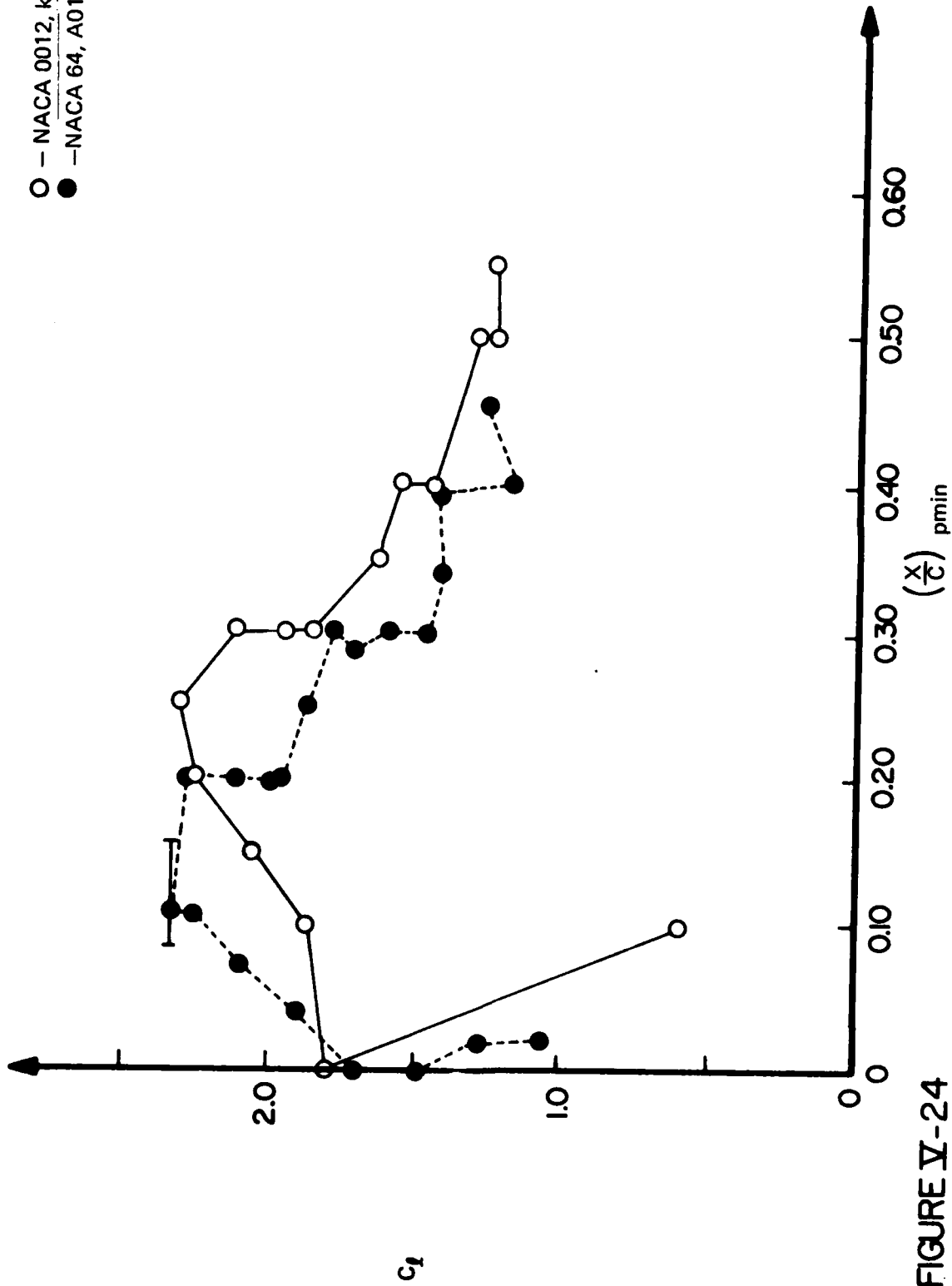
FIGURE V-24

VARIATION OF LIFT COEFFICIENT WITH SUCTION PEAK LOCATION (UPPER SURFACE), U_{∞} = 32 - 33 fps, $_{max}$ = 60°
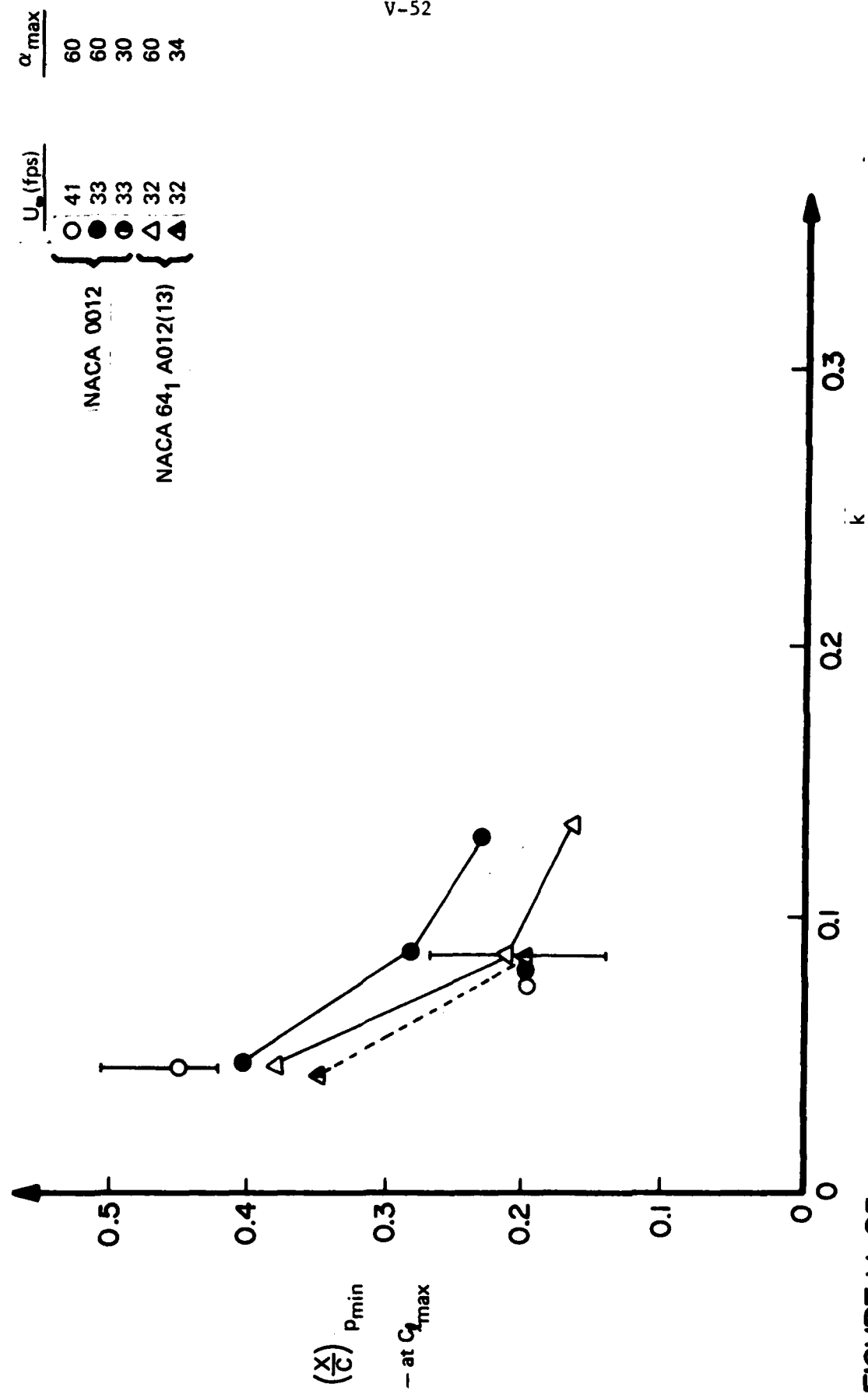
FIGURE V-25

SUCTION PEAK LOCATION AT MAXIMUM LIFT COEFFICIENT - VARIATION WITH PITCH RATE
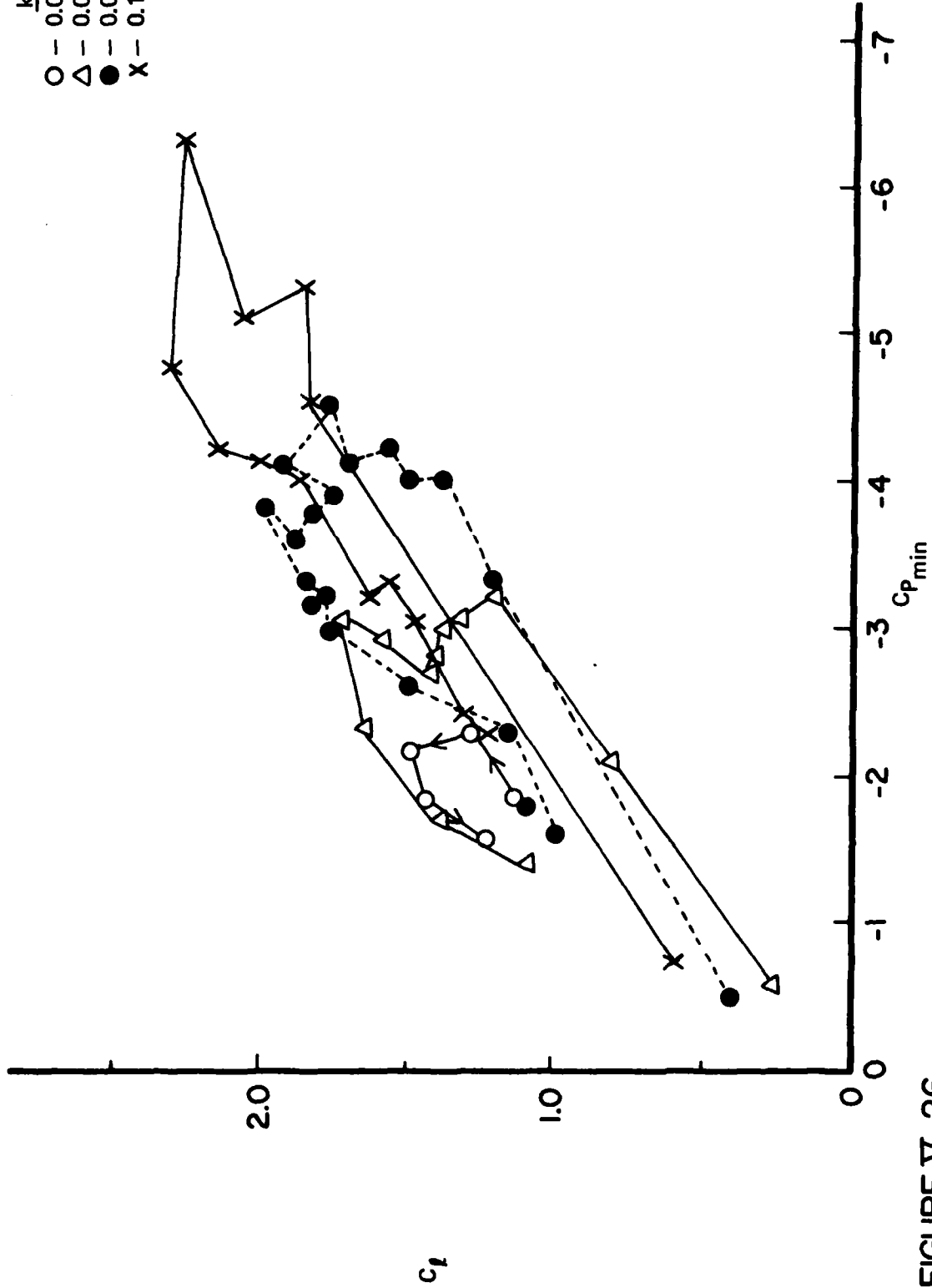
FIGURE V-26

VARIATION OF LIFT COEFFICIENT WITH MINIMUM PRESSURE COEFFICIENT — EFFECT OF PITCH RATE,
NACA 0012, $\alpha_{max} = 60^0$
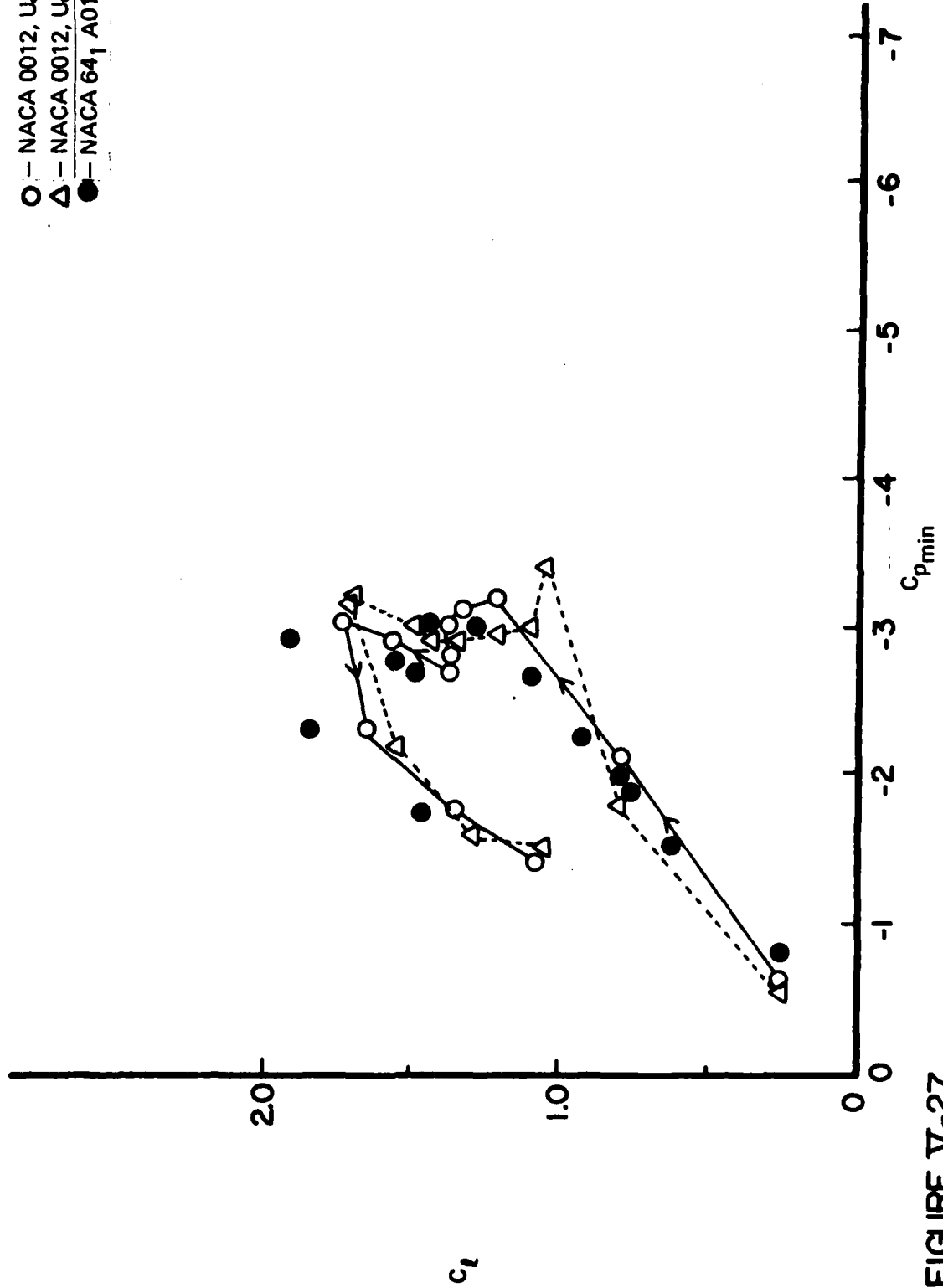
FIGURE V-27

VARIATION OF LIFT COEFFICIENT WITH MINIMUM PRESSURE COEFFICIENT, $k \cong 0.045, \overline{\alpha_{max}} = 60^0$
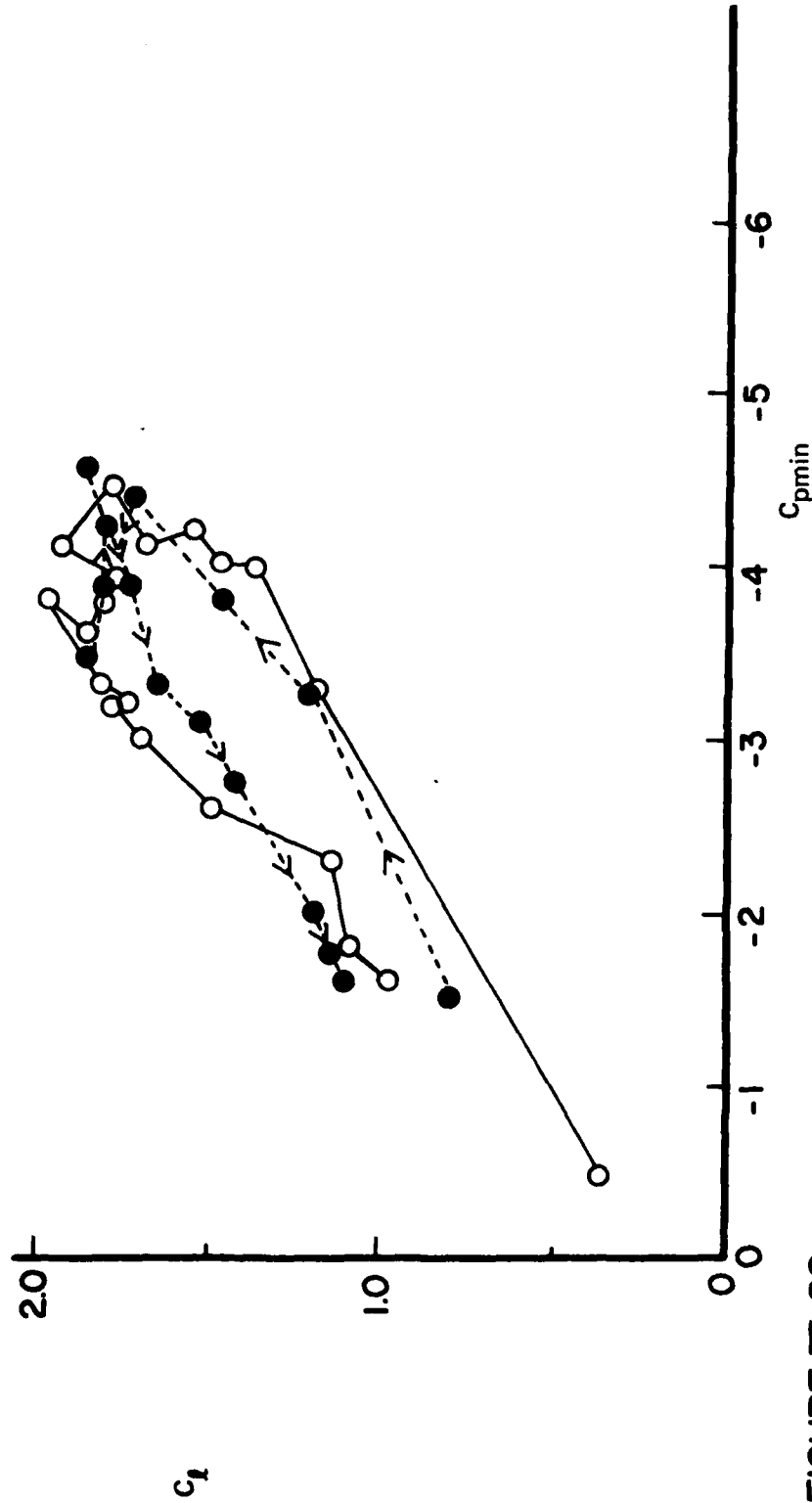
FIGURE V-28

VARIATION OF LIFT COEFFICIENT WITH MINIMUM PRESSURE COEFFICIENT, $U_\infty = 33$ fps, $\alpha_{max} = 60°$
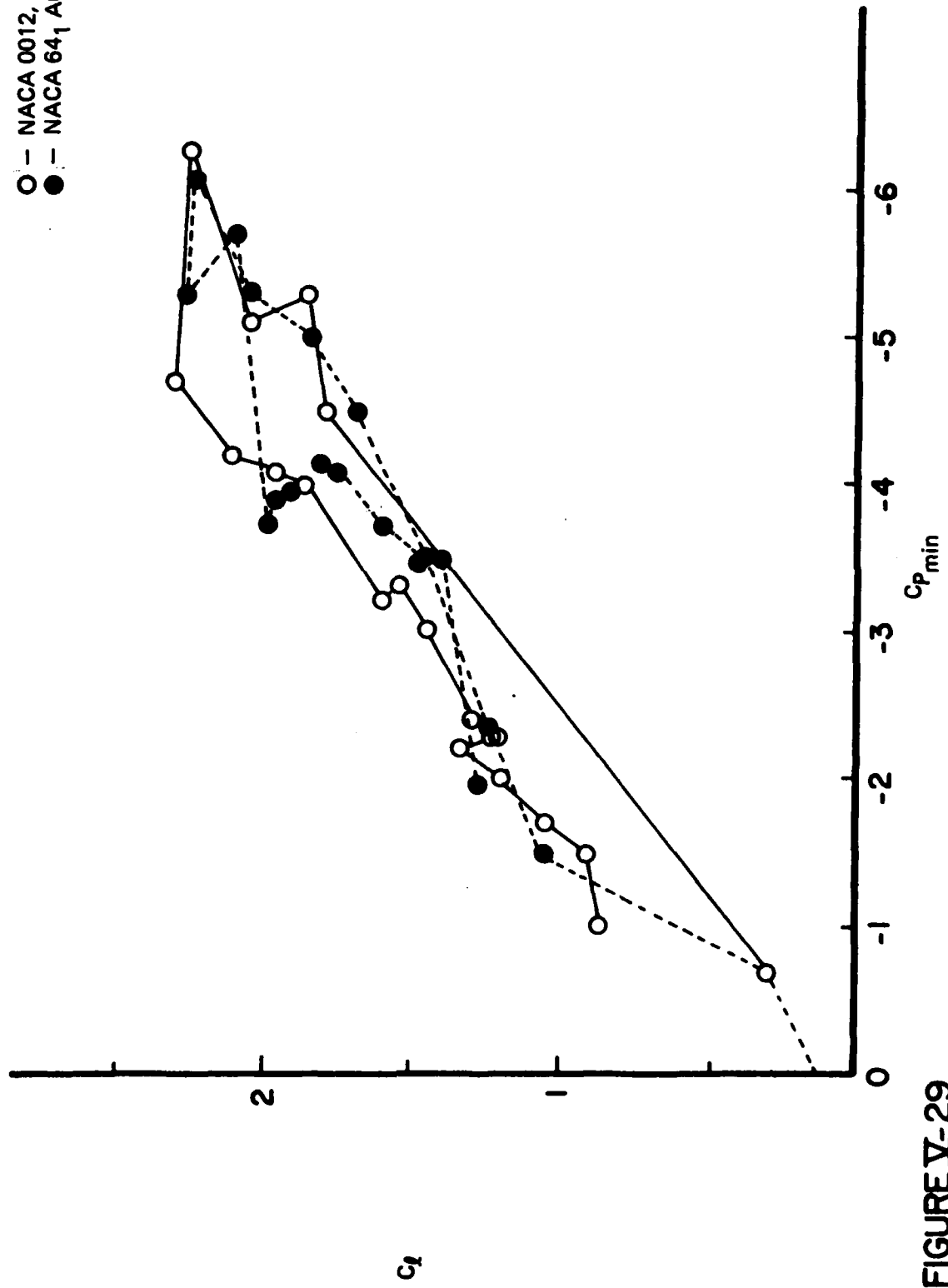
FIGURE V-29

VARIATION OF LIFT COEFFICIENT WITH MINIMUM PRESSURE COEFFICIENT, $U_\infty = 33$ fps, $\alpha_{max} \cong 60^\circ$
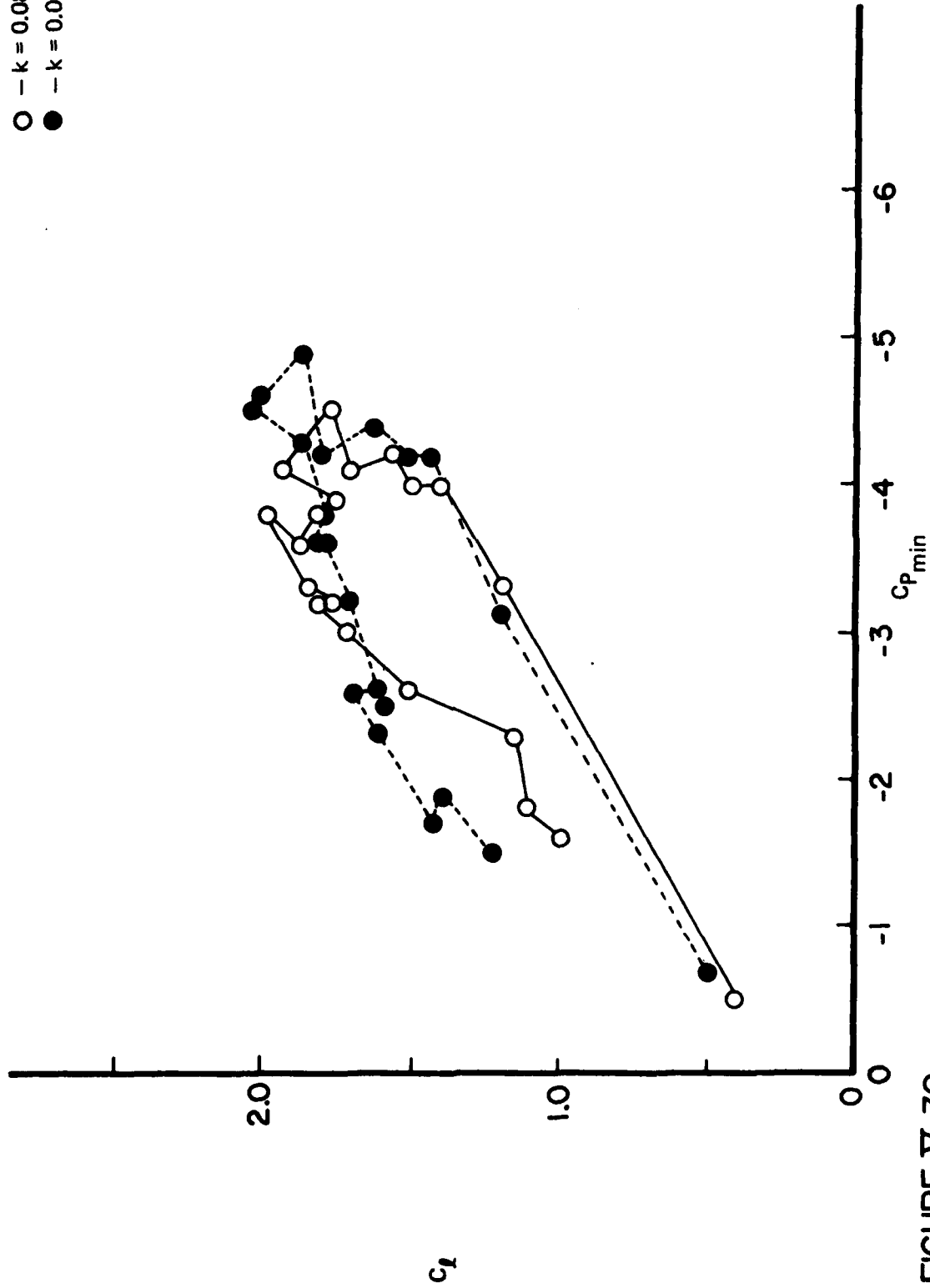
FIGURE V-30

VARIATION OF LIFT COEFFICIENT WITH MINIMUM PRESSURE COEFFICIENT, NACA 0012, $U_\infty = 33$ fps
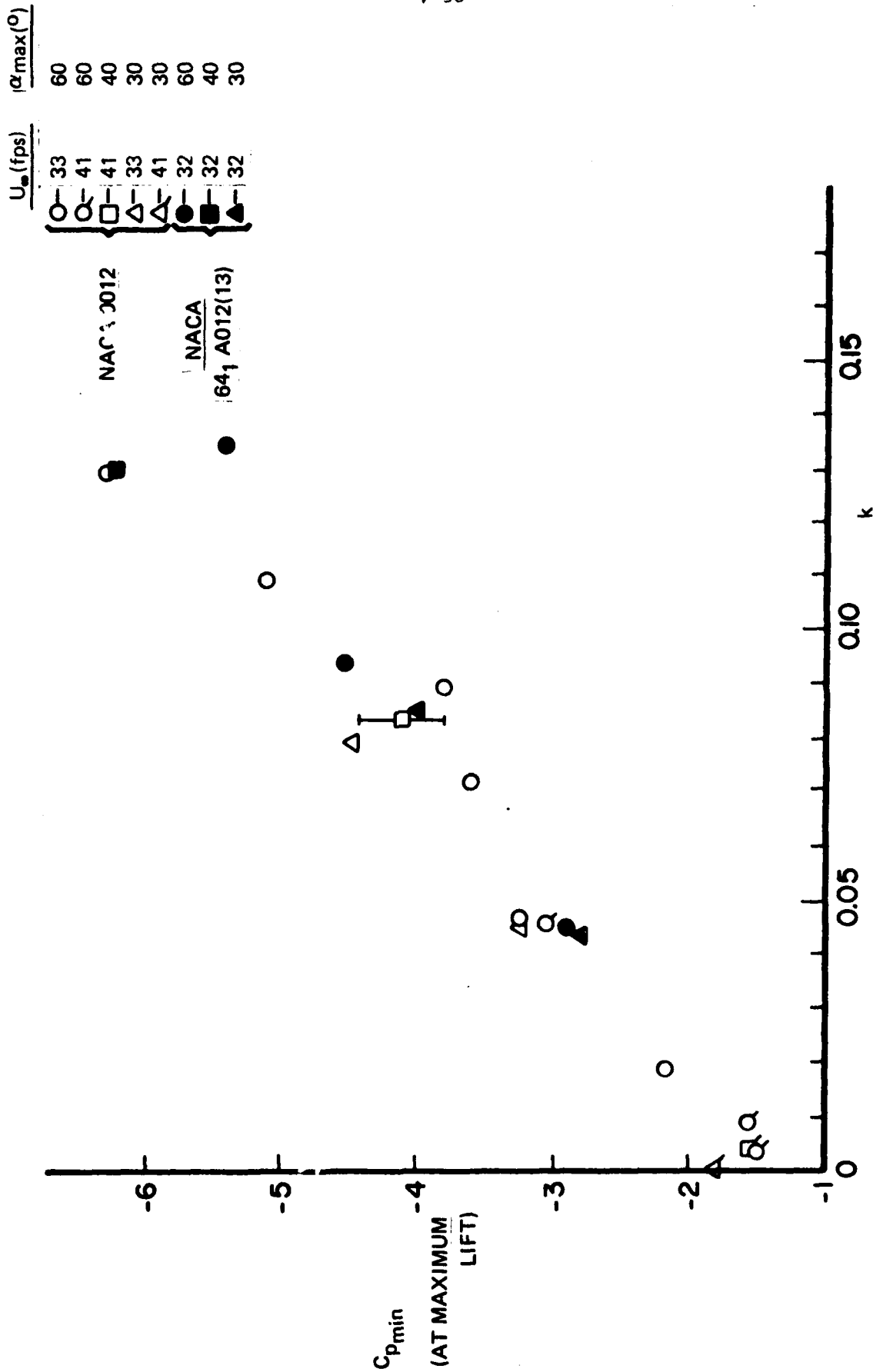
FIGURE V-31
MINIMUM PRESSURE COEFFICIENT OR MAXIMUM LIFT — VARIATION WITH PITCH RATE

VI. SUMMARY AND CONCLUSIONS

Results of the present investigation involving those measurements which focus on the effects of constant pitch rate airfoil motions can be summarized as follows:

(a) The generation of airfoil constant pitch rate motions over a wide range of parametric flow conditions has been successfully demonstrated using the FJSRL two-degree-of-freedom unsteady motion apparatus. Cycle-to-cycle motion repeatability was observed to be excellent.

(b) For both airfoils investigated, increases in pitch rate were found to further delay the onset of unsteady leading edge separation as inferred from upper airfoil surface pressure distributions. However, the delay was found to increase less rapidly at progressively higher values of the dimensionless pitch rate.

(c) At incidence angles well in excess of the static stall value, the appearance of a steep suction spike on the airfoil upper surface was followed by its subsequent reduction in intensity and spatial diffusion as it traversed downstream. This phenomenological behavior, apparent to varying degrees in all of the experiments, is consistent with that observed by other investigators principally in harmonically-induced dynamic stall experiments. The evolution of this peak is believed to be controlled by the behavior of the unsteady leading edge separation vortex.

(d) Maximum lift coefficients in excess of three times the steady flow (no motion) static lift coefficient were observed in some cases at high pitch rates.

(e) A dimensionless lift impulse function was defined and proposed as a suitable measure for comparing the effectiveness of various motion types on sustained lift optimization.

(f) It was observed that neither the highest motion rates nor the largest pitch amplitudes resulted in the maximum values of the pitch impulse parameter. For rigid airfoil rotation at constant rate, the maximization of the unsteady lift appears to occur at intermediate values of the pitch rate. For a given rate ($\dot{\alpha}$), the optimum impulse occurs when the maximum incidence angle closely approximates the angle at which leading edge separation would have been expected had the pitch-up motion continued unaltered.

VII

ACKNOWLEDGEMENTS

VIII

REFERENCES

1. Carr, L.W., McAlister, K. W., and McCroskey, W. J., "Analysis of the Development of Dynamic Stall Based on Oscillating Airfoil Experiments," NASA TN D-8382, January 1977.

2. McCroskey, W. J., Carr, L. W., and McAlister, K. W., "Dynamic Stall Experiments on Oscillating Airfoils," AIAA Journal, Vol. 14, No. 1, January 1976, pp. 57-63.

3. McCroskey, W. J., "Some Current Research in Unsteady Fluid Dynamics - The 1976 Freeman Scholar Lecture," Journal of Fluids Engineering, March 1977, pp. 8-39.

4. McAlister, K. W., Carr, L. W., and McCroskey, W. J., "Dynamic Stall Experiments on the NACA 0012 Airfoil," NASA Technical Paper 1100, January 1978.

5. Ham, Norman D., "Aerodynamic Loading on a Two-Dimensional Airfoil During Dynamic Stall," AIAA Journal, Vol. 6, No. 10, October 1968, pp. 1927-1934.

6. Ham, N. D., and Garelick, M. S., "Dynamic Stall Considerations in Helicopter Rotors," Journal of the American Helicopter Society, Vol. 13, April 1968, pp. 49-55.

7. McCroskey, W. J., McAlister, K. W., Carr, L. W., Pucci, S. L., Lambert, O. and Indergand, R. F., "Dynamic Stall on Advanced Airfoil Sections," Journal of the American Helicopter Society, July 1981, pp. 40-50.

8. McCroskey, W. J. and Pucci, S. L., "Viscous-Inviscid Interaction on Oscillating Airfoils in Subsonic Flow," AIAA Journal, Vol. 20, No. 2, February 1982, pp. 167-174.

9. Ham, N. D., "Some Recent MIT Research on Dynamic Stall," Journal of Aircraft, Vol. 9, No. 5, May 1972, pp. 378-379.

10. Williams, J. C., III, "Mathematical Criterion for Unsteady Boundary-Layer Separation," AIAA Journal, Vol. 18, No. 3, March 1980, pp. 335-337.

11. McAlister, K. W. and Carr, L. W., "Water-Tunnel Experiments on an Oscillating Airfoil at Re = 21,000," NASA TM-78446, March 1978.

12. Rossow, V. J., "Lift Enhancement by an Externally Trapped Vortex," AIAA Paper 77-672, AIAA 10th Fluid and Plasmadynamics Conference, Albuquerque, NM, June 27-29, 1977.

13. Huang, M. K. and Chow, C. Y., "Trapping of a Free Vortex by Joukowski Airfoils," AIAA Journal, Vol. 20, No. 3, March 1982, pp. 292-298.

14. Saxena, L. S., Fejer, A. A., and Morkovin, M. V., "Effects of Periodic Changes in Free Stream Velocity on Flows Over Airfoils Near Static Stall," Nonsteady Fluid Dynamics, Proceedings of the Winter Annual Meeting ASME, San Francisco, CA, December 10-15, 1978, pp. 111-116.

15. Retelle, J. P., "Unsteady Boundary Layer Flow Reversal in a Longitudinal Oscillating Flow," Frank J. Seiler Laboratory Technical Report, SRL-TR-78-0006, August 1978.

16. Hsieh, B. J., "Dynamic Stall on Oscillating Airfoils in Oscillating Free Streams," Ph.D. Dissertation, Illinois Institute of Technology, Chicago, IL, May 1979.

17. Favier, D., Maresca, O., and Rebont, J., "Dynamic Stall Due to Fluctuations of Velocity and Incidence," AIAA Journal, Vol. 20, No. 7, July 1982, pp. 865-871.

18. Ho, C. M. and Chen, S. H., "Unsteady Wake of a Plunging Airfoil," AIAA Paper 80-1446, AIAA 13th Fluid and Plasma Dynamics Conference, Snowmass, CO, July 14-16, 1980.

19. Kramer, Max, "Die Zunahme des Maximalauftriebes von Tragflügeln bei plötzlicher Anstellwinkel-vergröszerung (Böeneffekt)," Zeitschrift für Flugtechnik und Motorluftschiffahrt, Vol. 23, No. 7, April 14, 1932, pp. 185-189.

20. Kawashima, S., Yamasaki, M. and Ando, Y., "Aerodynamic Response for the Airfoil Experiencing Sudden Change in Angle of Attack," Nihon Koku Gakkai; Transactions of the Japan Society for Aeronautical and Space Sciences, Vol. 21, August 1978.

21. "Subsonic and Trisonic Wind Tunnel Facilities," Department of Aeronautics, U.S. Air Force Academy, 1977.

22. Francis, M. S., Keesee, J. E., and Retelle, J. P., Jr., "A Two-Degree-of Freedom Oscillator for Unsteady Aerodynamics Applications," FJSRL-TR-81-0007, ADA-102356, F. J. Seiler Research Laboratory, July 1981.

23. Hegna, H. A., "The Numerical Solution of Incompressible Turbulent Flow Over Airfoils," AIAA 81-0047, AIAA 19th Aerospace Sciences Meeting, St. Louis, MO, January 12-15, 1981.

IX

APPENDIX

Table III-1

Model Motion Parameters – NACA 0012

			Pitch Motion		Translational Motion		
Test #	U_∞(fps)	Type[+]	$k = \dot{\alpha}c/2U_\infty$ [*]	$\alpha_{max}^{(o)}$	Type[+]	Rate/Freq	Notes
1	41.6	A	0.001	31	None		Constant pitch
2	41.2	A	0.001	22			rate motion
3	41.2	A	0.005	57			only
4	41.3	A	0.005	41			
5	41.9	A	0.005	22			
6	41.9	A	0.009	61			
7	41.4	A	0.009	41			
8	41.4	A	0.010	21			
9	41.7	A	0.018	60			
10	33.1	A	0.047	60			
11	41.2	A	0.046	60			
12	67.9	A	0.044	58			
13	41.7	A	0.045	30			
14	40.9	A	0.073	57			
15	33.1	A	0.089	56			
16	33.2	A	0.079	34			
17	33.2	A	0.081	25			
18	33.2	A	0.080	15			
19	33.2	A	0.108	55			
20	33.9	A	0.130	55			
21	41.4	B	0.042	27	None		Constant pitch
22	33.2	B	0.076	23			w/abrupt return
23	33.6	B	0.101	22			to initial incidence angle
24	41.5	C	$\ddot{\alpha} = .45$ rad/s^2	56	None		Constant pitch
25	41.2	C	$\ddot{\alpha} = 16.1$ rad/s^2	62			acceleration
26	41.9	C	$\ddot{\alpha} = 66.4$ rad/s^2	61			only
27	41.0	C	$\ddot{\alpha} = 152.0$ rad/s^2	60			
28	41.3	C	$\ddot{\alpha} = 200.2$ rad/s^2	61			
29	42.6	A	$k = 0.058$	27	F	$\ddot{x} = 19.7$ ft/s^2	Combined motion w/delayed pitch up

[+]see Figure III-3

[*]dimensionless parameter, k, based on pitch rate unless otherwise noted

Table III-2

Model Motion Parameters – NACA $64_1A012(13)$

		Pitch Motion			Translational Motion		
Test #	U_∞(fps)	Type[+]	$k = \dot{\alpha}c/2U_\infty$	$\alpha_{max}^{(o)}$	Type[+]	Rate/Freq	Notes
30	32.1	A	0.045	37	None		Constant pitch rate
31	32.1	A	0.045	58			motion only
32	32.1	A	0.084	37			$k = \dot{\alpha}c/2U_\infty$
33	32.1	A	0.094	59			
34	32.1	A	0.131	38			
35	32.5	A	0.136	59			
36	32.5	A	0.171	39			
37	32.8	A	0.173	60			
38	32.1	A	0.211	59			
39	32.1	B	0.043	29			
40	32.1	None		12	E	$\dot{x} = -5.0$ fps	Airfoil at fixed
41	32.1	None		20	E	$\dot{x} = -5.0$ fps	incidence
42	32.5	A	0.137	19	E	$\dot{x} = -4.8$ fps	Combined motion w/
43	32.1	A	0.143	38	E	$\dot{x} = -5.1$ fps	delayed start in pitch
44	32.1	A	0.143	20	E	$\dot{x} = 4.9$ fps	
45	32.2	A	0.145	39	E	$\dot{x} = 4.8$ fps	
			$k' = \omega c/2U_\infty$	$\alpha_f^{(o)}$			
46	32.1	D	0.133	5	None		$\alpha_{max} = 30^\circ$, all harmonic
47	32.1	D	0.134	10			cases
48	32.0	D	0.135	16			
49	32.0	D	0.135	21			
50	32.1	D	0.135	26			
51	32.1	D	0.244	10			
52	32.1	D	0.246	26			
53	32.1	D	0.373	10			
54	32.1	D	0.375	26			

[+]see Figure III-3

END

FILMED

11-83

DTIC
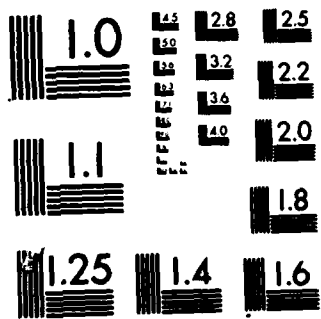
MICROCOPY RESOLUTION TEST CHART
NATIONAL BUREAU OF STANDARDS-1963-A

SUPPLEMENTARY

INFORMATION

AN INVESTIGATION OF AIRFOIL DYNAMIC STALL
WITH LARGE AMPLITUDE MOTIONS

ERRATA

The following corrections should be annotated with reference to the figures and illustrations:

Page	Figure Number	Correction
II-21	II-7	An additional pressure transducer should appear at the airfoil leading edge, $x/c = 0.0$; note with "x".
III-8,9	III-1,2	Axes labels missing; Abscissa label is "x/c"; Ordinate label is "C_p".
III-12 – III-30	III-5 – III-10	Axes labels missing; Abscissa label is "x/c"; Ordinate label is "C_p".
III-16	III-6	Figure (H) label incorrect; should be labeled "34.4°".
IV-6	IV-2	Change label from "Steady Flow Lift Coefficients, NACA 0012 Airfoil" to "Steady Flow Lift Coefficients, NACA $64_1A012(13)$ Airfoil".
IV-17	IV-13	Change location label on ordinate from "$C_{l_{max}}$" to "$C_{l_{max_s}}$".
IV-18	IV-14	Change location label on abscissa from "$t_{max} - C_l$" to "$t_{C_{l_{max}}}$".
IV-19	IV-15	4 labels in legend should be changed from "...,$_{max}$ =" to "...,α_{max} =".
V-21	V-1	Ordinate label missing; label should read "$(x/c)_{P_{min}}$".
V-33	V-13(a)	Label "(A)" should read "(a)"; ordinate label "$\alpha_{C_l mx}$" should read "$\alpha_{C_{l_{mx}}}$".

Page	Figure Number	Correction
V-34	V-13(b)	Ordinate label "$\alpha_{C_{\ell mx}}$" should read "$\alpha_{C_{\ell_{mx}}}$".
V-35	V-14(a)	Ordinate label "$C_{\ell_{MX}}$" should read "$C_{\ell_{mx}}$".
V-37,38	V-15	Ordinate label "$C_{M_{MN}}$" should read "$C_{M_{mn}}$".
V-39	V-16(a)	In legend, 3rd line from top should note "$\diamondsuit$ $\alpha_{max} = 60^O$, $U_\infty = 68$ fps".
V-41	V-17(a)	Ordinate label "$\overline{\Delta C_\ell}$" should read "$\overline{\Delta C_\ell}$"; in legend, 6th label from top should be changed from "O" to "⊘".
V-42	V-17(b)	Figure title should read "Variation with α_{max}".
V-44	V-19(a)	In legend, 6th symbol from top should be changed from "O" to "⊗".
V-48 – V-51	V-21 – V-24	Abscissa label should read "$(x/c)_{P_{min}}$".
V-50	V-23	In legend, change "NACA $64, A012(13)_1$..." to "NACA $64_1 A012(13)$, ...".
V-51	V-24	In figure title, change "... fps, $_{max} = 60^O$" to "... fps, $\alpha_{max} = 60^O$".
V-58	V-31	In figure title, change "... OR MAXIMUM..." to "... AT MAXIMUM...".